Special Reports
No. 6

The Modification of Electromagnetic Scattering Cross Sections in the Resonant Region

A Symposium Record, Volume I

J.K. SCHINDLER   1/Lt, USAF

R.B. MACK

Editors

Preface

This is the fii st volume of a two-volume collection of papers presented at the Symposium on the Modification of Electromagnetic Scattering Cross St ctions in the Resonant Region held on 4 June 1963 at the Air Force Cambridge Research Laboratories.

Papers in the present volume establish the need for techniques which significantly reduce the electromagnetic scattering cross section of bodies in the frequency range where wavelength is comparable to the body size. One technique which holds promise for use in the resonance region is impedance loading of the body surface. This technique is discussed in several papers. Other papers give results demonstrating the effects that material properties have in changing cross sections in the resonant region.

Volume II of the collection is cla sified. It contains the papers "Radar Absorbing Materials for the Resonance Region (U)" by K. M. Siegel and "Comm nt on Some Radar Camouflage Problems (U)" by W.F. Bahret.

Contents

This Document Contains
Missing Page/s That Are
Unavailable In The
Original Document

OR are
Blank. pg
that have
Been Removed

**BEST
AVAILABLE COPY**

Foreword

We organized this conference to emphasize resonant region scattering because
we thought there were significant results to report. Using the technical ideas and
techniques discussed June 4th, we believe the scattering properties of important
radar targets can be significantly modified by reactive loading recessed into the
targets. As is often the case in science, the experimental findings are out in ad-
vance of theoretical and even conceptual explanations.

We were gratified by the high-quality papers and audience at this symposium.
It is hoped that you will now look at this record critically to find the contradictions,
mistakes, and anomalous data. A sound national effort on this theme should add
another tool for controlling the scattering of bodies.

In my opinion the unsolved problems are these: What other general shapes
besides the electric dipole (rod) or string of dipoles (multiply loaded rod) will have
a minimum total scattering cross section upon application of suitable localized
loading? Montgomery[1] hints that there might be a class of symmetrical shapes
with such properties. What is, for example, the suitable loading to reduce the
total cross section of a body representable by both electric and magnetic dipoles?
What is the significance of adding loss to the terminal loads on longer rods[2] (over
$\lambda/2$ in length) to maximize scatter reduction? How does one make the transition
from a frequency range where specular reflections are dominant and where matched
dipoles[3] or ordinary absorbing materials provide minimum back scattering to the

resonant region where slightly lossy and lossless reactive loadings appear to do the job? Does the Conductron paper's discussion[4] of surface impedance loading suitable for resonant shapes answer this question, or is the situation significantly different for terminal loading with discrete network impedance ports on the body? Can the reactive loading method be used to redirect scattering in the forward scatter direction, for example, as absorbers tend to do, rather than reduce the total cross section?

Why do the values of inductive reactive loading needed to minimize scattering cross section decrease appreciably as the rod is made thicker?[5] Why is the band-width better with dual loading than with single (mid-point) loading on rods of otherwise similar shapes? Is the desired reactive loading vs. frequency for minimum back scatter approximately a constant value as the data show?[6] When the input impedances vs. frequency characteristics for positions of loading on a scatterer are known, can they be synthesized by known passive networks or will the desired frequency response violate Foster's reactance theorem? Do the external modes on the object (spherical harmonics in the case of a sphere, for example) dictate the proper positions for the terminal loadings and even the internal cavity structure in order to realize the proper phase relations of the surface currents to produce minimum, total, or differential cross section? Why does the bistatic radar cross section of a rod center loaded to produce minimum monostatic radar scattering for all attitudes increase after a bistatic angle of 20 to 30 degrees? Can scattering from two orthogonal polarization vectors be treated independently by suitable orthogonal loading on the objects?

When the volume of the object rather than its surface is available, what values of the constitutive parameters will augment, reduce, or otherwise modify the scattering of resonant objects? The work of Avco[7] (plasma media) and Atlas[8] (dielectrics) hints at unusual possibilities here.

Can reactive loading methods be successfully combined with shaping or absorbing techniques to cover a large bandwidth for a large angular region of observation?

There are provisional and perhaps correct answers to all these questions. Probably they will all be answerable and fall like a row of dominoes as our understanding of the resonant region scattering and the influence of strategically located terminal loads improves.

In spite of unanswered questions, some very useful engineering results are available. Thick cargo-carrying bodies can be reduced significantly in scatter cross section for all attitudes over the peak of the first resonance hump. This loading can be recessed into the body and with coaxial or lumped network impedance could be packaged pretty conveniently. At Ohio State[9] and Boeing[10] good strides are being made to combine and control antenna and object scattering by judicious use of impedance loading. I hope the prodding, provocation, and discussions of this

conference will help to bolster the theoretical picture and bring useful applications rather soon.

<div align="right">C. J. SLETTEN</div>

References

1. C. G. Montgomery, R. H. Dicke, and E. M. Purcell, Principles of Microwave Circuits, McGraw-Hill, New York, 1948, pp 329-3.3.

2. Kun-Mu Chen, and Valdis Liepa, The Minimization of the Backscattering of a Cylinder by a Central Loading, Vol. I this report.

3. Universität Göttingen Technical Reports done under the indicated Air Force Cambridge Research Laboratories contract:

   a. H. J. Schmitt, Microwave Optics and Absorption of Electromagnetic Energy; Phase C: Absorption of Micro-waves by Resonance Absorbers, Contract No. AF61(514)-799, 1955.

   b. H. J. Schmitt, Absorption and Transmission of Electromagnetic Waves; Phase E: Absorption of Micro-waves by Multiple Resonance Absorbers, Contract No. AF61(514)-876, 1956.

   c. H. J. Schmitt, Absorption and Transmission of Electromagnetic Waves; Phase A: Absorption of Micro-waves by Multiple Resonance Absorbers, Contract No. AF61(514)-1041, 1957.

   d. F. Wiekhorst, Absorption and Transmission of Electromagnetic Waves; Phase B: Absorption of Micro-waves by Magnetic Resonance Absorbers (Magnetic Dipole Absorbers), Contract No. AF61(514)-1041, 1957.

4. K. M. Siegel, Radar Absorbing Materials for the Resonance Region (U), Vol. II this report.

5. C. J. Sletten, et al, Scattering from Thick Reactively Loaded Rods, Vol. I this report.

6. B. -O. Ås, and H. J. Schmitt, Back-scattering Cross Section of Reactively Loaded Cylindrical Antennas, Cruft Laboratory, Harvard University, Scientific Report No. 18, Contract No. AF19(604)-786, AFCRL.

7. N. Pedersen, and L. Malmstrom, Absorption Resonance Effects in Plasma Spheres, Vol. I this report.

8. D. Atlas, et al, Back-scatter by dielectric spheres (refractive index ~ 1.6), IEEE Trans. on Ant. and Prop., AP-11: 68, 1963.

9. E. Kennaugh, Research on Loaded Terminal Scatterers, Vol. I this report.

10. W. P. Hansen, Backscatter Reduction of Long, Thin Bodies by Impedance Loading, Vol. I this report.

This Document Contains
Missing Page/s That Are
Unavailable In The
Original Document

OR are
Blank. pg
that have
Been Removed

**BEST
AVAILABLE COPY**

THE MODIFICATION OF ELECTROMAGNETIC SCATTERING CROSS SECTIONS IN THE RESONANT REGION

I. Some Thoughts on Scattering Cross Sections in the Resonance Region

Richard B. Mack and Philipp Blacksmith, Jr.
Microwave Physics Laboratory
Air Force Cambridge Research Laboratories
Bedford, Massachusetts

One certain way to start an argument in even a small group of people familiar with electromagnetic scattering is to use the expression "resonance region". Someone will immediately object that for most shapes there is no resonance in the usual circuit sense of zero susceptance and maximum current. Someone else will point to the maxima and minima in curves of scattering cross section vs. frequency, and then the discussion really begins. Such instances simply reaffirm what most of us readily admit - that when the characteristic dimensions of a target are of the same order of magnitude as the wavelength, the electromagnetic properties are immersed in a considerable cloud of mystery.

A thin dipole is by far the simplest of such targets, for it has essentially a one-dimensional line current. In this case, the measured and computed back-scatter cross sections, current distributions, and driving-point admittances can

be closely correlated to give a clear picture of its behavior. However, as soon as currents on the scatterer are permitted to have additional components, such clarity vanishes. The sphere, for example, is a simple three-dimensional shape that still requires four to seven terms of the Mie solution to describe its properties, even when ka is only 1.0 to 1.5. Already there is some difficulty in developing an intuitive feeling for the results. For most shapes, including the very interesting complex ones, even this kind of a solution is not presently available when the body dimensions are comparable in size to the wavelength of the impinging wave. If the scatterer is made of dielectric or lossy material, the situation is further complicated. The result is that our ability to use or modify target properties in the resonance region is severely limited.

Determining the scattering cross sections from an interesting shape and learning to modify them are the first steps necessary toward an ultimate goal of controlling the scattering properties - developing a simple positive method to make the cross sections appear larger or negligibly small as desired. Alternatively, if energy is to be received by or transmitted from the scatterer, the problem is to place antenna structures so they intercept the currents with maximum efficiency or excite the body to concentrate radiated energy in a desired direction.

Although the scattering properties of a target are usually examined by themselves in graphs of σ vs. angle or ka, their principal application is in determining how susceptible a target may be to detection by a radar. It is interesting to examine some common cross sections from this point of view. The radar range equation is

$$R_{max} = \left[\frac{P_t \, G^2 \, \lambda^2 \, \sigma}{S_{min} \, (4\pi)^3} \right]^{1/4} \tag{1}$$

where R_{max}, P_t, G, S_{min}, λ are, respectively, the maximum range, the power transmitted, antenna gain, minimum detectable signal, and the wavelength. σ is the backscatter cross section of the target. Note that P_t, S_{min}, G, and λ are properties of the radar and independent of the target, whereas the backscatter cross section is not an exclusive property of the target because it is a function of the wavelength.

The obvious and most important conclusion from Eq. (1) is that large changes in σ are necessary to produce significant changes in R_{max}. For example, a 12 db decrease in σ only decreases the maximum detectable range by half; a 40 db decrease is required in σ to reduce R_{max} by 90 percent. This is illustrated in Figure 1 for a radar which can just detect a target of 1 m^2 cross section at 1000 miles.
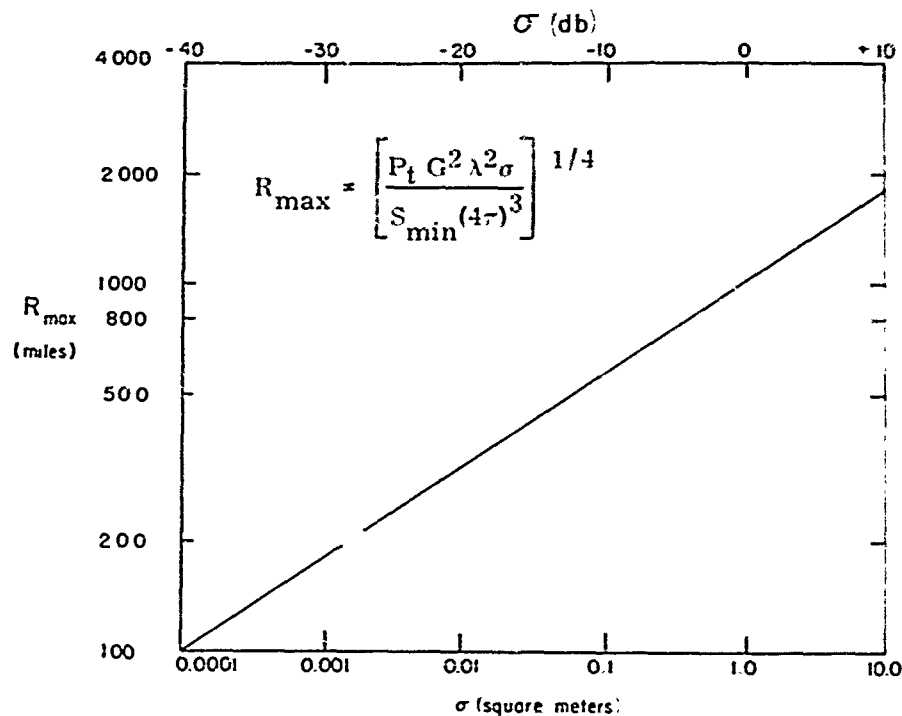
Figure 1. Variation of Maximum Range With Backscatter Cross Section. Normalized to 1000 miles for a 1 m² target.

In Figure 2 the backscatter cross sections of several metal targets are compared as a function of k"a", where "a" is a characteristic dimension for each particular target and is listed on the figure. Data for the sphere is theoretical; that for the other curves is experimental [1-5] For values of k"a" greater than 7 or 8 , there are large differences between the values of σ from a sphere and those from a flat plate at normal incidence However, when k"a" is about 1. 1, the cross sections from all but the dipole are within a 4db range. This produces a corresponding difference in R_{max} of about ±12 percent from an average value. If the flat plate, an extreme example, is excluded there is a considerable range of k"a" over which the remaining curves are separated by not more than 12 db, which corresponds to a variation of 2 to 1 in R_{max} While this is a significant decrease in R_{max} it could be compensated by existing state-of-the-art techniques For example, a larger antenna producing 6 db additional gain would be sufficient to restore the original value of R_{max} .

Also, when k"a" is near 1, the variation of backscatter cross section with target aspect for the different shapes is very similar to the variation observed from a dipole. This is further discussed and illustrated in the paper by Sletten, et al.

Consider now the detection of a class of targets having different shapes but approximately the same size. What frequency band should be used to detect the

4

targets at the greatest distances? Assume P_t/S_{min} and the antenna gain, G, to be constant. The target size will be considered constant and frequency will be the variable. Actually, the powers and sensitivities which are available make the ratio P_t/S_{min} decrease as the frequency is increased. Assuming the antenna gain to be constant means that once the desired frequency is determined, the antenna will be made sufficiently large to provide the required gain. At lower frequencies where large reflectors become impractical, multiplate techniques might be used. The ideal would be to always design the antenna so it produces the maximum obtainable gain which, from considerations of mechanical tolerances and coherence, is currently estimated to be about 65 to 70 db. Within a chosen frequency band, the antenna will have a fixed size and its gain will exhibit the usual frequency dependence. This is not considered in the following.

With these assumptions, the radar range equation can be written as

$$R_{max} = K \left[\sigma \lambda^2\right]^{1/4} \quad , \quad K = \left[\frac{P_t G^2}{(4\pi)^3 S_{min}}\right]^{1/4} \tag{2}$$

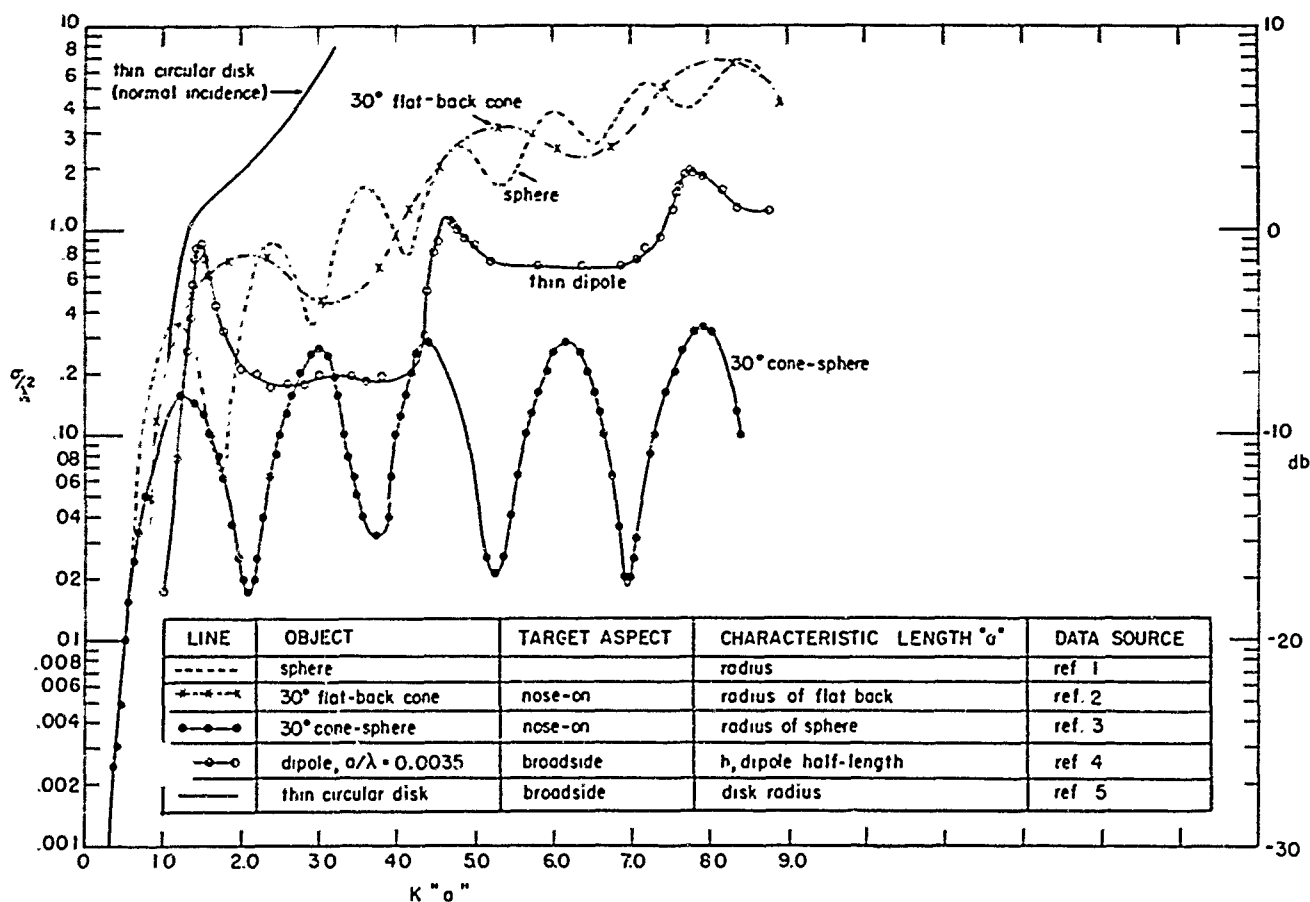| LINE	OBJECT	TARGET ASPECT	CHARACTERISTIC LENGTH "a"	DATA SOURCE
------	sphere		radius	ref 1
+-·+--·+	30° flat-back cone	nose-on	radius of flat back	ref. 2
•—•—•	30° cone-sphere	nose-on	radius of sphere	ref. 3
-○—○	dipole, a/λ = 0.0035	broadside	h, dipole half-length	ref 4
———	thin circular disk	broadside	disk radius	ref 5

Figure 2. Comparison of Scattering Cross Sections for Various Shapes

Thus, unless σ varies at least as f^2 or $1/\lambda^2$, R_{max} will decrease as the frequency is increased. In the Rayleigh region where the target dimensions are much smaller than a wavelength, the backscatter cross sections of many objects are known to vary as $1/\lambda^4$. With such targets and frequencies R_{max} changes as $\sqrt{f}$ where f is the frequency. The Rayleigh backscatter cross section of a sphere, for example, is

$$\sigma = \frac{9\lambda^2}{4\pi}\,(ka)^6 \qquad\qquad . \tag{3}$$

and

$$R_{max} = K\pi\,\frac{9\pi}{4}\,\frac{D}{\sqrt{\lambda}} \quad \text{or} \quad \frac{R_{max}}{KD} = \frac{5.122}{\sqrt{k_1}} \tag{4}$$

where D = sphere diameter = $2a$, $k = \frac{2\pi}{\lambda}$, $k_1 = \frac{\lambda}{D}$.

At the other frequency extreme, the optics region where target dimensions are much larger than a wavelength, the backscatter cross sections of many objects are independent of frequency. With these targets and frequencies, R_{max} changes as $\frac{1}{\sqrt{f}}$, decreasing as the frequency is increased. The optics cross section of a sphere, for example, is

$$\sigma = \pi a^2 \tag{5}$$

and

$$R_{max} = K\left(\frac{\pi}{4}\right)^{\frac{1}{4}}D^{\frac{1}{2}}\sqrt{\lambda} \quad \text{or} \quad \frac{R_{max}}{KD} = 0.9414\sqrt{k_1} \quad . \tag{6}$$

In contrast, a flat plate which is much larger than a wavelength gives

$$\sigma = \frac{4\pi A^2}{\lambda^2}\,, \quad A = \text{plate area} \tag{7}$$

and

$$R_{max} = K(4\pi)^{\frac{1}{4}}\,D \qquad\qquad \text{square plate } (D = \text{edge length}) \tag{8}$$

$$R_{max} = K(4\pi)^{\frac{1}{4}} \sqrt{\pi/4} \;\; D \qquad \text{circular plate (D = diameter)} \tag{9}$$

so that R_{max} is independent of frequency.

When k"a" is between about 0.2 and 10, the so-called resonance region, values of σ/λ^2 can be taken from Figure 2. Let T be a given value of σ/λ^2 in Figure 2. Then

$$\frac{R_{max}}{KD} = T^{\frac{1}{4}} k_1 \;\; , \;\; k_1 = \lambda/D \tag{10}$$

and the usual oscillations of σ vs. k"a" are modulated by the dependence on λ (or 1/f).

Some typical curves of the normalized maximum range, $\frac{Rmax}{KD}$, vs. k"a" are given in Figure 3 for the backscatter cross sections of Figure 2. Again, "a" is a characteristic length for the target as given in the table of Figure 2, and D may be considered as an average or most probable target size equal to 2 "a". Under the assumption discussed above and for the targets considered, Figure 3 clearly demonstrates the desirability of choosing a frequency which either places k"a" between about 0.5 and 2 or makes k"a" as low as is compatible with the obtainable antenna sizes. Since for many targets D is quite large, Figure 3 also emphasizes the need for physically large antennas which have high gain at the lower frequencies.

The most commonly discussed methods of modifying the cross sections of targets are shaping and the use of absorbers. Figures 2 and 3 indicate that shaping is effective at larger values of k"a" but is not very effective when k"a" is near 1. Likewise, absorbers are effective at larger k"a" values, but at smaller k"a" values they are either not particularly effective or are bulky at lower frequencies.

Most of the symposium papers are concerned with a third method of modifying the cross sections. This method has been called "reactive loading" and is especially applicable to targets in the range of small k"a" and at lower frequencies where the more common methods lose their effectiveness. Reactive loading holds the further promise of providing a simple means of not just modifying but of actually controlling the cross sections by simply closing or opening a switch.

It is hoped that the symposium and its record will not only lead to improved techniques for controlling scattering cross sections in the resonance region, but will also lead to a better understanding of basic scattering properties when the object dimensions are comparable in size to a wavelength.
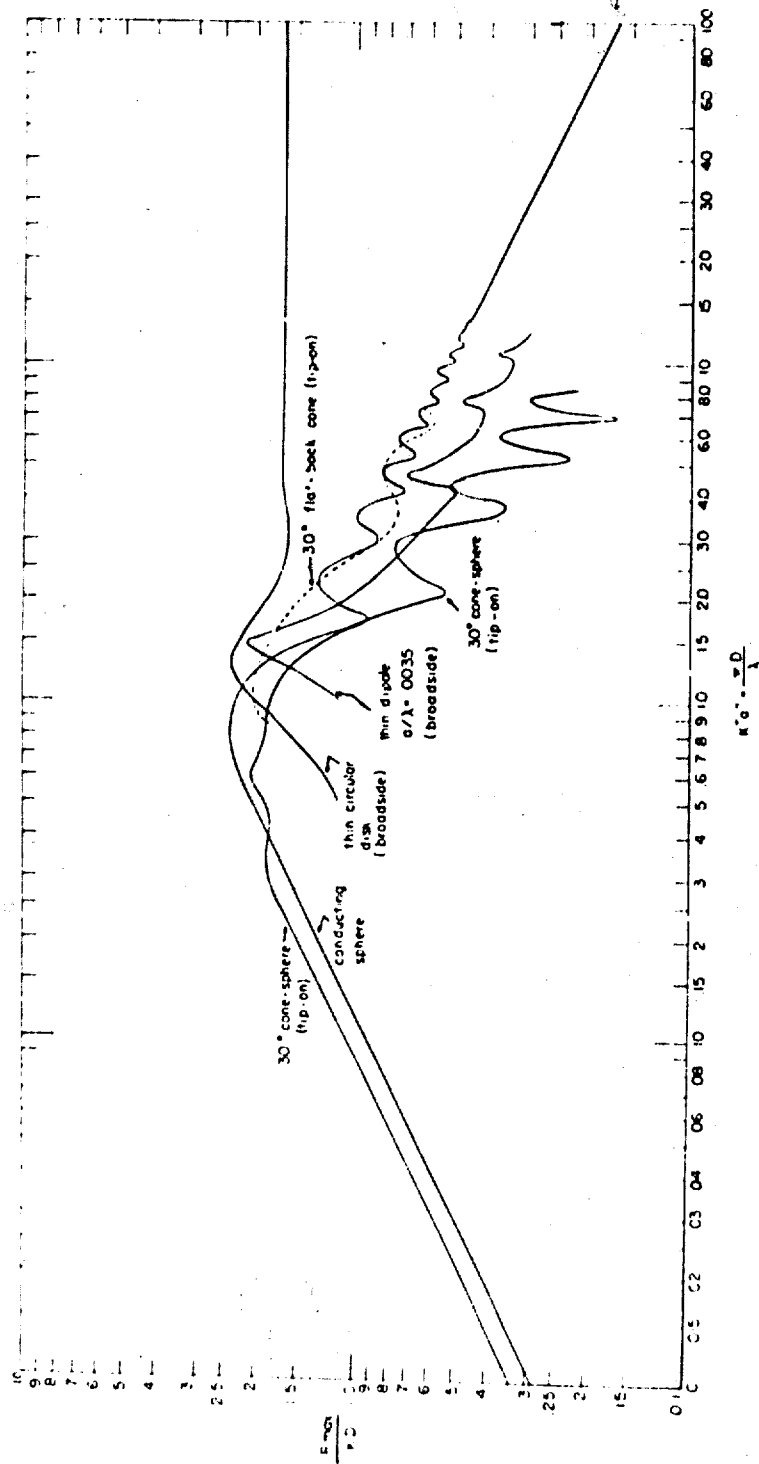
Figure 3. The Normalized Maximum Range for Detection of Targets of Figure 2.

References

1. M. E. Bechtel, Scattering Coefficients for the Backscattering of Electro-magnetic Waves from Perfectly Conducting Spheres, CAL Report No. AP/RIS-1, Cornell Aeronautical Laboratory, Inc., Buffalo 21, N. Y., 1962.

2. J. C. Keys and R. I. Primich, The Radar Cross Section of Right Circular Metal Cones - 1, DRTE Report No. 1010, Defence Research Telecommuni-cations Establishment, Ottawa, Canada, 1959.

3. R. E. Kleinman and T. B. A. Senior, Diffraction and Scattering by Regular Bodies - II: the Cone, S. R. No. 5, p. 134, Studies in Radar Cross Sections XLVIII, University of Michigan, Radiation Laboratory, Ann Arbor, Mich., 1963.

4. J. Sevick, Experimental and Theoretical Results on the Back-Scatter Cross Sections of Coupled Antennas, T. R. No. 150, The Cruft Laboratory, Harvard University, Cambridge, Mass., 1952.

5. R. G. Kouyoumjian, Calculation of the Echo Area of Several Scatterers of Simple Geometry by the Variational Method, The McGill Symposium Record, Part II, AFCRC-TR-59-118(II), 1959.

6. D. L. Moffatt, Low Radar Cross Sections, the Cone-Sphere, T. R. No. 1223-5, The Antenna Laboratory, Ohio State University, Columbus, Ohio, 1962.

II. The Minimization of the Backscattering of a Cylinder By Central Loading*

Kun-Mu Chen and Valdis Liepa
The Radiation Laboratory
The University of Michigan

Abstract

A theoretical and experimental study of the minimization of the backscattering of of a thin cylinder by central loading is presented. The induced current on a centrally loaded cylinder illuminated by a plane wave at normal incidence is theoretically determined and experimentally measured. The magnitude and phase of the induced current can be greatly changed by a central impedance The optimum loading to achieve zero backscatter in the broadside direction has been determined for a thin cylinder shorter than 2 wavelengths. The optimum central impedance for the purpose of minimizing the broadside backscattering from a thin cylinder over a wide range of frequencies has also been determined.

!

1. INTRODUCTION

The first known use of reactive loading to minimize scattering was by Iams[1] who applied the technique to metallic posts used in a parallel plate pillbox structure. The idea of using this technique to decrease the radar cross section of objects in space was suggested and employed by Sletten[2] in 1950. The backscattering of a cylinder with and without a central load has been studied by several authors.[3,4,5] The information available to date is that if a cylinder of near a half wavelength is loaded with a high reactive impedance at its center, its backscattering cross section can be significantly reduced. The exact way in which the reactive loading behaves and the optimum method of loading are still not well understood. It is the purpose of this paper to present a theoretical and an experimental study of the subject in order to clarify the nature of the loading and also to present an optimum loading for reducing to zero the broadside backscattering from a cylinder.

We study the problem from the viewpoint of the induced current on a metallic object illuminated by an electromagnetic wave, since the induced current plays the most fundamental role in the scattering. We consider a perfectly conducting cylinder with a small radius and a length shorter than 2 wavelengths, and assume that a plane wave is incident broadside on the cylinder. A current is induced on the cylinder by the incident plane wave, and this induced current in turn produces a scattered electromagnetic field. If an impedance is added at the center of the cylinder, the induced current and the scattered field are modified. There are three methods by which the addition of a central impedance can reduce the scattered field. These are: (a) by reducing the magnitude of the induced current; (b) by reversing the phase of the induced current over some part of the cylinder; and (c) by a combination of (a) and (b). The third method is the most effective for reducing the scattering, and we shall show that with central loading it is possible to reduce the broadside backscattering to zero.

In Section 2, we determine theoretically the induced current on the cylinder with central loading by applying an integral equation method. This induced current is expressed as a function of cylinder dimensions and the central impedance. In Section 3, we study the induced current on a cylinder without loading. In Section 4, the induced current on a cylinder loaded with an infinite impedance is found. In Section 5, we study the induced current on a cylinder with a resonant length for various central impedances. In Section 6, the induced current on a cylinder with an anti-resonant length is studied for various central impedances. Through Sections 3 to 6, theoretical and experimental results are compared. In Section 7, the experimental method is described. In Section 8, we obtain the optimum impedance for zero broadside backscattering from a thin cylinder. The optimum impedance required to minimize the broadside backscattering from a thin cylinder over a wide range of frequencies is also included.

In this paper, attention has been given only to the broadside case, since the highest return is in this direction. We have limited our analysis to a thin cylinder in the interest of simplicity in developing the theory. The case of a thicker cylinder and the case of the oblique backscattering will, however, be studied later. The use of multiple loading on a cylinder will also be investigated in the future.

2. INDUCED CURRENT

The geometry of the problem is as shown in Figure 1. A cylinder with a radius a and a length 2h is assumed to be perfectly conducting. A plane electromagnetic wave with the E field parallel to the axis is incident normally to the cylinder. At the center of the cylinder a lumped impedance Z_L is connected. The dimensions of interest are

$$\frac{1}{4} \lambda < 2h < 2\lambda$$

$$\beta_o^2 a^2 \ll 1$$

where λ is the wavelength and β_o is the wave number. The second condition implies that the cylinder is thin and that we can assume that only the axial current is induced.
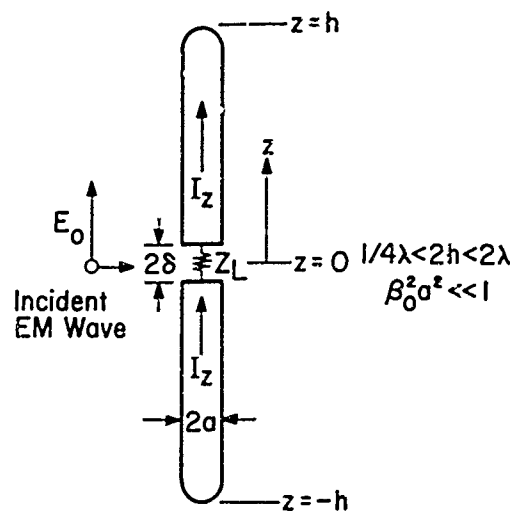

Figure 1. Cylinder with Central Loading Illuminated by an Electromagnetic Wave

2.1 Integral Equation for the Induced Current on the Cylinder

In order to determine the induced current on the cylinder, we apply an integral equation method. The integral equation for the induced current is derived first.

The incident tangential electric field is assumed to be

$$E_z^{in} = E_o \tag{1}$$

where E_o is constant along the cylinder.

The tangential electric field at the cylinder surface, maintained by the current and charge on the cylinder, is

$$E_z^a = - \frac{\partial \phi}{\partial z} - j\omega A_z \tag{2}$$

where ϕ is the scalar potential maintained by the charge, and A_z is the tangential component of the vector potential maintained by the current. By using the Lorentz condition

$$\phi = j \frac{\omega}{\beta_o^2} \nabla \cdot \vec{A} \tag{3}$$

Eq. (2) can be expressed as

$$E_z^a = - j \frac{\omega}{\beta_o^2} \left(\frac{\partial^2}{\partial z^2} + \beta_o^2 \right) A_z . \tag{4}$$

The electric field maintained across the gap at the center of the cylinder is related to the voltage drop across the center load as follows:

$$\int_{-\delta}^{\delta} E_z^g \, dz = -V^L = Z_L I_z(z=0) = Z_L I_o \tag{5}$$

where V^L is the voltage drop across the center load Z_L and I_o is the induced current at the center of the cylinder. From Eq. (5), E_z^g can be expressed as

$$E_z^g = Z_L I_o \, \delta(z) . \tag{6}$$

If the cylinder is perfectly conducting, the tangential electric field at the surface of the cylinder, excluding the gap, vanishes. That is

$$E_z^a + E_z^{in} = 0 \quad \text{for} \quad \delta \leq z \leq h \quad \text{and} \quad -h \leq z \leq -\delta. \tag{7}$$

At the gap, the electric field is continuous. That is

$$E_z^a + E_z^{in} = E_z^g = Z_L I_o \delta(z), \text{ for } -\delta \leq z \leq \delta. \tag{8}$$

Actually, a single equation can be obtained by combining Eqs. (7) and (8) and using the result with Eq. (4) over the whole length of the cylinder to obtain

$$\frac{\partial^2}{\partial z^2} A_z + \beta_o^2 A_z = -j \frac{\beta_o^2}{\omega} \left(E_o - Z_L I_o \delta(z) \right) \text{ for } -h \leq z \leq h. \tag{9}$$

Equation (9) is an inhomogeneous differential equation for A_z. The general solution is the sum of the complimentary function and a particular integral as follows:

$$A_z = \frac{-j}{v_o} \left[C_1 \cos \beta_o z + C_2 \sin \beta_o z + \theta(z) \right]. \tag{10}$$

In Eq. (10) v_o is $1/\sqrt{\mu_o \epsilon_o}$, C_1 and C_2 are arbitrary constants. $\theta(z)$ is a particular integral and can be expressed as

$$\theta(z) = \int_o^z \left[E_o(s) - Z_L I_o(s) \right] \sin \beta_o(z-s) \, ds$$

$$= \frac{E_o}{\beta_o} (1 - \cos \beta_o z) - \frac{1}{2} Z_L I_o \sin \beta_o |z|. \tag{11}$$

If E_o is assumed to be constant along the cylinder, C_2 can be proved to be zero from the symmetry. Equation (10) then becomes

$$A_z(z) = \frac{-j}{v_o} \left[C_1 \cos \beta_o z + \frac{E_o}{\beta_o} (1 - \cos \beta_o z) - \frac{1}{2} Z_L I_o \sin \beta_o |z| \right]$$

$$\text{for} \quad -h \leq z \leq h. \tag{12}$$

From Eq. (12), C_1 can be expressed in terms of $A_z(h)$ as

$$C_1 = \sec \beta_o h \left[j \, v_o \, A_z(h) - \frac{E_o}{\beta_o} \, (1 - \cos \beta_o h) + \frac{1}{2} Z_L \, I_o \sin \beta_o h \right] . \tag{13}$$

With Eqs. (12) and (13) we obtain the following equation:

$$A_z(z) - A_z(h) = \frac{-j}{v_o} \sec \beta_o h \left[\left(j \, v_o \, A_z(h) - \frac{E_o}{\beta_o} \right) \quad (\cos \beta_o z - \cos \beta_o h) \right.$$
$$\left. + \frac{1}{2} Z_L \, I_o \sin \beta_o (h - |z|) \right] \quad \text{for } -h \le z \le h . \tag{14}$$

On the other hand, the left hand side of Eq. (14) is related to the induced current on the cylinder in the following way:

$$A_z(z) - A_z(h) = \frac{\mu_o}{4\pi} \int_{-h}^{h} I_z(z') \, K_d(z, z') \, dz' \tag{15}$$

where

$$K_d(z, z') = K_a(z, z') - K_a(h, z') \tag{16}$$

$$K_a(z, z') = \frac{\exp \left[-j\beta_o \sqrt{(z - z')^2 + a^2} \right]}{\sqrt{(z - z')^2 + a^2}} \tag{17}$$

and $I_z(z')$ is the induced current on the cylinder.

An integral equation for the induced current on the cylinder is then obtained by equating Eqs. (14) and (15) as follows:

$$\int_{-h}^{h} I_z(z') \, K_d(z, z') \, dz' = \frac{-j4\pi}{\zeta_o} \sec \beta_o h \left[\left(j \, v_c \, A_z(h) - \frac{E_o}{\beta_o} \right) (\cos \beta_o z - \cos \beta_o h) \right.$$
$$\left. + \frac{1}{2} Z_L \, I_o \sin \beta_o (h - |z|) \right] \tag{18}$$

where $\zeta_o = 120\pi$ and (18) is valid for $-h > z > h$. It is noted that $A_z(h)$ and I_o in the right-hand side of Eq. (18) are the functions of $I_z(z)$ and are still unknown.

2.2 Solution for the Induced Current on a Cylinder

The right-hand side of Eq. (18) suggests a form for the solution of $I_z(z)$ as

$$I_z(z) = C_c (\cos \beta_o z - \cos \beta_o h) + C_s \sin \beta_o (h - |z|) . \tag{19}$$

It is then reasonable to divide Eq. (18) into two parts as follows:

$$C_c \int_{-h}^{h} (\cos \beta_o z' - \cos \beta_o h) K_d(z, z') \, dz'$$

$$= \frac{-j4\pi}{\zeta_o} \sec \beta_o h \left(j v_o A_z(h) - \frac{E_o}{\beta_o} \right) (\cos \beta_o z - \cos \beta_o h) \tag{20}$$

$$C_s \int_{-h}^{h} \sin \beta_o (h - |z'|) K_d(z, z') \, dz'$$

$$= \frac{-j2\pi}{\zeta_o} \sec \beta_o h \, Z_L \, I_o \sin \beta_o (h - |z|) . \tag{21}$$

Equations (20) and (21) are valid for $-h \le z \le h$ and also well matched at the end points, $z = \pm h$. To find the constants, C_c and C_s, we can match both sides of Eqs. (20) and (21) at the center of the cylinder, $z = 0$.

By setting $z = 0$ in Eq. (20), C_c is determined as

$$C_c = \frac{-j4\pi}{\zeta_o T_{cd}} \sec \beta_o h \left(j v_o A_z(h) - \frac{E_o}{\beta_o} \right) (1 - \cos \beta_o h) \tag{22}$$

where

$$T_{cd} = \int_{-h}^{h} (\cos \beta_o z' - \cos \beta_o h) K_d(0, z') \, dz' . \tag{23}$$

By setting $z = 0$ in Eq. (21), C_s is determined as

$$C_s = \frac{-j2\pi}{\zeta_o T_{sd}} \sec \beta_o h \, Z_L \, I_o \sin \beta_o h \tag{24}$$

where

16

$$T_{sd} = \int_{-h}^{h} \sin \beta_o (h - |z'|) \, K_d(0, z') \, dz' \quad . \tag{25}$$

Substitution of Eqs. (22) and (24) in Eq. (19) gives

$$I_z(z) = \frac{-j4\pi}{\zeta_o} \left[\frac{1}{T_{cd}} \left(j \, v_o \, A_z(h) - \frac{E_o}{\beta_o} \right) (\sec \beta_o h - 1)(\cos \beta_o z - \cos \beta_o h) \right.$$

$$\left. + \frac{1}{2T_{sd}} Z_L \, I_o \tan \beta_o h \sin \beta_o (h - |z|) \right]. \tag{26}$$

Equation (26) is not the final form of the solution of $I_z(z)$ because $A_z(h)$ and I_o are still unknown.

Since $I_o = I_z(z = 0)$, we can express I_o in terms of $A_z(h)$ by letting $z = 0$ in (26), and Eq. (26) can then be arranged as

$$I_z(z) = \frac{-j4\pi}{\zeta_o} \left(j \, v_o \, A_z(h) - \frac{E_o}{\beta_o} \right) \left[M' (\cos \beta_o z - \cos \beta_o h) + N' \sin \beta_o (h - |z|) \right] \tag{27}$$

where

$$M' = \frac{1}{T_{cd}} \quad (\sec \beta_o h - 1) \tag{28}$$

$$N' = \frac{-Z_L \tan \beta_o h(\sec \beta_o h + \cos \beta_o h - 2)}{T_{cd} \, Z_L \tan \beta_o h \sin \beta_o h - j \, 60 \, T_{cd} \, T_{sd}} \quad . \tag{29}$$

Equation (27) still has one unknown, $A_z(h)$, and to determine this we do the following. From the definition of vector potential, we have

$$A_z(h) = \frac{\mu_o}{4\pi} \int_{-h}^{h} I_z(z') \, K_a(h, z') \, dz' \tag{30}$$

where $K_a(h, z')$ is defined in Eq. (17). If Eq. (27) is substituted in Eq. (30), we obtain

$$A_z(h) = \frac{j E_o}{v_o \beta_o} \frac{M' T_{ca} + N' T_{sa}}{1 - M' T_{ca} - N' T_{sa}} \tag{31}$$

where

$$T_{ca} = \int_{-h}^{h} (\cos \beta_0 z' - \cos \beta_0 h) K_a'(h, z') \, dz' \tag{32}$$

$$T_{sa} = \int_{-h}^{h} \sin \beta_0 (h - |z'|) K_a(h, z') \, dz' \tag{33}$$

Now a final form of the solution of $I_z(z)$ can be obtained if Eq. (31) is substituted in Eq. (27). After rearrangement, the final solution for $I_z(z)$ can be summarized as follows:

$$I_z(z) = \frac{jE_0}{30\beta_0} \left(\frac{1}{\cos \beta_0 h - M T_{ca} - N T_{sa}} \right) \left[M(\cos \beta_0 z - \cos \beta_0 h) - N \sin \beta_0 (h - |z|) \right] \tag{34}$$

where

$$M = \frac{1}{T_{cd}} (1 - \cos \beta_0 h) \tag{35}$$

$$N = \frac{-Z_L \sin \beta_0 h (1 - \cos \beta_0 h)^2}{T_{cd} Z_L \sin^2 \beta_0 h - j\, 60 T_{cd} T_{sd} \cos \beta_0 h} \tag{36}$$

and T_{cd}, T_{sd}, T_{ca}, T_{sa} are defined in Eq. (23), (25), (32), and (33).

Equation (34) gives a complete expression for the induced current on a cylinder with a central load, Z_L, when illuminated by a constant electric field, E_0, at broadside. The accuracy of Eq. (34) is high and its form is simple and suitable for the further development of theory. It is checked experimentally in later sections.

As a matter of completeness and convenience, integrals T_{cd}, T_{sd}, T_{ca}, and T_{sa} are expressed in terms of better-known integrals as follows:

$$T_{cd} = C_a(h, 0) - C_a(h, h) - \cos\beta_0 h \left[E_a(h, 0) - E_a(h, h) \right] \tag{37}$$

$$T_{sd} = \sin \beta_0 h \left[C_a(h, 0) - C_a(h, h) \right] - \cos \beta_0 h \left[S_a(h, 0) - S_a(h, h) \right] \tag{38}$$

$$T_{ca} = C_a(h, h) - \cos \beta_0 h\, E_a(h, h) \tag{39}$$

18

$$T_{sa} = \sin \beta_{c} h \, C_{a}(h,h) - \cos \beta_{o} h \, S_{a}(h,h) \tag{40}$$

where

$$C_{a}(h,0) = \int_{-h}^{h} \cos \beta_{o} z' \, K_{a}(0,z') \, dz' \tag{41}$$

$$C_{a}(h,h) = \int_{-h}^{h} \cos \beta_{o} z' \, K_{a}(h,z') \, dz' \tag{42}$$

$$E_{a}(h,0) = \int_{-h}^{h} K_{a}(0,z') \, dz' \tag{43}$$

$$E_{a}(h,h) = \int_{-h}^{h} K_{a}(h,z') \, dz' \tag{44}$$

$$S_{a}(h,0) = \int_{-h}^{h} \sin \beta_{o} z' \, K_{a}(0,z') \, dz' \tag{45}$$

$$S_{a}(h,h) = \int_{-h}^{h} \sin \beta_{o} z' \, K_{a}(h,z') \, dz' \tag{46}$$

The integrals of Eqs. (41) to (46) can be calculated by using a digital computer.

3. INDUCED CURRENT ON A CYLINDER WITHOUT CENTRAL LOADING

The first and the simplest case to be studied is a cylinder without loading. The induced current on the cylinder can be found from Eq. (34) by letting $Z_{L} = 0$. That is

$$I_{z}(z) = \frac{jE_{o}}{30 \, \beta_{o}} \left(\frac{1 - \cos \beta_{o} h}{(T_{cd} + T_{ca}) \cdot \cos \beta_{o} h - T_{ca}} \right) (\cos \beta_{o} z - \cos \beta_{o} h) \, .$$

Figure 2. $I_z(0)$ vs h/λ when $\beta_0 a = 0.11$, $f = 1.088$ kMc, $Z_L = 0$.

The results obtained in this section are not unexpected. The induced current reaches a resonant peak on a cylinder with a length of 0.43λ or a length of 1.4λ for $\beta_0 a = 0.11$. Obviously, these current peaks imply large backscattering signals. We propose to eliminate these current peaks by the use of suitable impedance loading.

4. INDUCED CURRENT ON A CYLINDER WITH AN INFINITE IMPEDANCE AS ITS CENTRAL LOAD

The second case to be studied is a cylinder with an infinite impedance loaded at its center. Theoretically, the induced current can be obtained from Eq. (34) by setting $Z_L = \infty$. Experimentally, an infinite impedance is approximated by a coaxial cavity tuned at its anti-resonance position. This coaxial cavity is built inside of the cylinder as described in a later section. The induced current on the loaded cylinder is then measured by a small probe.
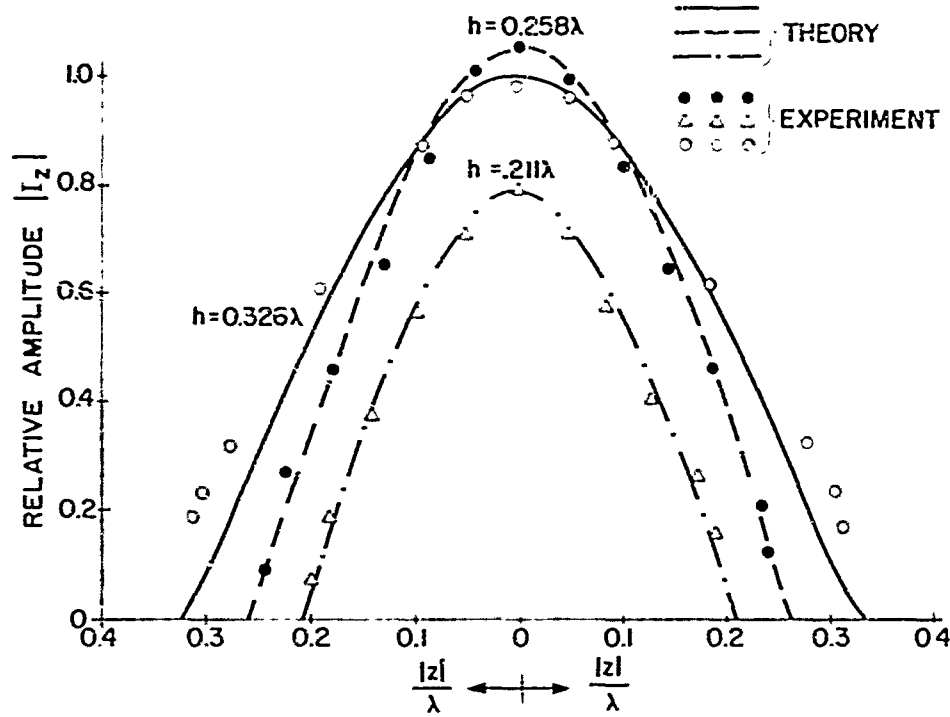
Figure 3. Distribution of $I_z(z)$ when $Z_L = 0$.

When $Z_L \simeq \infty$, from Eqs. (35) and (36)

$$\frac{N}{M} = \frac{-(1-\cos\beta_o h)}{\sin\beta_o h} \qquad \text{for } \beta_o h \neq n\pi . \tag{51}$$

The substitution of Eq. (51) in Eq. (34) gives

$$I_z(z) = \frac{-jE_o}{30\beta_o} \left[\frac{(1-\cos\beta_o h)[\sin\beta_o|z| - \sin\beta_o h + \sin\beta_o(h-|z|)]}{\sin\beta_o h [C_a(h,0) - (2-\cos\beta_o h)C_a(h,h) - \cos\beta_o h \, E_a(h,0) + E_a(h,h)]} \right]$$
$$\left. - (1-\cos\beta_o h)^2 \, S_a(h,h) \right] \tag{52}$$

The induced current in this case is zero at the center of the cylinder, and is distributed along the cylinder as a combined curve of a sine and a shifted sine curve.

The maximum induced current occurs at

$$z = \frac{h}{2}, \qquad \text{for } \beta_o h < 2\pi \tag{53}$$

and is given by

$$I_z\left(\frac{h}{2}\right) = \frac{-jE_o}{30\,\beta_o} \frac{2\sin\frac{\beta_o h}{2}\left(1-\cos\frac{\beta_o h}{2}\right)(1-\cos\beta_o h)}{\left[\sin\beta_o h\,[C_a(h,0)-(2-\cos\beta_o h)C_a(h,h)-\cos\beta_o h\,[C_a(h,0)+E_a(h,h)]\right.} \cdot$$
$$\left. -(1-\cos\beta_o h)^2\,S_a(h,h)\right]$$

(54)

The theoretical value of $I_z(\frac{h}{2})$ as a function of h/λ is shown graphically in Figure 4 in comparison with an experimental curve. The experimental results are obtained with the coaxial cavity set near its anti-resonance position The agreement between theory and experiment is not very good. The discrepancy is due to the fact that it is impossible to obtain experimentally an infinite impedance from a coaxial cavity structure. This reasoning is supported by the fact that there is closer agreement between theory and experiment for $Z_L = j2000\,\Omega$.
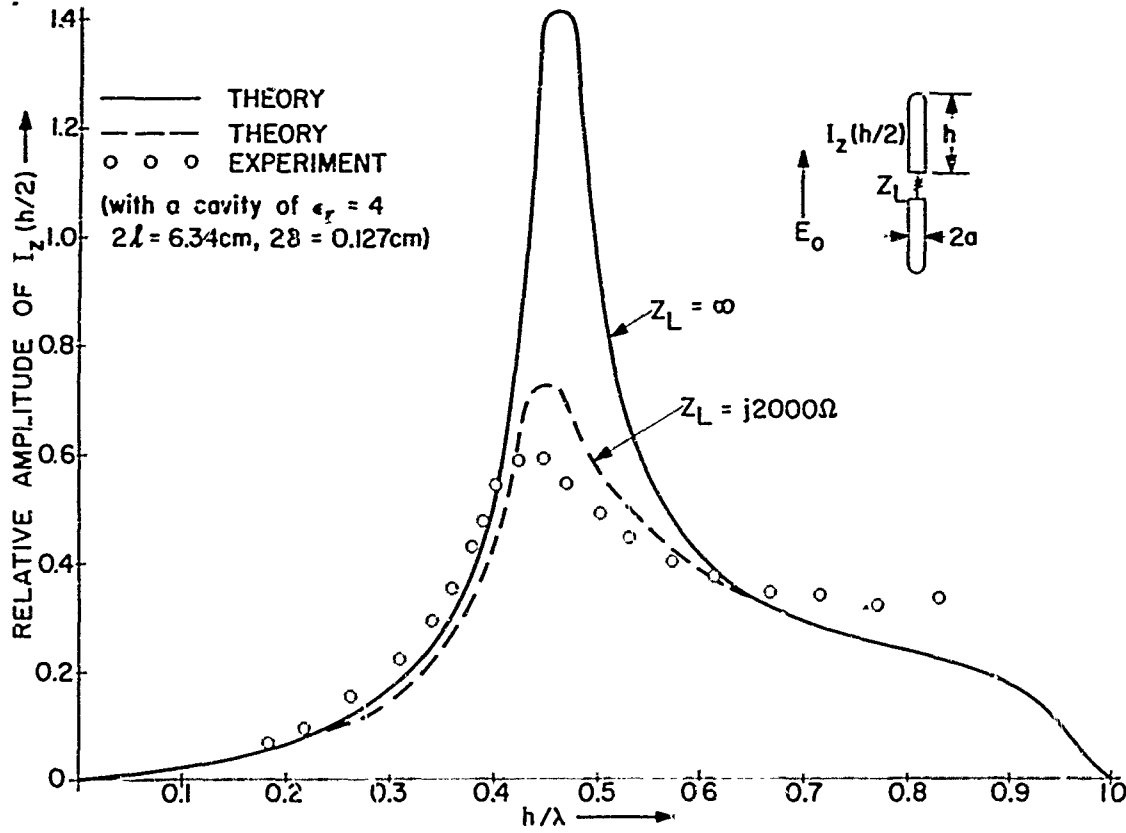
Figure 4. I_z(h/2) vs h/λ when $\beta_o a = 0.11$, f = 1.088 kMc, Z_L = large.

The distribution of the induced current on three cylinders of different lengths and loaded with infinite impedances is shown graphically in Figure 5. The agreement between theory and experiment is good for these cases.
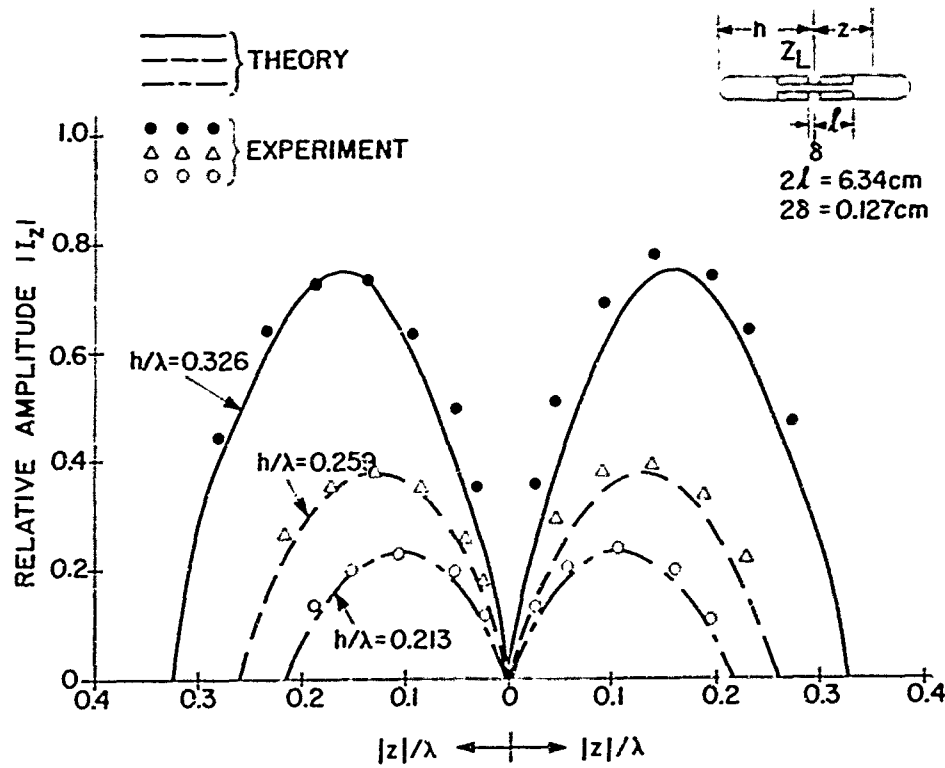
Figure 5. Distribution of $I_z(z)$ for $h = 0.213\lambda$, $h = 0.259\lambda$, and $h = 0.326\lambda$ when $Z_L = \infty$.

The important information obtained with infinite impedance at the center of the cylinder is as follows: The induced currents at resonant lengths, namely $2h = 0.43\lambda$ and $2h = 1.4\lambda$, are greatly reduced by this loading. However, the induced current appears to have a peak when $2h = 0.9\lambda$ with this loading. This current peak should be suppressed if a low scattering over a wide frequency range is desired. We then conclude that an infinite impedance, or a very high impedance, for the central loading is not an optimum from the viewpoint of minimizing the scattering over a wide range of frequencies. We shall seek an optimum loading in later sections.

5. INDUCED CURRENT ON A CYLINDER OF NEAR RESONANT LENGTH WITH VARIOUS CENTRAL IMPEDANCES

In this section the effect of the central impedance on the induced current of the cylinder with a resonant length is studied. For experimental convenience, we choose the following specific case:

$$a = 0.0173\lambda$$
$$2h = 0.43\lambda$$
$$Z_L = jX_L .$$

The last condition restricts the central impedance to be purely reactive, since only a reactive impedance is obtained experimentally from a coaxial cavity.

With the above conditions, the theoretical value of the induced current can be expressed as

$$I_z(z) = \frac{jE_o}{30\beta_o} M \left[\frac{(\cos \beta_o z - 0.216) + \frac{N}{M} \sin (77.5^\circ - |\beta_o z|)}{j0.215 - \frac{N}{M} (0.218 - j0.25)} \right] \tag{55}$$

where

$$\frac{N}{M} = \frac{-0.765 X_L}{0.955 X_L - 24.6} . \tag{56}$$

The relative magnitude of $I_z(z)$ is calculated and shown graphically in Figures 6a and 6b for the following values of Z_L: $0, \infty, -j1600\Omega, -j800\Omega, -j600\Omega,$ $j1600\Omega, j800\Omega, j600\Omega,$ and $j400\Omega$. In these curves, we observe the following facts:

(1) When $Z_L = 0$ (no loading), the induced current is very large and distributes along the cylinder as a shifted cosine curve.

(2) When $Z_L = \infty$, the magnitude of the induced current is greatly reduced from the value for $Z_L = 0$ and the distribution of the induced current becomes double humped with a null at the center.

(3) When Z_L is capacitive and finite, the induced current is smaller than the case of $Z_L = 0$ but larger than for $Z_L = \infty$.

(4) When Z_L is inductive and finite, the magnitude of the induced current is smaller than the case of $Z_L = \infty$ and the induced current starts to have three loops along the cylinder; it is of interest to note that the phase of the current at the center loop is reversed.
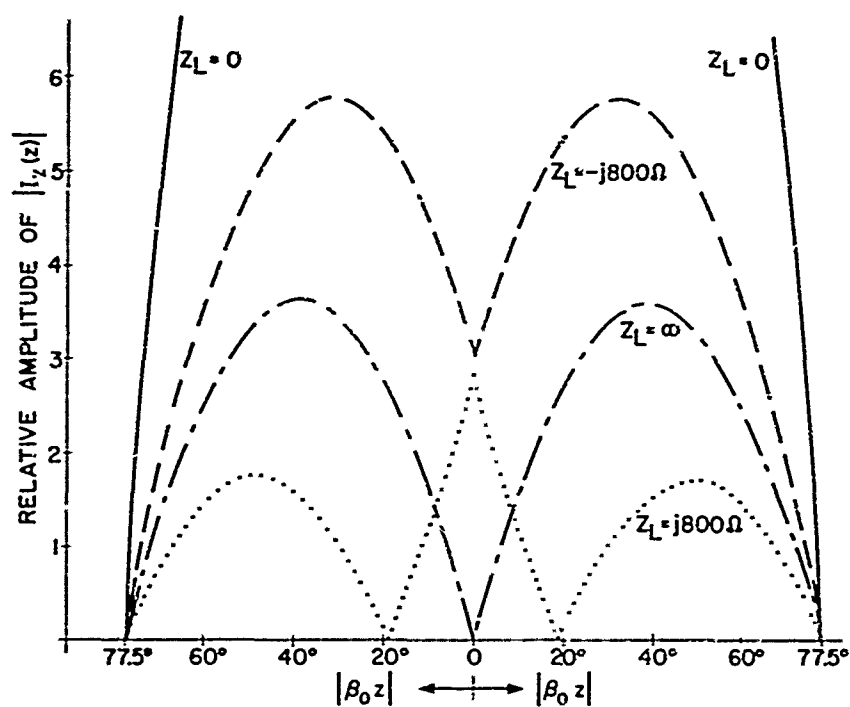
(a)
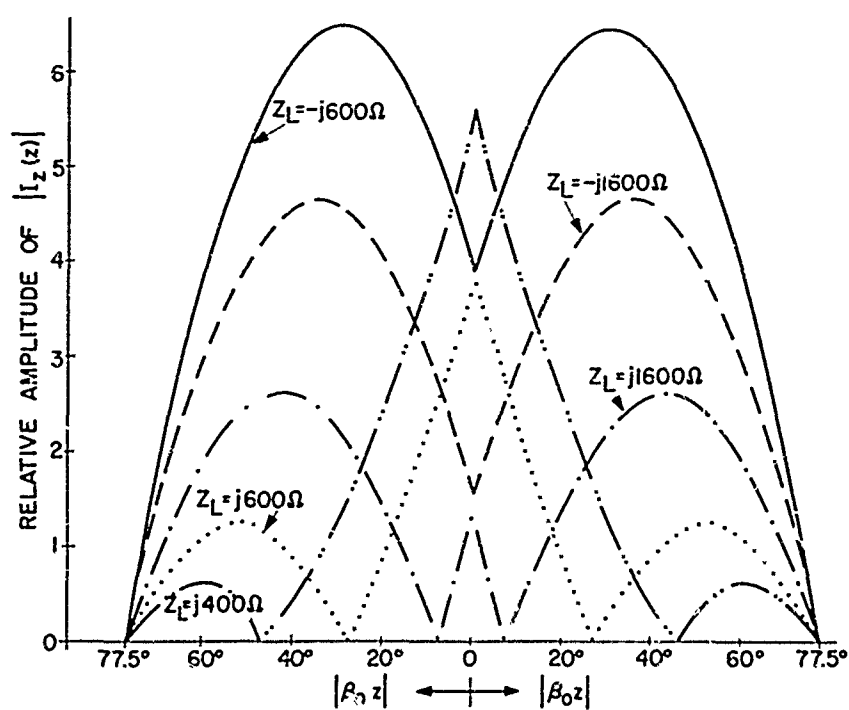
(b)

Figure 6. Current Distribution, $I_z(z)$, on Cylinder of $h = 0.215\lambda$, $a = 0.0173\lambda$ for Different Central Loads, Z_L (Theoretical).
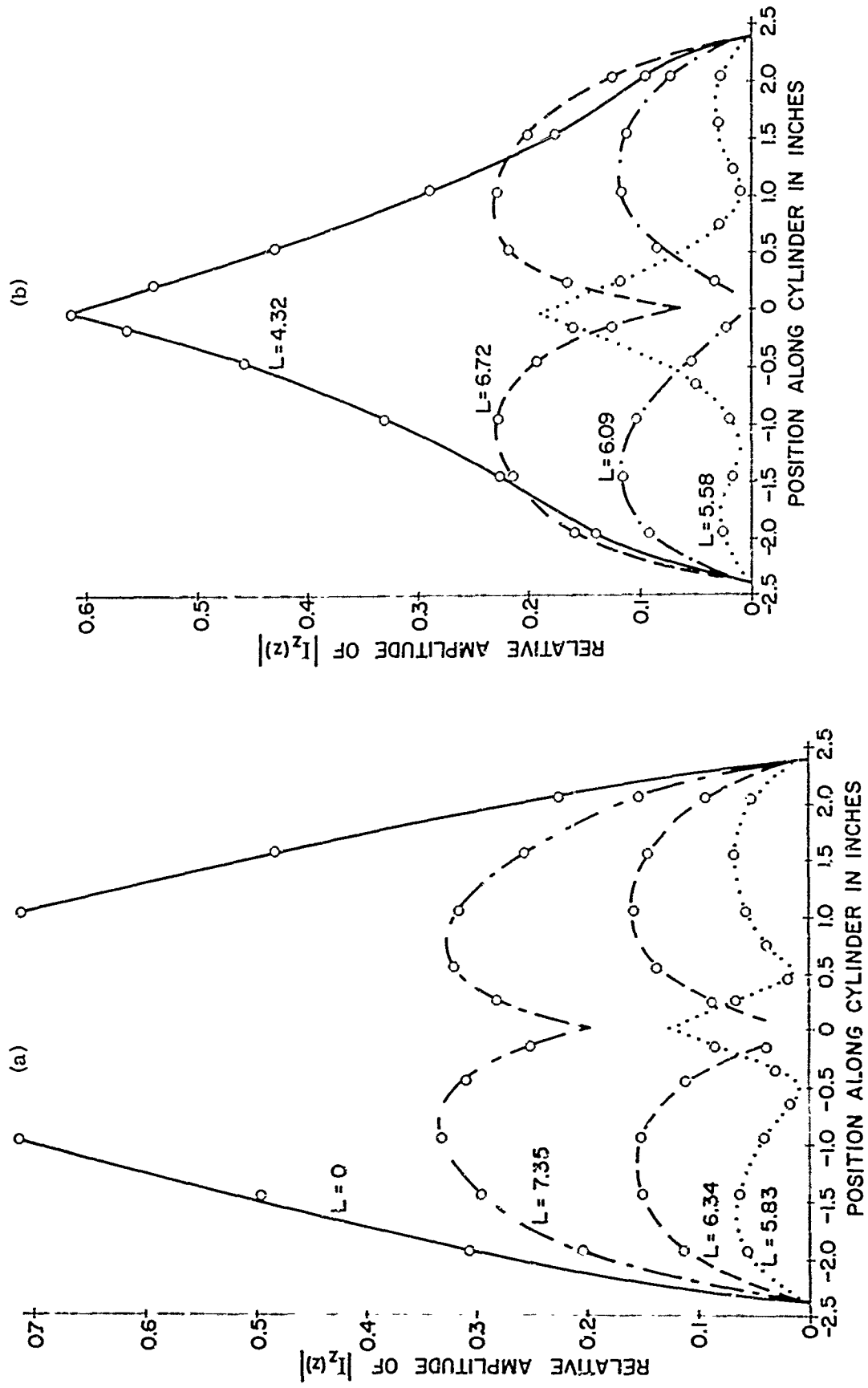
Figure 7. Current Distribution on a Cylinder of $h = 0.215\lambda$, $a = 0.0173\lambda$ with Cavity Lengths, $L(cm)$. (Experimental)

The most important and significant information obtained from Figures 6a and 6b is that when Z_L is inductive and of some finite value, the magnitude of the induced current is reduced to a value smaller than the case of $Z_L = \infty$ and the phase of the induced current is reversed at the center part of the cylinder. It is, therefore, possible to reduce the broadside backscattering from a cylinder to zero by properly adjusting the value of Z_L. In effect, the optimum impedance for zero broadside backscattering from a cylinder of this size is inductive and it has a small resistive component, as we shall see in a later section.

To obtain an experimental verification to the theoretical results shown in Figures 6a and 6b, we measured the induced current along a cylinder of this specified dimension and with various cavity lengths. The experimental results are shown in Figures 7a and 7b. We obtained a family of curves which closely resemble the theoretical curves shown in Figures 6a and 6b. When the cavity length (total length) is longer than 6.2 cm, the impedance of the cavity is capacitive; it becomes inductive for cavity lengths shorter than 6.2 cm. It It should be noted that the effective cavity length is greater than these values since it is loaded with a dielectric material for which $\epsilon = 4.0$. The approximate value of the cavity impedance is calculated by using a standard impedance formula for a transmission line and assuming that a capacitance of $0.4\,\mu\mu f$ is shunted across the gap at the center of the cylinder.

The comparison between theory and experiment is made in Figure 8 where theoretical curves for $Z_L = -j\,800\Omega$, ∞, and $j\,800\Omega$ are shown. These curves are compared with experimental results for $\ell = 3.32$ cm, 3.10 cm, and 2.91 cm where ℓ is the half length of the coaxial cavity. The agreement between theory and experiment is very good. This indicates also that the calculated value of the cavity impedance is quite close to the corresponding theoretical impedance.

6. INDUCED CURRENT ON A CYLINDER OF NEAR ANTI-RESONANT LENGTH WITH VARIOUS CENTRAL IMPEDANCES

In this section we study the effect of the central impedance on the induced current of a cylinder with an anti-resonant length. The dimensions of the cylinder and the central impedance are chosen to be

$$a = 0.0173\lambda$$

$$2h = 0.9\lambda$$

$$Z_L = j\,X_L.$$

Figure 8. Current Distribution along a Cylinder as a Function of Central Load
h = 0.215 λ_o (Theoretical and Experimental).

Again we consider only the reactive loading.

The theoretical value of the induced current for this case is:

$$I_z(z) \doteq \frac{jE_o}{30\,\beta_o}\,M\left[\frac{(\cos\beta_o z + 0.951) + \frac{N}{M}\sin(162° - |\beta_o z|)}{-0.911 + j\,0.217 - \frac{N}{M}(0.111 - j\,0.128)}\right] \tag{57}$$

where

$$\frac{N}{M} \doteq \frac{-0.604\,X_L}{0.096\,X_L + 71 - j\,52.2} \tag{58}$$

The relative magnitude of $I_z(z)$ is calculated and shown graphically in Figure 9a and 9b for values of Z_L as follows: 0, ∞, $-j1600\Omega$, $-j800\Omega$, $-j600\Omega$, $j1600\Omega$, $j800\Omega$ and $j600\Omega$. This family of curves is quite different from those of the preceding section. Although a purely reactive impedance reduces the magnitude of the induced current and tends to reverse the phase of the induced current, it is not possible to reduce the broadside backscattering to zero because current nulls do not occur in this case. Actually, an optimum impedance for zero broadside backscattering from a cylinder of this size should have a large resistive component, as is shown in a later section.

The experimental results for the induced current on the above cylinder with various cavity lengths are summarized in Figure 10. The general shapes of the experimental curves are similar to those in the theoretical curves. The comparison between theory and experiment is made in Figure 11. Three typical theoretical curves are compared with the corresponding experimental results. The agreement between theory and experiment is good but not as good as in the case of a shorter cylinder.

7. THE EXPERIMENT

In Figure 12 is shown the block diagram of the equipment used for the current measurement on the reactively loaded cylinders. In the experiment the cylinder is illuminated at broadside by a plane wave of 1.088 kMc from a L-band horn antenna with the electric field vector polarized in the direction parallel to the cylinder. A conventional probing method with a small current probe was employed to measure the induced current amplitude on the cylinder.
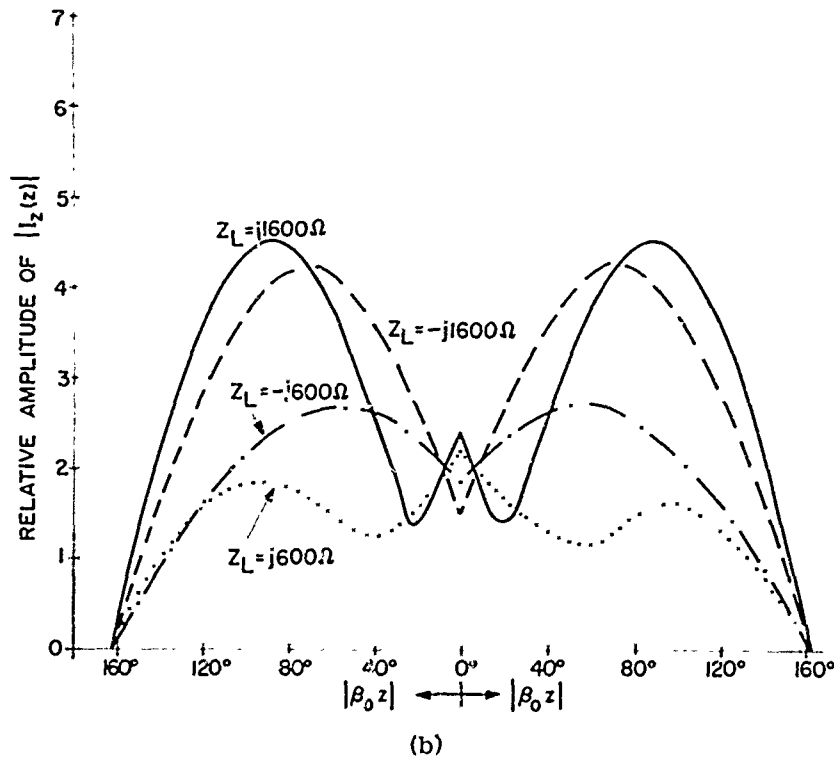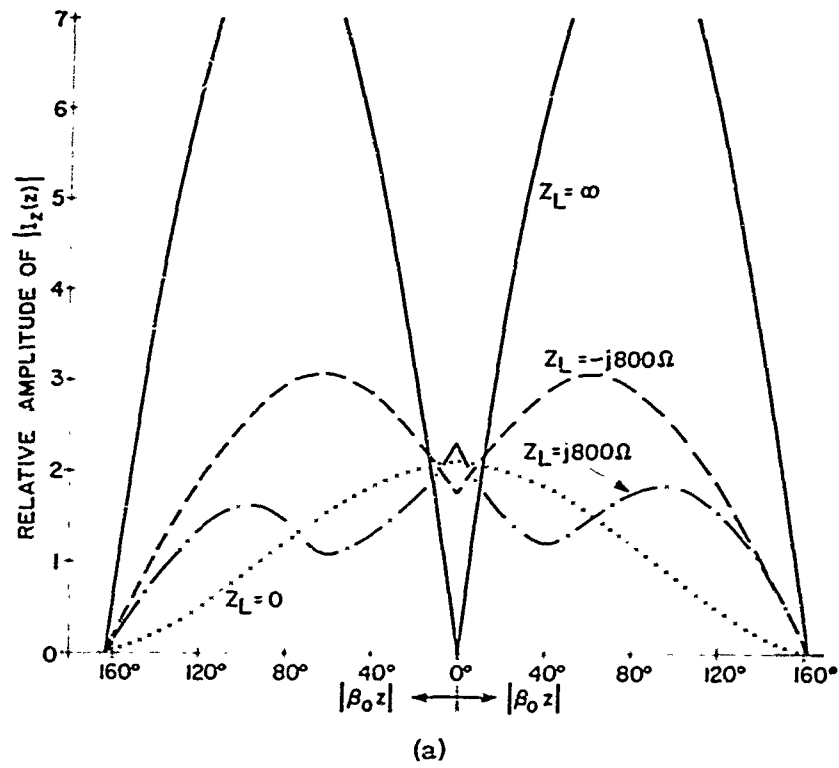
Figure 9. Current Distribution, $I_z(z)$, on a Cylinder of $h = 0.45\lambda$, $a = 0.0173\lambda$ for Different Central Load (Theoretical).

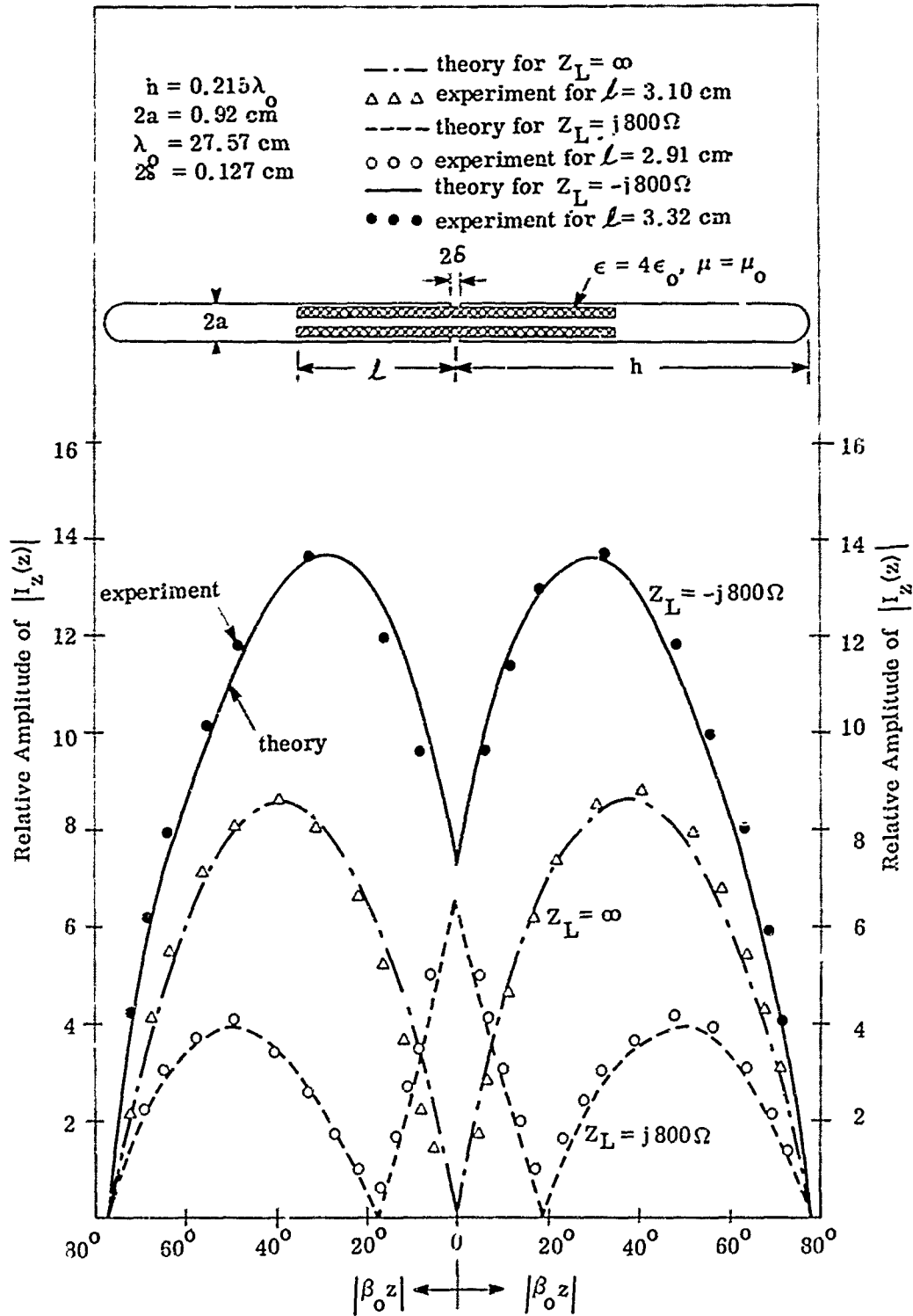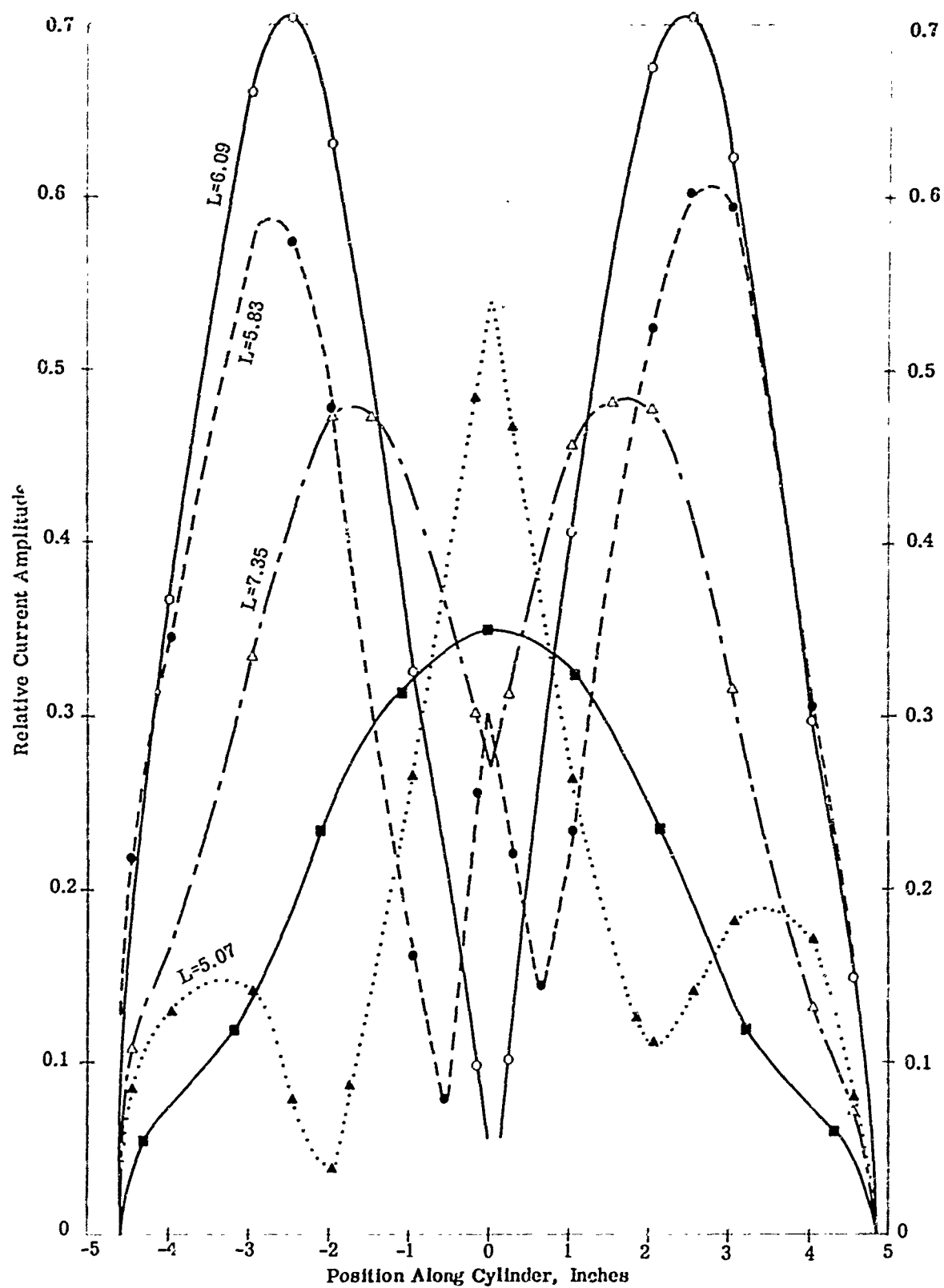Figure 10. Current Distribution on a Cylinder of h = 0.45λ, a = 0.173λ with Different Cavity Lengths, L(cm) (Experimental).
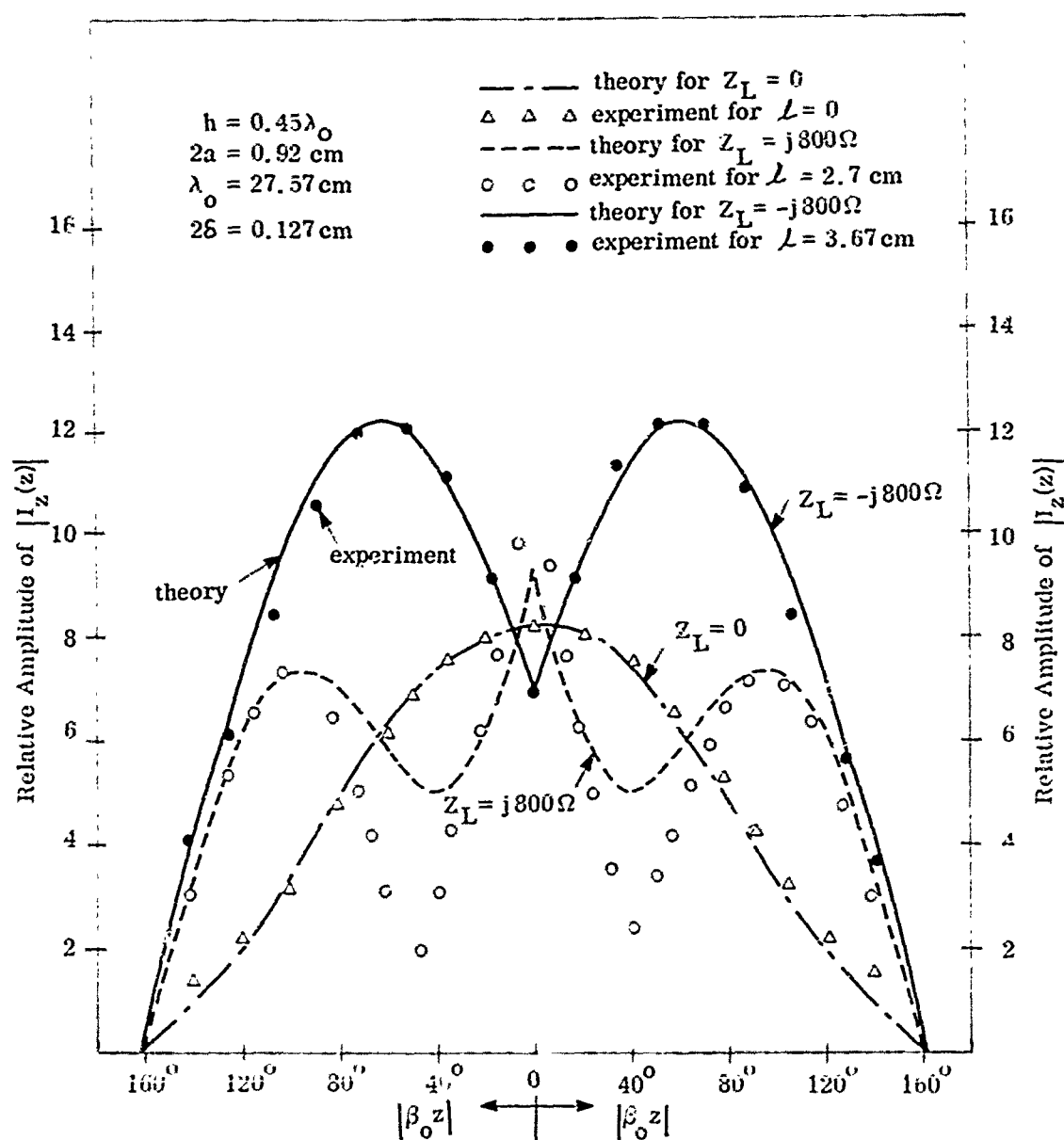
Figure 11. Current Distribution along a Cylinder as a Function of Central Load for h = 0.45 λ_o (Theoretical and Experimental).

The coaxial line leading from the probe was covered with radar absorbing material (RAM) and oriented perpendicular to the E field to minimize the influence of its presence. The measurement area was lined with RAM to reduce unwanted reflections.

Figure 13 shows partially disassembled components of the loaded cylinder. The diameter of the cylinder is about 0.95 cm and its length can be changed from 10 cm(h = 0.182λ) to 51.29 cm(h = 0.93λ) by the combination of center and end pieces of different lengths. The center sections of the cylinder contain a symmetric
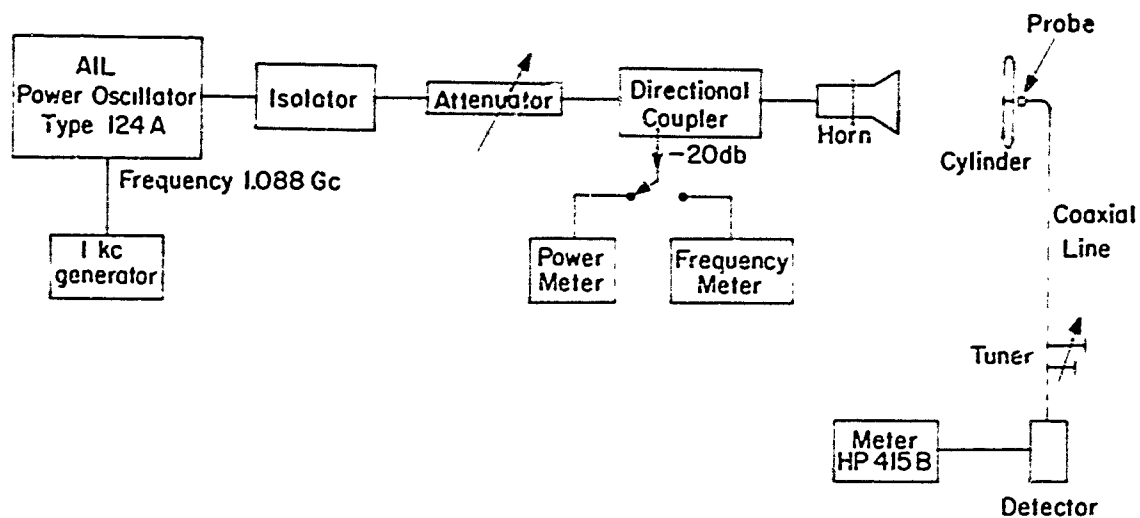
Figure 12. Block Diagram of the Experimental Setup
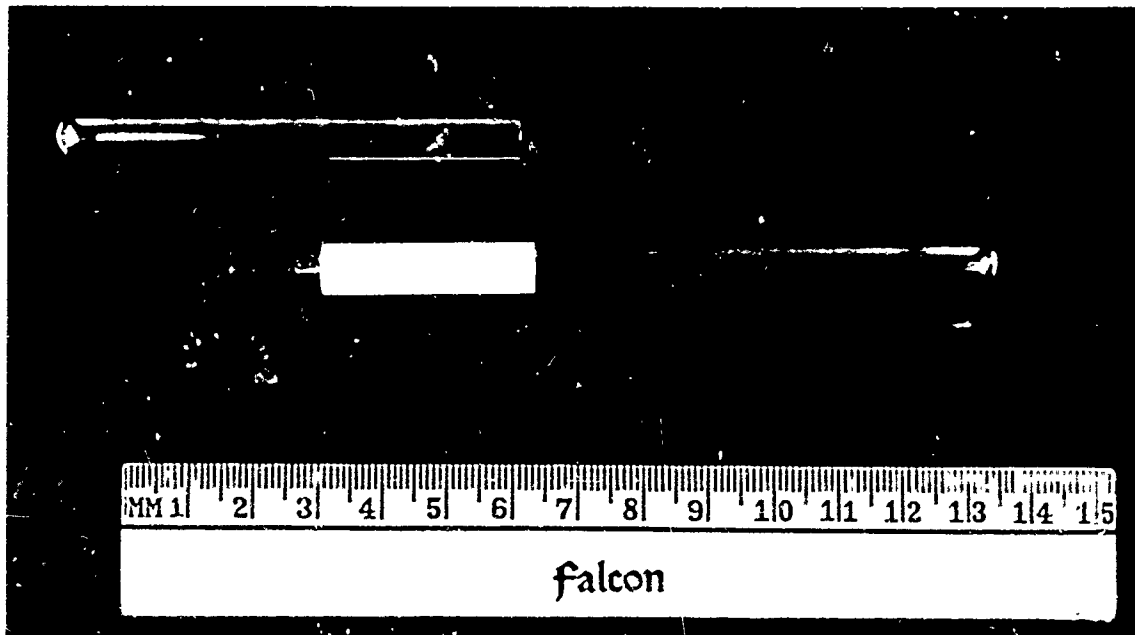
Figure 13. Cylinder with Coaxial Cavity

coaxial cavity with its input gap at the center of the cylinder. By varying the cavity length, various input reactances that represent the central loads of the cylinder are obtained. The coaxial cavity is filled with a dielectric in order to reduce the required cavity length. The dielectric used is a styracast with a dielectric constant of 4 and a loss tangent of 0.0001.

8. OPTIMUM IMPEDANCE FOR ZERO BROADSIDE BACKSCATTERING FROM A THIN CYLINDER

In the preceding sections we have concentrated on finding the induced current on a cylinder as a function of the cylinder dimension and the central impedance. We now seek to find an optimum impedance for zero broadside backscattering from a thin cylinder.

The induced current has been found in Eqs. (34) and (36). The scattered field due to this induced current can be found as follows:

The vector potential maintained by the induced current on the cylinder in the far zone of the cylinder is

$$
\begin{aligned}
A_z = \frac{\mu_o}{4\pi} \frac{jE_o}{30\beta_o} &\left(\frac{1}{\cos\beta_o h - M T_{ca} - N T_{sa}} \right) \\
&\cdot \left[M \int_{-h}^{h} (\cos\beta_o z - \cos\beta_o h) \frac{\exp(-j\beta_o R)}{R} dz \right. \\
&\left. + N \int_{-h}^{h} \sin\beta_o(h - |z|) \frac{\exp(-j\beta_o R)}{R} dz \right]
\end{aligned}
\tag{59}
$$

where

$$
R = R_o - z\cos\theta = \text{distance between a point on the cylinder and the observation point.}
$$

The scattered electric field in the far zone of the cylinder can be obtained as

$$
E_\theta^s = -j\omega A_\theta = j\omega A_z \sin\theta .
\tag{60}
$$

The corresponding Poynting vector is

$$
P^s = \frac{1}{2\zeta_o} |E_\theta|^2 .
\tag{61}
$$

The scattered field in the broadside direction can be obtained by letting

$$
\theta = 90° \quad \text{and} \quad R = R_o .
\tag{62}
$$

We then obtain

$$E_\theta^S (\theta = 90°) = \frac{2}{\beta_o} E_o \frac{\exp(-j\beta_o R_o)}{R_o} \left[\frac{M(\sin\beta_o h - \beta_o h \cos\beta_o h) + N(1 - \cos\beta_o h)}{\cos\beta_o h - M T_{ca} - N T_{sa}} \right]$$

(63)

and

$$P^S(\theta = 90°) = \frac{2}{\zeta_o} \frac{E_o^2}{\beta_o^2 R_o^2} \left| \frac{M(\sin\beta_o h - \beta_o h \cos\beta_o h) + N(1 - \cos\beta_o h)}{\cos\beta_o h - M T_{ca} - N T_{sa}} \right|^2$$

(64)

The Poynting power density of the scattered field in the broadside direction is thus expressed as a function of the central impedance because N in Eq. (64) is a function of Z_L, as expressed in Eq. (36).

To minimize the broadside backscattering to zero, we can simply make $P^S(\theta = 90°)$ equal to zero. That is,

$$\frac{N}{M} = -\frac{\sin\beta_o h - \beta_o h \cos\beta_o h}{1 - \cos\beta_o h} .$$

(65)

Using Eqs. (35) and (36), Eq. (65) can be rewritten as

$$\frac{Z_L \sin\beta_o h (1 - \cos\beta_o h)}{Z_L \sin^2\beta_o h - j60 T_{sd} \cos\beta_o h} = \frac{\sin\beta_o h - \beta_o h \cos\beta_o h}{1 - \cos\beta_o h} .$$

(66)

By solving for Z_L in Eq. (66), we obtain the optimum central impedance for zero broadside backscattering as

$$\left[Z_L \right]_0 = \frac{-j60 T_{sd}(1 - \beta_o h \cot\beta_o h)}{2\cos\beta_o h - 2 + \beta_o h \sin\beta_o h}$$

(67)

where

$$T_{sd} = \sin\beta_o h \left[C_a(h, 0) - C_a(h, h) \right] - \cos\beta_o h \left[S_a(h, 0) - S_a(h, h) \right]$$

as expressed in Eq. (38).

Equation (67) gives the complete expression for the optimum central impedance for zero broadside backscattering from a thin cylinder. This optimum central

impedance is a function of the cylinder dimension and its numerical value can be calculated quite easily. The expression should prove useful in practical design

We consider a cylinder with a = 0.0173λ and calculate $\left[Z_L\right]_0$
as a function of the cylinder length h. The result is shown graphically in Figure 14. From this figure we observe the following:

(1) In general, the optimum central impedance for zero broadside backscattering should have both the resistive and the reactive component.

(2) For a cylinder shorter than 1 wavelength (or h < 0.5λ), the optimum impedance is inductive and requires a resistive component.

(3) For a cylinder longer than 1 wavelength (or h > 0.5λ), the optimum impedance is inductive or capacitive but requires a negative resistive component.
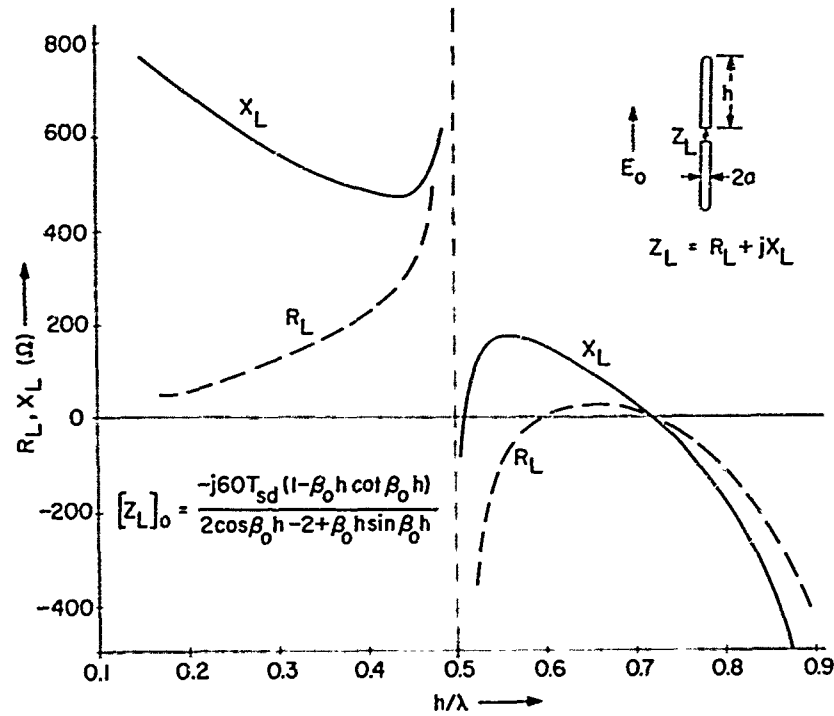
Figure 14. Optimum Central Impedance, $[Z_L]_0$, for Zero Backscattering from a Cylinder of Radius a=0.0173λ, as a Function of Cylinder Length

These results indicate that for a cylinder shorter than 1 wavelength, a passive impedance loaded at the center of the cylinder can reduce the broadside backscattering to zero. However, an active impedance is required to obtain zero broadside backscattering from a cylinder longer than 1 wavelength. Of course, an active impedance may not be needed if the cylinder is loaded at two points.

We also consider the case of a thicker cylinder with a = 0.0517λ. The optimum impedance for zero broadside backscattering is obtained as a function of the

cylinder length h and shown graphically in Figure 15; and is seen to be similar to that in Figure 14. The resistive component remains relatively constant with respect to the change of the cylinder thickness, but the reactive component is reduced almost by a factor of two for the thicker cylinder.
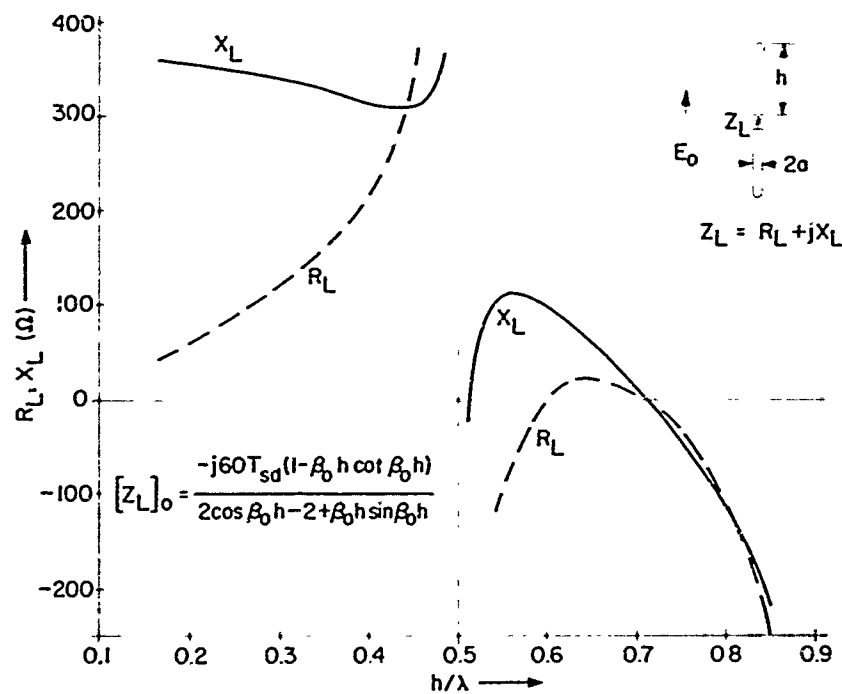
Figure 15. Optimum Central Impedance, $[Z_L]_0$, for Zero Backscattering from a Cylinder of Radius a=0.0517λ, as a Function of Cylinder Length

To determine bandwidth characteristics of this technique, we calculate the optimum impedance for the purpose of minimizing the broadside backscattering from a fixed cylinder over a wide range of frequencies. We consider a cylinder with h = 4 cm, a = 0.476 cm to cover a frequency range from 1 kMc to 3 kMc. The frequency characteristic of the optimum impedance is shown graphically in Figure 16. Within this frequency range the optimum impedance is inductive and requires a resistive component. This impedance appears to be obtainable by a simple network synthesis. It is also noted that to cover a wider range of frequency, an active impedance is needed to reduce the broadside backscattering to zero.

A final remark is necessary at this point. Although we have exclusively studied the broadside illumination, the optimum loading obtained in this study is also effective for the case of the oblique illumination. To support this statement the experimental measurement of the induced current by a plane wave incident from different angles are presented in Figures 17 and 18. In these figures we
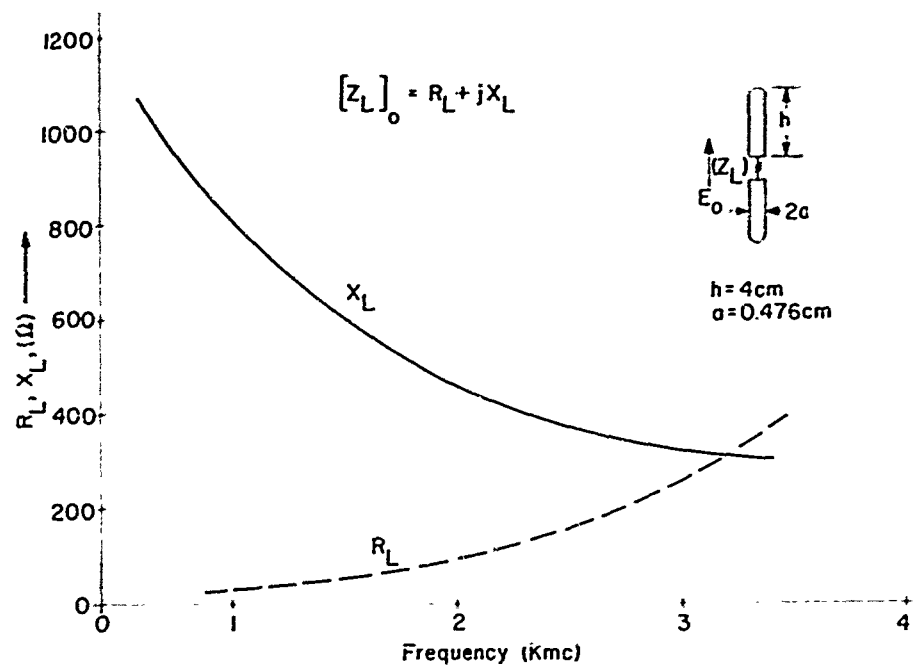
Figure 16. Optimum Central Impedance, $[Z_L]_0$, for Zero Backscattering from a Cylinder with h=4 cm , a=0.476 cm Over the Frequency Range of 1 kMc to 3 kMc
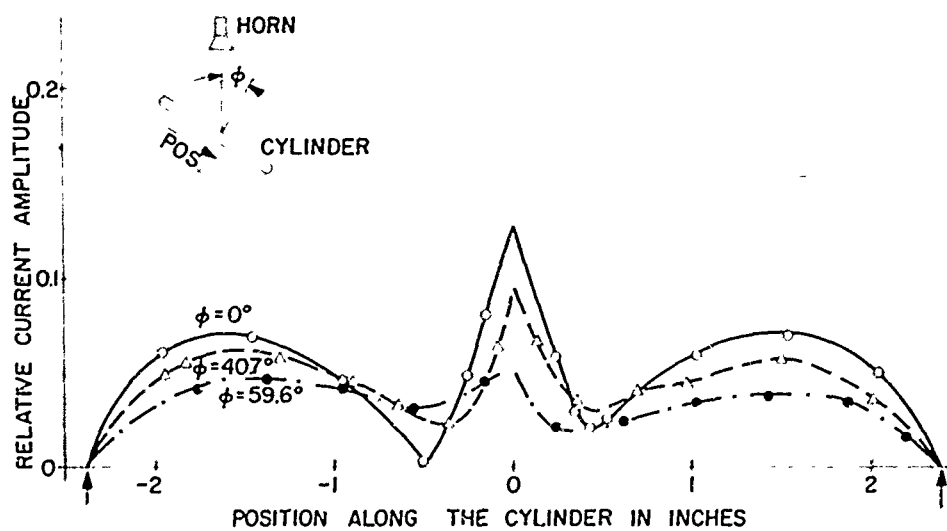
Figure 17. Current Distributions on a Center Loaded Cylinder Due to Plane Waves of Different Incident Angle.

$$h = 0.215\lambda_0$$
$$2\delta = 0.050 \text{ in.}$$
$$\epsilon_r = 4$$
$$L = 5.83 \text{ cm}$$

The current scale is Relative to the Maximum Current (1.0) on an Unloaded Cylinder with h = 0.215λ_0, ϕ = 0.
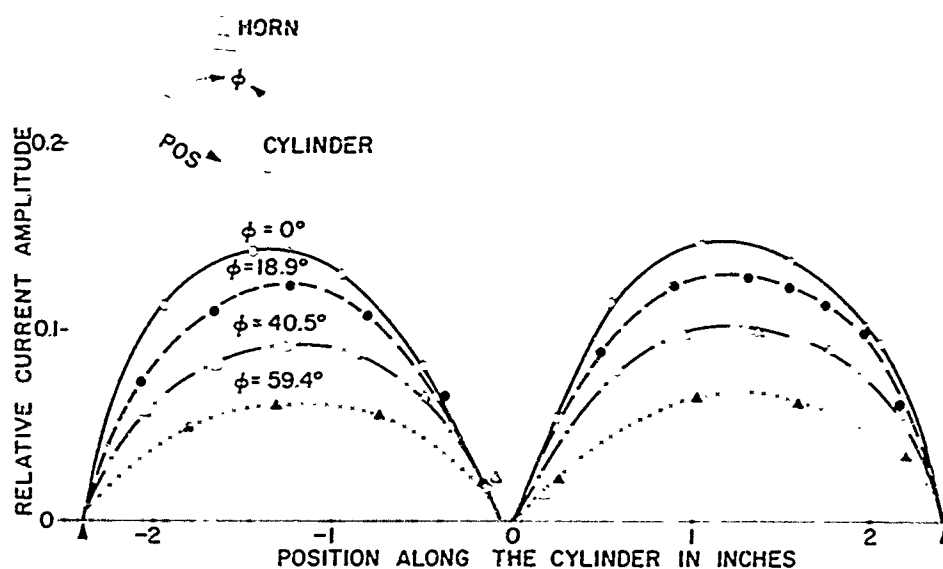
Figure 18. Current Distributions on a Center Load Cylinder Due to
Plane Waves of Different Incident Angles

$$h = 0.215\lambda_0$$
$$2\delta = 0.050 \text{ in}$$
$$\epsilon_r = 4$$
$$L = 6.?1 \text{ cm}$$

The Current Scale is Relative to the Maximum Current (1.0) on an
Unloaded Cylinder with $h = 0.215\lambda_0$, $\phi = 0$.

observe that the only change on the induced current for the oblique illumination is
the reduction in its magnitude. The distribution of the induced current is practi-
cally unchanged from the case of the broadside illumination. Additional study on
the oblique illumination case will be made in the future.

9. CONCLUSION

We have studied the effect of central loadings on the induced current on a thin
cylinder that is illuminated by a plane wave at normal incidence. It is found that
both the induced current and the scattered field can be greatly modified by a cen-
tral load. Through theoretical analysis and experimental measurement, we have
good understanding about the exact nature of the loading for the reduction of the
scattering.

We have also obtained the optimum central loading to eliminate the broadside
backscattering from a thin cylinder. A relatively simple formula for the optimum
impedance is presented, and it should prove useful in practical design situations.
Although an impedance which can easily be obtained by a simple network synthesis

40

is sufficient to reduce to zero the backscattering f. om a cylinder shorter than 1 wavelength, it appears that an active impedance is required to eliminate the back-scattering from a cylinder longer than 1 wavelength. This difficu.ty can probably be overcome by loading the cylinder at two points with two passive impedances. An investigation of this possibility is in progress.

Acknowledgments

The authors are grateful to Mr. Ralph E. Hiatt and to Dr. T. B. A. Senior for helpful discussions on this work.

References

1. H. A. Iams, Radio Wave Conducting Device, U. S. Patent No. 2, 528, 367, October 31, 1950.

2. C. J. Sletten, Air Force Cambridge Research Laboratories Private Communication, 1962.

3. R. W. P. King, The Theory of Linear Antennas, Harvard University Press, 1956, pp 506-511.

4. Yueh-Ying Hu, Backscattering Cross Section of a Center-loaded Cylindrical Antenna, IRE Transaction on Antenna and Propagation, Jan. 1958, pp 140-148.

5. B. -O. Ås and H. J. Schmitt, Backscattering Cross Section of Reactively Loaded Cylindrical Antennas, Harvard University Cruft Laboratory, Scientific Report No. 18, August 15, 1958.

III. Backscatter Reduction of Long Thin Bodies By Impedance Loading

W. P. Hansen, Jr.
Aero-Space Division
The Boeing Company
Seattle, Washington

Abstract

An impedance-loading technique for backscatter reduction of long thin bodies is discussed and experimental verification of the technique presented. It is shown that a significant reduction in the backscatter is possible while providing a receiving capability. The body is thus converted into an antenna that has a high ratio of receiving cross section to backscattering cross section under conditions of low backscatter.

I. INTRODUCTION

Backscattering from a long thin body in the region of longitudinal incidence has been evaluated by Peters[1,2] in terms of a traveling-wave antenna mode excited on the body by an incident wave. In this paper, an impedance-loading technique is described which effectively results in cancelling the backscatter field produced by such a mode. The body is considered as an asymmetrical dipole antenna, and the value of load impedance necessary to accomplish the cancellation of backscatter is determined. Using the Smith-chart representation of Kennaugh and Green[3] for

antenna scattering, the backscattering cross section is evaluated for any load imped-
ance at the frequency under consideration.

An incident wave with the plane of polarization parallel to the axis of the body
excites a traveling wave on the body. This wave is reflected from the rear point,
producing a secondary traveling wave on the body. It is this backward wave that
results in the large backscattering cross section. Elimination of the reflected wave
from the rear point would affect a large reduction in backscattering over a range of
aspect angles in which the travelling-wave mode is the primary mode. It is thus
postulated that a set of antenna terminals be constructed near the rear point so as to
absorb the incident wave without reflection, or to reflect part of the received signal
with the proper phase and amplitude to cancel that which is not coupled to the ter-
minals. In this paper, such a technique is shown to be possible.

2. IMPEDANCE LOADING

In order to evaluate the backscattering characteristics of a long thin body with
an impedance load near the rear point, the general concept of antenna scattering
should be considered. The electric field scattered by an antenna as a function of
load impedance is given by[3]

$$\bar{E}(Z_L) = \bar{E}(0) - \frac{Z_L Z_A}{Z_L + Z_A} I(0)\, \bar{E}^T \tag{1}$$

where

$Z_L = R_L + jX_L$ is the load impedance,

$Z_A = R_A + jX_A$ is the antenna impedance,

$\bar{E}(0)$ is the scattered field of the antenna with $Z_L = 0$,

$\bar{E}^T$ is the electric field transmitted by the antenna when excited by a unit
voltage source, and

$I(0)$ is the current through the load $Z_L = 0$.

This equation may also be written as[3]

$$\bar{E}(Z_L) = \bar{E}(Z_A^*) + \Gamma\, \bar{E}^{AM} \tag{2}$$

where

Z_A^* is the complex conjugate of Z_A,

$\bar{E}(Z_A^*)$ is the structural scattered field,

$$\bar{E}^{AM} = \frac{Z_A^2}{2R_A} I(0) \bar{E}^T \text{ is the antenna-mode scattered field,}$$

$$\Gamma = \frac{1 - Z_L^N}{1 + Z_L^N} \text{ is the reflection coefficient, and}$$

$$Z_L^N = \frac{Z_L + jX_A}{R_A} \text{ is the normalized load impedance.}$$

If the condition

$$\Gamma \bar{E}^{AM} = -\bar{E}(Z_A^*) \tag{3}$$

is fulfilled, then the scattered field $E(Z_L)$ is zero. In order to accomplish this over some range of aspect angles, one should have

$$\frac{\bar{E}^{AM}}{\bar{E}^{AM}} = \frac{\bar{E}(Z_A^*)}{|\bar{E}(Z_A^*)|} \tag{4}$$

over that range. The load impedance is then adjusted to provide the proper phase and amplitude of the reflection coefficient so as to fulfill Eq. (3).

The long thin body with a set of terminals near the rear point may be considered as an asymmetrical dipole antenna. For a high degree of asymmentry, the primary mode in the region of longitudinal incidence is the traveling-wave mode. When short-circuited, this asymmetrical dipole reduces to the long thin body considered by Peters[1,2]. From Eq. (1) the structural scattering $E(Z_A^*)$ may be written as

$$\bar{E}(Z_A^*) = \bar{E}(0) - \bar{E}^{AM} e^{-j2\phi} \tag{5}$$

where ϕ is the phase angle of the antenna impedance. One can also write[1]

$$\bar{E}(0) = \gamma \bar{E}_0^{AM} \tag{6}$$

where γ is the reflection coefficient at the end of the body and $\overline{E}_0^{AM}$ is the field radiated by the traveling-wave antenna mode excited on the short-circuited body. Thus Eq. (4) should hold for the long, thin body in the region of longitudinal incidence. Considering only the components of Eqs. (3), (5), and (6), the reflection coefficient necessary for cancellation then becomes

$$ -\Gamma = \gamma \frac{E_0^{AM}}{E^{AM}} - e^{-j2\phi}. \tag{7} $$

If $E_0^{AM} = E^{AM}$ and γ is constant as a function of aspect angle, then it should be possible to find a load impedance that would result in cancelling the structural scattering. If $E_0^{AM} \neq E^{AM}$, then the load impedance would need to be varied as a function of aspect angle to affect the cancellation.

For the case considered, the terminals are some finite distance from the end of the body so that E_0^{AM} and E^{AM} are not identical. However, if the distance is sufficiently small they are nearly the same. In this case it should be possible to find a load impedance that would result in considerable reduction in backscattering over some range of aspect angles.

3. EXPERIMENTAL EVALUATION

In order to verify that effective cancellation of the structural scattering is possible, an experimental evaluation was made. The test model, shown in Figure 1, consists of a 30-degree ogive with a coaxial-fed probe extending from the rear of the model. Backscatter and receiving cross sections were measured at a frequency of 2000 Mc with the plane of polarization parallel to the axis of the body. For these measurements, the model was supported on a polyurethane foam tower. A small coaxial cable was brought out from the model and connected to an adjustable load impedance, a power meter, and to other equipment located at the base of the tower. For the polarization used, the coaxial cable was perpendicular to the incident electric field, hence its effect on the measurements was sufficiently small.

The model was positioned at an aspect angle corresponding to the peak of the main lobe, and the load impedance was adjusted for minimum backscatter. In this manner, the peak of the main lobe was reduced by 30 db. The entire backscatter pattern was then measured, the results of which are shown in Figure 2. It is seen that an effective backscatter reduction of 20 db is accomplished over the main lobe. The 30-db reduction of the peak of the main lobe is not maintained for other aspect angles because of the difference between the two antenna modes E^{AM} and E_0^{AM}, as
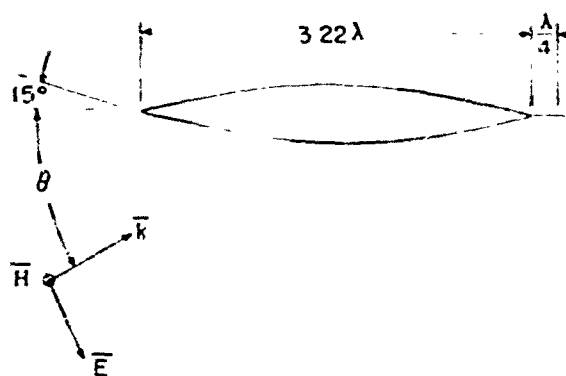
Figure 1. Backscatter Model

Figure 2. Backscatter Reduction Characteristics
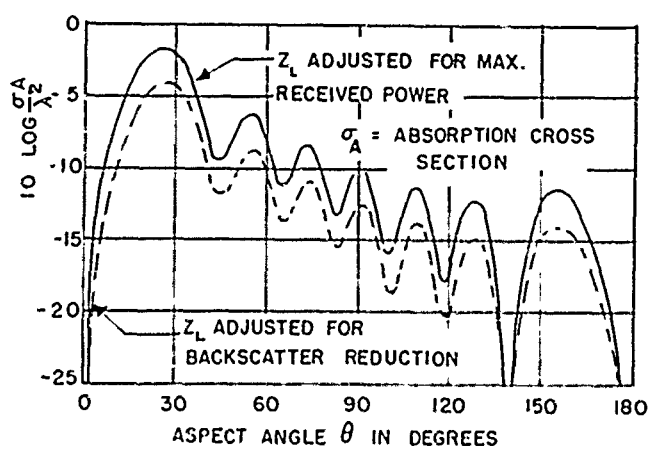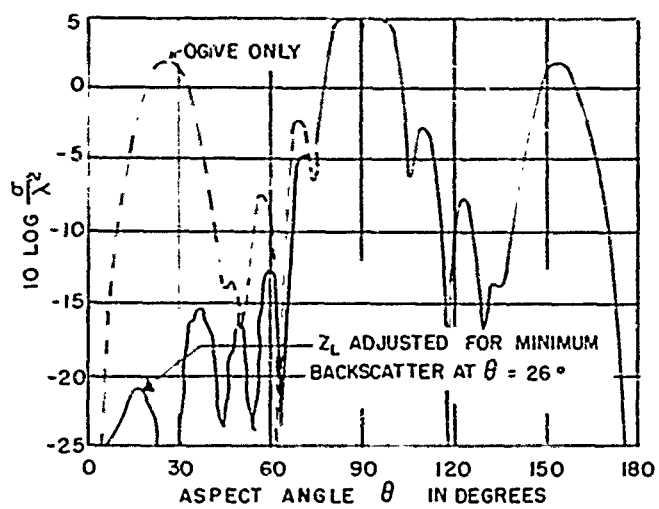
Figure 3. Receiving Characteristics

indicated by Eq. (7). In order to maintain nearly complete cancellation, the load impedance would need to be adjusted as a function of aspect angle.

The receiving characteristics of the model were evaluated under conditions of minimum backscatter and maximum received power. These characteristics are shown in Figure 3, and indicate that the received power under conditions of minimum backscatter is 3 db less than the maximum received power obtained. Thus, one-half of the received power is reflected from the terminals with the proper phase and amplitude to effectively cancel the structural scattering. For the condition of maximum received power, a backscatter reduction of only 5 db was accomplished. The measured values of antenna impedance and the load impedance necessary for minimum backscatter were found to be

$$Z_A = 82 - j15 \text{ ohms}$$

and

$$Z_L = 68 - j98 \text{ ohms.}$$

As shown by Kennaugh and Green,[3] Eq. (2) may be represented on a Smith-chart impedance diagram. This allows the backscattered field to be evaluated for any load impedance by experimentally evaluating the backscattering cross section for two particular values of load impedance. From Z_A and Z_L given above, the normalized load impedance Z_L^N corresponding to minimum backscatter is found to be 0.74-j1.3 . Circles about this point represent constant backscatter, as shown in Figure 4. Additional measurements allow calibration of these circles in backscattering cross section.

The reflection coefficient $|\Gamma|$ is found to be 0.61 so that $|\Gamma|^2 = 0.37$. Thus, only about one-third of the received power should be required to cancel the structural scattering. It is expected that if various losses can be eliminated in the experimental apparatus, the increased power corresponding to this reflection coefficient could be measured.

4. CONCLUSION

It has been shown that backscattering due to the traveling-wave mode on a long thin body can effectively be cancelled by an impedance-loading technique. Furthermore, the cancellation is accomplished with only a small reduction in received power. Using the Smith-chart representation of antenna scattering, the backscattering cross section is evaluated for any load impedance at the frequency under consideration.

O EXPERIMENTAL PCINTS
$db\lambda^2 = 10 \ LOG\frac{\sigma}{\lambda^2}$

$\sigma = +4 \, db\lambda^2$

$\sigma = +2 \, db\lambda^2$

$\sigma = 0 \, db\lambda^2$

$|\Gamma|^2 = 0.37$

$\sigma = -3 \, db\lambda^2$

$\sigma = -10 \, db\lambda^2$

$\sigma = -30 \, db\lambda^2$
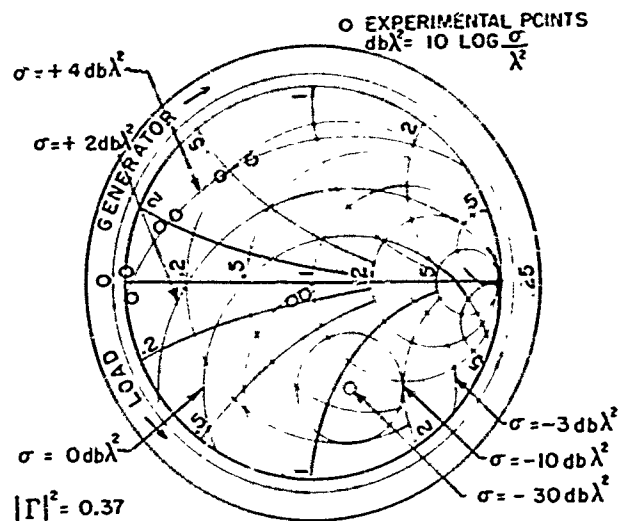
Figure 4. Backscattering From an Asymmetric Dipole

Although the impedance-loading technique as described for the long thin body
is rather frequency sensitive, it may be possible to extend the bandwidth by select-
ing the proper thickness and asymmetry of the scattering body. This coupled with
a feedback system for control of the load impedance may result in a large back-
scatter reduction over a wide bandwidth and wide range of aspect angles. Prelim-
inary experiments in this area indicate hopeful results.

References

1. L. Peters Jr., End-fire echo area of long, thin bodies, IRE Transactions on
   Antennas and Propagation, AP-6: 133-139, January 1958.

2. L. Peters Jr., Echo Area Properties of Bodies Due to Certain Traveling
   Wave Modes, Antenna Lab., The Ohio State University Research Foundation
   Report 777-19, May 18, 1960. Prepared under contract AF 33(616)-5341.
   Air Research and Development Command, Wright Air Development Center,
   Wright-Patterson Air Force Base, Ohio.

3. R. B. Green, The Effect of Antenna Installations Upon the Echo Area of an
   Object, The Ohio State University Research Foundation Report 1109-3,
   September 29, 1961. Prepared under contract AF 33(616)-7386, Aero-
   nautical Systems Division, Air Force Systems Command, Wright-Patterson
   Air Force Base, Ohio.

This Document Contains
Missing Page/s That Are
Unavailable In The
Original Document

OR are
Blank pg?
that have
Been Removed

**BEST
AVAILABLE COPY**

IV. Theoretical and Experimental Investigation of Backscattering From a Cavity-Loaded Monopole

Werner W. Gerbes and William J. Kearns
Microwave Physics Laboratory
Air Force Cambridge Research Laboratories
Bedford, Massachusetts

Abstract

Backscattering from a monopole (linear scatterer) can be considerably diminished and almost suppressed if it is grounded in a cavity and the protruding length of the monopole does not exceed 0.45λ. The optimum depth of the cavity is about 0.25λ.

The good agreement between theory and experiment justifies the rather bold theoretical assumptions made to avoid involved mathematics and implies their usefulness in similar problems.

1. INTRODUCTION

So far as we know, backscattering from a linear scatterer grounded in a cavity has not previously been studied, either theoretically or experimentally. The only work coming close to ours is the experimental and theoretical work on unloaded antennas cited by R. W. P. King in The Theory of Linear Antennas, Harvard University, 1956, pp. 508, 509, 516.

In our initial (1956) study of backscattering from a grounded scatterer, we restricted ourselves to the case of a monopole projecting from the center of a cylindrical cavity in a plane, perfectly conducting screen (Figure 1); the monopole was excited by a wave traveling along the surface S with an electric vector E parallel to the scatterer. The restriction to cavity-loaded monopoles was actually unnecessary, since the formulas obtained led easily to a generalization for monopoles loaded with an arbitrary impedance. Although we demonstrate this possibility in the text, we did not change our study to the general case because it had been stimulated by, and the experiments conducted for, the specific question of cavity-loaded monopoles.

A further restriction we set was to consider only unmodulated, harmonic, electromagnetic waves. In a sequel to this report we will deal with cases of oblique-incidence waves and modulated or pulsed electromagnetic waves.
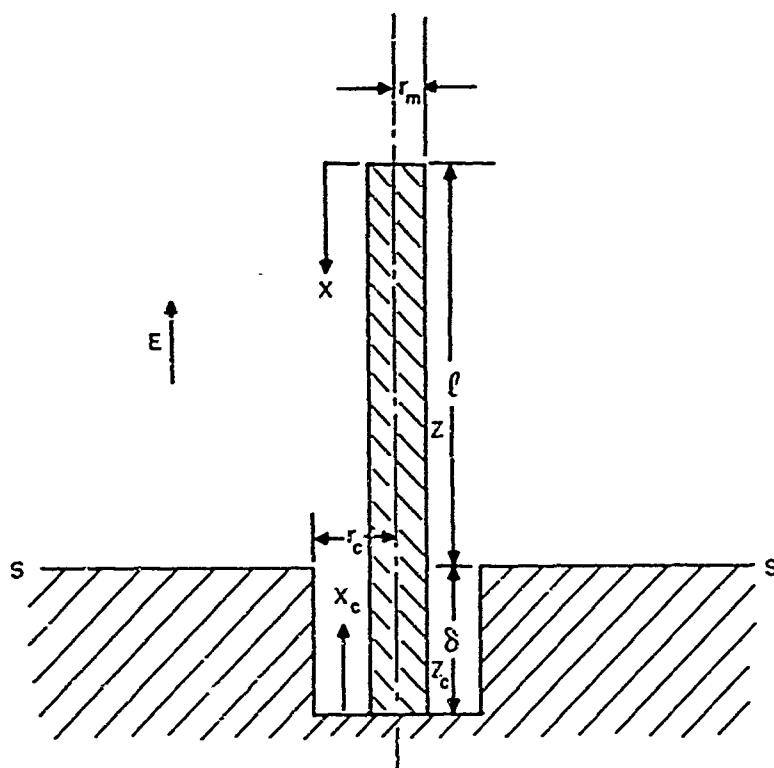
Figure 1. Scheme of Scatterer Arrangement

As in almost all antenna problems, an exact solution with present techniques is difficult if not impossible; the more or less dubious initial assumptions of a theoretical treatment must be justified by experimental substantiation. To keep the

m..thematical treatment relatively simple, we made rather far-fetched assumptions;[*] however, we carefully checked the theory by conducting very reliable experiments. These experiments were conducted by Mr. William Kearns after some exploratory measurements by Mr. H. Poehler. The experimental setup and method of measurements are described in Appendix A.

2. THEORY

Our theoretical approach to the problem (see Figure 1) was based on the idea that (1) the part of the monopole outside the cavity could be regarded as a lossy line of length l, having a char..cteristic impedance Z with an additional voltage dV per element imposed by the incoming electric field E; and (2) the part of the monopole within the cavity could be regarded as a lossless line of length δ, having a characteristic impedance Z_c, grounded at the bottom of the cavity. Strictly, this holds only for $\delta \gg r_c$ (r_c = radius of cavity), but to simplify the mathematics we extended it to cases where $\delta \ll r_c$.

Length x and x_c on lines l and δ are measured toward the screen surface S. Their currents are considered to be positive in the direction measured. The electrical field strength E of the incident wave is taken to be normal to the surface and positive in the outward direction. The field strength of the incident wave is arbitrarily considered to be zero in the cavity.

We then get the two basic relations:

$$
\left.
\begin{aligned}
\frac{\partial V}{\partial x} &= -RI - L\frac{\partial I}{\partial t} - E(t, x), \\
\frac{\partial I}{\partial x} &= -GV - C\frac{\partial V}{\partial t},
\end{aligned}
\right\}
\tag{1}
$$

where, as customary, V is voltage, R is resistance, I is current, G is shunt conductance, L is inductance, and C is capacitance, all per unit length.

If we suppose that the incoming plane wave is incident parallel to the screen surface S, then E along the scatterer is a function of only the time t.

We subject Eq. (1) to a Laplace transform with respect to time and then to another with respect to length. This simplifies the rather involved analysis and

---

[*] An essential disagreement between experimental and theoretical results would demand a "second- or third-order" closer theoretical approach. How immensely such a closer approach complicates the formulas is seen by comparing our formulas given in King's book for an even easier problem.

gives the final formula:[*]

$$\mathcal{E} \sim \left| \Gamma l \ - \tanh (\Gamma l) \ \frac{1 + \frac{Z_c}{Z} \tanh (\Gamma_c \delta) \ 2 \tanh \left(\frac{\Gamma l}{2}\right)}{1 + \frac{Z_c}{Z} \tanh (\Gamma_c \delta) \tanh (\Gamma l)} \right|^2 , \qquad (2a)$$

where $\mathcal{E}$ represents the backscattered energy

$$\Gamma = \left[(R + \omega L) \ (G + j\omega C) \right]^{\frac{1}{2}}$$

$$Z = \left[\frac{R + j\omega L}{G + j\omega C} \right]^{\frac{1}{2}}$$

and Γ_c and Z_c are the analogous quantities for the cavity parameters R_c, L_c, G_c, and C_c. Specialized for $\delta = 0$,

$$\mathcal{E}_o \sim | \ \Gamma l \ - \tanh (\Gamma l) |^2 , \ \mathcal{E}_o = 0 \text{ for } l = 0 \text{ only}. \qquad (2b)$$

Equation (2b) describes the behavior of the unloaded monopole directly connected with a conducting plane and also, of course, the backscattering of a dipole of length $2l$ in freespace.

If $l << \lambda$, then $2 \tanh (\Gamma l)$ goes to 1. Therefore, everything after the minus sign of Eq. (2a) becomes a constant that will be small compared with Γl. Thus $\mathcal{E} \sim |\Gamma l|^2 \sim l^2$. The backscattered energy increases as the second power of the length of a very long monopole.

If $l << \lambda$, then $2 \tanh \frac{\Gamma l}{2} \cong \tan (\Gamma l)$ and $\mathcal{E} \sim |\Gamma l \ - \tan (\Gamma l)|^2 \sim |(\Gamma l)^3|^2 \sim l^6$.

The backscattered energy increases as the sixth power of the length of a very short monopole.

Unfortunately, the evaluation of Eqs. (2a) and (2b) is so complicated [even the seemingly simpler formula (2b)] that it was not feasible to carry out calculations for general properties. Equation (2a) was, therefore, calculated with a computer for certain combinations of the parameters so as to obtain families of theoretical curves for comparison with the experimental ones. The parameters Z_c/Z, Γ, and Γ_c had to be chosen as close as possible to the experimental conditions, but with simplifications necessary to keep the calculations within reasonable limits.

---

[*] The complete analysis is given in the report AFCRL-63-355 "Theoretical and Experimental Investigation of Backscattering From a Cavity-loaded Monopole" by Werner W. Gerbes and William J. Kearns.

The complex propagation constant for the upper part of the monopole, $\Gamma = \alpha + i\beta$, where α is the attenuation constant and β is the phase constant, is naturally only approximately a constant. But we can set β equal to that of freespace, so that $\beta = 2\pi/\lambda = \omega/c$. The attenuation constant α is related to the radiation resistance of the monopole. To avoid complicated calculations, we considered α a parameter and calculated a family of curves for every depth of the cavity, setting $\Gamma = \alpha + i\omega/c$.

In the complex propagation constant for the lower part of the monopole (Γ_c), we set $\alpha_c = 0$ because the radiation of this part can be neglected. The phase constant was again taken as approximately equal to that of freespace. Therefore,

$$\beta_c = \frac{\omega}{c} \quad \text{and} \quad \Gamma_c = i\frac{\omega}{c}.$$

For Z_c we used the formula for capacitance of a coaxial cable, and for Z we used the formula for capacitance of an elongated rotational ellipsoid. The characteristic resistance is inversely proportional to the capacitance per unit length C. Thus $Z_c/Z = C/C_c$. Now

$$C_c = \frac{1}{2 \ln \dfrac{r_c}{r_m}}; \quad C = \frac{\sqrt{\left(\dfrac{\ell}{2r_m}\right)^2 - 1}}{\dfrac{1}{r_m} \operatorname{arcosh}\left(\dfrac{\ell}{2r_m}\right)}.$$

Therefore, with $\ell/2r_m = p$,

$$\frac{Z_c}{Z} = \ln \frac{r_c}{r_m} \; \frac{\sqrt{1 - \dfrac{1}{p^2}}}{\operatorname{arcosh} p}, \tag{3}$$

54

where r_m is the radius of the monopole, r_c is the radius of the cavity, and l is the upper length of the monopole. Evidently, Z_c/Z is a function of l and further complicates the numerical calculation.

For monopoles of small length, if $p \to 1$, $Z_c/Z \to 0/0$. Ordinary evaluation by differentiation gives

$$\frac{Z_c}{Z} \to \ln \frac{r_c}{r_m} \quad,$$

a constant with respect to l. For monopoles that are very long, if $p \gg 1$, a short calculation gives us

$$\frac{Z_c}{Z} \to \frac{\ln \dfrac{r_c}{r_m}}{\ln \dfrac{l}{r_m}} \to 0 \,,$$

showing that for very long monopoles Eq. (2a) changes to Eq. (2b), the equation for a monopole without a cavity. This means the cavity has no effect on the back-scattering of very long monopoles. To simplify calculation of the curves in Figures 2 and 3 we used $Z_c/Z = 1$ as a convenient mean value, which automatically precludes use of the formula for long monopoles.

Basically, there are two ways of deriving the attenuation constant α:
(1) directly, from the radiation resistance of a monopole divided by the length;
(2) indirectly, from measurements of a monopole projecting from a plane surface without a cavity. But both ways, owing to the assumptions on which our whole theory had to be based, lead to more involved calculations without assuring any greater accuracy. We therefore arbitrarily chose δ and α as parameters for the calculation of the families of theoretical curves, and compared them with the families of curves measured for the parameters δ and r_m. All measurements and calculations were based on six values of the parameter δ listed as follows, in inches, and as related to the wavelength used (33 mm):

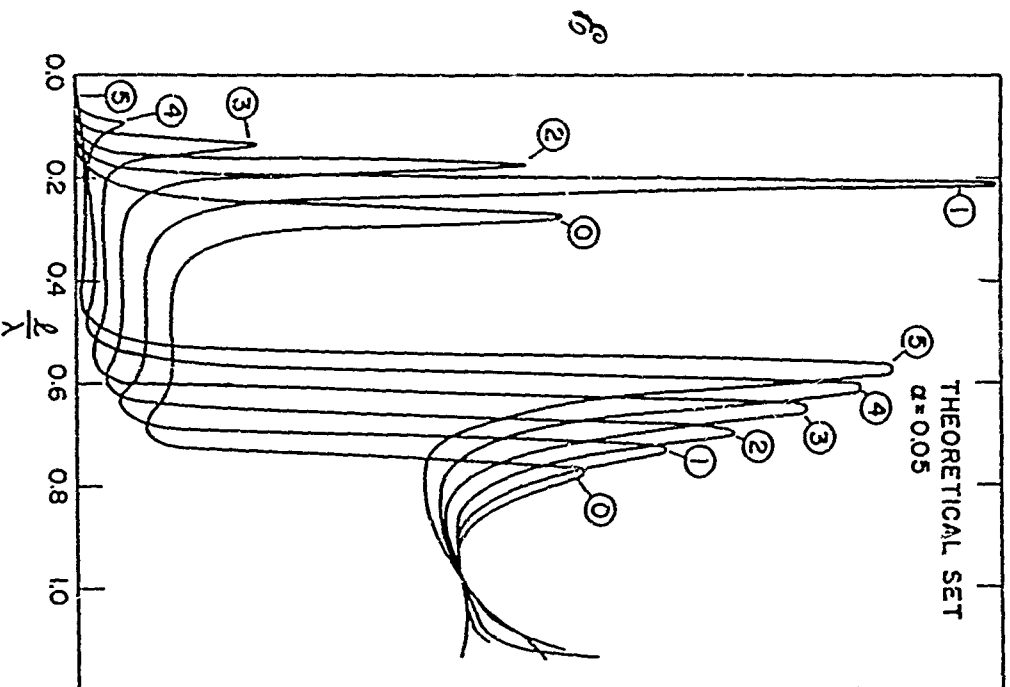| curve	0	1	2	3	4	5
δ (in.)	0.00	0.05	0.10	0.15	0.20	0.25
δ/λ	0.00	0.04	0.08	0.12	0.16	0.20

Figure 2. Backscattered Energy vs Protruding Length of Monopole Calculated for the Six Standard Depths of the Recess and α = 0.05
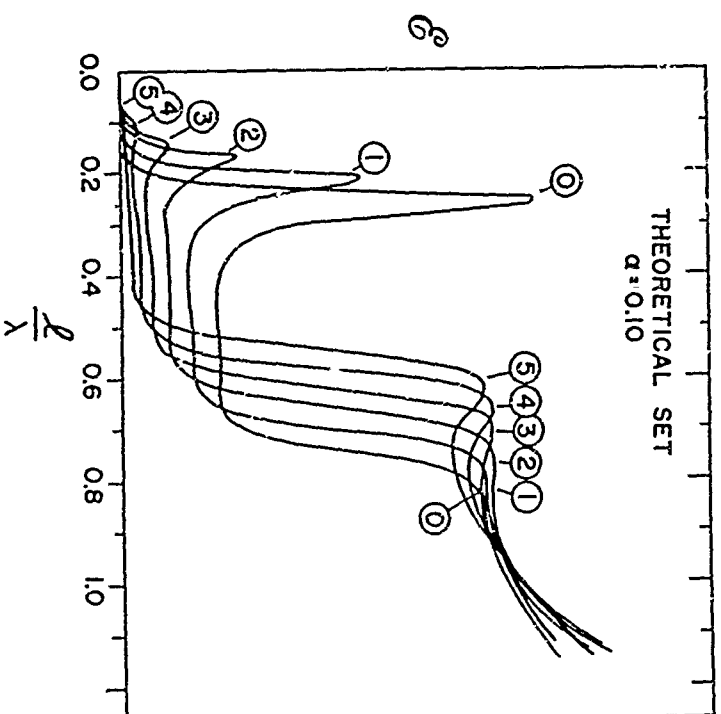

Figure 3. Backscattered Energy vs Protruding Length of Monopole Calculated for the Six Standard Depths of the Recess and α = 0.10

It may be appropriate to mention at this time that the theoretical and experimental sets not only match substantially in shape, but even coincide quantitatively more than we had a right to expect from the somewhat far-fetched assumptions of the theory.

The theoretical set of curves of backscattered energy as a function of the protruding length l of the monopole for $\alpha = 0.05$ (which means a somewhat low radiation resistance or a high characteristic impedance) is shown in Figure 2. The curves rise with the sixth power to a first sharp maximum, then drop to show an area of low but nearly constant backscattering followed by an additional slight depression. They then rise to a second maximum and drop to a second depression that is not nearly as low as the first. This behavior repeats itself over and over.[*]

Obviously, the first depression after the first maximum is the only area that exhibits sufficient backscattering suppression. With a recess 0.20λ deep, the unsuppressed backscattering is apparently only 2 percent of the maximum scattering of the unrecessed monopole.

Figure 3 shows the theoretical set for $\alpha = 0.10$, which means monopoles with somewhat higher radiation resistances than shown in Figure 2. The curves present the same characteristics as the curves of the previous set, but naturally not so pronounced since a higher radiation resistance means more strongly damped circuits with smaller resonance effects. In this case, also, a recess of at least 0.20λ suppresses about 98 percent of the maximum scattering of the unrecessed monopole.

Figures 2 and 3 indicate that for satisfactory scatter suppression the protruding length of the recessed monopole must be less than 0.45λ. If the monopole protrudes more than 0.45λ, backscattering cannot be sufficiently suppressed by means of a cavity.

These theoretical results are thoroughly confirmed by the experiments. Figure 4 shows the experimental set for a rod 1/16 in. thick. The shape of the curves, the shift, and the areas of possible scatter suppression are the same as in the theoretical sets, except that the first maxima are relatively lower with respect to the second maxima than in the theoretical sets (probably due to the choice of $Z_c/Z = 1$). Figure 5 shows the experimental set for a rod 1/32 in. thick. This set also shows good agreement with the theory.

Both experimental and theoretical curves show a definite shift of the maxima of the curves with increasing depth of the recess. Although it appears that the positions of the maxima would coincide if the curves were plotted versus the sum of the protruding and recessed lengths, closer investigation reveals that they would still not exactly coincide.

---

[*] Our simple theory obviously yields the same characteristics as those produced by the more complicated formulas cited in King's book.

In Eq. (2a) the parameters of the cavity appear only in the grouped form: Z_c tanh $(\Gamma_c \delta)$, which represents the impedance of the recessed part. Thus, since the recess acts as an impedance, backscattering could be suppressed just as well by grounding the monopole over a specified impedance. Consequently, if in Eq. (2a) we substitute a general impedance $\mathscr{Z}$ for the term Z_c tanh $(\Gamma_c \delta)$, we obtain the formula for the general case of backscattering from a monopole grounded over an impedance:

$$\mathscr{B} \sim \left| \Gamma \ell \; - \tanh \; (\Gamma \ell) \; \frac{1 + \frac{\mathscr{Z}}{Z} \; 2 \tanh \frac{\Gamma \ell}{2}}{1 + \frac{\mathscr{Z}}{Z} \tanh \; (\Gamma \ell)} \right|^2 \quad . \tag{2b}$$

In this form the final formula also covers the case of backscattering from a center-loaded rod in space.

Two theoretical curves and two experimental curves for each of the basic parameters are compared in Figures 6 to 11. The shape, and even the size, of the curves demonstrates the surprisingly good agreement between theory and experiment.

The results of experiments conducted for some recesses deeper than assumed for theoretical evaluation are given in Figures 12 and 13. These indicate that suppression of backscattering can be achieved with recesses deeper than 0.20λ, but that the frequency range of suppression becomes smaller with increased depth.

It has been shown, both theoretically and experimentally, that backscattering from a monopole can be considerably diminished and almost suppressed if the monopole is grounded in a cavity and its protruding length ℓ does not exceed 0.45λ; with increasing length, cavity-loading becomes increasingly ineffective. Suppression is optimum when the cavity depth is about 0.25λ; deeper recesses narrow the suppression bandwidth considerably.

58

Figure 5. Backscattered Energy vs Protruding Length of Monopole Measured for the Six Standard Depths of the Recess and $2r_m = 1/32$ in.
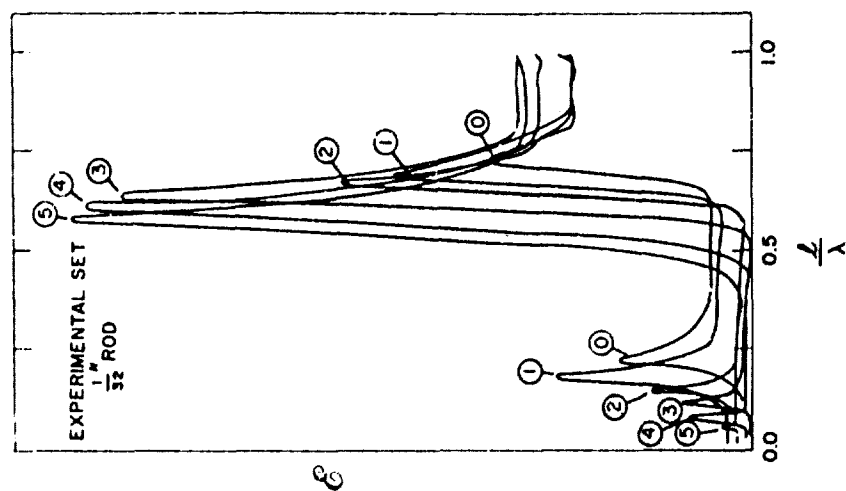
Figure 4. Backscattered Energy vs Protruding Length of Monopole Measured for the Six Standard Depths of the Recess and $2r_m = 1/16$ in.

½ FRAMES

Figure 7. Backscattered Energy vs Protruding Length of Monopole Calculated With $a = 0.05$ and $a = 0.10$ and Measured With $2r_m = 1/16$ in. and $2r_m = 1/32$ in. for a Depth of Recess of $\delta = 0.05$ in.
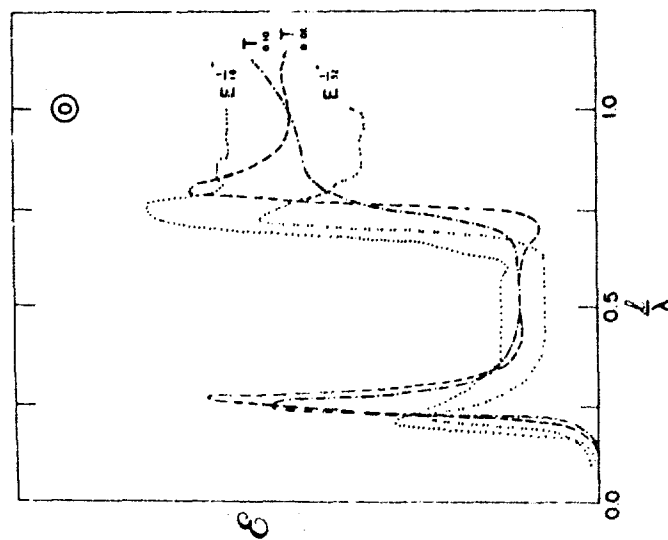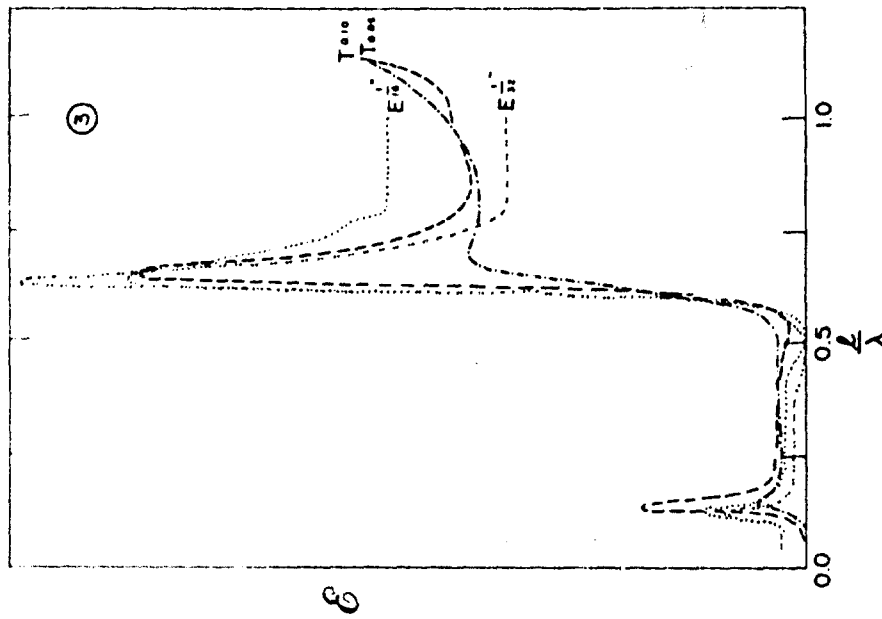
Figure 6. Backscattered Energy vs Protruding Length of Monopole Calculated With $a = 0.05$ and $a = 0.10$ and Measured With $2r_m = 1/16$ in. and $2r_m = 1/32$ in. for a Depth of Recess of $\delta = 0.00$ in.

1/2 FRAMES

Figure 9. Backscattered Energy vs Protruding Length of Monopole Calculated with $\alpha = 0.05$ and $\alpha = 0.10$ and Measured with $2r_m = 1/16$ in. and $2r_m = 1/32$ in. for a Depth of Recess of 0.15 in.

Figure 8. Backscattered Energy vs Protruding Length of Monopole Calculated with $\alpha = 0.05$ and $\alpha = 0.10$ and Measured with $2r_m = 1/16$ in. and $2r_m = 1/32$ in. for a Depth of Recess of $\delta = 0.10$ in.
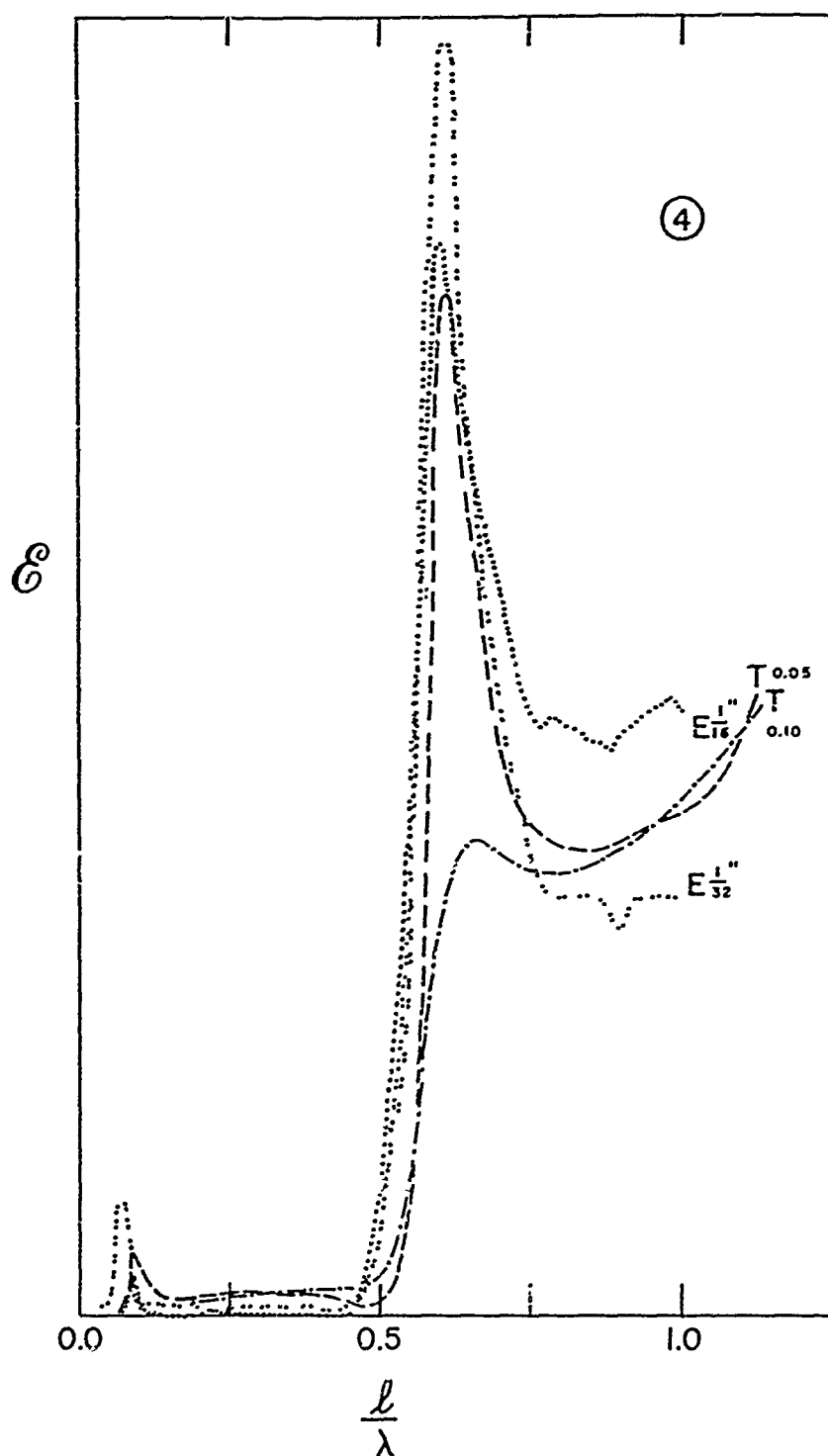
Figure 10. Backscattered Energy vs Protruding Length of Monopole
Calculated With α = 0. 05 and α = 0. 10 and Measured with $2r_m$ = 1/16
in. and $2r_m$ = 1/32 in. for a Depth of Recess of δ = 0. 20 in.
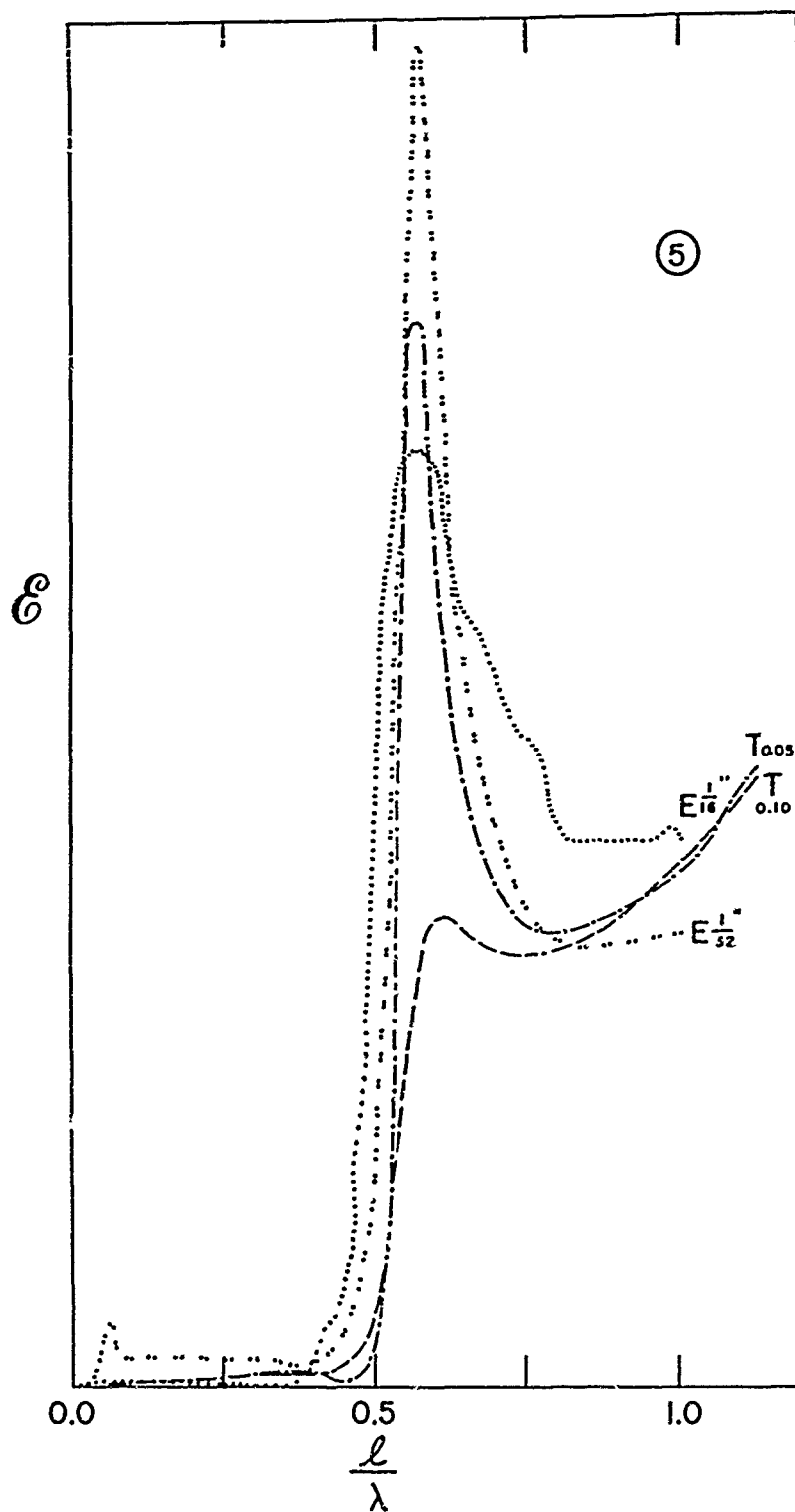
Figure 11. Backscattered Energy vs Protruding Length of Monopole Calculated With α = 0. 05 and α = 0. 10 and Measured With $2r_m$ = 1/16 in. and $2r_m$ = 1/32 in for a Depth of Recess of δ = 0. 25 in.

Figure 13. Backscattered Energy vs Protruding Length of Monopole Measured for Five Recesses Deeper Than the Standard Depths and $2r_m = 1/32$ in.

Figure 12. Backscattered Energy vs Protruding Length of Monopole Measured for Five Recesses Deeper Than the Standard Depths and $2r_m = 1/16$ in.

63
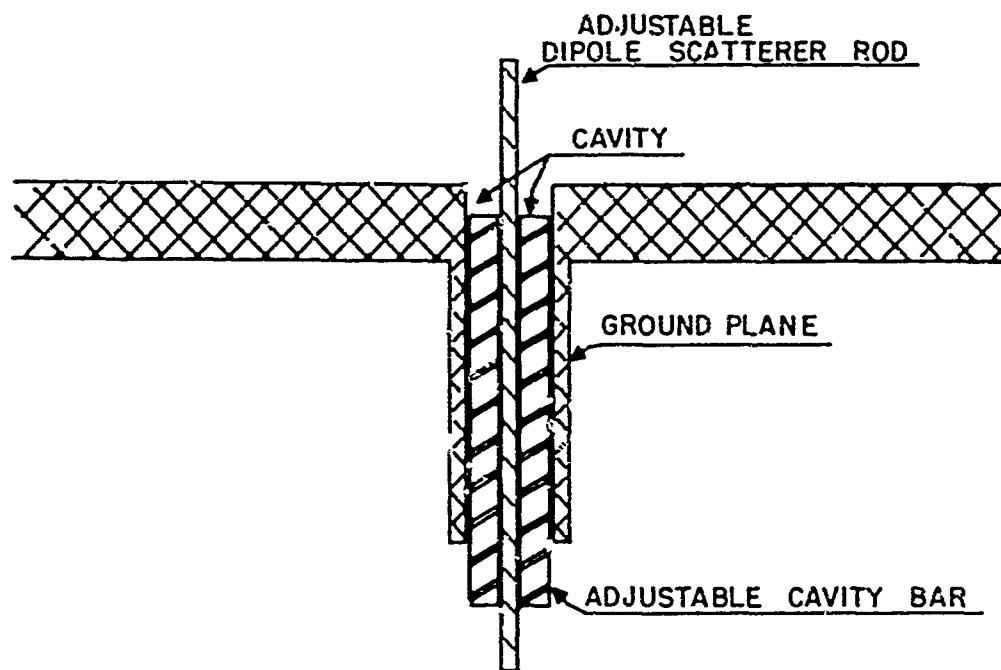
Figure 14. Cross Section of the Mechanical Setup
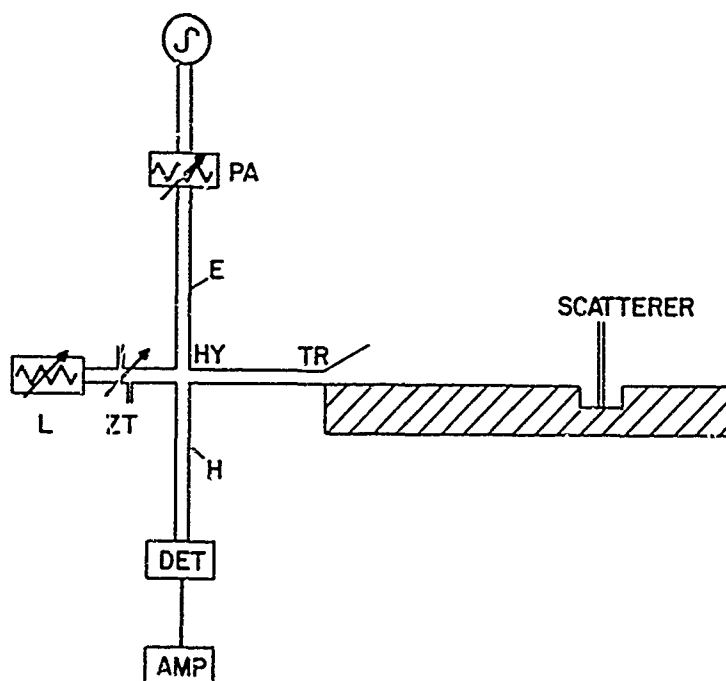
Figure 15. Scheme of the Experimental Arrangement

Appendix A

1. EXPERIMENTS

The backscattering from a monopole grounded in a cavity was measured for various heights of the monopole above the ground plane and for various depths of the cavity. A variable-depth cavity was obtained by machining a hole into the ground plane and precision-fitting a sliding circular brass bar into the hole. A brass rod was precision-fitted into a hole drilled through the center of the bar. This was the monopole, also variable in height and independent of the adjustments made in the cavity (Figure 14).

In the block diagram (Figure 15) showing the experimental arrangement of the apparatus, the symbols are as follows:

T_1 a stabilized frequency source operating at 9080 Mcps, modulated at 1000 cps

PA   precision waveguide attenuator

E   transmitter arm

HY   hybrid junction isolating arms H and E

H   receiver arm, containing a crystal detector and a bolometer amplifier for recording the signal level

Z_T adjustable impedance transformer attached to the third arm of HY , offering better isolation from the rest of the circuit when used with L

L   precision adjustable load, attached to the third arm of HY

TR   fourth arm, carrying the transmitted signal and reflected signal

2. MEASUREMENT PROCEDURES

2.1. Without a scatterer on the ground plane, Z_T was tuned for the minimum signal return, which was found to be at about 85 db below the transmitted signal. Since this was approximately the same as the inherent noise level of the amplifier, the reference level was arbitrarily chosen to be 10 db above noise. For all measurements the reflected signal was attenuated to the reference point, and the amount of attenuation read on a calibrated db scale was recorded at the value of the signal return.

2.2. For the first set of measurements, the top of the circular brass bar was left on a level with the ground plane so that no cavity existed. The top of the 1/16-in.-diameter monopole was raised to a height of 1λ above the ground plane, and a measurement taken. The monopole was then successively depressed so that its height above the ground plane was regularly reduced in increments of 0.025 in., and readings taken until the monopole had reached zero height above the plane.

2.3. The monopole was then again extended to a height of 1λ above the plane. This time the circular bar was depressed into the ground plane, creating a cavity, and the measurements described in Step 2.2 were repeated. The depth of the cavity was regularly increased in increments of 0.05 inch. In each case the monopole was raised to the same 1λ height above the ground plane and incrementally reduced until the height was again zero.

2.4. To determine the influence of the ratio of monopole diameter to wavelength on the curves, identical measurements were made with a monopole of half the diameter (1/32 in.) and an appropriate cavity bar. A comparison of the data for both monopoles shows that the curves are essentially the same, except that the shape is more pronounced in the case of the thin rod.

2.5. As a standard reference, a hemisphere 0.437 in. in diameter was placed at the same point at which the monopole had stood. The return from the hemisphere was noted to be 13.8 db above the arbitrary reference level for the monopole.

V. Scattering From Thick Reactively Loaded Rods

C. J. Sletten, P. Blacksmith, F. S. Holt, and B. B. Gorr
Microwave Physics Laboratory
Air Force Cambridge Research Laboratories
Bedford, Massachusetts

1. INTRODUCTION

For objects whose dimensions are large in terms of wavelength, considerable reduction in backscattering cross section, σ, can be obtained in certain specified directions by shaping the object. Again, for objects large compared to wavelength, considerable reduction in σ for all target attitudes can be attained by coating the object with absorbing material. For objects whose dimensions are of the order of a wavelength, it was conjectured that the techniques of shaping and coating with absorbing material would lose their effectiveness in reducing σ, and that additional techniques would be required for effective control. One such additional technique, namely passive reactive loading, has been the subject of considerable experimental investigation at AFCRL.

This paper is principally concerned with an examination of the effectiveness of the three techniques — shaping, coating with absorbing material, and passive reactive loading — individually and in combination, in reducing σ for objects of resonant dimensions.

2. EXPERIMENTAL SETUP AND DEFINITIONS

All experimental measurements were made at S band on the AFCRL freespace scattering range at the Ipswich Field Test Site, Ipswich, Massachusetts. All targets were placed on a styrofoam column and rotated 360° about the vertical axis of the column. Elongated objects were always mounted with their long dimension horizontal; for such objects, horizontal polarization means polarization parallel to the long dimension, and vertical polarization means polarization perpendicular to the long dimension.

The terms peak σ_H and peak σ_V are used to designate the maximum σ under, respectively, horizontal and vertical polarization conditions for those target aspects attained by rotating the objects 360° about a vertical axis. The term overall peak σ denotes the larger of peak σ_H and peak σ_V. For some of the plots the peak σ's are normalized for each target to the overall peak σ for that target under unloaded or shorted conditions. The angle of rotation of the target about the vertical axis is designated by θ. Unless otherwise explicitly stated, all elongated objects are approximately 2 in. long, that is, $\lambda/2$ at S band.

3. BACKSCATTER REDUCTION BY MEANS OF ABSORBING MATERIAL

Conductron, Inc. absorbing material, Sample No. 17 - 109, has been tested on several shapes in the resonance region. In all cases the targets were metal plates coated with the absorbing material on one side only. The target configurations were a 1.2λ by 1.2λ square, a $\lambda/2$ by $\lambda/2$ square, a $\lambda/2$ by $\lambda/4$ rectangle, and a $\lambda/2$ by $\lambda/8$ rectangle. Figure 1 presents the results for vertical polarization, and Figure 2 the results for horizontal polarization.

The solid curves are σ vs. target angle θ for the metal side of the target, and the dashed curves are σ vs. θ for the absorber side of the target. The σ scale is in db with an arrow denoting a reference value of $\sigma_o = 29.2$ sq cm (the backscattering cross section of a 1.25-in.-diameter metal sphere).*

For vertical polarization (Figure 1), the absorbing material produces a large reduction in peak σ_V for all targets. For horizontal polarization (Figure 2), the absorbing material is very effective for the square targets but relatively ineffective for the elongated targets (Figures 2c and 2d). Note that for the metal side of the $\lambda/2$ by $\lambda/8$ target, the peak σ_V is down from the peak σ_H about 8 db. Thus for elongated targets of this type, the condition under which least reduction in peak can be achieved by means of absorbing material (that is, horizontal polarization) is just the condition under which peak σ is greatest. Conversely, for the same

---

*This reference value σ_o appears in many of the subsequent plots.

type of target the condition under which <u>greatest</u> reduction in peak σ can be achieved by means of absorbing material (that is, vertical polarization) is just the condition under which the peak σ is <u>least</u>.
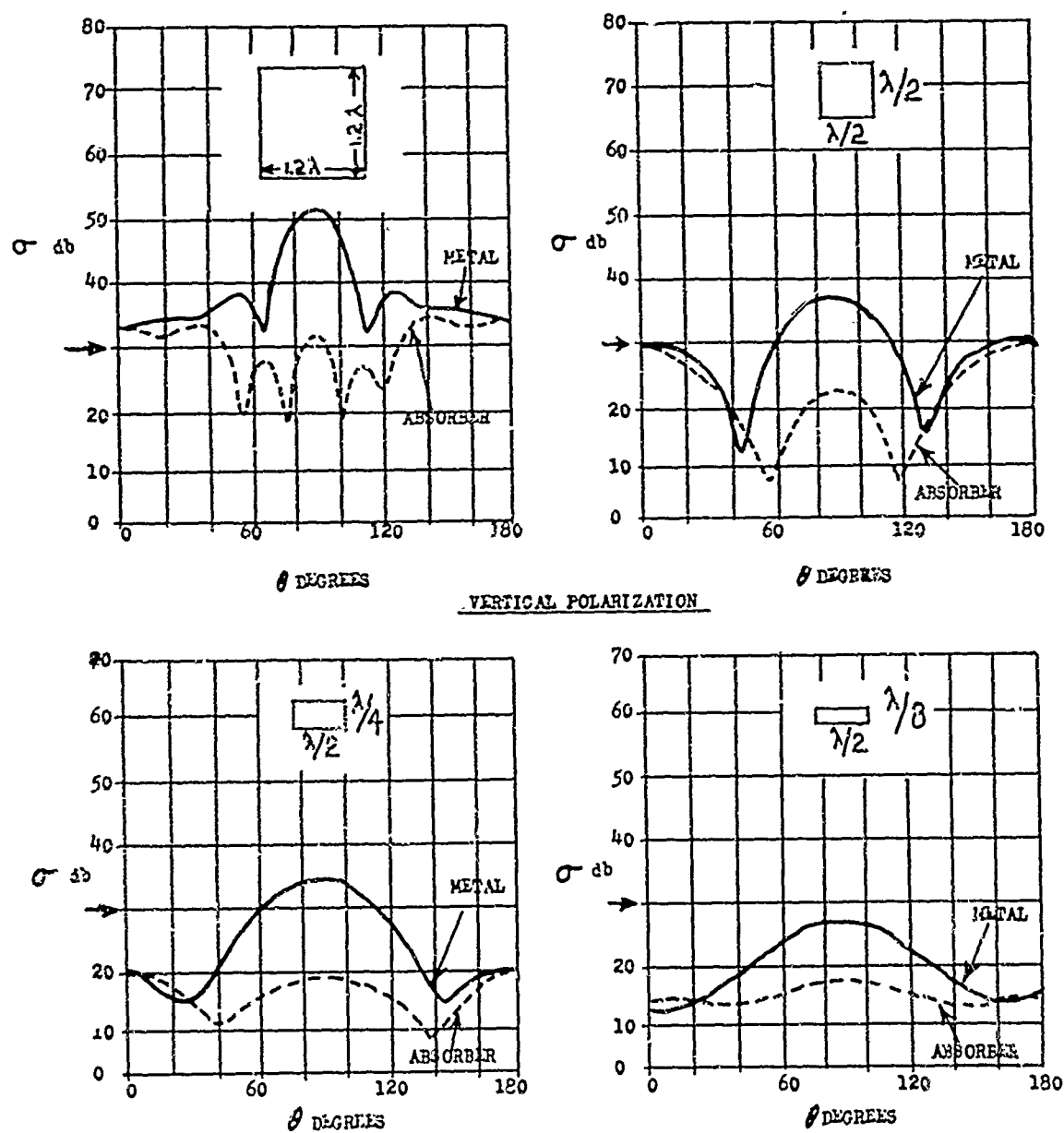
Figure 1. Backscattering Cross Section σ vs Target Angle θ for Conductron, Inc. Absorbing Material Sample Number 17-109. Polarization Vertical.
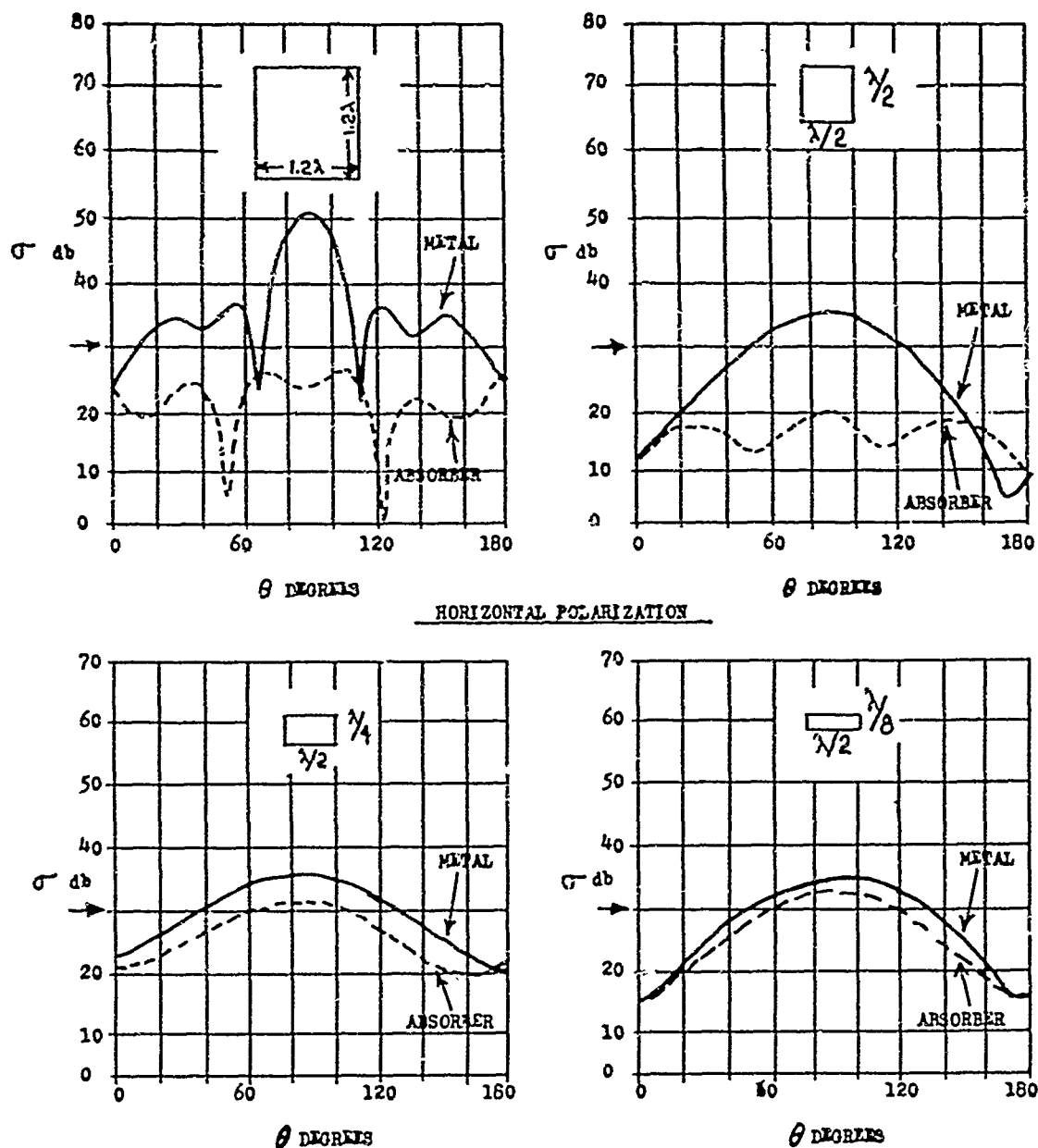
Figure 2. Backscattering Cross Section σ vs Target Angle θ for Conductron, Inc. Absorbing Material Sample Number 17-109. Polarization Horizontal.

4. BACKSCATTER REDUCTION BY MEANS OF TARGET SHAPING

In Figure 3 backscattering cross section σ vs. target angle θ is shown for a cylindrical rod and a truncated cone under horizontal polarization. The dimensions of the targets are shown in the figure. Changing from the cylindrical shape to the conical shape, although reducing the volume by a factor of approximately 3, did not reduce the peak σ_H; rather, it slightly increased it. Also note that σ did not decrease for the nose-on aspect of the cone compared with the rod.
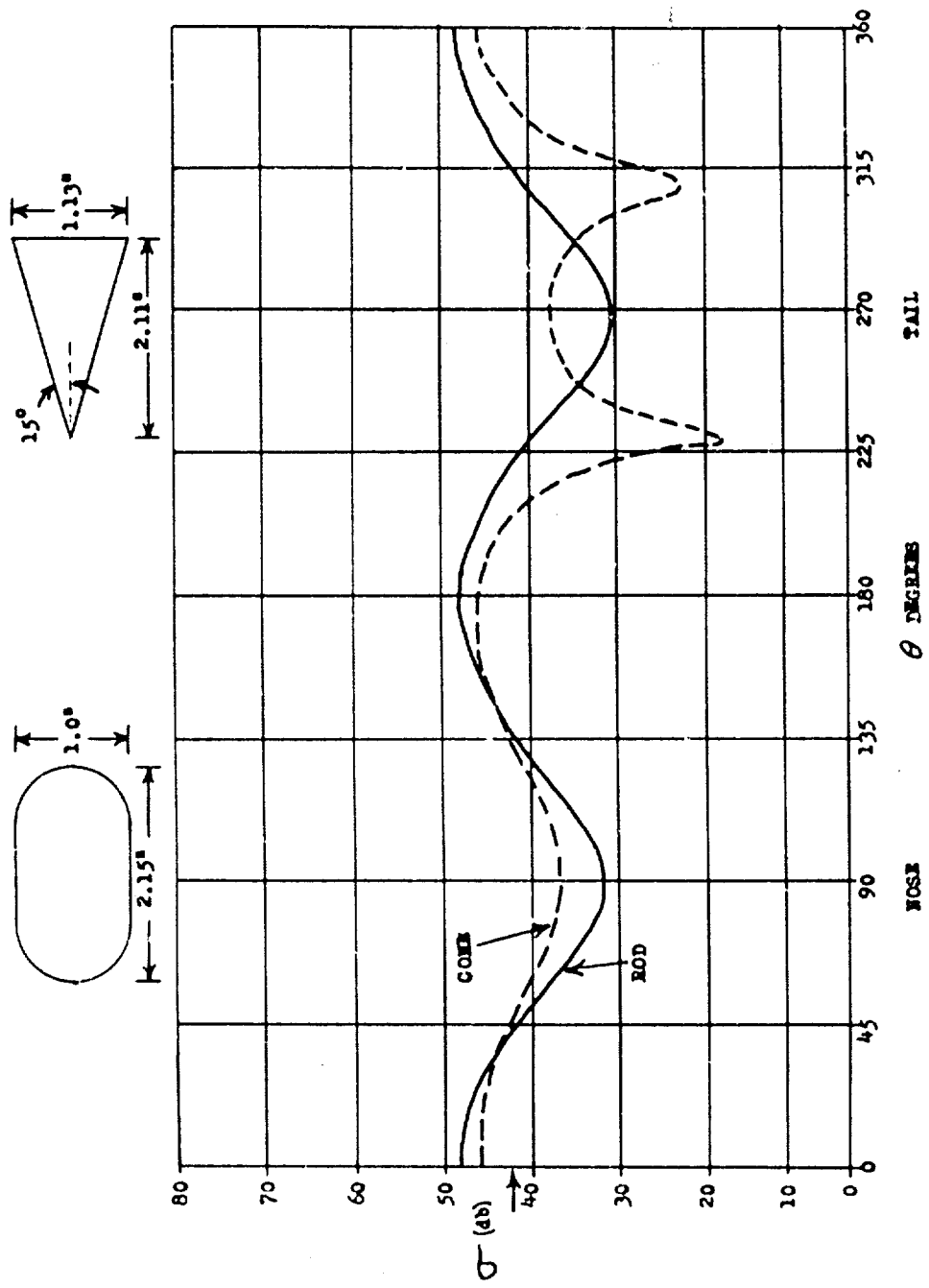
Figure 3. Backscattering Cross Section σ vs Target Angle θ for a Rod and a Cone. Polarization Horizontal. Frequency = 3100.8 Mcps.

The effect of rod diameter on peak σ_V and peak σ_H for rods approximately $\lambda/2$ long is shown in Figure 4. The curves show that peak σ_H is essentially independent of rod diameter over the range of values considered and that peak σ_V increases with rod diameter. For rods approximately $\lambda/2$ long, it is clear that overall peak σ occurs for horizontal polarization. It is also clear that peak σ_V can be controlled by rod diameter but peak σ_H cannot.

If the desired level of reduction in overall peak σ is arbitrarily set at 15 db below the overall peak σ for a solid $\lambda/2$ rod, then, at least for vertical polarization, this can be achieved by using a rod whose diameter is $\lambda/8$ or less. Clearly then, to achieve the desired level of reduction in overall peak σ for a rod, peak σ_H must be reduced. Neither the absorbing material nor the target shapes tested were effective in reducing peak σ_H. This leads then to consideration of the passive reactive loading technique.

5. BACKSCATTER REDUCTION BY MEANS OF PASSIVE REACTIVE LOADING

Early work in the technique of reducing peak σ_H appears in a patent filed in 1946 by Harley A. Iams.[1] In this disclosure Iams described the use of coaxial loading together with dielectric coating to effect wide-band scatter reduction for metal spacer posts in parallel plate construction. Iams claimed that symmetrical loading at separated, symmetrically placed points (double loading) produced wider-band performance than asymmetrical loading at separated asymmetrically placed points or loading at one point (single loading).

In 1948 C. J. Sletten at AFCRL successfully designed spacer posts for the parallel plate region of the Volir Antenna[2], using the Iams idea Sletten also attempted to multiply load a rod to produce a low backscattering freespace object. This attempt was unsuccessful but Sletten's ideas motivated both a theoretical and experimental investigation of passive reactive loading of monopoles over a ground plane to reduce backscattering by Gerbes, Poehler, and Kearns in 1957.[3]

In 1958 AFCRL supported further research in passive reactive loading of thin monopoles (about $\lambda/45$ in diameter) over a ground plane to reduce backscattering by As and Schmitt at Cruft Laboratory, Harvard University.[4] The Harvard experimental results agreed well with their theoretical results and included multiple as well as single loading.

Independent work using passive reactive loading techniques has been carried out by Andrew Alford Consulting Engineers, Inc. in the reduction of scatter from radio towers. Currently this company is investigating the possibilities of wide-band backscatter reduction by means of active control of reactive loading.

In the last few years under Air Force support the Ohio State University Research Foundation and the University of Michigan Radiation Laboratory have
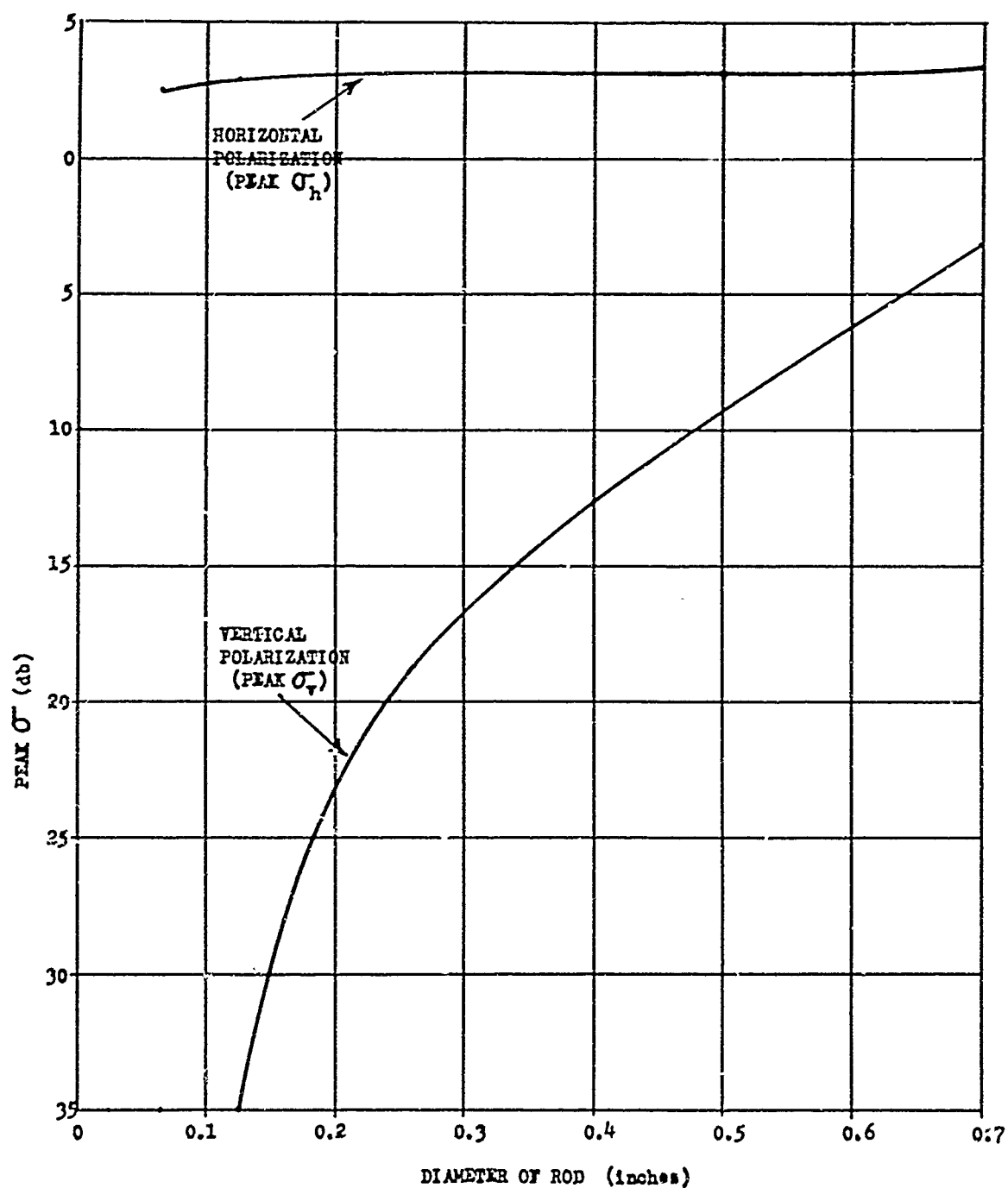
Figure 4. Peak σ vs Rod Diameter for Rod Length $\lambda/2$

investigated reactive loading of various configurations, including rods and slots, to reduce backscattering.

Current investigations at AFCRL have been primarily concerned with the effectiveness of passive reactive loading in reducing peak σ_H for metal rods approximately $\lambda/2$ long and $\lambda/8$ to $3\lambda/8$ in diameter. Three typical single-loaded rods

are shown in Figure 5, and cross sections with dimensions are shown in Figure 6. Note the gap extending circumferentially around the rod and the symmetrical coaxial loading cavities. Figure 7 shows a typical double-loaded rod.
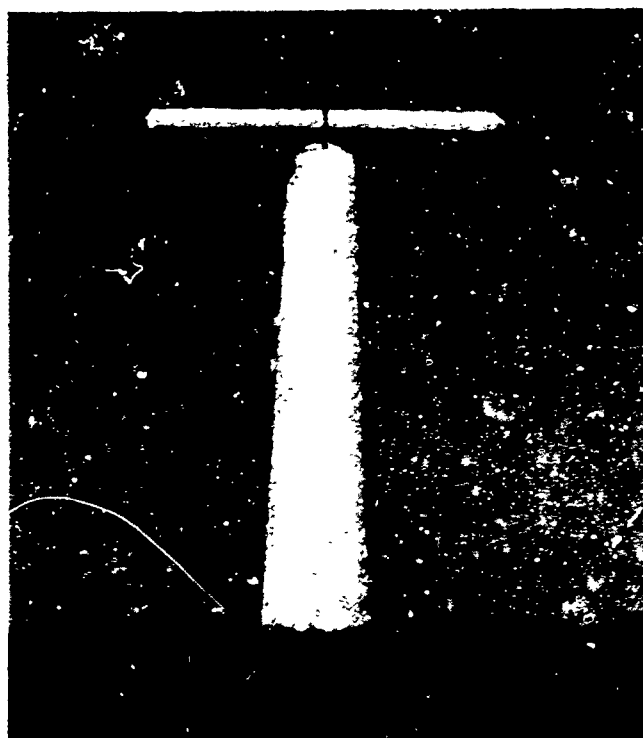
Figure 5. Typical Single Loaded Target Models

Curves of σ vs. target angle θ for the target shown in Figure 6a under horizontal polarization conditions as a function of the total loading cavity length C are shown in Figure 8. The curve labeled C = 0 is for the unloaded or solid rod. As C increases, σ drops significantly until, at C = 0.281 in., peak σ_H has dropped approximately 25 db below overall peak σ. Note that in the broadside aspect σ has been reduced by approximately 40 db. The value of C for minimum peak σ_H, designated as C_{min}, is most easily determined from a plot of normalized peak σ_H vs. C. Curves of this type are shown in Figure 9 for two different rod diameters (see Figures 6a and 6b). For D = 0.5 in., C_{min} = 0.281 in.; for D = 1.0 in., C_{min} = 0.105 in. Apparently the tuning for minimum peak σ_H is less critical for D = 1.0 in. than for D = 0.5 in., as evidenced by the broader minimum.

The dual cavities used in the loading configurations (see Figure 10) are effectively in series. This was experimentally verified by using only one cavity and tuning for minimum peak σ_H. The resultant inductive load was equal to the sum of the loads of the two symmetric cavities of the usual configuration under minimum
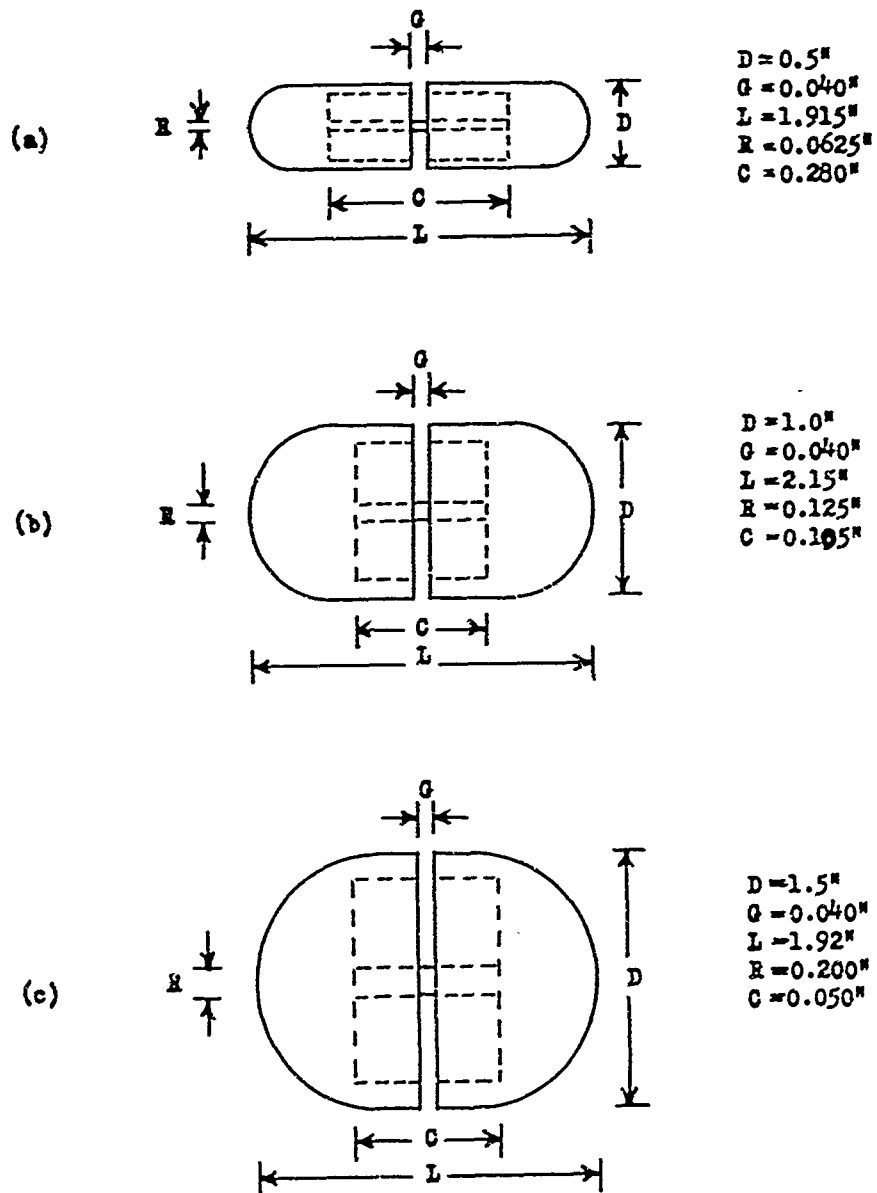
Figure 6.   Dimensions of Target Models Shown in Figure 5

peak σ_H conditions. The circumferential gap that is present in the loading con-
figuration acts as a shunt capacitance across the cavity loads. To determine the
effect of the gap width G on the load impedance required for minimum peak σ_H,
loaded rods with gaps of 0.040 in. and 0.080 in. were tested. Figure 10 shows
that for the two different gap sizes the individual cavity depths C' required for
minimum peak c_H conditions were nearly equal. It is therefore concluded that
the effect of the shunt capacitance associated with the gap is small.

Figure 7. Typical Double Loaded Target Model

The effect of rod diameter D and rod length L on C_{min} is shown in Figure 11.
From Figure 11a it is clear that C_{min} decreases as D increases, and from
Figure 11b it is apparent that C_{min} changes little with L over the range con-
sidered. The latter indicates that there is some hope for bandwidth.

6. MONOSTATIC, BISTATIC, AND BANDWIDTH MEASUREMENTS ON VARIOUS TARGETS

6.1 Monostatic Comparison of Cylindrical Shape with Double Conical Shape

A comparison of the backscattering from a cylindrical rod loaded and unloaded
with the backscattering from a double conical shape loaded and unloaded is shown
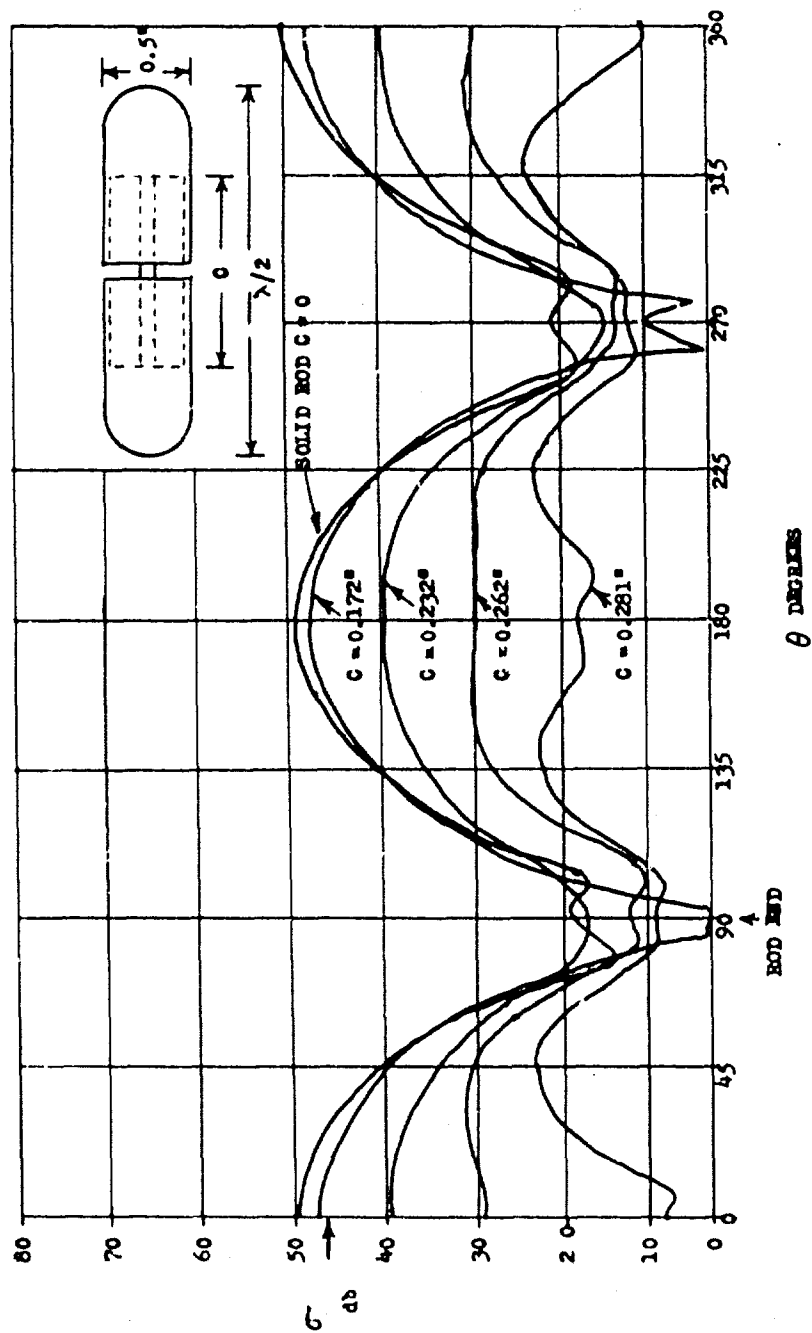
Figure 8. Backscattering Cross Section σ vs θ Target Angle for Various Loadings of a Single Loaded Rod. Polarization Horizontal. Frequency = 3100.8 Mcps.

77
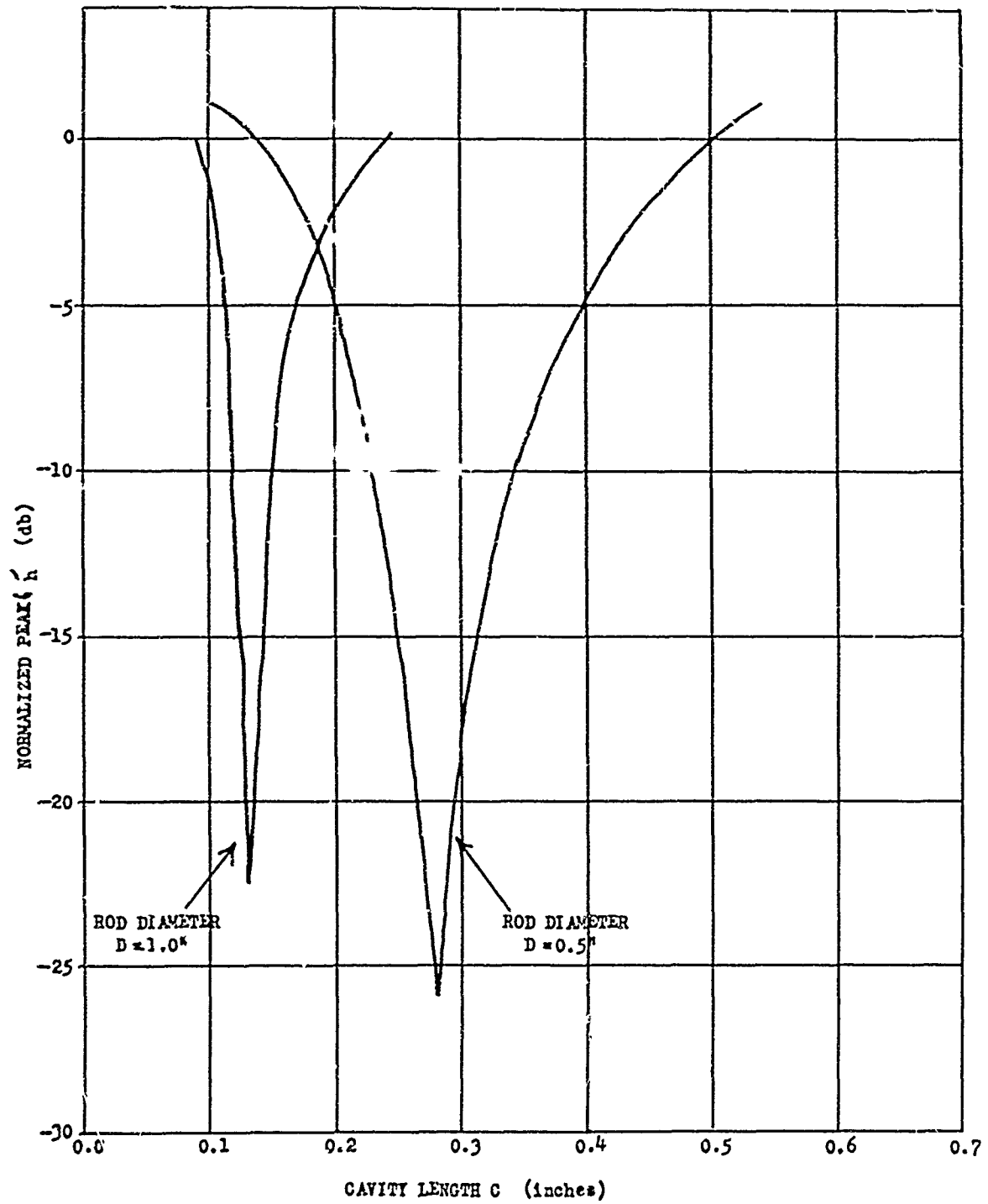
Figure 9. Normalized Peak σ_h vs Cavity Length C for Single Loaded $\lambda/2$ Rods of Diameter 0. 5 inch and 1. 0 inch.

(a) EQUIVALENT CIRCUIT GEOMETRY

(b) PEAK σ_H VS c' FOR SINGLE LOADED $\lambda/2$ RODS WITH DIFFERENT SHUNT CAPACITANCE (GAP G)
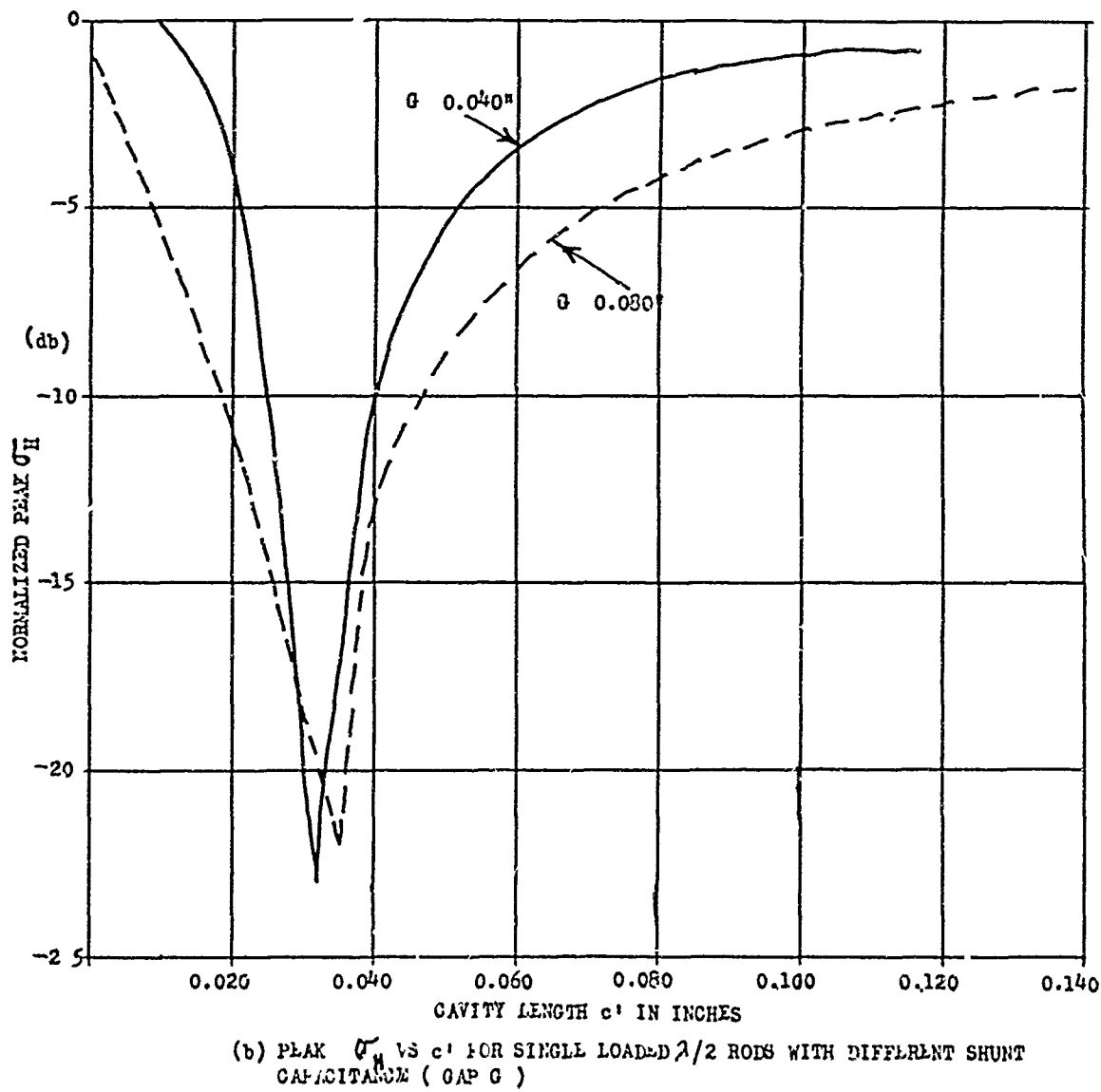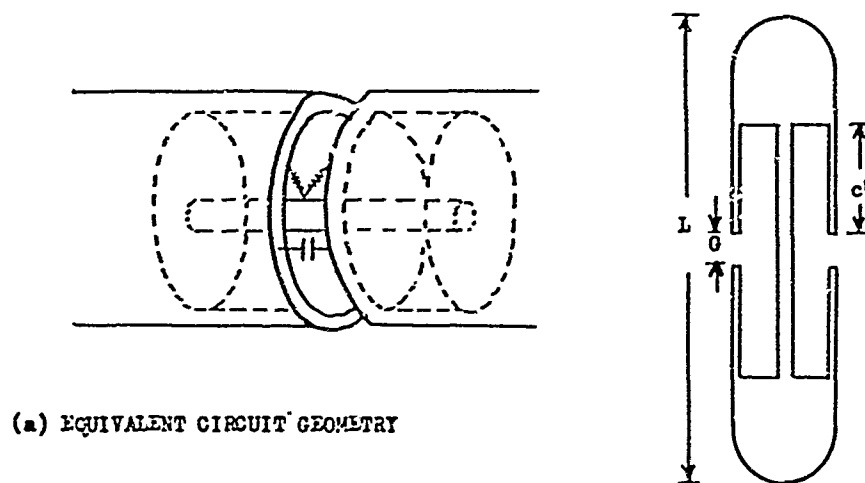
Figure 10. Single Loaded Rod Equivalent Circuit Geometry and Measured Effects of Changes in Shunt Capacitance (Gap G)
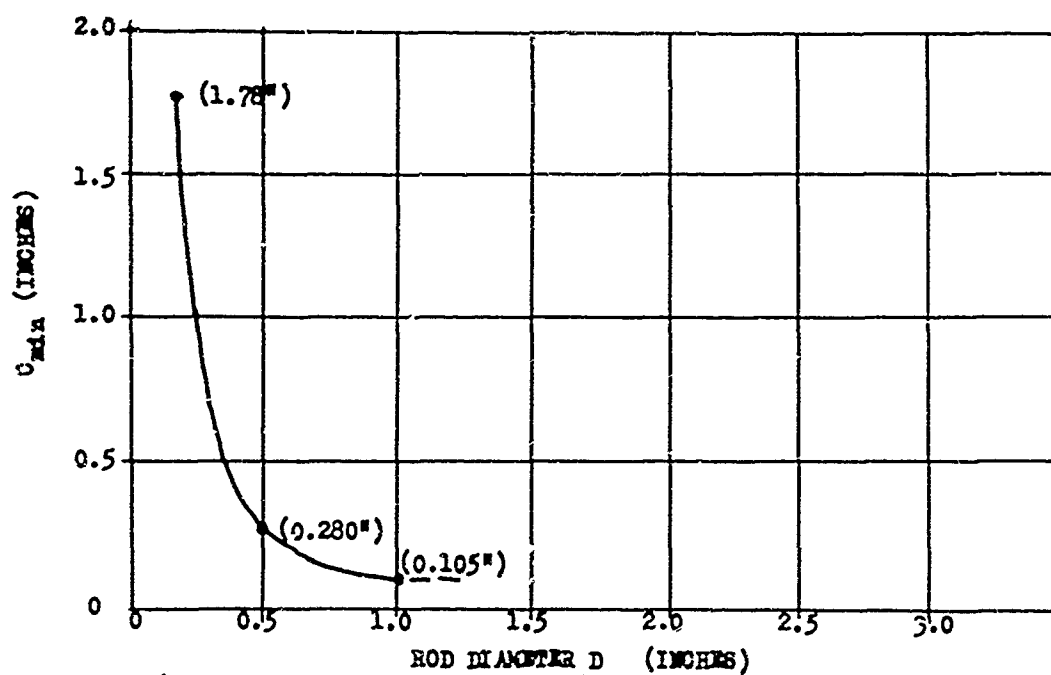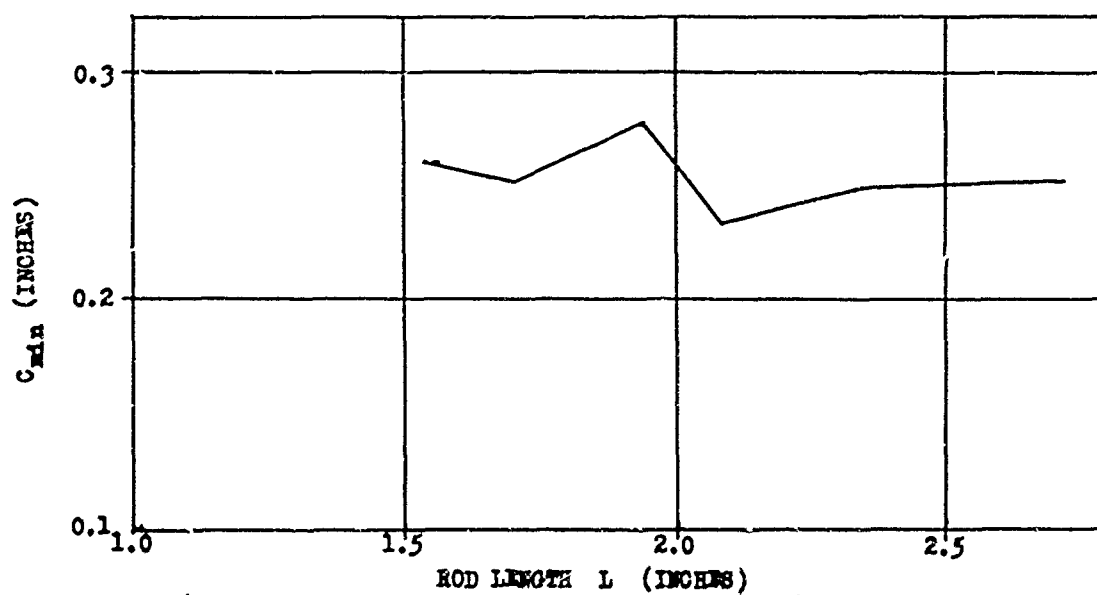
Figure 11. Total Cavity Length for Minimum Backscattering C_{min} vs Rod Diameter D and Rod Length L. Polarization Horizontal. Frequency = 3100.8 Mcps.

in Figure 12. Dimensions of the objects are given in Figures 6a and 13a. The solid curves of Figure 12 are σ vs. θ for the unloaded configurations, and the dashed curves are σ vs. θ for the loaded configurations tuned for minimum peak σ_H. Comparison of the solid curves of Figures 12a and 12b shows that peak σ_H, the maximum σ under horizontal polarization conditions, is the same for both target shapes. The dashed curves in Figures 12a and 12b show the large reduction in peak σ_H to be gained for both shapes by reactive loading.

For both shapes with polarization vertical, it is strikingly evident from comparison of the solid and dashed curves in Figures 12c and 12d that the reactive loading has practically no effect on σ; that is, there is very little difference between the solid and dashed curves.

The conclusion here is that for vertical polarization the loading cavities as presently designed do not couple with the induced currents on the surfaces of the targets. Comparison of Figures 12c and 12d indicates that peak σ_V is about 6 db less for the double conical shape than for the cylindrical rod shape. This result is to be expected since the average diameter of the double cone is considerably less than that of the rod.

Clearly, then, changing the shape from cylindrical to double conical did not reduce the overall peak σ, whereas reactive loading reduced the overall peak σ by at least 15 db. The condition for which shaping had an appreciable effect, that is, vertical polarization, is just the condition for which peak σ_V for the rod is already down 16 db from peak σ_H. Note the similarities of these conclusions to those obtained from using absorbing material.

6.2 Bandwidth Characteristics

Three different reactively loaded target configurations were examined over the frequency range 2500 to 3000 Mcps. In each case the target was tuned for minimum peak σ_H at a frequency near the center of the band. The configurations were a single loaded rod, a single loaded double conical shape, and a double loaded rod. The dimensions of the targets are shown in Figures 6b, 13a, and 13b. Curves of normalized peak σ_H vs. frequency are shown in Figure 14, and the approximate -15 db bandwidth is indicated for each target.

Apparently double loading produces considerably wider bandwidth than single loading, while double conical shaping with a single loading results in even wider bandwidth. It is interesting to note here that although shaping does not decrease the overall peak σ at a single frequency, it does apparently increase the bandwidth.

6.3 Bistatic Characteristics

Bistatic reflection measurements for horizontal polarization were made on a single loaded rod (see Figure 13c) and on a double loaded rod (see Figure 13b).
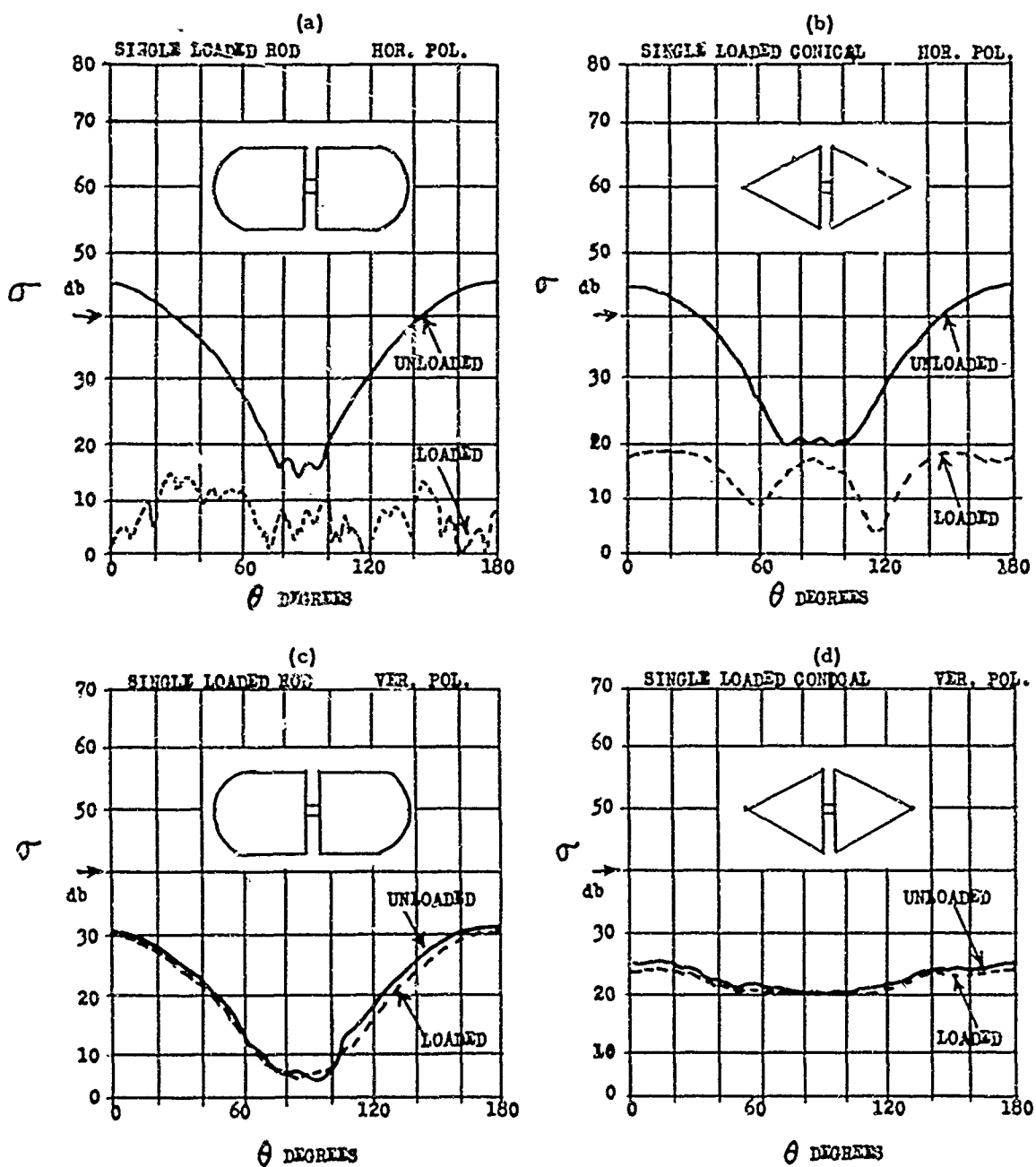
Figure 12. Backscattering Cross Section σ vs Target Angle θ for Single Loaded Rod (Figure 6a) and Single Loaded Double Conical Shape (Figure 13a).

(a)

L – 2.18"
G – 0.040"
D – 0.500"
R – 0.0625"
C – 0.350"
T – 0.261"

SINGLE LOADED DOUBLE CONICAL SHAPE

(b)

L – 2.15"
G – 0.040"
D – 1.00"
R – 0.125"
C – 0.135"
T – 0.875"

DOUBLE LOADED ROD

(c)

L – 2.17"
G – 0.090"
D – 1.00"
R – 0.125"
C – 0.105"
T – 0.875"
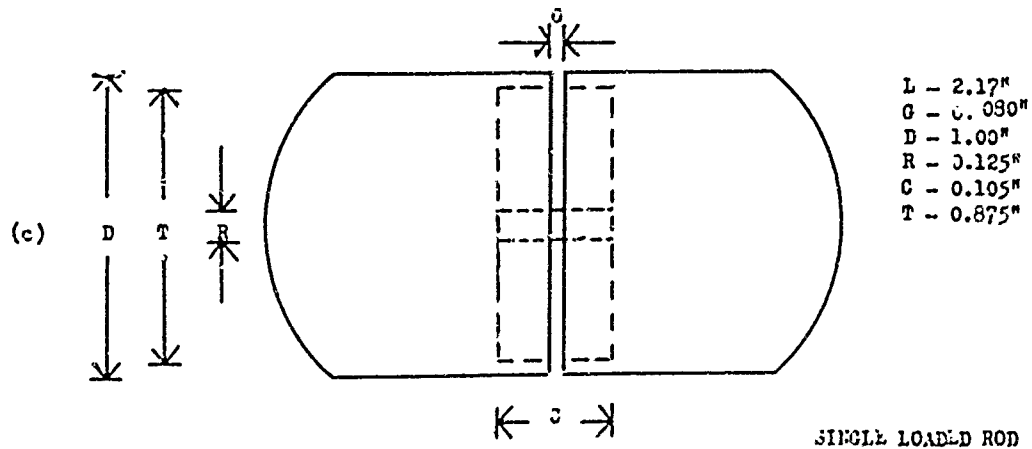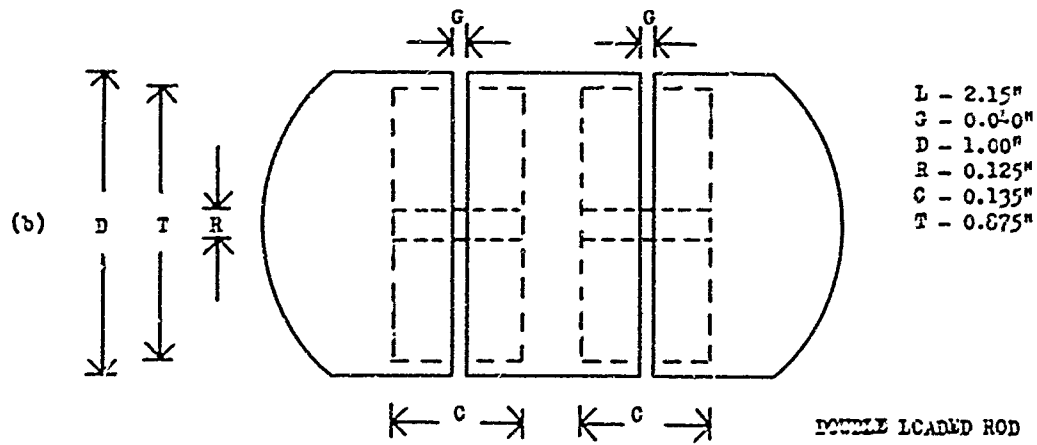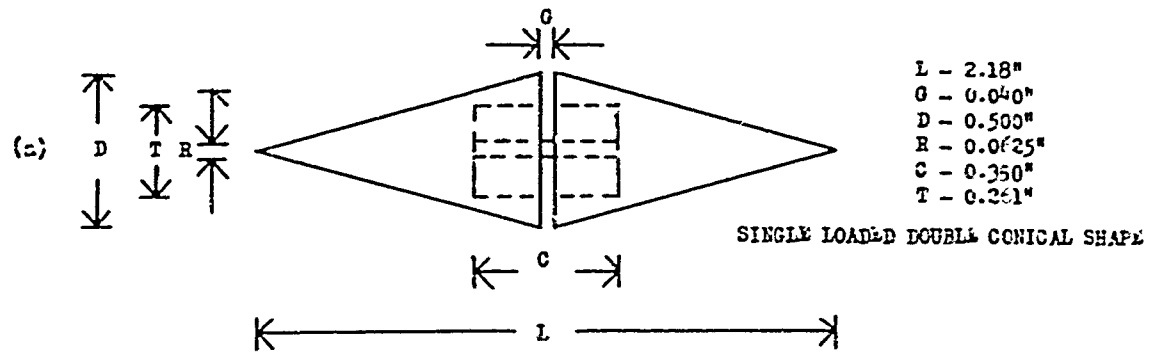
SINGLE LOADED ROD

Figure 13.   Dimensions of Target Models
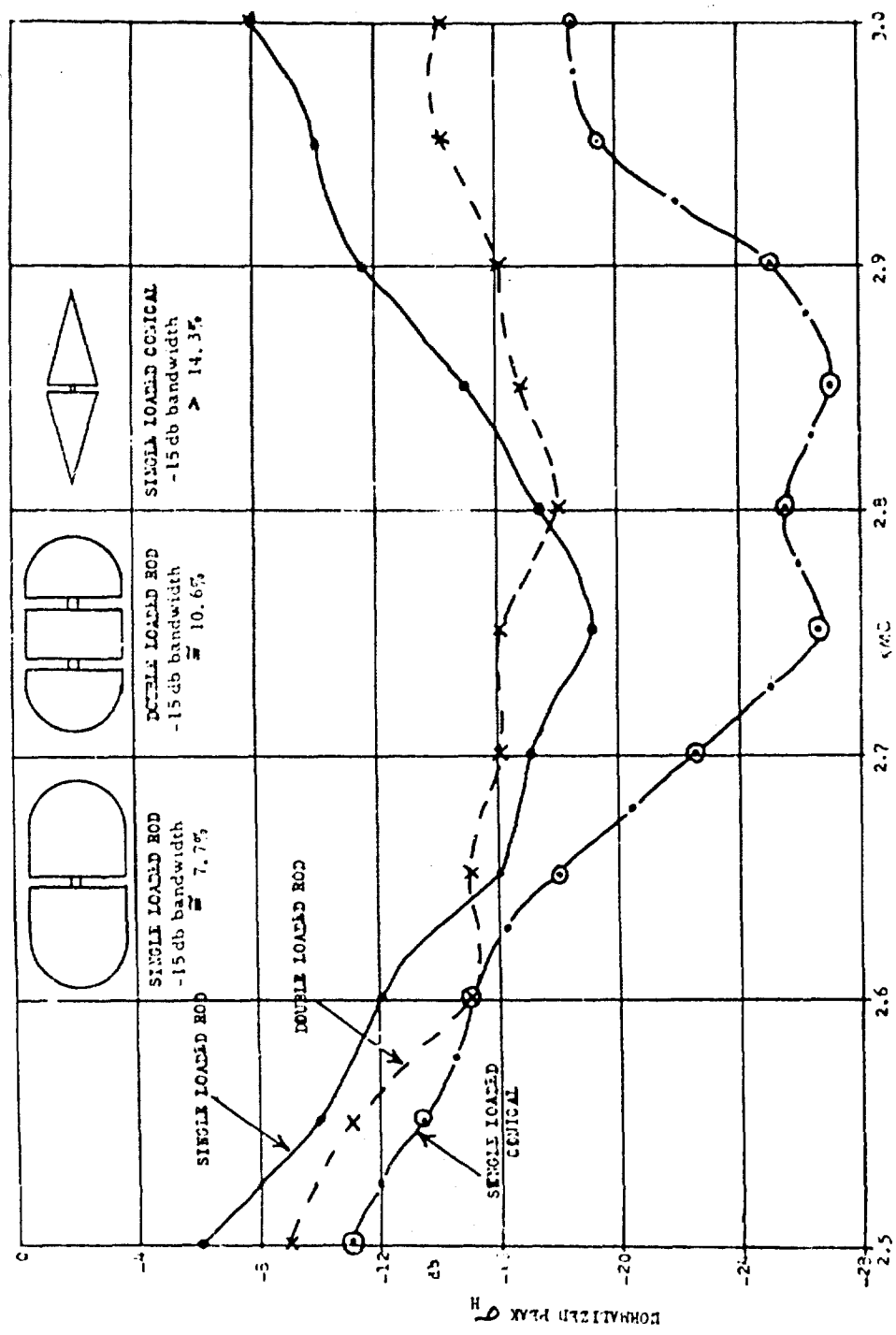
Figure 14. Peak σ_H vs Frequency for a Single Loaded Rod (Figure 6b), Doubled Loaded Rod (Figure 13b) Single Loaded Conical Shape (Figure 13a)

For each bistatic angle α , each target was rotated 360° and the peak bistatic cross section determined. These measured peak bistatic cross sections were then normalized to the overall peak backscattering cross section of the unloaded configuration. Curves of normalized peak bistatic cross section vs. bistatic angle α for both targets are shown in Figure 15. For each target the peak bistatic cross section increases with bistatic angle; in the neighborhood of α = 90° it approaches the reference value, that is, the overall peak σ for an unloaded or solid rod. For bistatic angles in the range α = 0° to α = 30°, the single loaded rod has lower peak return than the double loaded rod though both are down at least 18 db from the reference value. The peak return from the double loaded rod is 15 db or more down from the reference value over the bistatic angular range α = 0° to α = 0.48°.

7. CONCLUSIONS

For elongated objects of length approximately $\lambda/2$, coating them with absorbing material or shaping them into the double conical form does not significantly reduce overall peak σ. The condition under which these two techniques have their greatest effect in reducing σ, that is, vertical polarization, is just the condition under which the σ for an elongated object is already well below its overall peak value. Fortunately, the condition under which overall peak σ occurs and under which the two above techniques are least effective in backscatter reduction, that is, horizontal polarization, is just the condition under which reactive loading has its greatest effect. Therefore, the three techniques tend to complement each other, and it is reasonable to expect that a combination of all three techniques should produce a good wideband minimum backscattering object.

8. CURRENT AND FUTURE WORK

The following investigations are either currently in progress or will be undertaken in the near future:

a. Use of slightly lossy rather than purely reactive loading to improve bandwidth characteristics.

b. Redesign of the slot configuration so that it will couple into the surface currents under vertical polarization conditions.

c. Determination of the existence of higher harmonic resonances of the loading cavity that may undesirably enhance the scattering.

d. Design of loading configurations to successfully reduce the scattering from spheres and jacks in the resonance region.
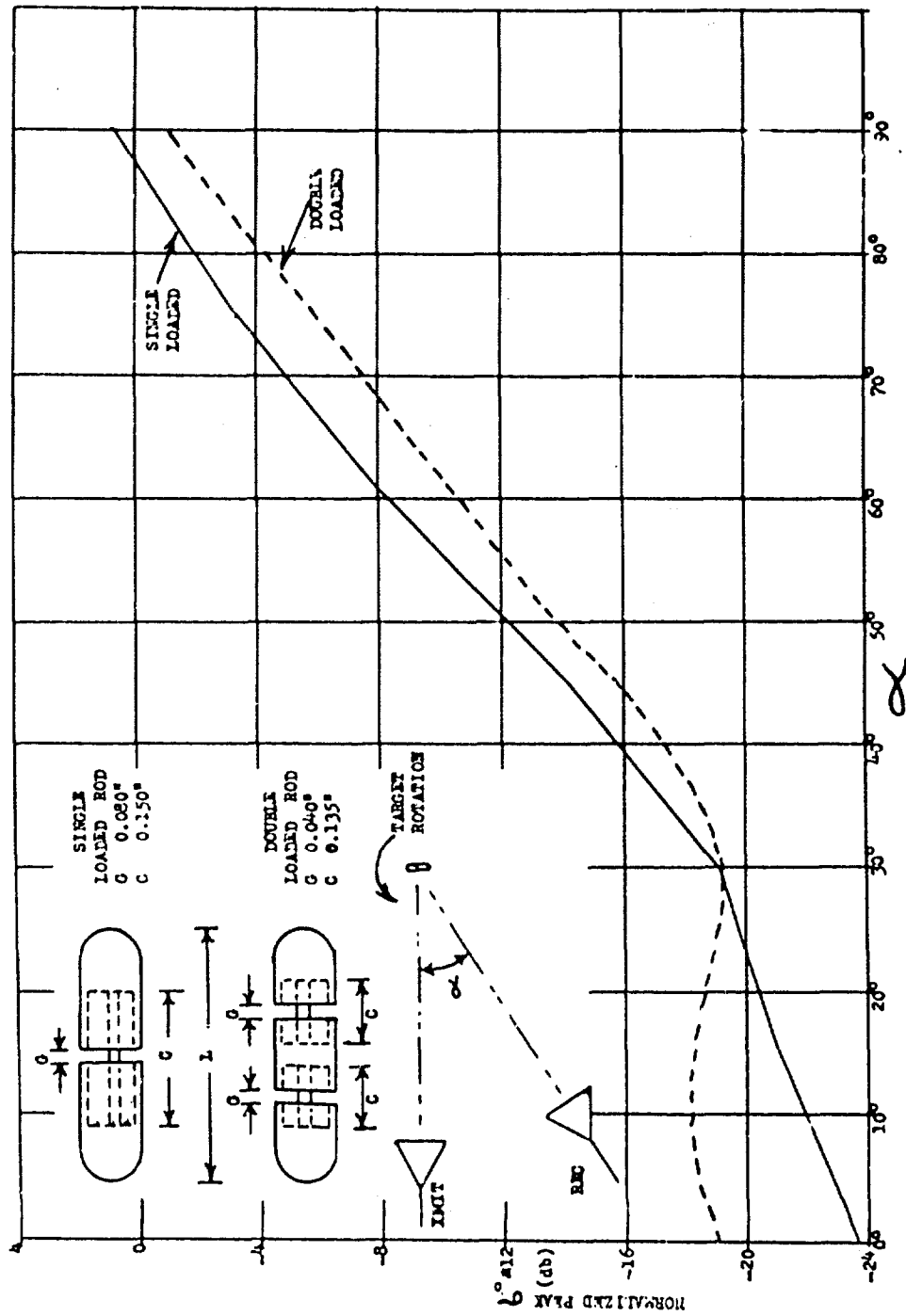
Figure 15. Normalized Peak Bistatic Scattering Cross Section σ_b vs Bistatic Angle α for a Single Loaded Rod (Figure 13c) and a Double Loaded Rod (Figure 13b)

86

Acknowledgment

References

1. H.A. Iams, Radio Wave Conducting Device, U.S. Patent No. 2,528,367, October 31, 1950, Filed March 9, 1946.

2. E.B. Chisholm, Antenna for Voir, Report No. E5062, Air Force Cambridge Research Center, Cambridge, Mass., December 1950.

3. W. Gerbes, H. Poehler, and W. Kearns, Back-Scattering from a Monopole Projecting from a Recessed Coaxial Cavity in a Plane Conducting Screen, Air Force Cambridge Research Center, Bedford, Mass. See also W.W. Gerbes and W.J. Kearns, Theoretical and Experimental Investigation of Backscattering From a Cavity-loaded Monopole, AFCRL-63-355, August 1963.

4. B.-O. Ås and H.J. Schmitt, Back-Scattering Cross-Section of Reactively Loaded Cylindrical Antennas, Cruft Laboratory, Harvard University, Cambridge, Mass., August 15, 1958.

This Document Contains
Missing Page/s That Are
Unavailable In The
Original Document

OR are
Blank pgs.
that have
Been Removed

**BEST
AVAILABLE COPY**

VI. Analysis of Loaded Terminal Scatterers*

Edward M. Kennaugh
Antenna Laboratory
Department of Electrical Engineering
The Ohio State University
Columbus, Ohio

I. INTRODUCTION

The echoing properties of antennas, or scatterers with one or more terminal pairs, have been the subject of continuing studies at our Laboratory. In addition to the new scattering parameters introduced by arbitrary terminal loadings, we are interested in the subtle difference between scattering by "good" antennas and by arbitrary objects. Since a "good" antenna acts as an efficient device for transfer of energy from a wave field to a terminal pair when receiving, and in the reverse direction when transmitting, it appears that its scattering properties should possess certain unique features. Among these, of course, is the strong dependence of these properties upon the coupling between the incident wave and the antenna upon termination.

Several of the applications of this study can be described. First, the determination of the parameters that relate scattering by an antenna to its load, and the selection of loads that will maximize or minimize the echo area. Next, the

design of more efficient modulated scatterers for use in field probing, passive communication links, or in radar target simulation. In many cases, the control of the echo from a specified object is desired, although neither an antenna nor terminal pairs have been specified. Use of antenna concepts can still be made, however, to find the characteristic modes that can most significantly contribute to echo area and determine what loadings are required. Finally, a unified theoretical treatment of scattering and radiating properties may best be achieved, at least for objects of resonant size, by considering these objects to be multi-mode antennas.

2. EFFECT OF TERMINATION UPON ANTENNA ECHO AREA

Initially, a fixed-source frequency and aspect were assumed, and the scattering properties of antennas or bodies with antennas mounted upon them were investigated as functions of the terminating impedance. It is easily shown that the echo signal is a function of three complex parameters and the load impedance:

$$E^S = \frac{E^S_{oc} Z_L + E^S_{sc} Z_A}{Z_L + Z_A} \tag{1}$$

where E^S is the phasor echo signal received when the antenna is terminated with Z_L, E^S_{oc} is that received when terminated with an open circuit, E^O_{sc} is that received with a short circuit termination, and Z_A is the antenna impedance at the load terminals. A more useful form of this equation is readily derived by use of the phasor E^S_M, the phasor echo signal received when the antenna is terminated with Z^*_A, the complex conjugate of the antenna impedance:

$$E^S = E^S_M - \tilde{\Gamma} (E^S_M - E^S_{oc}). \tag{2}$$

is the modified voltage reflection coefficient corresponding to the load Z_L:

$$\tilde{\Gamma} = \frac{Z_L - Z^*_A}{Z_L + Z_A} . \tag{3}$$

Note that the definition of $\tilde{\Gamma}$ differs from that normally used, whenever Z_A is not a real quantity, and is such that $\tilde{\Gamma}$ will always lie on the unit circle for reactive loads Z_L and inside the unit circle for passive lossy loads.

A graphical interpretation of Eq. (2) is that the phasor signal received as a function of load impedance Z_L is proportional to the difference between a fixed

phasor and the phasor $\tilde{\Gamma}$. Thus, if one plots the modified reflection coefficient on a pseudo-Smith chart, the vector from $\tilde{\Gamma}$ to the tip of the fixed phasor has a length proportional to the echo signal received as $\tilde{\Gamma}$ (or Z_L) is varied. Such a geometrical interpretation is shown in Figure 1 for several values of the fixed phasor component.
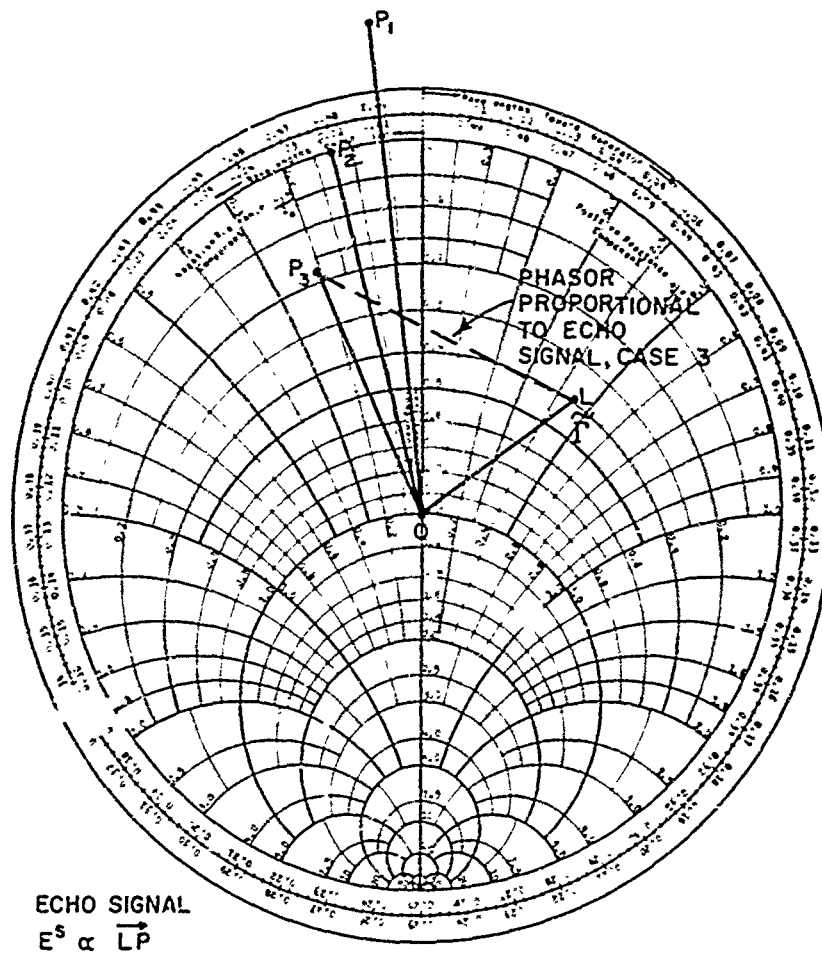
ECHO SIGNAL
$E^S \propto \overrightarrow{LP}$

Figure 1. Dependence of Phasor Echo Signal on Load Reflection Coefficient

We might assume that three different aspects of a single antenna correspond to the phasor values $\overline{OP}_1$, $\overline{OP}_2$, $\overline{OP}_3$. For aspect 1, the fixed component exceeds the load-dependent component and it is not possible to eliminate the echo signal by use of a passive load, but it can be varied between amplitudes proportional to $OP_1 + 1$ and $OP_1 - 1$ by use of reactive loads. For aspect 2, the fixed component equals the load-dependent component and the echo signal can be eliminated or maximized by use of reactive loading. For aspect 3, the fixed component is less than the load-dependent component and the echo signal can be eliminated by using

a lossy load corresponding to the point P_3, or maximized by a reactive load.

One must bear in mind that the geometrical diagram omits a factor of proportionality, so that only relative echo signal amplitude and phase can be determined; the factor omitted is proportional to the geometric mean of the antenna power gains in the directions of source and receiver as well as the usual radar range parameters.

Since the variation of echo signal with load is uniquely related to antenna and scatterer parameters, we have considered the use of variable reactive loads to determine these parameters solely through scattering measurements. Combining graphical and analytical techniques, it is possible to quickly reduce echo signal amplitude data for several calibrated reactive loads to determine antenna impedance, gain, and scattering parameters at a single aspect and frequency. These techniques and their application are fully described by Garbacz.[1, 2, 3]

3. AVERAGE ECHO AREA AND TOTAL SCATTERING CROSS SECTION

The graphical interpretations of Figure 1 are limited to individual aspects of the scattering antenna, but it is frequently necessary to consider how average echo area over a range of aspects or polarizations varies with antenna termination. Green[4] has shown how a slight modification to Figure 1 can be made to permit its use in such a case. We merely add a positive constant to the square of the distance previously derived for echo signal amplitude in Figure 1 to obtain a quantity proportional to the average echo area and to determine its dependence upon $\tilde{\Gamma}$. As shown in Figure 2, the average echo area of an antenna is proportional to a constant C plus the square of the distance PL, where L is the point corresponding to the modified reflection coefficient of the load defined by Eq. (3).

Depending upon the position of the fixed point P, one would achieve minimum average echo area with a reactive (P outside or on unit circle) or lossy load (P inside unit circle). In every case, maximum average echo area can be obtained with a reactive load. The echo power can be averaged in this manner over orientations of source and of receiver, including variations in polarization, but it is assumed that the source frequency remains constant. From averaged cross section values obtained with as few as four loads, it is possible to construct a diagram such as Figure 2 that will yield the average cross section for any load impedance.

Of special interest is the case where the source remains fixed and the receiving antenna varies over all bistatic angles to obtain the average scattering cross section of an antenna. One may then consider how the total energy scattered by an antenna compares with that absorbed as a function of termination. In the early literature on antenna scattering, it was often erroneously assumed that an antenna

must back-scatter at least as much energy as it absorbs. Although no such restriction exists, a more fundamental relation possibly applies between total scattering and absorption cross sections of an antenna. If we postulate that an antenna may not absorb more than it scatters, this would imply that the value of C and the location of P in Figure 2 would be restricted in the case of averaged bistatic scattering.

AVERAGE ECHO AREA $\propto C + (PL)^2$
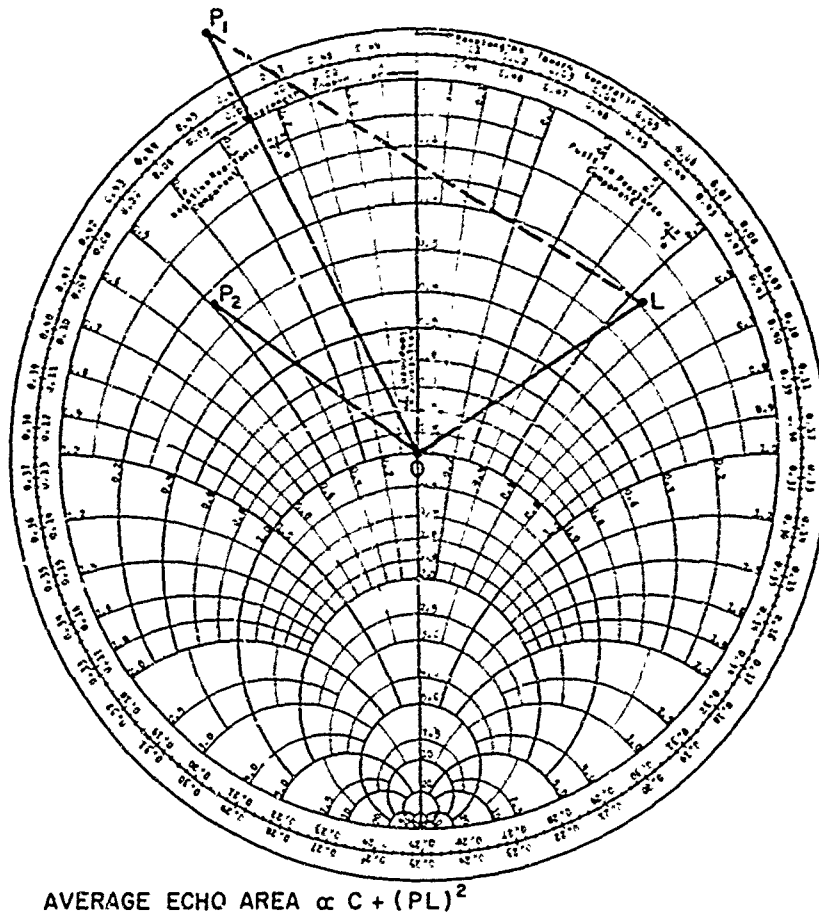
Figure 2. Dependence of Average Echo Power on Load Reflection Coefficient

Green[4] used the concept of Figure 2 to present calculated average scattering cross section for a cylindrical antenna as a function of load, and included contours of constant average scattering and constant absorption cross section on the chart, as shown in Figure 3.

It is possible to find a load impedance that will maximize the ratio of absorption to scattering cross section; the maximum ratio obtained in this case is 4·1, obtained at point B where the power absorbed is approximately 50 percent of that

for a matched termination. Note that the scattering and absorption cross sections are approximately equal when the absorption coefficient is a maximum.

$\bar{\sigma}$ = SCATTERING CROSS-SECTION
σ_A = ABSORPTION CROSS-SECTION
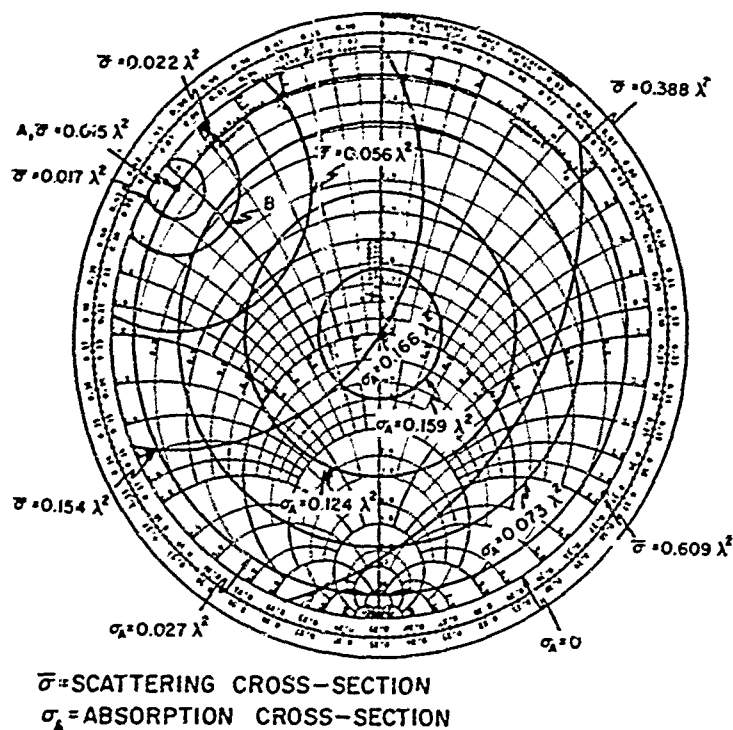
Figure 3. Contours of Constant Total Scattering and Absorption Cross Sections as Function of Load Reflection Coefficient, Cylindrical Antenna

The relation between scattering and absorption cross sections of any object is implied by its albedo, which is the ratio of scattering cross section to extinction (total) cross section. Since the extinction cross section is the sum of scattering and absorption cross sections, an object with an albedo less than 1/2 absorbs more than it scatters.

Results obtained by Deirmendjian[5] for the scattering by lossy dielectric spheres show that the albedo is below 1/2 for lossy dielectric spheres less than 2 wavelengths in diameter, for a complex index of refraction 1.315 - i.4298. For the same index, the ratio of absorption to scattering cross sections is approximately 5 for a sphere circumference of 1 wavelength, where the absorption cross section is slightly less than the geometrical cross section.

To what extent can a lossy dielectric sphere be considered an antenna with a lossy termination? From a practical point of view there does not appear to be any way to extract useful power from such a structure, but a more fundamental difference is the distributed loss rather than the lumped loss corresponding to a definite terminal pair.

4. APPLICATION OF ANTENNA CONCEPTS TO ARBITRARY LOADINGS

It would be useful to fit more general types of leading or scatterer perturbation to the model of Figures 1 and 2. For example, the effect of a slot or gap of variable depth in a conducting object might be considered as a variable reactive load on a hypothetical terminal pair. From Figure 1, if this model may be used, we would expect the phasor echo signal to trace out a circular locus as the depth is varied. Through experimental or theoretical studies of the effect of gap depth, we should then be able to determine the applicability of Figure 1 to more general types of loss-less perturbations. Similarly, it may be shown that a purely resistive load variation should lead to a circular locus for the phasor scattered signal, and it might be possible to assess the effect of changes in conductivity of a part of the scatterer by the single terminal pair concept with an effective lumped load of variable resistance.

In short, when the single-mode concept applies, we should expect a circular locus for the phasor echo signal under loss-less perturbations of the scatterer. When this is not obtained, it may be possible to treat the scatterer as a multi-terminal antenna with variable loading at more than one terminal pair. The analysis of such configurations is currently under study.

5. ANALYSIS OF ARBITRARY SCATTER AS MULTI-MODE ANTENNA

When one considers an arbitrary scatterer as a multi-mode antenna, it follows that the echo area as a function of source and receiver directions can be expressed as

$$\sigma(\Theta_s, \phi_s; \Theta_r, \phi_r) = \sum_i C_i F_i(\Theta_s, \phi_s) F_i(\Theta_r, \phi_r) \tag{4}$$

where Θ_s, ϕ_s are the spherical coordinates of the source and Θ_r, ϕ_r those of the receiver (both assumed infinitely remote), and

$F_i(\Theta, \phi)$ = radiation patterns of the individual modes and

C_i = constants determined by "terminal" conditions.

It is assumed that the mode fields are mutually orthogonal and that there are a finite number with $|C_i|$ greater than some arbitrary minimum value. The number required would necessarily increase with the size of the scatterer, but in the resonance region the number would be less than 10 in many cases.

These orthogonal or "normal" modes as we have called them are simply related to the eigenvectors of the target scattering matrix, and the C_i are determined from the corresponding eigenvalues. The associated patterns are useful for analysis of the transmitting, receiving, or scattering properties of the object. We would expect the effect of perturbations to the object shape, such as those produced by slots, cavities, or changes in surface impedance, to be represented by changes in the constants C_i, as reflecting the change in "terminal" conditions. Further, the relative importance of the various modes is indicated by the magnitude of the associated C_i, so that one may determine what radiating or scattering patterns will be most readily excited on the object.

Our present goals are to extract, by a combination of theoretical and experimental methods, the "normal" mode patterns of a scattering object (at a single frequency) and to determine the associated constants C_i as influenced by various perturbations of the scatterer surface and by lumped loadings.

6. EXPERIMENTAL INVESTIGATIONS

Experimental techniques have been developed for measuring antenna parameters with conventional echo-measuring systems, using modulated or variable reactive loads. To permit rapid measurement of echo-signal amplitude as a function of load, a self-contained programmed load unit was devised. This battery-driven device can be mounted within a model of a scattering object containing an antenna and will automatically vary the position of a sliding coaxial or waveguide short through a full cycle, giving characteristic pips on the echo pattern corresponding to each 1/72 in. of travel. Typical 10 kMc echo patterns obtained from a stub antenna on a 7.0 - in. - diameter sphere and from a 1 1/2 in. x 2 7/8 in. compound rectangular horn are shown in Figure 4.

A second means of varying antenna termination under consideration employs an electrically switched load. As a part of this study, the echo area variation with bias of a germanium switching diode was investigated. Figure 5 presents the variation in broadside echo area obtained with bias over a range of X-band frequencies. It is clear that large changes in cross section of an object in the resonance region can be obtained through electrical tuning.

The effect of a rectangular slot upon the echo area of a small flat plate was also studied. An analysis by Green using the superposition of plate scattering and slot radiation patterns to predict the effect of the slot was verified. By use of a small shorting bar at the center of the slot, the echo area of the slot-plate combination can be varied by approximately 15 db. Some of the experimental results are shown in Figure 6.
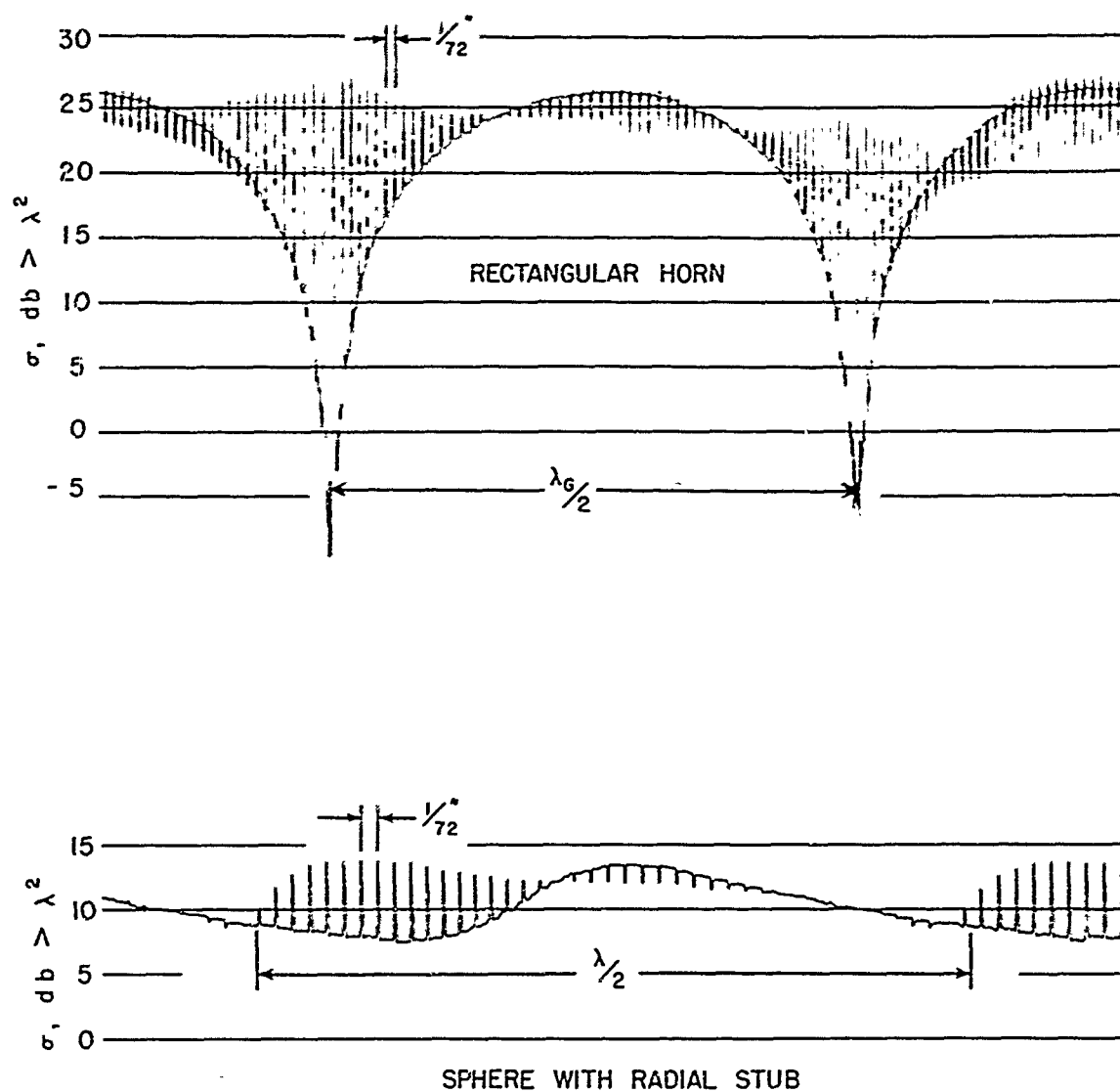
Figure 4. Measured Antenna Echo With Programmed Load Variations

7. CONCLUSION

Various concepts of interest in the analysis of scattering by objects that possess one or more terminal pairs (real or virtual) have been described. We have briefly summarized the contribution of our co-workers, R. Green, R. Garbacz, D. Moffatt. and S. Skarote. Additional information can be obtained from the References and Bibliography listed below.
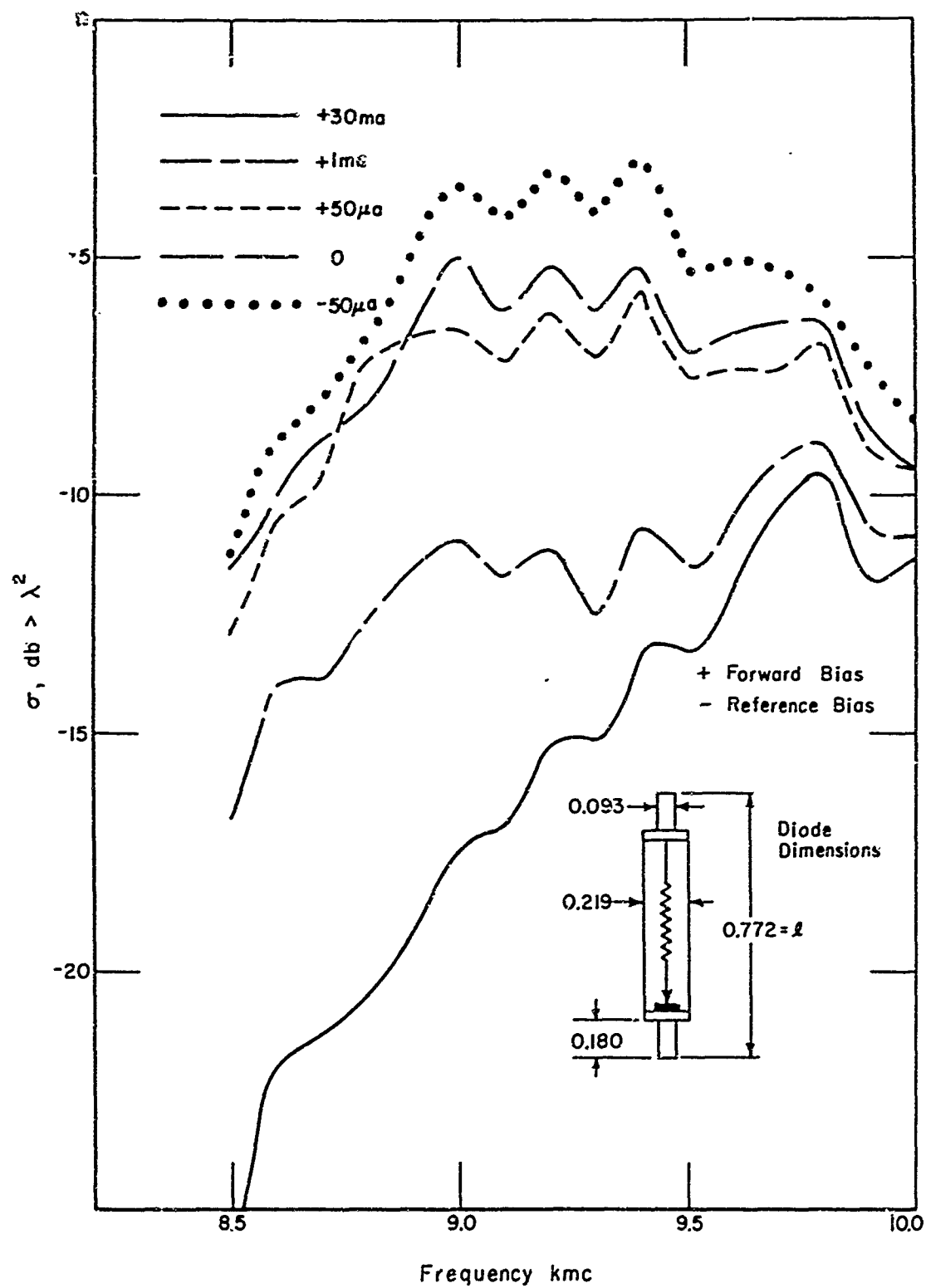
Figure 5. Effect of Bias and Frequency Upon Echo Area of Germanium Diode
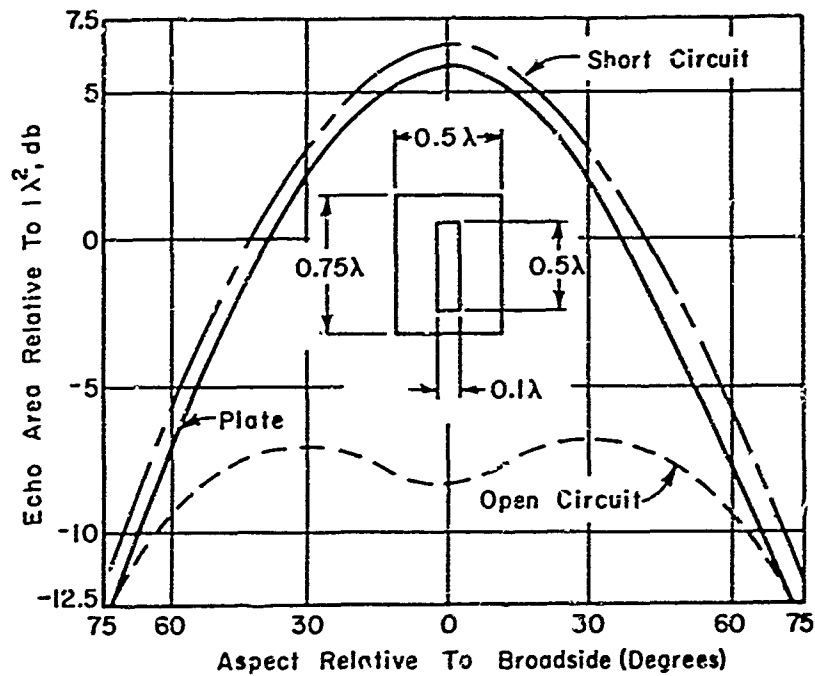
Figure 6. Echo Patterns of Rectangular Plate With Slot

References

1. D. Diermendjiar., JOSA, Vol. 51, June 1961.

2. R. J. Garbacz, The Determination of Antenna Parameters by Scattering
    Cross Section Measurements: I, Antenna Impedance, Report 1223-8,
    30 September 1962. AD 286 760

3. R. J. Garbacz, The Determination of Antenna Parameters by Scattering
    Cross Section Measurements: II, Antenna Gain, Report 1223-9,
    30 November 1962. AD 297 953

4. R. J. Garbacz, The Determination of Antenna Parameters by Scattering
    Cross Section Measurements: III, Antenna Scattering Cross Section,
    Report 1223-10, 30 November 1962.

5. R. B. Green, The Effect of Antenna Installations Upon the Echo Area of
    an Object, Report 1109-3, 29 September 1961. AD 274 041

6. R. B. Green, The Echo Area of Small Rectangular Plates with Linear
    Slots, to be published in IEEE Transactions on Antennas and Propagation.

Bibliography

1. Copeland, J. R., Robertson, W. J., Green, R. B., and Mikuteit, S., Antennafiers for Echo Area Control, Report 903-30, 15 December 1962. AD 292 979

2. Kennaugh, E. M., The Echoing Area of Antennas, Report 601-14, 20 December 1957. AD 152 786

3. Moffatt, D. L., Model Measurements of Antenna Scattering Cross Section, Report 1223-12, to be published.

4. Peters, L., Jr., End-Fire Echo Area of Long, Thin Bodies, IRE Transactions on Antennas and Propagation, Vol. AP-6, No. 1, January 1958.

5. Richmond, J. H., A Modulated Scattering Technique for Measurement of Field Distribution, IRE Transactions on Microwave Theory and Techniques, Vol. MTT-3, No. 4, July 1955.

VII. Some Bounds to the Behavior of Small Resonant Scatterers

Roger F. Harrington
Electrical Engineering Department
Syracuse University
Syracuse 10, New York

A loaded scatterer is an object to which one or more lumped-parameter impedance elements are connected. It has been shown that a small scatterer can be resonated to greatly enhance its scattering cross section.[1] In the vicinity of resonance, the echo area of a small singly loaded scatterer is given by[2]

$$\sigma \approx \frac{\lambda^2}{\pi} \left| \frac{G R_{in}}{Z_{in} + Z_L} \right|^2 \tag{1}$$

where λ is the wavelength, G is the directive gain of the scatterer when used as a transmitting antenna, $Z_{in} = R_{in} + jX_{in}$ is the input impedance to the scatterer when used as an antenna, and Z_L is the loading impedance.

According to Eq. (1), the echo area of a small resonant scatterer is completely determined by its properties when used as an antenna. Hence, known limitations to the behavior of antennas[3] can be used to obtain corresponding limitations to the behavior of scatterers. If the general formula for echo area[1] is used instead of Eq. (1), bounds to the behavior of scatterers of arbitrary sizes and loads can be obtained.

The following are results abstracted from the more general antenna theory.[3] Let $\underline{a}$ denote the radius of the smallest sphere that can contain an antenna. Then for small (ka < 1) loss-free antennas, the minimum quality factor obtainable is

$$Q_{min} = \frac{1}{2} [(ka)^{-1} + (ka)^{-3}] \tag{2}$$

where $k = 2\pi/\lambda$ is the wavenumber. This minimum Q is obtained when the electric-dipole mode and the magnetic-dipole mode are equally excited. If a high Q antenna is resonated by an input reactance, the bandwidth of the antenna is related to the Q by

$$\beta = \frac{\Delta\omega}{\omega_r} = \frac{1}{Q} \tag{3}$$

where ω_r is the resonant frequency and $\Delta\omega$ is the frequency difference between points for which $|Z|$ has fallen to $1/\sqrt{2}$, its value at resonance. Under the condition of minimum Q, the maximum antenna gain is

$$G_{max} = 3 \tag{4}$$

for small loss-free antennas. If only the electric-dipole mode or only the magnetic-dipole mode is excited, instead of both, then the minimum Q is twice that of Eq. (1) and the gain is one-half that of Eq. (4).

Applying the above results to small resonant scatterers, from Eqs. (1) and (4) one finds that the maximum echo area obtainable from a small (ka < 1), loss-free, resonant ($Z_L = -jX_{in}$) scatterer is

$$\sigma_{max} = \frac{9}{\pi} \lambda^2 \approx 2.86\lambda^2 . \tag{5}$$

In the case of an actual scatterer, losses can reduce σ, as discussed later. Equation (5) can be compared to an electric-dipole scatterer, or a magnetic-dipole scatterer, for which the resonant echo area is[1]

$$\sigma_{dipole} = \frac{9}{4\pi} \lambda^2 = \frac{1}{4} \sigma_{max} . \tag{6}$$

Hence, small, loss-free, dipole scatterers can give one-quarter the maximum possible echo area.

It has been noted[2] that because a small resonant scatterer behaves as a series or parallel resonant circuit it is characterized by a gain-bandwidth product

$$\sqrt{\sigma}\,\beta = \text{constant.} \tag{7}$$

Using Eqs. (2), (3), and (5) in Eq. (7), one finds the maximum gain-bandwidth product for small, loss-free, resonant scatterers

$$(\sqrt{\sigma}\,\beta)_{max} = (\frac{3\lambda}{\sqrt{\pi}}) \frac{2}{(ka)^{-1} + (ka)^{-3}} \approx 3.38\,\lambda\,(ka)^3 \tag{8}$$

where $\underline{a}$ is the radius of the smallest sphere that can contain the scatterer. For resonant dipole scatterers (electric or magnetic), both $\sqrt{\sigma}$ and β are at most one-half the maximum. Hence,

$$(\sqrt{\sigma}\,\beta)_{dipole} \leq \frac{1}{4}\,(\sqrt{\sigma}\beta)_{max} \tag{9}$$

showing that gain-bandwidth products for dipoles cannot be greater than one-quarter of the optimum.

When practical scatterers are made small compared to wavelength the radiation resistance becomes small, and the conductor losses become significant. A careful consideration of the general formula[1] for echo area shows that, if the current distribution on the scatterer is not changed much, instead of Eq. (1)

$$\sigma \approx \frac{\lambda^2}{\pi} \left| \frac{G\,R_{rad}}{Z_{in} + Z_L} \right|^2 \tag{10}$$

where R_{rad} is the radiation resistance. The maximum echo area of a lossy scatterer is obtained when $Z_L = -jX_{in}$, in which case Eq. (10) gives

$$\sigma_{max} \approx \frac{1}{\pi}\,\lambda^2\,G^2 \left| \frac{R_{rad}}{R_{rad} + R_{loss}} \right|^2 = \sigma_0 \left| \frac{R_{rad}}{R_{rad} + R_{loss}} \right|^2 \tag{11}$$

104

where R_{loss} is the loss resistance in both the scatterer and the load, and σ_o is the loss-free echo area. Similarly, the Q of the scatterer, which is determined by the resonance curve of $Z_{in} + Z_L$, becomes

$$Q = Q_o \left(\frac{R_{rad}}{R_{rad} + R_{loss}} \right) \tag{12}$$

where Q_o is the Q of the loss-free scatterer. Forming the gain-bandwidth product of Eq. (7) and then using Eq. (3), one finds

$$\sqrt{\sigma}\, \beta = \sqrt{\sigma_o}\, \beta_o \ . \tag{13}$$

Hence, the gain-bandwidth product is unchanged by losses, assuming that the current distribution on the scatterer is unchanged. The primary effect of losses therefore is to reduce the echo area according to Eq. (11) and to reduce the Q according to Eq. (12), without changing the gain-bandwidth product.

References

1. R. F. Harrington, Small resonant scatterers and their use for field measurements, IRE Trans. on Microwave Theory and Techniques, Vol. MTT-10, pp. 165-174, May 1962.

2. R. F. Harrington, Field measurements using active scatterers, communication to the IEEE Trans. on Microwave Theory and Techniques, Vol. MTT-11, September 1963.

3. R. F. Harrington, Effect of antenna size on gain, bandwidth, and efficiency, Journal of Research N. B. S., Vol. 64D, pp. 1-12, Jan. - Feb. 1960.

VIII. A Determination of the Scattering From a Cavity-Backed Plane Surface

J. K. Schindler, 1/Lt, USAF *
Microwave Physics Laboratory
Air Force Cambridge Research Laboratories
Bedford, Massachusetts

F. V. Schultz
School of Electrical Enginee.ing
Purdue University
Lafayette, Indiana

1. INTRODUCTION

One possible technique for evaluating the scattered return from surface-loaded, conducting, scattering bodies consists of separating the scattered field into two terms. One term consists of the scattered field from the body with all loading structures short-circuited at the surface of the body, that is, the unloaded body. The additional term represents what is essentially the radiation effects of the aperture that couples the loading structure and the exterior domain. Of course the incident field plus the unloaded return gives a zero tangential electric field over the whole surface of the assumed perfectly conducting scattering body. The additional scattered field term is then necessary to account for the non-zero tangential electric fields induced by the excitation in the coupling aperture.

With this technique the problem of analyzing the scattering from a surface-loaded body is broken into two problems, the usual unloaded scattering problem for the body under consideration plus the problem of determining the radiation from structures equivalent to aperture antennas located on the surface of the scattering body. The aperture antennas are of course excited in a very special way by the external radiation.

A key problem then is the determination of how the aperture fields are excited by the incident radiation and, further, how the magnitude and phase of the aperture fields depend upon the cavity parameters. A knowledge of this latter dependence allows one to determine how the cavity may be made to control the reradiated energy in such a fashion as to appropriately modify the radar return from the body.

In this work we briefly consider the analysis of the scattering from a highly idealized cavity-loaded structure. The structure consists of an infinite plane backed by an infinitely long rectangular cavity and coupled through the plane by a narrow, infinitely long aperture parallel to the cavity axis. We do not approach this problem in an effort to minimize the return from an infinite screen; rather, it is believed that the results obtained for this idealized structure will be of assistance in the analysis of more practical three-dimensional bodies.

For example, the aperture fields obtained may approximate those excited in a cavity-loaded finite body, if the principal radii of curvature of the scattering surface are large at the point of loading and if resonant aperture and cavity lengths are avoided. At worst, one would expect the same qualitative behavior of the aperture fields in the finite body as is exhibited by the aperture fields in the present problem. In addition, the results of the present work will provide a comparison for the results of simpler though more approximate schemes for the calculation of the aperture fields in finite bodies.

2. THE PROBLEM AND ITS FORMULATION

We consider the scattering of a plane electromagnetic wave from a plane screen of infinite extent in all directions and backed by an infinitely long rectangular cavity. The cavity is coupled through the screen by an infinitely long slit parallel to the axis of the cavity. A cutaway view of the structure is shown in Figure 1 and a cross sectional view is shown in Figure 2. The structure is assumed to be excited by a monochromatic plane wave (with time variation $\exp(j\omega t)$) having an arbitrary polarization and arbitrary polar and azimuthal angles of incidence, θ_o and ϕ_o, respectively. (See Figure 1.)

The portion of space where electromagnetic fields may exist is divided naturally into two regions: the cavity, given by $-b < x < b$, $-a < y < 0$, and the semi-infinite half space, where $y > 0$.
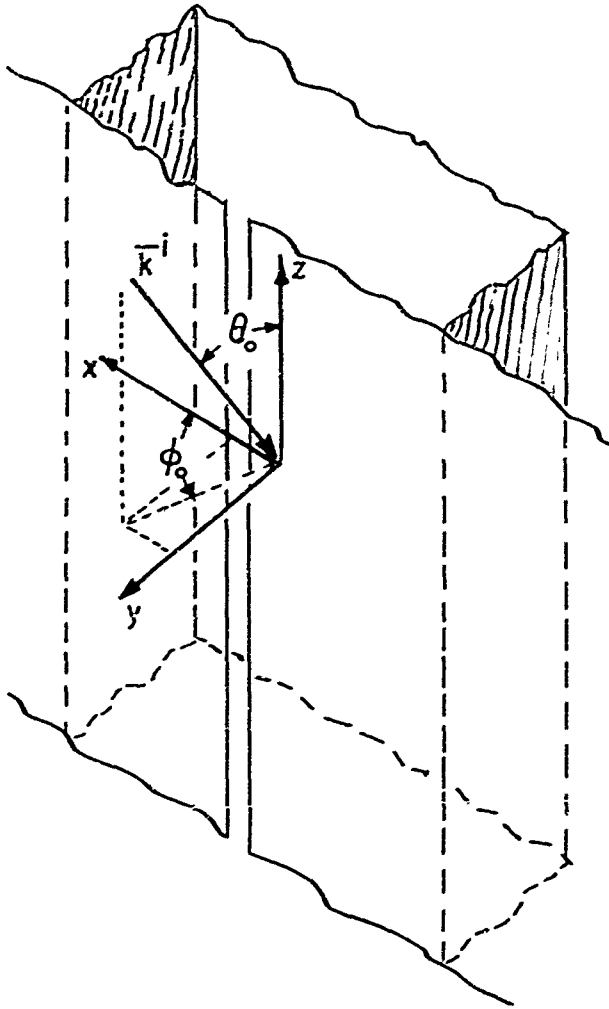
Figure 1. Typical Cross Section Taken
between Two Constant z Planes Showing
Cavity-Backed Infinite Plane Screen and
Direction of Incidence of Excitation
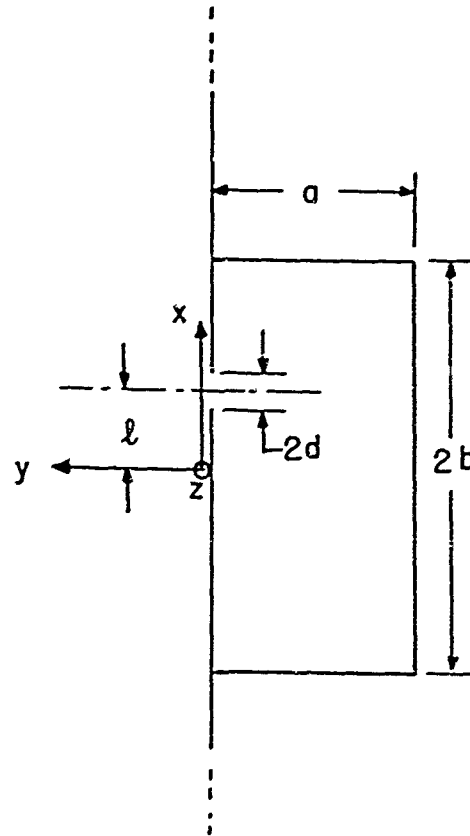
Figure 2. Cross-Sectional View
of the Cavity Showing the Dimen-
sion Parameters of the Structure

In each of these regions, the electromagnetic field may be expressed as a linear
superposition of divergenceless solutions to the homogeneous vector Helmholtz
equation.

In the cavity region, the fields are expressed as the superposition of a discrete,
doubly infinite set of modes, both transverse magnetic to z and transverse electric
to z modes being included. To these expressions we apply the boundary conditions
which require zero tangential electric field on the cavity surfaces, $y = -a$, $-b \leq x$
$\leq b$ and $x = \pm b$, $-a \leq y < 0$. The resultant expressions for the cavity electric
field, E^c , and the cavity magnetic field, H^c , are

$$\overline{E}^c = \sum_{n=0}^{\infty} \left[\overline{i}_x \left(j \frac{n\pi}{2b} d_n \cos \theta_o - m_n c_n \right) \cos \frac{n\pi}{2b} (x+b) \sin m_n (y+a) \right.$$

$$+ \overline{i}_y \left(j m_n d_n \cos \theta_o + \frac{n\pi}{2b} c_n \right) \sin \frac{n\pi}{2b} (x+b) \cos m_n (y+a)$$

$$\left. + \overline{i}_z \ \beta \sin \theta_o \ d_n \sin \frac{n\pi}{2b} (x+b) \sin m_n (y+a) \right] \tag{1}$$

$$\overline{H}^c = \frac{i}{Z_o} \sum_{n=0}^{\infty} \left[\overline{i}_x \left(m_n d_n - j \frac{n\pi}{2b} c_n \cos \theta_o \right) \sin \frac{n\pi}{2b} (x+b) \cos m_n (y+a) \right.$$

$$+ \overline{i}_y \left(-\frac{n\pi}{2b} d_n - j m_n c_n \cos \theta_o \right) \cos \frac{n\pi}{2b} (x+b) \sin m_n (y+a)$$

$$\left. + \overline{i}_z \ \beta \sin \theta_o \ c_n \cos \frac{n\pi}{2b} (x+b) \cos m_n (y+a) \right]. \tag{2}$$

Here c_n and d_n, $n=0, 1, \ldots$, are unknown complex constants, $Z = \sqrt{\mu_o / \epsilon_o}$, $\beta = k \sin \theta_o$, $(k = 2\pi/\lambda)$, and $m_n = \left[\beta^2 - \left(\frac{n\pi}{2b} \right)^2 \right]^{1/2}$. The assumed harmonic time and z variation, $\exp \left[j (\omega t + kz \cos \theta_o) \right]$, has been suppressed from these expressions.

In the exterior half space the total fields are written as the sum of three terms in accordance with the discussion given in the introduction. The first term is the incident field, $\overline{E}^i$, which is known. The second term is the unloaded scattered field, $\overline{E}^{s1}$, which is the field which would exist when the aperture $l-d \le x \le l+d$ is replaced by a perfectly conducting sheet. The unloaded scattered field is simply the field specularly reflected from an infinite screen and is thus known from elementary calculations. The third term in the field expression is the loaded scattered field. This field is that which is produced by the existence of non-zero aperture fields. It is these field quantities, denoted by $\overline{E}^{s2}$ and $\overline{H}^{s2}$, that we wish to compute.

Let us concentrate on expanding these latter field quantities. It is known that if ϕ is a solution to the homogeneous scalar Helmholtz equation and $\overline{a}$ is any constant vector, the vector functions $\overline{M}$ and $\overline{N}$, defined by

$$\overline{M} = \nabla x (\overline{a} \phi) \tag{3}$$

$$\overline{N} = 1/k \ (\nabla \times \overline{M}) , \tag{4}$$

are purely solenoidal solutions to the vector Helmholtz equation. Moreover, there exist collections of the functions of Eqs. (3) and (4) which are a basis for the expansion for the most general solenoidal solution to the vector Helmholtz equation. With ϕ of the form (suppressing the harmonic time dependence)

$$\phi(x, y, z) = \Psi(x, y) \exp (jkz \cos \theta_0) , \tag{5}$$

Ψ may be written as

$$\Psi(x, y) = \frac{1}{(2\pi)^{1/2}} \int_{-\infty}^{\infty} c(\alpha) \exp \{j [\lambda(\alpha)y - \alpha x] \} d\alpha , \tag{6}$$

where

$c(\alpha)$ is an unknown to be determined, and

$$\lambda(\alpha) = \begin{cases} j(\alpha^2 - \beta^2)^{1/2} & |\alpha| \geq \beta \\ (\beta^2 - \alpha^2)^{1/2} & |\alpha| \leq \beta . \end{cases}$$

It may be readily verified that Eq. (6) substituted into Eq. (5) gives a result that obeys the scalar Helmholtz equation. Further, as the cylindrical radius $\rho = (x^2 + y^2)^{1/2}$ becomes large, Eq. (5) appears in the form of a diverging cylindrical wave and thus obeys the radiation condition.

We now use in Eqs. (3) and (4) the result of substituting Eq. (6) into Eq. (5). Using both transverse electric to z and transverse magnetic to z field expressions, the quantities $\overline{E}^{S2}$ and $\overline{H}^{S2}$ take the form

$$\begin{aligned} \overline{E}^{S2} = & \ \bar{i}_x \frac{1}{\sqrt{2\pi}} \int_{-\infty}^{\infty} \left[j \lambda(\alpha) c(\alpha) + \alpha D(\alpha) \cos \theta_0 \right] \exp \{ j [\lambda(\alpha)y - \alpha x] \} d\alpha \\ & + \bar{i}_y \frac{1}{\sqrt{2\pi}} \int_{-\infty}^{\infty} \left[j\alpha c(\alpha) - \lambda(\alpha) D(\alpha) \cos \theta_0 \right] \exp \{ j [\lambda(\alpha)y - \alpha x] \} d\alpha \\ & + i_z \frac{\beta \sin \theta_0}{\sqrt{2\pi}} \int_{-\infty}^{\infty} D(\alpha) \exp \{ j [\lambda(\alpha)y - \alpha x] \} d\alpha \end{aligned} \tag{7}$$

$$\overline{H}^{s}2 = \frac{j}{Z_o}\left[\frac{1}{\sqrt{2\pi}}\int_{-\infty}^{\infty}\left[\alpha\ c(\alpha)\ \cos\ \theta_o + j\lambda(\alpha)\ D(\alpha)\right]\exp\{j[\lambda(\alpha)y - \alpha x]\}\ d\alpha\right.$$

$$+ \bar{i}_y\ \frac{1}{\sqrt{2\pi}}\int_{-\infty}^{\infty}\left[-\lambda(\alpha)\ c(\alpha)\ \cos\ \theta_o + j\alpha\ D(\alpha)\right]\ \exp\{j[\lambda(\alpha)y - \alpha x]\}\ d\alpha$$

$$\left.+ \bar{i}_z\ \frac{\beta\ \sin\ \theta_o}{\sqrt{2\pi}}\int_{-\infty}^{\infty}c(\alpha)\ \exp\{j[\lambda(\alpha)y - \alpha x]\}\ d\alpha\right]\ . \tag{8}$$

Here $D(\alpha)$ is also unknown and is to be determined.

Our objective at this point is to use the results of Eqs. (1), (2), (7), and (8) to form integral equations for the x and z components of the aperture electric field. The technique used is similar to that proposed by Lewin[1] for a class of waveguide discontinuity problems.

If $\underline{E}_z(x)$ denotes the unknown z component of the electric field in the aperture, then the boundary condition requiring continuity of the tangential electric fields at $y = 0$ interface gives

$$\overline{E}^c \cdot \bar{i}_z\bigg|_{y=0} = \begin{cases} \underline{E}_z(x) & l-d \leq x \leq l+d \\ \\ 0 & \text{otherwise} \end{cases} \tag{9}$$

when $-b \leq x \leq b$. Substituting for E^c and using the orthogonality of the sine functions gives

$$\beta b\ \sin\ \theta_o\ \sin\ m_p\ a\ d_p\ =\ \int_{l-d}^{l+d}\underline{E}_z(x)\ \sin\ \frac{p\pi}{2b}\ (x+b)\ dx$$

$$=\ \frac{2b}{p\pi}\int_{l-d}^{l+d}\underline{F}(x)\ \cos\ \frac{p\pi}{2b}\ (x+b)\ dx\ ,$$

where

$$\underline{F}(x)\ \equiv\ \frac{d}{dx}\ \underline{E}_z(x)\ . \tag{10}$$

The last equality follows from an integration by parts as suggested by the work of Lewin.

In a similar fashion the continuity of $\bar{E}$ relation gives

$$\left(\bar{E}^i + \bar{E}^{S1} + \bar{E}^{S2}\right) \cdot \bar{i}_z\big|_{y=0} = \begin{cases} \underline{E}_z(x) & l\text{-d} \leq x \leq l\text{+d} \\ \\ 0 & \text{otherwise} \end{cases} \tag{11}$$

for all x . Note that $\left(\bar{E}^i + \bar{E}^{S1}\right) \cdot \bar{i}_z\big|_{y=0} = 0$ from the definition of these quantities. Substituting for $\bar{E}^{S2}$ from Eq. (7) into this result and computing the Fourier transform of the equation gives

$$\beta \sin \theta_0 \, D(\alpha) = \frac{1}{\sqrt{2\pi}} \int_{l\text{-d}}^{l\text{+d}} \underline{E}_z(x) \, \exp(j\alpha x) \, dx$$

$$= \frac{j}{\sqrt{2\pi}} \, P\left[\frac{1}{\alpha} \int_{l\text{-d}}^{l\text{+d}} \underline{F}(x) \, \exp(j\alpha x) \, dx\right] . \tag{12}$$

The last equality follows from an integration by parts. Also, P denotes that the Cauchy principal value of the expression is to be taken upon an integration with respect to α .

In addition to the conditions above, let us require the continuity of the tangential components of the magnetic field in the aperture, $l\text{-d} \leq x \leq l\text{+d}$. That is, we require

$$\left(\bar{H}^i + \bar{H}^{S1} + \bar{H}^{S2}\right) \cdot \bar{i}_z\big|_{y=0} = \bar{H}^c \cdot \bar{i}_z\big|_{y=0} \qquad l\text{-d} \leq x \leq l\text{+d} \tag{13}$$

$$\left(\bar{H}^i + \bar{H}^{S1} + \bar{H}^{S2}\right) \cdot \bar{i}_x\big|_{y=0} = \bar{H}^c \cdot \bar{i}_x\big|_{y=0} \qquad l\text{-d} < x < l\text{+d} . \tag{14}$$

Note that due to the definition of $\bar{H}^{S1}$, $(\bar{H}^i + H^{S1}) \cdot \bar{i}_z\big|_{y=0} = 2 H^i \cdot \bar{i}_z\big|_{y=0}$ and $(\bar{H}^i + \bar{H}^{S1}) \cdot \bar{i}_x\big|_{y=0} = 2 H^i \cdot \bar{i}_x\big|_{y=0}$. After substituting for $\bar{H}^{S2}$ from Eq. (8) and for $\bar{H}^c$ from Eq. (2), we note that the second equation added to $-j \cos \theta_0/\beta \sin \theta_0$ times the x-derivative of the first equation gives a result involving only the unknown quantities $D(\alpha)$ and d_n, $n=0, 1, 2, \ldots$. Substituting for these unknowns from Eqs. (12) and (10) respectively gives an equation in the single unknown $\underline{F}$. A rearrangement of this result leads to the integral equation

$$\int_{-1}^{+1} \underline{F}(\lambda d + l)\,[\,G(\lambda-\tau) + H(\lambda,\tau)\,]\,d\lambda \;=\; E_o\,(\tau d + l) \qquad -1 \le \tau \le +1 , \tag{15}$$

where

$$\lambda \;=\; \frac{\eta - l}{d} , \qquad \tau = \frac{x - l}{d}$$

$$G(\lambda-\tau) \;=\; \frac{d}{2}\, P \int_{-\infty}^{\infty} \frac{\lambda(\alpha)}{\alpha}\; \exp[\,j\alpha d(\lambda-\tau)\,]\, d\alpha$$

$$H(\lambda,\tau) \;=\; 2d \sum_{n=1}^{\infty} \frac{m_n}{n}\, \cot m_n\, a\, \sin \frac{n\pi}{2b}\, (\tau d + l + b)\, \cos \frac{n\pi}{2b}\, (\lambda d + l + b)$$

$$E_o(\tau d + l) \;=\; -j\, 2\pi\beta\, \sin\theta_o\, Z_o \left[\, \overline{H}^i \cdot \overline{i}_x\Big|_{y=0} \;-\; \frac{j\cot\theta_o}{\beta d}\, \frac{\partial}{\partial\tau}\, \overline{H}^i \cdot \overline{i}_z\Big|_{y=0}\, \right] .$$

The solution to this integral equation , $\underline{F}$, along with the relation

$$\underline{E}_z(x) \;=\; d \int_{-1}^{(x-l)/d} \underline{F}(\lambda d + l)\, d\lambda , \tag{16}$$

makes possible the determination of the z component of the aperture electric field. Remember in connection with Eq. (16) that $\underline{F} = d/dx\, \underline{E}_z(x)$ and that $\underline{E}_z(l - d) = 0$.

Let us consider now the derivation of a second integral equation, the solution of which is related to the x component of the aperture field. Let $\underline{E}_x(x)$ denote the x component of the electric field in the aperture. Continuity of the x component of the electric field at $y = 0$ then gives

$$\overline{E}^c \cdot \overline{i}_x\Big|_{y=0} \;=\; \begin{cases} \underline{E}_x(x) & l-d \le x \le l+d \\[2mm] 0 & \text{otherwise} \end{cases} \tag{17}$$

for $-b \le x \le b$. Substituting for $\overline{E}^c$ from Eq. (1) in this expression and adding $-jd \cot\theta_o$ times the x derivative of Eq. (9) $\left[\text{with } E^c \text{ substituted from Eq. (1)}\right]$ gives

$$-\beta d \sum_{n=0}^{\infty} m_n c_n \sin m_n a \cos \frac{n\pi}{2b} (x+b) = \begin{cases} \underline{G}(x) & l-d \le x \le l+d \\ \\ 0 & \text{otherwise} \end{cases} \qquad (18)$$

for $-b < x < b$. Here

$$\underline{G}(x) = \beta d \, \underline{E}_x(x) - jd \cot \theta_o \, \underline{F}(x) \ . \qquad (19)$$

Using the orthogonality properties of the Fourier cosine series gives

$$(\epsilon_n - 3) \, m_n \, b \, \beta d \, c_n \sin m_n a = \int_{l-d}^{l+d} \underline{G}(x) \cos \frac{n\pi}{2b} (x+b) \, dx \ , \qquad (20)$$

where

$$\epsilon_n = \begin{cases} 1 & n = 0 \\ \\ 2 & n \ne 0 \ . \end{cases}$$

In a similar fashion, continuity of $\overline{E}$ at the $y=0$ plane requires

$$\left((\overline{E}^i + \overline{E}^{S1} + \overline{E}^{S2}) \cdot \overline{i}_x = \begin{cases} \underline{E}_x(x) & l-d \le x \le l+d \\ \\ 0 & \text{otherwise} \end{cases} \right. \qquad (21)$$

for all x . Again, noting that $(\overline{E}^i + \overline{E}^{S1}) \cdot \overline{i}_x \big|_{y=0} = 0$, substituting for $\overline{E}^{S2}$ from Eq. (7), and adding $-jd \cot \theta_o$ times the x derivative of Eq. (11) with $\overline{E}^{S2}$ substituted from Eq. (7) gives

$$j \frac{\beta d}{\sqrt{2\pi}} \int_{-\infty}^{\infty} \lambda(\alpha) \, c(\alpha) \exp(-j\alpha x) \, d\alpha = \begin{cases} \underline{G}(x) & l-d \le x \le l+d \\ \\ 0 & \text{otherwise} \ . \end{cases} \qquad (22)$$

Upon taking the Fourier transform of this result, there results

$$j \beta d \lambda(\alpha) \, c(\alpha) = \frac{1}{\sqrt{2\pi}} \int_{l-d}^{l+d} \underline{G}(x) \exp(j\alpha x) \, dx \ . \qquad (23)$$

At this point let us consider Eq. (13). Substituting for $\overline{H}^{S2}$ from Eq. (8) and for $\overline{H}^C$ from Eq. (2) and using the fact that $(\overline{H}^i + \overline{H}^{S1}) \cdot \overline{i}_z|_{y=0} = 2\overline{H}^i \cdot \overline{i}_z$, we find a relation in the unknowns c_n , $n=0, 1, 2,\ldots$, and $c(\alpha)$. Substituting for the c_n's from Eq. (20) and for $c(\alpha)$ from Eq. (23) and rearranging the result gives the integral equation

$$\int_{-1}^{+1} \underline{G}(\lambda d + l)\ [I(\lambda - \tau) + J(\lambda, \tau)]\ d\lambda\ =\ E_1(\tau d + l)\ ,\quad -1 \leq \tau \leq +1\ ,\tag{24}$$

where

$$I(\lambda - \tau)\ =\ \frac{d}{\pi}\int \frac{\alpha}{\lambda(\alpha)}\ \exp\left[j\alpha d(\lambda - \tau)\right] d\alpha$$

$$J(\lambda, \tau)\ =\ \frac{\pi d}{b^2}\sum_{n=1}^{\infty}\frac{n}{m_n}\cot m_n a\ \sin\frac{n\pi}{2b}\ (\tau d + l + b)\ \cos\frac{n\pi}{2b}\ (\lambda d + l + b)$$

$$E_1(\tau d + l)\ =\ \frac{-j\,4\,Z_o}{\sin\theta_o}\ \frac{\partial}{\partial\tau}\left(\overline{H}^i \cdot \overline{i}_z(\tau d + l)\Big|_{y=0}\right)\ .$$

Due to the relation defining $\underline{G}$, Eq. (19), the solution to Eq. (24) along with the solution $\underline{F}$ of Eq. (15) makes possible the calculation of $\underline{E}_x$.

3. PROBLEM SOLUTION

The complexity of the integral Eqs. (15) and (24) seems to preclude any exact solution. Instead, we consider a standard perturbation technique in order to obtain an approximate solution under the assumption of a small aperture width in wave-lengths.

Consider the integral equation

$$\int_L f(x)\ A(x, y)\ dx\ =\ g(y)\tag{25}$$

where A and g are known functions and f is an unknown function to be determined. Expanding A and g in a series in the dimensionless parameter ϵ and assuming a similar expansion exists for the unknown f results in

$$A(x, y) = \sum_{n=0}^{\infty} \epsilon^n A^n(x, y) ,$$

$$g(y) = \sum_{n=0}^{\infty} \epsilon^n g^n(y) ,$$

$$f(x) = \sum_{n=0}^{\infty} \epsilon^n f^n(x) .$$

Substituting these expansions into Eq. (25) and assuming the equality of the coefficients of like powers of ϵ yields the following sequence of integral equations:

$$\int_L f^0(x) A^0(x, y) \, dx = g^0(y)$$

$$\int_L f^1(x) A^0(x, y) \, dx = g^1(y) - \int_L f^0(x) A^1(x, y) \, dx$$

and so forth. Thus, if an integral equation having a kernel of the form of A^0 is solvable, then each integral equation in the above sequence is solvable for the successive approximations f^0, f^1, f^2, ... It should be noted that the right-hand side of each equation is a known function provided the previous equations in the sequence have been solved.

Let us apply this perturbation technique to the integral Eq. (15) for $\underline{F}$. The small parameter ϵ in this development will be taken to be βd. To apply the technique, we require series expansions in βd for the functions G, H, and E_o defined following Eq. (15). A detailed evaluation of $G(\lambda - \tau)$ reveals that

$$G(\lambda - \tau) = -P\left[\frac{1}{\lambda - \tau}\right] + O(\beta d)^2 .$$

Also,

$$H(\lambda, \tau) = -P \left[\frac{1}{\lambda - \tau} \right] + 0(\beta d)$$

and

$$E_0(\tau d + l) = j 2\pi\beta \sin\phi_0 \, \bar{i}_z \cdot \bar{e} \exp(j\beta l \cos\phi_0) + 0(\beta d) .$$

Here $\bar{e}$ is a vector in the direction of the $\bar{E}$ polarization of the incident wave and of magnitude equal to the incident electric field.

Substituting these results, along with the assumed βd expansion for $\underline{F}$,

$$\underline{F}(\lambda d + l) = \underline{F}^0(\lambda d + l) + \beta d \, \underline{F}^1(\lambda d + l) + \dots , \tag{26}$$

into Eq. (15) and equating the coefficients of $(\beta d)^0$ gives

$$\frac{P}{\pi} \int_{-1}^{+1} \frac{\underline{F}^0(\lambda d + l) \, d\lambda}{\lambda - \tau} = -j\beta \sin\phi_0 \, \bar{i}_z \cdot \bar{e} \exp(j\beta l \cos\phi_0) \quad -1 \le \tau \le +1 . \tag{27}$$

This is a singular integral equation of the form considered by Tricomi.[2] The solution to Eq. (27) is

$$\underline{F}^0(\lambda d + l) = \frac{-j\beta\lambda \sin\phi_0 \, \bar{i}_z \cdot \bar{e} \exp(j\beta l \cos\phi_0)}{(1 - \lambda^2)^{1/2}} ,$$

where we have used the fact that

$$\int_{-1}^{+1} \underline{F}^0(\lambda d + l) \, d\lambda = 0 .$$

This latter result follows since

$$0 = \frac{E_z(l + d) - E_z(l - d)}{d} = \int_{-1}^{+1} \underline{F}(\lambda d + l) \, d\lambda = \sum_{n=0}^{\infty} \left[\beta d \right]^n \int_{-1}^{+1} \underline{F}^n(\lambda d + l) \, d\lambda ,$$

or

$$\int_{-1}^{+1} \underline{F}^n (\lambda d + \ell) \, d\lambda = 0 \qquad n = 0, 1, 2, \ldots \quad .$$

Here the first equality follows since the z component of the aperture field must be zero at the edges of the aperture. The second equality follows from the definition of $\underline{F}$ given following Eq. (10), and the third equality follows from a substitution of the assumed βd expansion for $\underline{F}$.

A continuation of the perturbation scheme yields integral equations of the form of Eq. (27) in the unknowns $\underline{F}^n$, $n = 1, 2, 3, \ldots$. These results substituted into Eq. (26) along with the condition Eq. (16) gives for the aperture field

$$\underline{E}_z(\lambda d + \ell) = \beta d (1 - \lambda^2)^{1/2} \sin \phi_o \, \bar{i}_z \cdot \bar{e} \, \exp (j\beta \ell \cos \phi_o) \left[j - \frac{\beta d \lambda}{2} \cos \phi_o + 0(\beta d)^2 \right]$$
$$-1 \leq \lambda \leq +1 \quad . \tag{28}$$

Applying this same perturbation technique to Eq. (24) we arrive at a sequence of integral equations of the same form as Eq. (27). Without going into detail,[*] there results for the x component of the aperture electric field

$$\underline{E}_x(\lambda d + \ell) = \frac{2 \, \bar{i}_{\phi_o} \cdot \bar{e} \, \exp (j\beta \ell \cos \phi_o)}{\beta d \pi (1 - \lambda^2)^{1/2} \Delta_o} + 0 \, (\beta d) \quad . \tag{29}$$

Here $\bar{i}_{\phi_o}$ is the unit vector $\bar{i}_\phi$ evaluated in the direction from which the incident wave arrives. Also,

$$\Delta_o = \frac{1}{2} + j \left\{ \frac{1}{\pi} \left[\gamma + \ln \left| \cos \frac{\pi \ell}{2b} \right| + \ln \left| \frac{\pi d}{4b} \right| + \ln \left| \frac{\beta d}{2} \right| \right. \right.$$
$$\left. \left. - 2 \sum_{n=1}^{\infty} \frac{1}{n} \left(\frac{\coth \left(\gamma_n \frac{n\pi \partial}{2b} \right)}{\gamma_n} - 1 \right) \cos^2 \frac{n\pi}{2b} (\ell + b) \right] - \frac{\cot \beta a}{2\beta b} \right\}$$

where γ = Euler-Mascheroni constant = 0.5772157 and $\gamma_n = \left[1 - (2\beta b / n\pi)^2 \right]^{1/2}$.

The results of Eqs. (28) and (29) for the z and x components of the aperture electric field are the main results to be obtained here. It should be noted, however,

[*] A detailed analysis of this and other aspects of the problem will be included in an AFCRL report in preparation.

that by applying the method of steepest descent to the Fourier integrals in the expressions for $\overline{E}^{S2}$ and $\overline{H}^{S2}$, Eqs. (7) and (8) respectively, it is possible to evaluate the far scattered fields produced by the non-zero aperture fields $\underline{E}_z$ and $\underline{E}_x$. We will not consider these results here.

4. DISCUSSION OF RESULTS

In this section we consider Eqs. (28) and (29) for the z and x components of the electric field in the aperture.

Consider the result for $\underline{E}_z$ first. We note that this field component is proportional to the z component of the incident electric field and is independent of all other components. Further, this field is $O(\beta d)$ and hence for a narrow aperture will be small. A more complete analysis reveals that the first term in the solution to involve the cavity parameters a, b, and l is $O(\beta d)^3$. Thus it would seem that for a narrow aperture the cavity will do little to change or control the z component of the aperture field.

Finally, it is interesting to note that near the aperture edge, $\lambda \rightarrow \pm 1$, $\left|\underline{E}_z\right|$ varies according to the square root of the distance from the edge. This is the known edge condition for electric field components parallel to a sharp edge.[3]

Let us consider also the more interesting result of Eq. (29) for $\underline{E}_x$. We note that the dominant term for βd small is the first term, it being $O(1/\beta d)$. This dominant term has the same spatial variation as the static electric field which would be produced in an infinitely long narrow slit by a potential difference across the slit. Near the edges, $\lambda \rightarrow \pm 1$, this component of the field is proportional to $\rho^{-1/2}$ where ρ is the distance to the edge. Again, this is the known edge condition for electric field components perpendicular to a sharp edge.[3]

It is of interest to consider $\underline{E}_x$ at the center of the aperture $(\lambda=0)$ when $l=0$, that is, $\underline{E}_x(0)$, as a function of the cavity parameters a and b. A detailed analysis of Eq. (29) for $\theta_0 = 90°$ and $\phi_0 = 45°$ reveals that $\underline{E}_x(0) = 0$ for ka = $n\pi$, n=0, 1, 2,... as long as kb $\neq$ pπ, p=1, 2,... and kd $\neq 0$. Thus the cavity appears to short circuit the aperture when the cavity depth is adjusted to integer multiples of a half wavelength.

There also occur combinations of the cavity dimensions a and b where what might be called "anti-resonances" occur. Here the dominant first term in the expression for $\underline{E}_x$ is a maximum in magnitude.

These "anti-resonance" dimensions are not odd integer multiples of a quarter wavelength as might be expected. Rather, these dimensions are given by the condition that

$$\text{Im } \Delta_G = 0 .$$

Further, it can be shown that this condition occurs in the range $0 < a/\lambda < 1/2$ when $q < 2b/\lambda < q + 1/2$, $q=0, 1, 2, \ldots$ and in the range $a/\lambda > 1/2$ for all values of $2b/\lambda$. A numerical analysis for the conditions $\frac{2d}{\lambda} = 0.1$, $i = 0$, $\Theta_{\circ} = 90°$, $c_{\circ} = 45°$ reveals that under these conditions the "anti-resonance" values of a/λ tend to $n/2$, $n=1, 2, 3, \ldots$ as $2b/\lambda$ becomes large. Also, the "anti-resonances" become sharper as $2b/\lambda$ becomes larger since the magnitude of the field varies rapidly to zero at $a/\lambda = n/2$.

Acknowledgment

References

1. L. Lewin, On the resolution of a class of waveguide discontinuity problems by the use of singular integral equations, IRE Trans. on Microwave Theory and Technique, MTT-9, p. 321, 1961.

2. F. G. Tricomi, Integral equations, in Pure and Applied Mathematics, Vol. 5, A Series of Texts and Monographs, Interscience Publishers, Inc., New York, p. 173-183, 1957.

3. J. Meixner, The Behavior of Electromagnetic Fields at Edges, Research Report No. EM-72, Division of Electromagnetic Research, Institute of Mathematical Sciences, New York University, 1954.

This Document Contains
Missing Page/s That Are
Unavailable In The
Original Document

OR are
Blank pgs.
that have
Been Removed

**BEST
AVAILABLE COPY**

IX. Some Concepts for Reducing Reflectivity From Antenna Apertures

Edwin M. Turner
Electromagnetic Environment Branch
Air Force Systems Command
Aeronautical Systems Division
Wright-Patterson AFB, Ohio

An elementary analysis of radar reflectivity will generally show that for high-speed aerospace vehicles the most difficult surfaces to conceal are those occupied by the antenna apertures. This is true because the antennas are generally focused, reciprocal, and linear devices, and they must be strategically placed to perform their assigned functions. Within the confines of these assumptions, one has a number of readily available alternatives to reduce the backscattering from antenna apertures; the alternatives include terminal loading, inductive loading, absorptive loading, and choosing antenna designs which are inherently low in reflectivity.

Often a more productive solution for the backscattering problem may be found from a study of the flight trajectory and the operational requirements of the system. For instance, an antenna configuration may be used over only a small part of the flight path, and it may be hidden from radar view throughout the remainder of the trajectory without being operationally objectionable. This may be accomplished by either changing the antenna patterns to produce a beam pointing in some innocuous direction, or by breaking the aperture up into small segments, each of which will resonate at frequencies above or below the operating frequencies of the tracking radars. These objectives may be achieved by the use of biased diodes, non-reciprocal ferrites in waveguides, switches, or by relay-operated shorts that

122

will change the resonance frequencies or the patterns of the apertures.

Examples of the techniques suggested herein are shown below in Figures 1 to 4.
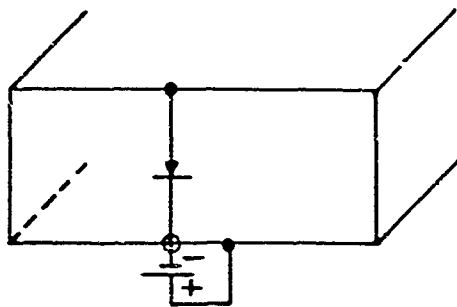
Figure 1. A Horn Aperture Shorted by Means of a Diode Switch Reduces Backscattering to Approximately That of a Flat Plate
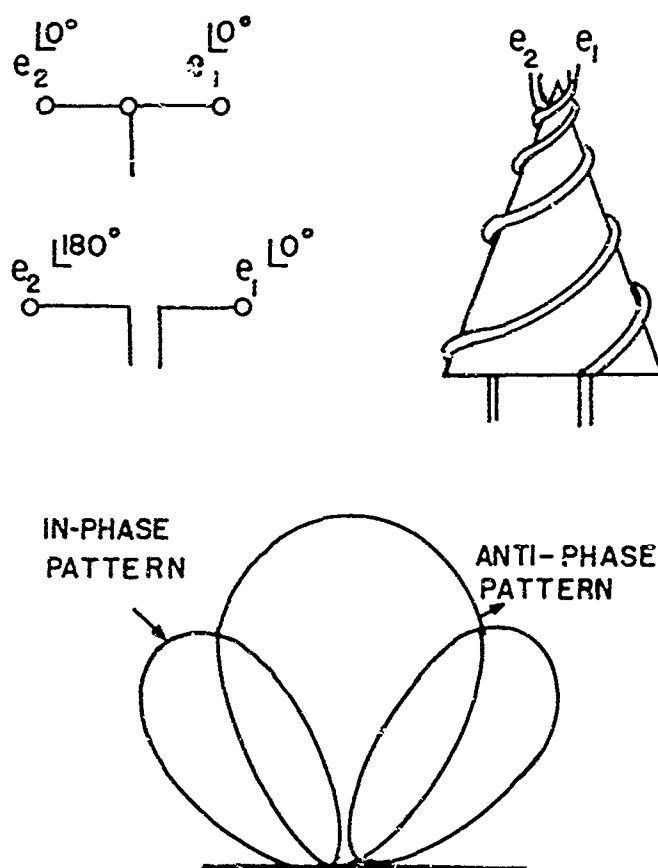
Figure 2. A Conical Spiral Antenna Showing Patterns for Both In-Phase and Anti-Phase Connections. A change in patterns can be achieved by means of placing a short across the feed terminals.
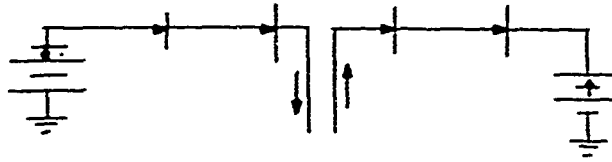
Figure 3. A Dipole Antenna With Forward Biased Diode Switches. A change in dc bias across diodes will segment the aperture.

TRANSMITTED BEAM

NORMAL
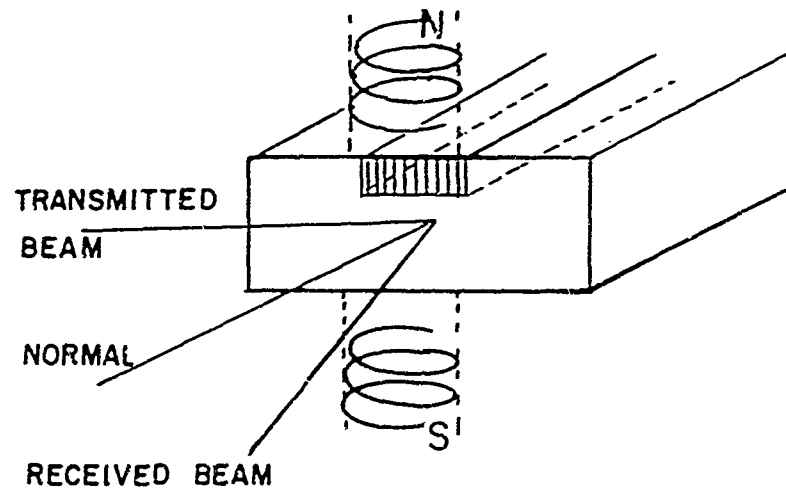
RECEIVED BEAM

Figure 4. An Open-Ended Wave-Guide Radiator Showing Non-Reciprocal Ferrite Phasing Element. The angle of divergence between the transmitted and received beams is proportional to the magnetic field across ferrite phase shifter.

This Document Contains
Missing Page/s That Are
Unavailable In The
Original Document

OR are
Blank pgs.
that have
Been Removed

**BEST
AVAILABLE COPY**

X. Radar Cross Section of Perfectly Conducting, Dielectric and Dielectrically Clad Infinite Cylinders at Arbitrary Incidence*

Abdelnour S. Thomas
A. S. Thomas, Inc.
Westwood, Massachusetts

1. INTRODUCTION

The work reported in the literature[1-7] on dielectrically clad cylinders prima-
rily treats normal incidence and in most cases is restricted to the geometrical
optics region. As far as could be ascertained by the author, the dielectrically clad
infinite cylinder at normal (broadside) incidence for a TM incident field was first
treated by C. C. Tang[7] with computed values of normalized radar cross section
experimentally verified. The more general case of arbitrary incidence was treated
by J. R. Wait[8] for a homogeneous non-metallic cylinder for an incident TM mode.
He, however, did not present any numerical data. The dielectrically clad cylinder,
following the work of Wait and Tang, is extended here to the more general case of
oblique incidence of either TM or TE modes for N concentric layers. The normal-
ized radar cross section in the plane of incidence has been computed for normal
and oblique incidence.

It is believed that a comparison of the normalized radar cross section of the
dielectrically clad and solid dielectric cylinders for small radii with that of the

perfect.) conducting cylinder would provide some insight into the problem of reducing the radar cross section of objects of small geometrical cross section.

2. FORMULATION

2.1 General

The equations of the incident, internal, and scattered fields at arbitrary incidence are presented here for a cylinder consisting of N homogeneous, concentric, non-metallic cylindrical layers. The expressions for the scattering coefficients for a single layer about a perfectly conducting core with an incident TM field ($H_z = 0$) are derived, and then the expressions for incident TE mode are given. These general expressions reduce to those for the solid homogeneous dielectric cylinders as well as to the solid metallic cylinder.

Consider a plane-wave incident on an infinite cylindrical obstacle at an angle Ψ_o with respect to the normal to the axis of the cylinder to be a pure TM wave. Using the coordinate system given in Figure 1, the incident, internal, and scattered fields may be written as follows:

(1) Incident Fields

$$E_z^{inc} = E_o \cos \Psi_o \sum j^n J_n(\beta_o r) F_n \tag{1}$$

$$E_\phi^{inc} = E_o \cos \Psi_o \sum j^n \left(\frac{-n k_o \sin \Psi_o}{\beta_o^2 r} \right) J_n(\beta_o r) F_n \tag{2}$$

$$H_z^{inc} \equiv 0 \tag{3}$$

$$H_\phi^{inc} = E_o \cos \Psi_o \sum j^n \left(\frac{-j k_o^2}{\omega \mu_o \beta_o} \right) J_n'(\beta_o r) F_n \tag{4}$$

(2) Internal Fields

$$E_z^m = \sum j^n \left(A_n^m H_n^{(1)}(\beta_m R_m) + B_n^m H_n^{(2)}(\beta_m R_m) \right) F_n \tag{5}$$
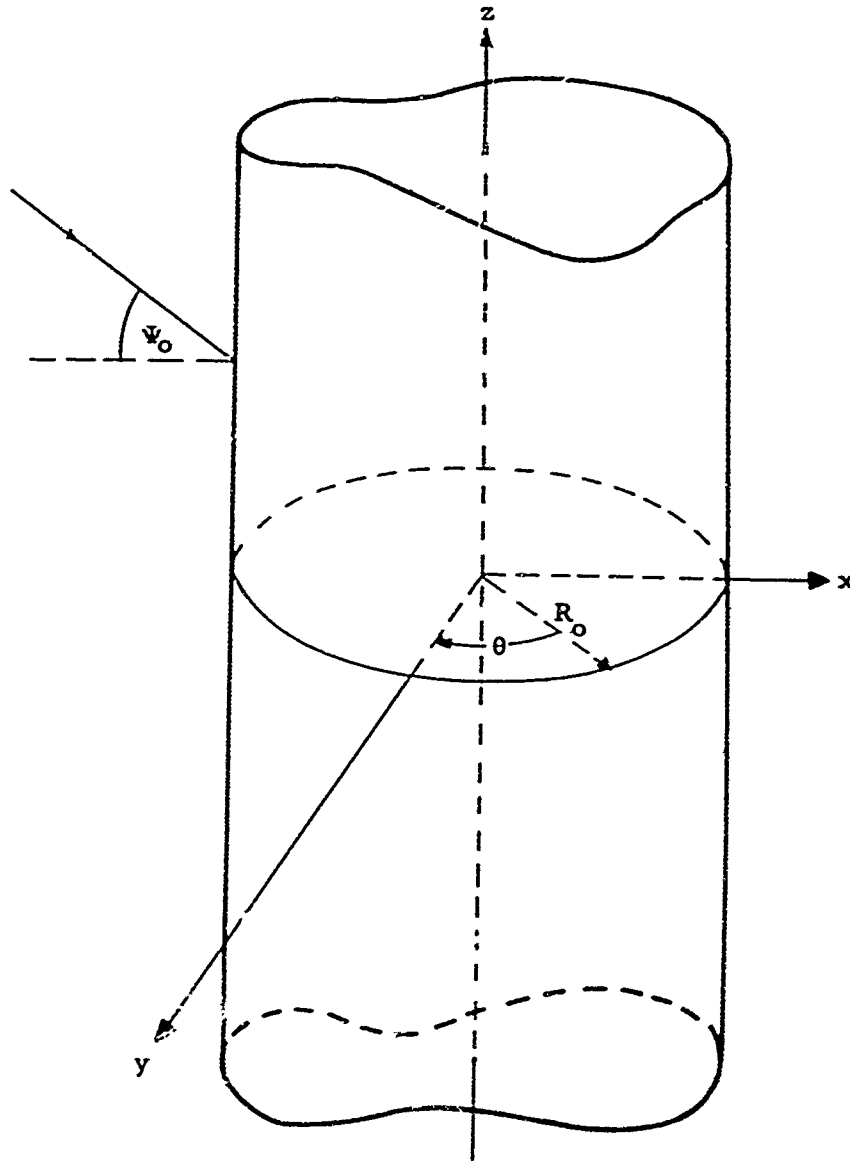
Figure 1. Cylindrical Coordinate System

$$E_\phi^m = \sum j^n \left(\frac{-nk_o \sin\Psi_o}{\beta_m^2 R_m} \left[A_n^m H_n^{(1)}(\beta_m R_m) + B_n^m H_n^{(2)}(\beta_m R_m) \right] \right.$$

$$\left. + j\frac{\omega\mu_m}{\beta_m} \left[\bar{A}_n^m H_n^{(1)\prime}(\beta_m R_m) + \bar{B}_n^m H_n^{(2)\prime}(\beta_m R_m) \right] \right) F_n \tag{6}$$

$$H_z^m = \sum j^n \left(\bar{A}_n^m H_n^{(1)}(\beta_m R_m) + \bar{B}_n^m H_n^{(2)}(\beta_m R_m) \right) F_n \tag{7}$$

$$H_\phi^m = \sum j^n \left(\frac{-nk_o \sin \Psi_o}{\beta_m^2 R_m} \left[\bar{A}_n^m H_n^{(1)}(\beta_m R_m) + \bar{B}_n^m H_n^{(2)}(\beta_m R_m) \right] \right.$$

$$\left. -j \frac{k_m^2}{\omega\mu_m\beta_m} \left[A_n^m H_n^{(1)'}(\beta_m R_m) + B_n^m H_n^{(2)'}(\beta_m R_m) \right] \right) F_n \qquad (8)$$

(3) Scattered Fields

$$E_z^{sc} = \sum j^n C_n H_n^{(2)}(\beta_o r) F_n \qquad (9)$$

$$E_\phi^{sc} = \sum j^n \left(\frac{-nk_o \sin \Psi_o}{\beta_o^2 r} C_n H_n^{(2)}(\beta_o r) + j \frac{\omega\mu_o}{\beta_o} \bar{C}_n H_n^{(2)'}(\beta_o r) \right) F_n \qquad (10)$$

$$H_z^{sc} = \sum j^n \bar{C}_n H_n^{(2)}(\beta_o r) F_n \qquad (11)$$

$$H_\phi^{sc} = \sum j^n \left(\frac{-nk_o \sin \Psi_o}{\beta_o^2 r} \bar{C}_n H_n^{(2)}(\beta_o r) - \frac{jk_o^2}{\omega\mu_o\beta_o} C_n H_n^{(2)'}(\beta_o r) \right) F_n \qquad (12)$$

where it is understood that the summation is from $n = -\infty$ to $n = \infty$

E_o = magnitude of the incident field

Ψ_o = angle of incidence with respect to the axis of the cylinder

$\beta_m = k_m \cos \Psi_m$, with $m = 0, 1, 2, \ldots$ N relating to the mth layer, with $m = 0$ free space external the cylinder

$k_m = 2\pi/\lambda \sqrt{\mu_m \epsilon_m}$,

f = operating frequency

μ_m = normalized permeability of the mth layer

ϵ_m = normalized permittivity of the mth layer

$F_n = \exp[-j(n\phi - k_m z \sin \Psi_m)]$

A_n^m, B_n^m, C_n^m = arbitrary constants relating to the TM mode

$\bar{A}_n^m, \bar{B}_n^m, \bar{C}_n^m$ = arbitrary constants relating to the assumed internal and scattered TE mode

$J_n, H_n^{(1)}, H_n^{(2)}$ = Bessel and Hankel functions with the primes relating to differentiation with respect to the argument.

2.2 Single Layer about a Perfectly Conducting Cylinder

Now, by equating the internal fields to the sum of the incident and scattered fields at the air interface:

$$E_o \cos \Psi_o J_n(x_o) + C_n H_n^{(2)}(x_o) = A_n H_n^{(1)}(x_1) + B_n H_n^{(2)}(x_1), \tag{13}$$

$$\frac{nk_o \sin \Psi_o}{\beta_o x_o} \left[E_o \cos \Psi_o J_n(x_o) + C_n H_n^{(2)}(x_o) \right] - j \frac{\omega \mu_o}{\beta_o} \bar{C}_n H_n^{(2)\prime}(x_o)$$

$$= \frac{nk_o \sin \Psi_o}{\beta_1 x_1} \left[A_n H_n^{(1)}(x_1) + B_n H_n^{(2)}(x_1) \right] - j \frac{\omega \mu_1}{\beta_1} \left[\bar{A}_n H_n^{(1)\prime}(x_1) + \bar{B}_n H_n^{(2)\prime}(x_1) \right] \tag{14}$$

$$\bar{C}_n H_n^{(2)}(x_o) = \bar{A}_n H_n^{(1)}(x_1) + \bar{B}_n H_n^{(2)}(x_1), \tag{15}$$

and

$$\frac{jk_o^2}{\omega \mu_o \beta_o} \left[E_o \cos \Psi_o J_n'(x_o) + C_n H_n^{(2)\prime}(x_o) \right] + \frac{nk_o \sin \Psi_o}{\beta_o x_o} \bar{C}_n H_n^{(2)}(x_o)$$

$$= \frac{nk_o \sin \Psi_o}{\beta_1 x_1} \left[\bar{A}_n H_n^{(1)}(x_1) + \bar{B}_n H_n^{(2)}(x_1) \right] + \frac{jk_1^2}{\omega \mu_1 \beta_1} \left[A_n H_n^{(1)\prime}(x_1) + B_n H_n^{(2)\prime}(x_1) \right] \tag{16}$$

where Ψ_1 = angle wave makes with normal in coating

$x_o = \beta_o R_o$

R_o = outer radius

$x_1 = \beta_1 R_o$

and setting at the metallic interface

$$\frac{B_n}{A_n} = -\frac{H_n^{(1)}(x_2)}{H_n^{(2)\prime}(x_2)} \tag{17}$$

and

$$\frac{\bar{B}_n}{\bar{A}_n} = -\frac{H_n^{(1)\prime}(x_2)}{H_n^{(2)\prime}(x_2)}, \tag{18}$$

the C_n and $\bar{C}_n$ may be readily obtained for the incident TM mode, giving:

$$C_n^{TM} = -\frac{VP - q_n^2 J_n(x_o) H_n^{(2)}(x_o)}{PN - \left[q_n H_n^{(2)}(x_o)\right]^2}, \tag{19}$$

and

$$\overline{C}_n = \frac{q_n s_o \left[H_n^{(2)\prime}(x_o) J_n(x_o) - H_n^{(2)}(x_o) J_n^{\prime}(x_o)\right]}{PN - \left[q_n H_n^{(2)}(x_o)\right]^2} \tag{20}$$

where: $N = s_1 H_n^{(2)}(x_o) D - s_o H_n^{(2)\prime}(x_o)$

$P = r_1 H_n^{(2)}(x_o) L - s_o H_n^{(2)\prime}(x_o)$

$V = s_1 J_n(x_o) D - s_o J_n^{\prime}(x_o)$

$$D = \frac{H_n^{(1)\prime}(x_1) H_n^{(2)}(x_2) - H_n^{(2)\prime}(x_1) H_n^{(1)}(x_2)}{H_n^{(1)}(x_1) H_n^{(2)}(x_2) - H_n^{(2)}(x_1) H_n^{(1)}(x_2)}$$

$$L = \frac{H_n^{(1)\prime}(x_1) H_n^{(2)\prime}(x_2) - H_n^{(2)\prime}(x_1) H_n^{(1)\prime}(x_2)}{H_n^{(1)}(x_1) H_n^{(2)\prime}(x_2) - H_n^{(2)}(x_1) H_n^{(1)\prime}(x_2)}$$

$$s_1 = \frac{\epsilon}{\sqrt{\epsilon - \sin^2 \Psi_o}}$$

$$s_o = \frac{1}{\cos \Psi_o}$$

$$r_1 = \frac{1}{\sqrt{\epsilon - \sin^2 \Psi_o}}$$

$$q_n = \frac{n\lambda \sin \Psi_o}{2\pi R_o} \left(\frac{1}{\epsilon - \sin^2 \Psi_o} - \frac{1}{\cos^2 \Psi_o}\right).$$

In the plane of incidence ($\phi = 0°$), σ may be written

$$\sigma = \frac{2\lambda \cos \Psi_o}{\pi} \left|\sum_{-\infty}^{\infty} (-1)^n C_n\right|^2. \tag{21}$$

Now note that the $\overline{C}_n$, Eq. (20), may be written as follows:

$$\overline{C}_n = \frac{n\lambda \sin \Psi_o}{2\pi R_o} G_n. \tag{22}$$

where

$$G_n = G_{-n},$$

hence, for

$$n = 0$$
$$\overline{C}_o = 0$$

and

$$\overline{C}_n + \overline{C}_{-n} = 0 \text{ for } n \neq 0.$$

Therefore, in the plane of incidence, the orthogonal mode is identically zero.

However, the scattered field in planes other than the plane of incidence will contain the orthogonal mode which will increase as a function of the angle Ψ_o and the angle ϕ of the plane of observation, with a maximum in the plane $\phi = 90°$. Also, if the axis of the cylinder is skewed with respect to the plane of incidence, the scattered field in the plane of incidence will contain the orthogonal mode.

In the plane of incidence, the C_n may be obtained for the TE incident mode (C_n^{TE}) by replacing E by H and H by $-E$, ϵ by μ and μ by ϵ throughout, giving:

$$C_n^{TE} = -\frac{MN - q_n^2 J_n(x_o) H_n^{(2)}(x_o)}{PN - \left[q_n H_n^{(2)}(x_o)\right]^2} \tag{23}$$

where

$$M = r_1 J_n(x_o) L - s_o J_n'(x_o),$$

and all other symbols are as previously defined.

For normal incidence, $\Psi_o = 0°$, $q_n = 0.0$. Eqs. (19) and (23) become the well-known equations for normal incidence

$$C_n^{TM} = -\frac{V}{N}, \tag{24}$$

and

$$C_n^{TE} = -\frac{M}{P}. \tag{25}$$

2.3 Solid Dielectric Cylinder

If x_2 is taken equal to zero, that is, a solid, homogeneous, non-metallic cylinder, Eqs. (19) and (23) immediately reduce to those for the solid dielectric cylinder at oblique incidence, with

$$C_n^{TM} = -\frac{VP - q_n^2 J_n(x_o) H_n^{(2)}(x_o) J_n^2(x_1)}{PN - \left[q_n H_n^{(2)}(x_o) J_n(x_1)\right]^2} \tag{26}$$

$$C_n^{TE} = -\frac{MN - q_n^2 J_n(x_o) H_n^{(2)}(x_o) J_n^2(x_1)}{PN - \left[q_n H_n^{(2)}(x_o) J_n(x_1)\right]^2} \ . \tag{27}$$

where

$$V = s_1 J_n(x_o) J_n'(x_1) - s_o J_n'(x_o) J_n(x_1)$$

$$P = r_1 H_n^{(2)}(x_o) J_n'(x_1) - s_o H_n^{(2)'}(x_o) J_n(x_1)$$

$$N = s_1 H_n^{(2)}(x_o) J_n'(x_1) - s_o H_n^{(2)'}(x_o) J_n(x_1)$$

$$M = r_1 J_n(x_o) J_n'(x_1) - s_o J_n'(x_o) J_n(x_1).$$

Again, for normal incidence,

$$C_n^{TM} = -\frac{V}{N} \ , \tag{28}$$

$$C_n^{TE} = -\frac{M}{P} \ . \tag{29}$$

2.4 Perfectly Conducting Cylinder

Setting $\epsilon = \infty$, Eqs. (19) and (23) for the dielectrically clad cylinder reduce to the following expressions for the perfectly conducting cylinder at oblique incidence:

$$C_n^{TM} = -\frac{J_n(x_o)}{H_n^{(2)}(x_o)} \tag{30}$$

$$C_n^{TE} = -\frac{J_n'(x_o)}{H_n^{(2)'}(x_o)} \tag{31}$$

Equations (30) and (31) are of the same form as the well-known equations for the perfectly conducting cylinder at normal incidence, except that at oblique incidence $x_o = k_o R_o \cos \Psi_o$. In all of the above, the factors $E_o \cos \Psi_o$ and $H_o \cos \Psi_o$ have been surpressed for all of the C_n's. It is interesting to note that, ignoring the factors $E_o \cos \Psi_o$ or $H_o \cos \Psi$, the σ for the perfectly conducting cylinder at

oblique incidence is identical to that of normal incidence with the radius reduced by the factor $\cos \Psi_o$.

3. COMPUTED NORMALIZED SIGMA

The normalized radar cross section

$$S = \frac{\sigma}{\pi R_o \cos \Psi_o} \tag{32}$$

was computed for perfectly conducting solid, homogeneous, dielectric, and dielectrically clad cylinders.

3.1 Metallic Cylinder

For the metallic cylinder, a single computation of σ versus R_o for both TE and TM incident modes is sufficient since, for other than normal incident, multiplying R_o/λ by $\cos \Psi_o$ will convert normal incidence to another angle of incidence Ψ_o.

Figure 2 is the well-known $\sigma/\pi R_o$ of normal incidence for a perfectly conducting infinite cylinder with the TM mode decreasing monotonically with increasing R_o/λ and the TE mode increasing monotonically to unity and then oscillating with damped oscillations as R_o/λ is increased and finally settling to the limiting value of $\sigma/\pi R_o = 1$.

3.2 Solid Dielectric Cylinder

In Figure 3, the normalized sigmas at normal incidence for TE and TM incident modes are given for $0.0002 \leq R_o/\lambda \leq 1.0$ and $\epsilon = 4.0$. Here the normalized sigmas for both TE and TM modes are monotonically increasing for values of $R_o/\lambda < 0.10$, and then both commence to oscillate with the oscillations increasing in amplitude and rising above unity with increased R_o/λ. It is interesting that the TM mode for small R_o/λ is approximately at the same level as the TE mode for the perfectly conducting cylinder. The level of course depends on the value of ϵ and will be higher for larger values of ϵ and lower for the lower values of ϵ. In Figure 4, the R_o/λ versus S is given for $\epsilon = 4$ and $\Psi = 84°$. In comparison with the metallic cylinder, the TE mode is considerably higher up to $R_o/\lambda = 0.2$ with the TE and TM modes very close in amplitude.

It has been found that the relative number of fluctuations (min to min) is related to the dielectric constants of the materials as $\sqrt{\epsilon_1 - 1} / \sqrt{\epsilon_2 - 1}$, where ϵ_1 is the permittivity of one cylinder and ϵ_2 the permittivity of another cylinder.
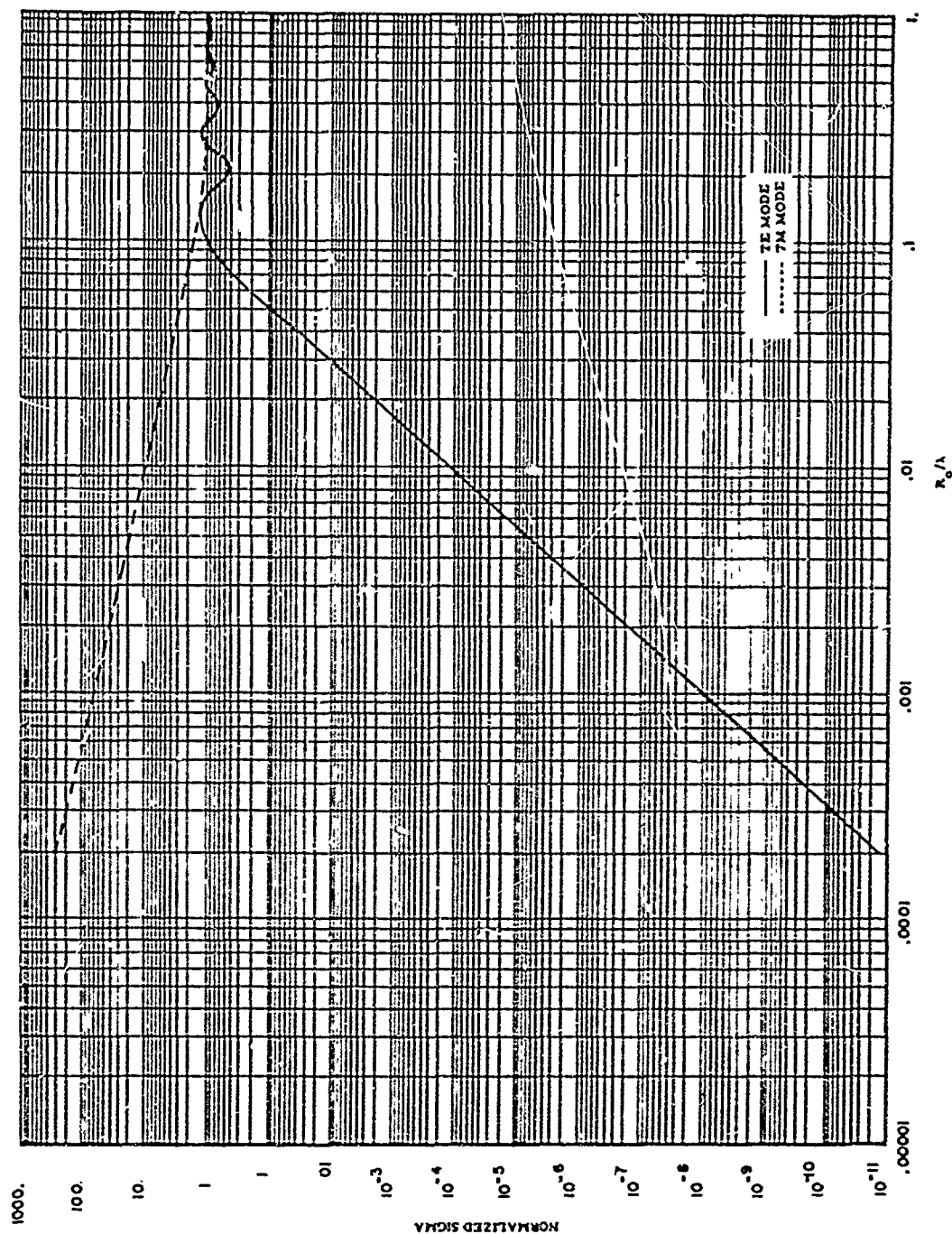
Figure 2. Perfectly Conducting Infinite Cylinder. Normalized Sigma vs R_o/λ. $\Psi_o = 0°$, $R_o/\lambda = 0.0002 \rightarrow 1.0$
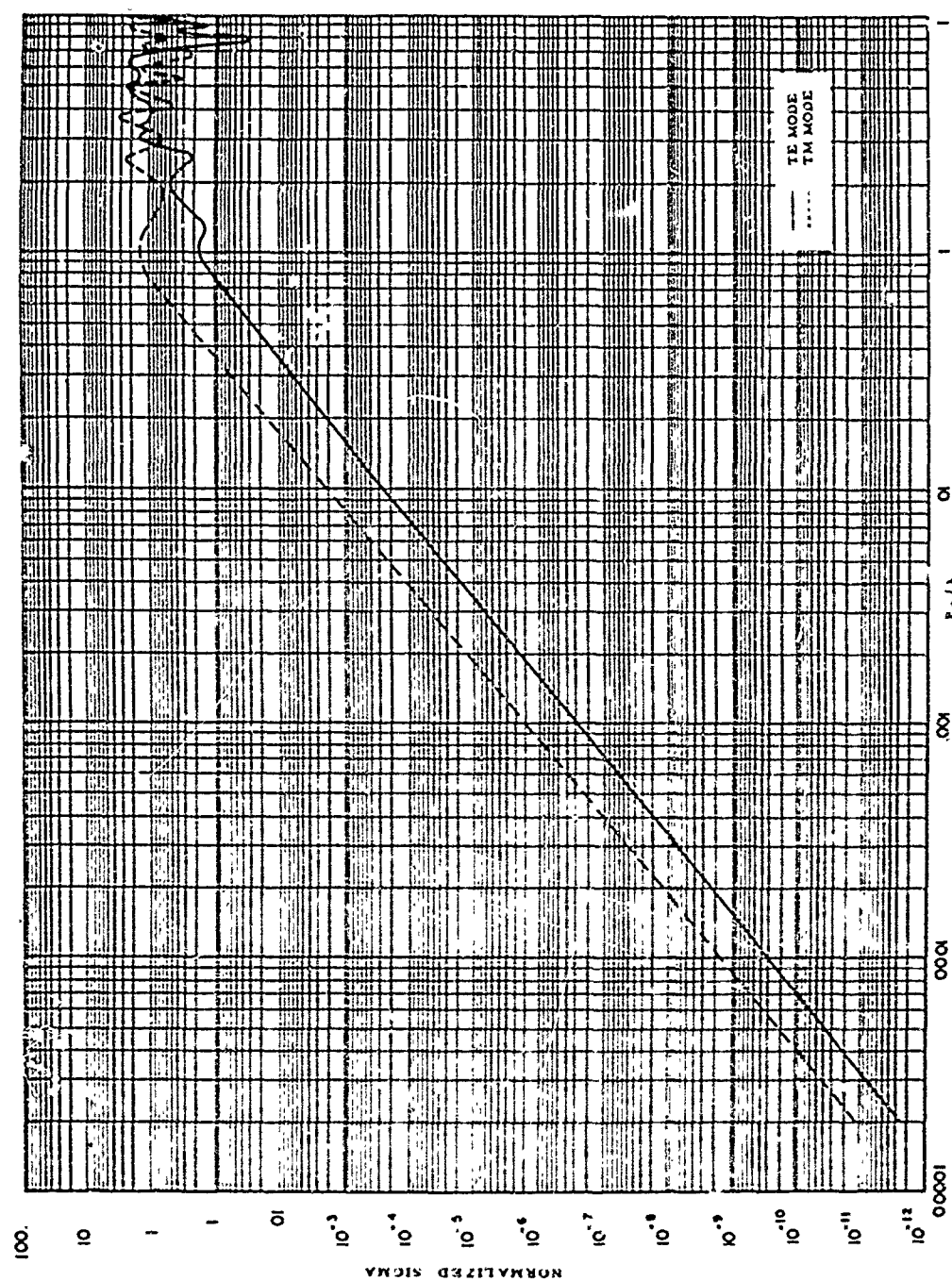
Figure 3. Solid Dielectric Infinite Cylinder. Normalized Sigma vs R_0/λ. $\psi_0 = 0°$, $\epsilon = 4.0$, $R_0/\lambda = 0.00002 \rightarrow 1.0$
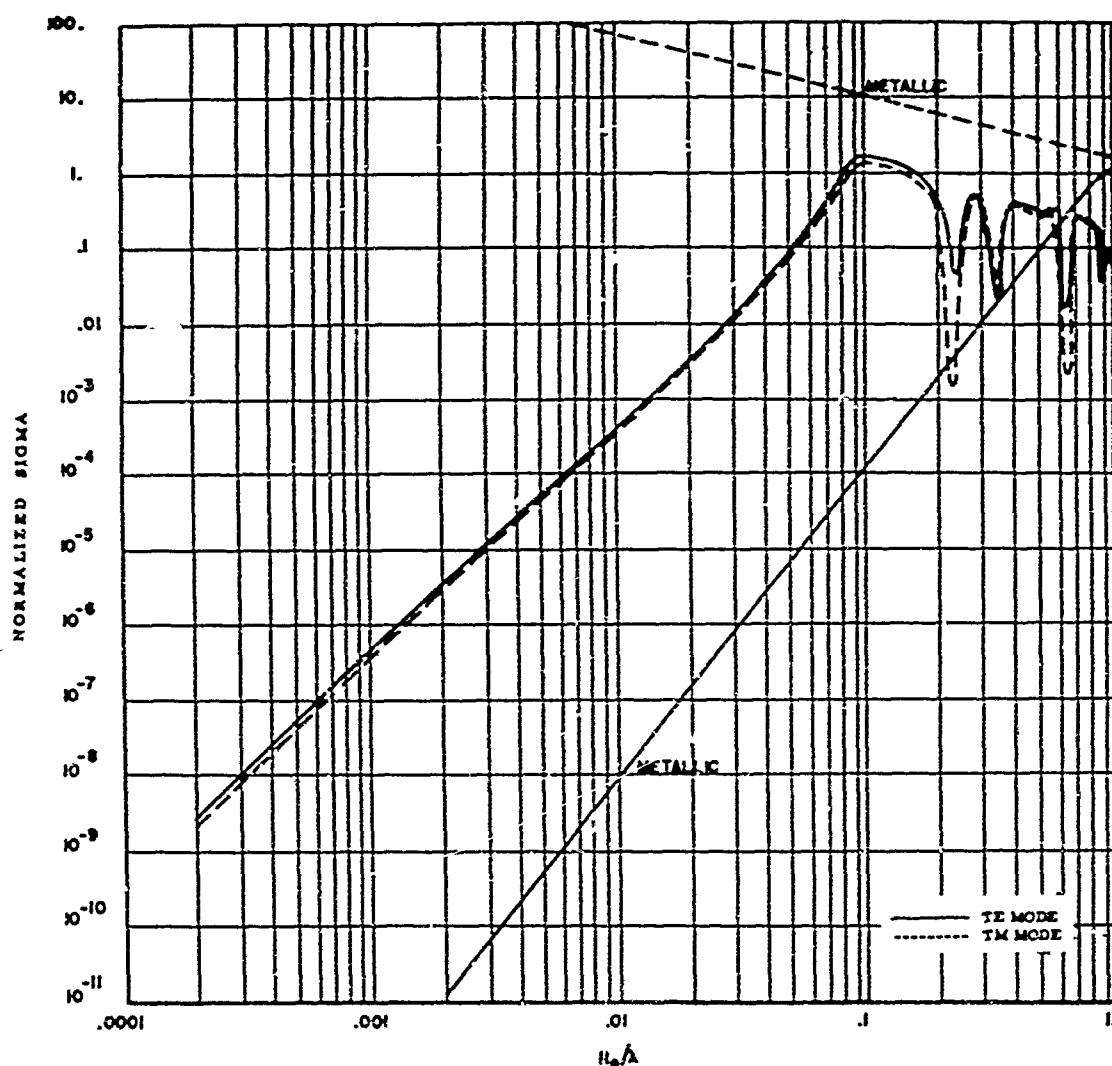
Figure 4. Solid Dielectric Cylinder vs Metallic Cylinder. Normalized Sigmas vs R_0/λ. $\Psi_0 = 84°$, $\epsilon = 4.0$, $R_0/\lambda = .0002 \rightarrow 1.0$.

3.3 Dielectrically Clad Cylinder

The normalized sigma versus R_0/λ for the range $0.0002 \leq R_0/\lambda \leq 1$ for shell thicknesses as determined by $R_1 = 0.9R_0$ and dielectric constant of the shell equal to 4.0 at normal incidence is given in Figure 5. Here again, unlike the perfectly conducting cylinder, the oscillations of the TE mode do not dampen out in the same manner as the TE mode of the perfectly conducting cylinder; rather, they increase in amplitude after $R_0/\lambda = 0.5$. For small R_0/λ, the TE mode of the dielectrically clad cylinder is significantly higher than that of the perfectly conducting cylinder, and the TM mode is significantly lower than that of the perfectly conducting cylinder.
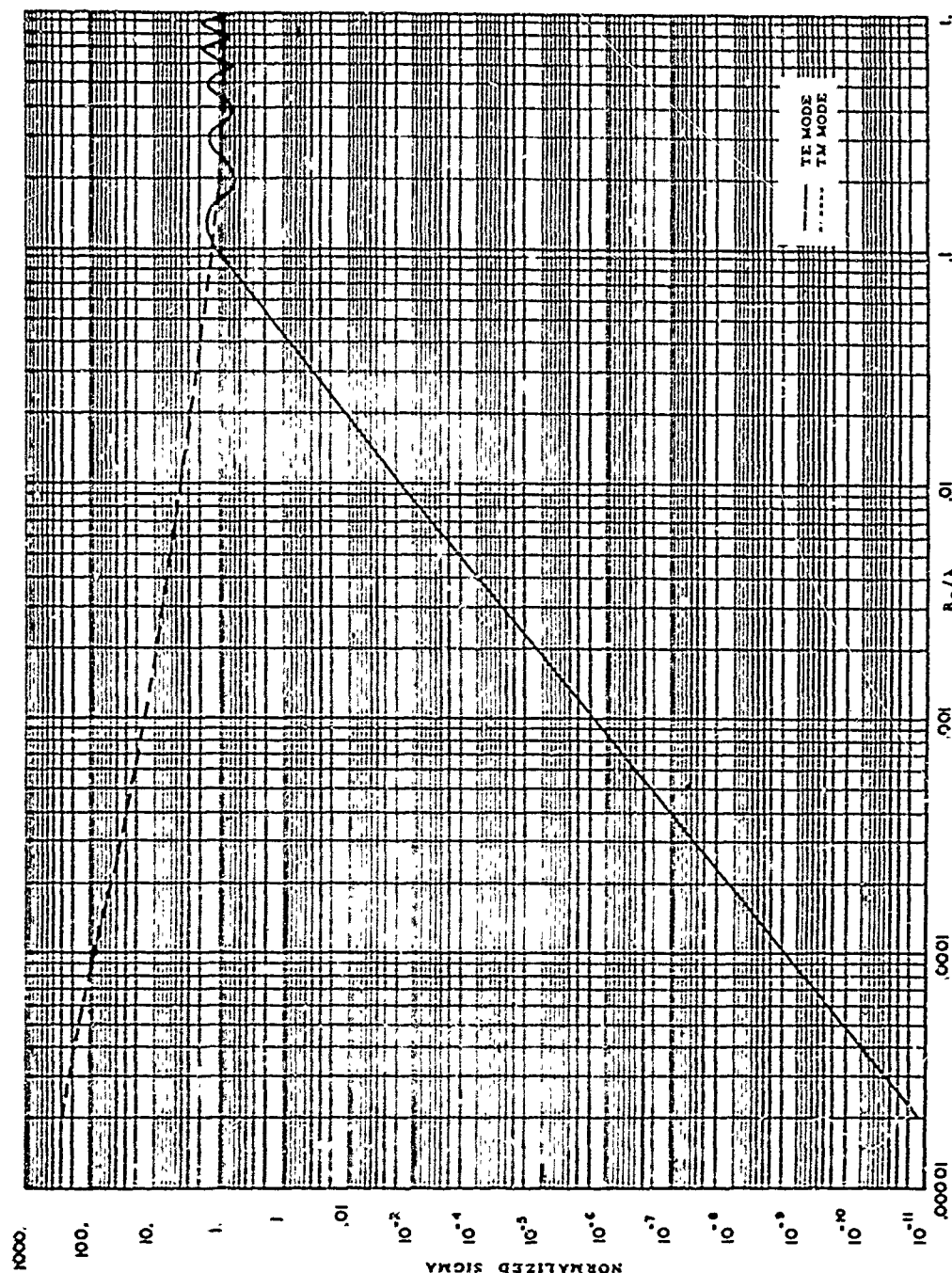
Figure 5. Dielectrically Clad Infinite Cylinder. Normalized Sigma vs R_o/λ. $\Psi_o = 0°$, $\epsilon = 4.0$, $R_1 = 0.9 R_o$, $R_o/\lambda = 0.0002 \rightarrow 1.0$

It is interesting to compare the dielectrically clad cylinder at normal incidence with the dielectrically clad sphere*, Figure 6. Note the considerable similarity between the sphere and the cylinder at normal incidence. Both the sphere and cylinder have burst of oscillations that dampen out and then resume. The first burst of oscillations from the sphere corresponds with the TE mode of the cylinder, and the second burst with the TM mode of the cylinder; when the oscillations of both modes of the cylinder are damped, so also are those of the sphere. Both sphere and cylinder have equal numbers of oscillations occuring at the same R_o/λ; however, the sphere differs from the cylinder in that the amplitude of the oscillations is larger for the sphere than for the cylinder.

Figure 7 shows normalized sigma, S, versus R_o/λ for a shell thickness of $0.1 R_o$, $\epsilon = 4.0$, and the angle of incidence equal to 84°, for $0.0002 \leq R_o/\lambda \leq 1.0$ in comparison with the perfectly conducting cylinder. Here the S for the TE mode of the dielectrically clad cylinder is significantly larger than the corresponding mode of the perfectly conducting cylinder for $R_o/\lambda \leq 0.2$.

Figures 8 and 9 give scan in angle for $R_1 = 0.9 R_o$ and $R_o = 0.78\lambda$, respectively, for $\epsilon = 4.0$ and $\epsilon = 2.56$. Here there is considerable similarity between the two values of ϵ; however, for the large ϵ, the S rises higher above unity than it does for the smaller ϵ.

The normalized σ, S, versus ϵ is given in Figure 10 for $\Psi = 45°$, $R_o/\lambda = 0.78$ and $R_1 = .702\lambda$.

---

* The sphere was computed by J. Rheinstein of MIT, Lincoln Laboratories
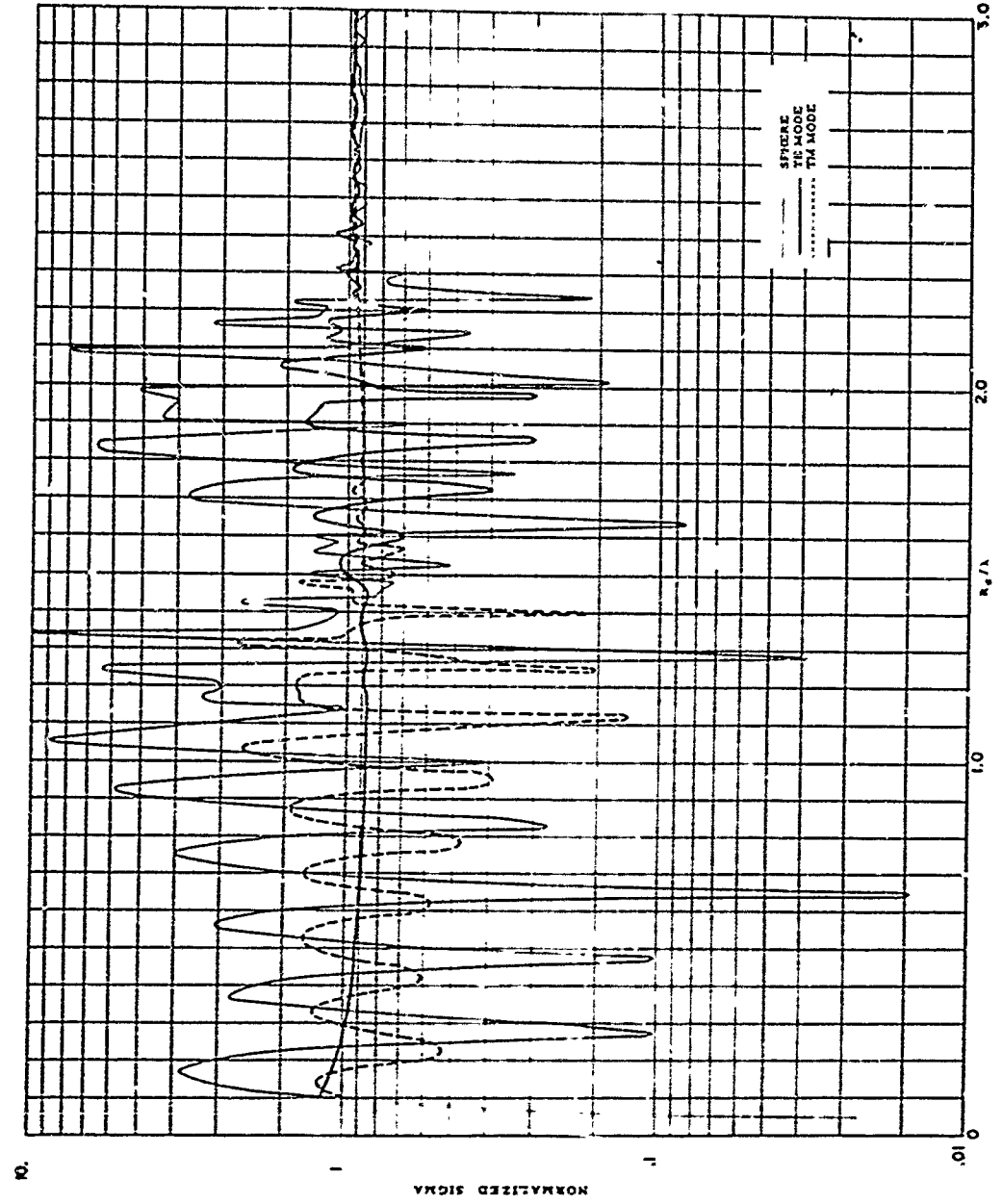
Figure 6. Dielectrically Clad Cylinder vs Dielectrically Clad Sphere. Normalized Sigma vs R_o/λ. $\Psi_o = 0°$, $\epsilon = 4.0$, $R_1 = 0.9R_o$, $R_o/\lambda = 0 \rightarrow 3.0$
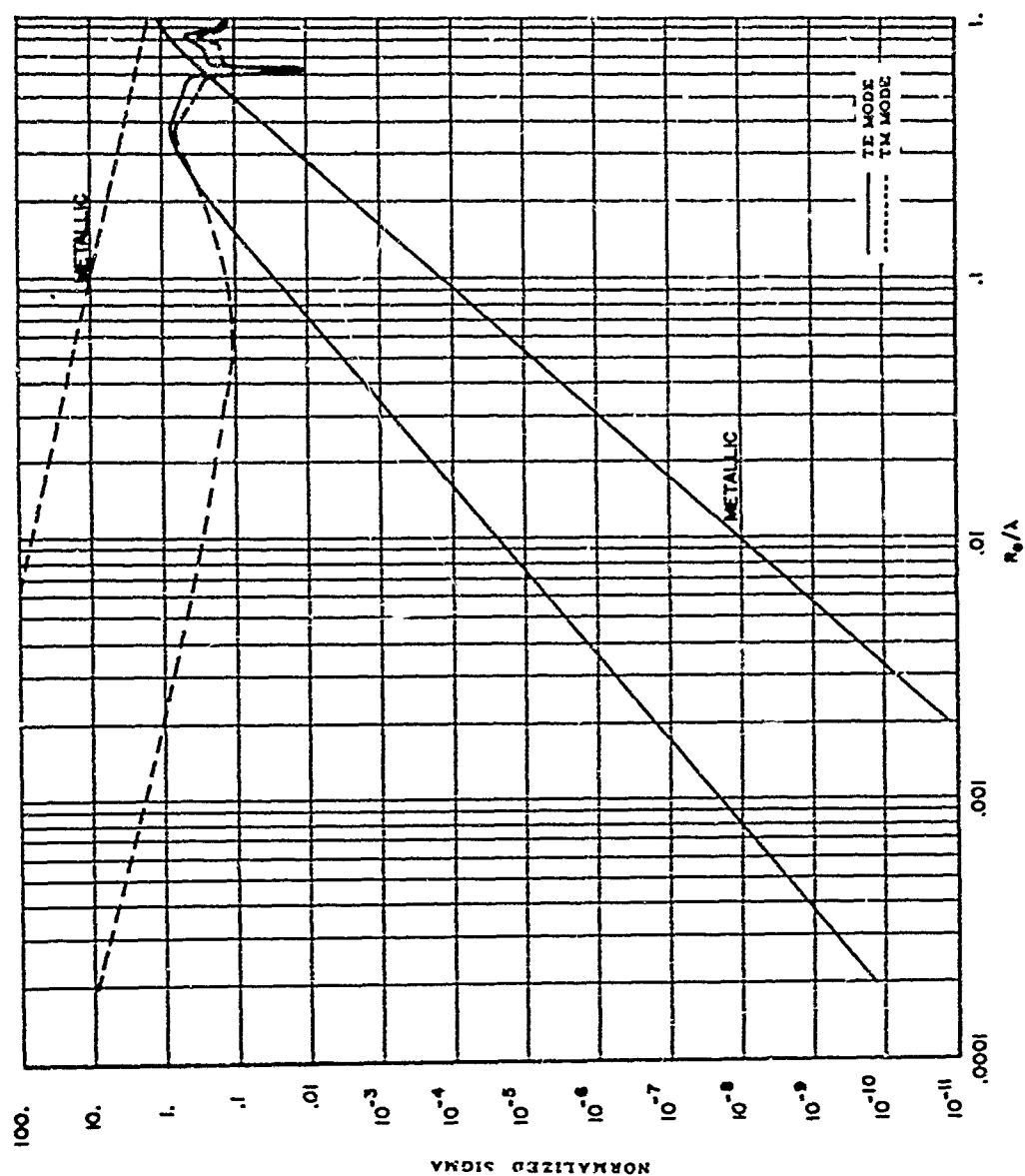
Figure 7. Dielectrically Clad Infinite Cylinder. Normalized Sigma vs R_o/λ, $\Psi_o = 84°$, $\epsilon = 4.0$, $R_1 = 0.9R_o$, $R_o/\lambda = 0.0002 \rightarrow 1.0$.

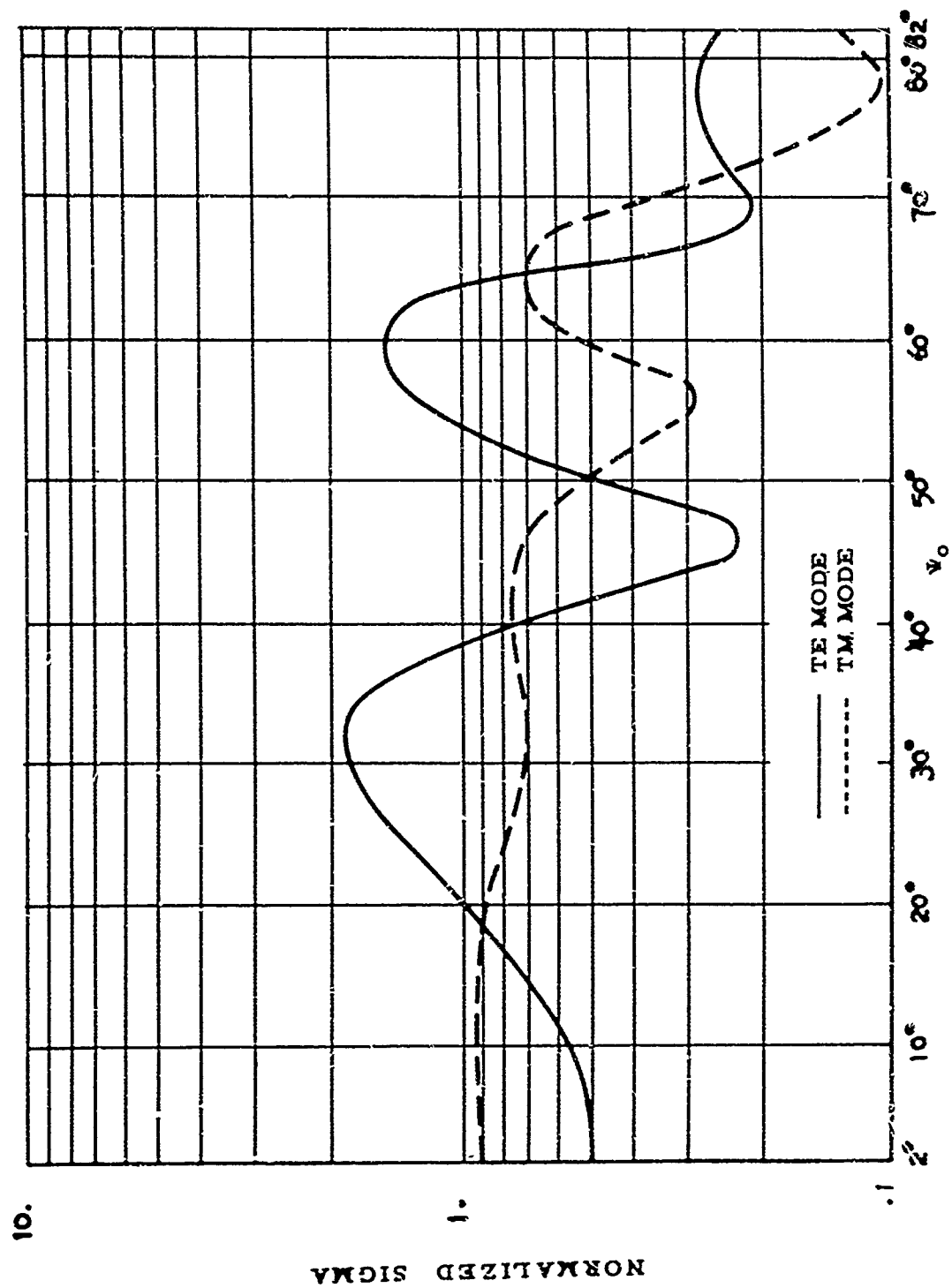Figure 8. Dielectrically Clad Infinite Cylinder. Normalized Sigma vs Angle of Incidence. $\epsilon = 4.0$, $R_1 = 0.9R_o$, $R_o = 0.78\lambda$
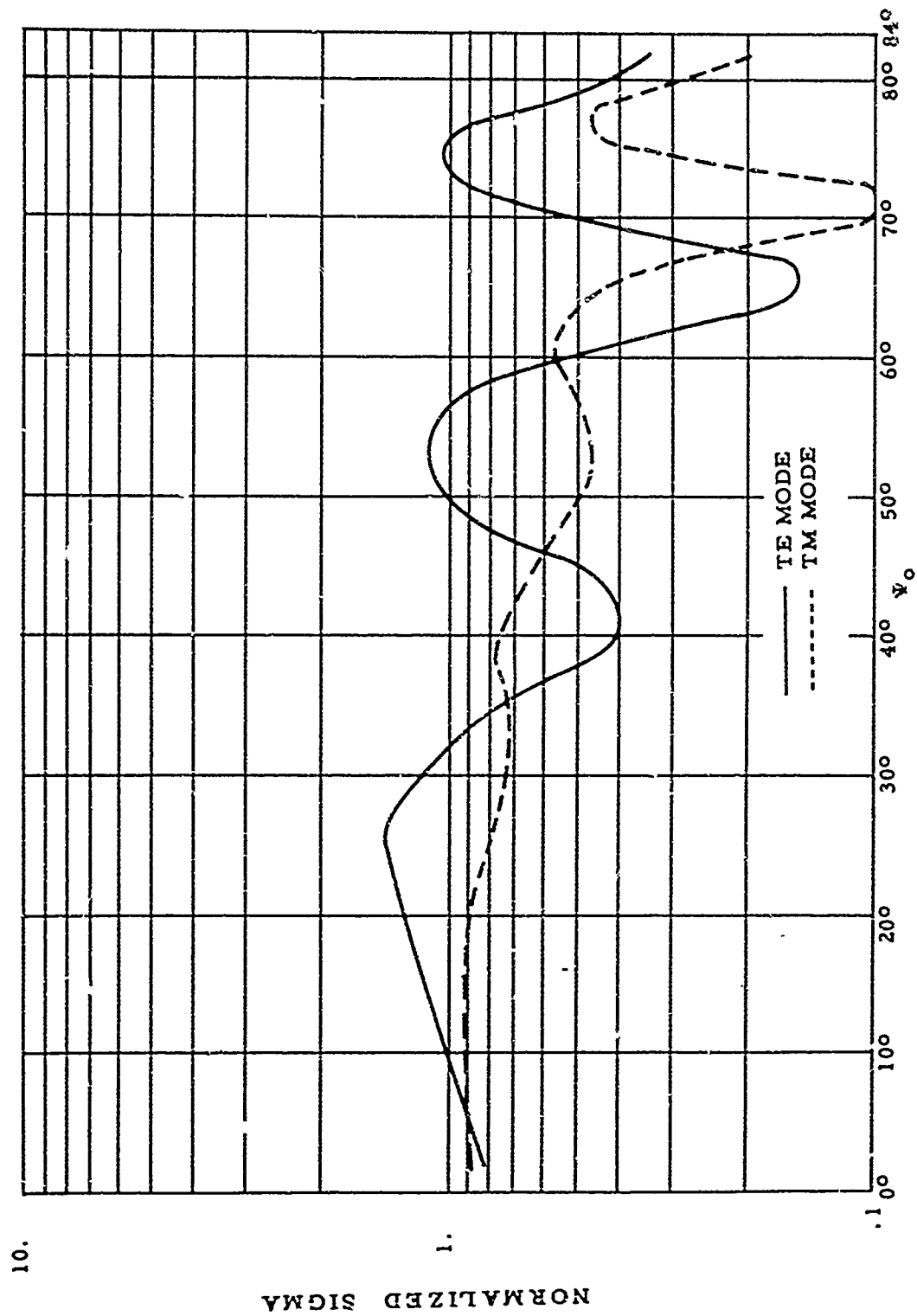
142

Figure 9. Dielectrically Clad Infinite Cylinder. Normalized Sigma vs angle of incidence. $\epsilon = 2.56$, $R_1 = 0.9 R_o$, $K_o = 0.78\lambda$
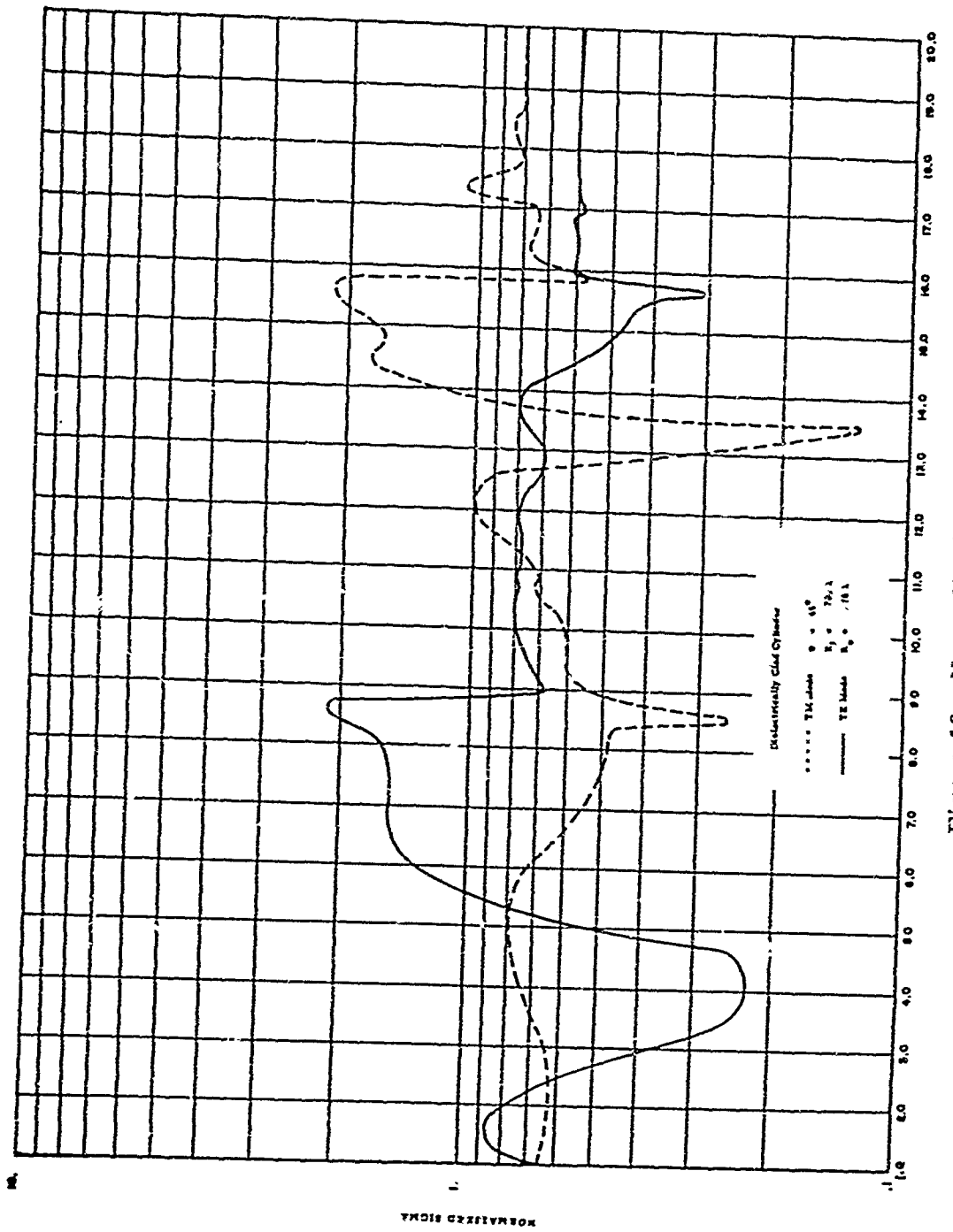
Figure 10. Normalized Sigma vs ϵ

References

1. W. Streifer and R. D. Kodis, On the Solution of a Transcendental Equation Arising in the Theory of Scattering by a Dielectric Cylinder, Brown University, Scientific Report 4561/17 under Contract AF19(604)-4561, June 1962.

2. R. D. Kodis, On the Theory of Diffraction by a Composite Cylinder, Brown University, Scientific Report AF-4561/15 under Contract AF19(604)-4561, December 1959.

3. R. D. Kodis, The Scattering Cross-Section of a Composite Cylinder, Brown University, Scientific Report AF-4561/15 under Contract AF19(604)-4561, December 1961.

4. C. W. Helstrom, Scattering of Electromagnetic Waves from Cylinders and Spheres Coated with a Dielectric Material, Westinghouse Research Laboratories, May 1961.

5. C W. Helstrom, Scattering from a Cylinder Coated with a Dielectric Material, Westinghouse Research Laboratories Scientific Paper 806-A800-PL, May 1961.

6. M. A. Plonus, Backscattering from a conducting cylinder with a surrounding shell, Canadian J. Phys. 38: 1665-1676, December 1960.

7. C. C.-H. Tang, Backscattering from Dielectric Coated Infinite Cylindrical Obstacles, 4 AD98809, Scientific Report No. 6 under Contract No. AF19(604)-786, Cruft Lab. Harvard, September 1956.

8   J. R. Wait, Electromagnetic Radiation from Sources on and near Cylindrical Surfaces, NBS Report 5553, January 1953.

XI. Effect of Surface Diffusivity Upon the Scattering Characteristics of a Plasma Sphere*

Philip J. Wyatt**

Plasmadyne Corporation

Abstract

The effect of varying the surface diffuseness of a spherical plasma region is examined in the resonance region. It is found that large changes in electron density may be readily compensated by modest changes in surface diffuseness as regards the scattering characteristics of such regions.

Since the re-entry characteristics of a great many objects often include large regions of highly ionized material, it is of particular interest to consider how slight structural modifications of these plasma volumes can appreciably affect the scattering of electromagnetic waves in the resonance region. For purposes of illustration, a hypothetical plasma will be examined whose structure is assumed to be spherically symmetric.[1] In this event, an earlier formalism developed by

!

** Now a member of the Technical Staff of the Defense Research Corporation, Santa Barbara, California.

the author[2] and others[3,4] will become immediately applicable as soon as an association between the conventional plasma variables and the so-called index of refraction is made.

For a plasma in local thermodynamic equilibrium, the electron density, N, and collision frequency, ν, are sufficient parameters to characterize its gross structural features. The minor contributions from the heavier ions are usually neglected in this approximation. The electron collision frequency itself is in general a rather complicated function of temperature and electron density.[5] Defining the plasma frequency, ω_p, by

$$\omega_p^2 = 4\pi \, Ne^2/m \, , \tag{1}$$

one may introduce the local dielectric constant

$$\epsilon = 1 - \frac{\omega_p^2}{\omega^2 + \nu^2} \left[1 - i \, \nu/\omega \right] \tag{2}$$

which depends upon the incident angular frequency ω as indicated. The electron charge and mass are indicated by e and m respectively.

If new the plasma frequency and collision frequency are functions of position, then ϵ also will be a function of position. The complex refractive index is given by the square root of ϵ and thus also varies with position. Since all variations are for the present example assumed radial, one has the situation described by Wyatt[2], namely a medium whose refractive index is a function of r only.

Consider now the following situation: Radiation of frequency $\omega/2\pi$ is incident upon a spherically symmetric plasma with a uniform interior. In terms of the vacuum wavelength, λ_{vac}, the dimensionless parameter $\rho = 2\pi r/\lambda_{vac}$ may be introduced. Thus

$$n(\rho) = \sqrt{\epsilon(\rho)} = \sqrt{1 - \omega_p(\rho)^2 \left[1 - i\nu(\rho)/\omega \right] / \left[\omega^2 + \nu(\rho)^2 \right]} \, . \tag{3}$$

For ρ less than some value a, say, both ω and ν are assumed constant and therefore one may write

$$n(\rho) = n_{OR} + in_{OI}, \quad o < \rho < a \, . \tag{4}$$

Surface diffusivity may now be introduced by letting $n(\rho)$ vary from the value given by Eq. (4) to the value 1.0 at some point b(> a), say, by letting

$$n(\rho) = n_R(\rho) + in_I(\rho), \quad a < \rho < b \tag{5}$$

$$n(\rho) = 1.0, \quad \rho > b$$

where $n_R(\rho)$ and $n_I(\rho)$ are real functions of ρ. This functional dependence of the complex refractive index may be deduced by assuming some realistic variation with ρ of ω_ρ and ν or, alternatively, by assuming a variation of $n(\rho)$ directly. Although either approach will yield a diffuse surface with similar characteristics, the latter assumption is more convenient for the present discussion.

In order that $n(\rho)$ and its first two derivatives be continuous throughout the entire range of interest, a convenient form factor of the Green-Wyatt type may be introduced as follows:

$$n(\rho) = n_R(\rho) + in_I(\rho)$$

where

$$n_R(\rho) = 1 + (n_{OR} - 1)\, \xi(\rho) \tag{6}$$

$$n_I(\rho) = n_{OI}\, \xi(\rho)$$

and the form factor $\xi(\rho)$ is given by

$$\xi(\rho) = 1, \quad o < \rho < a$$

$$= \frac{1}{2} - 15Z/16 + 10Z^3/16 - 3Z^5/16, \quad a < \rho < b \tag{7}$$

$$= 0, \quad \rho > b$$

$$Z = \left[\rho - \frac{1}{2}(b+a) \, / \, \frac{1}{2}(b-a) \right].$$

The parameters a and b may be related to the half fall-off distance $\rho_o \, (= 2\pi r_o / \lambda_{vac} = k r_o)$ and the surface thickness T (diffuseness), if one defines the term "thickness" to mean the 0.9 to 0.1 fall-off distance. Thus for the form chosen in Eq. (7)

$$a = \rho_o - 0.99868T \tag{8}$$

$$b = \rho_o + 0.99868T.$$

The variables of interest are illustrated in Figure 1 for the case where $n_{OR} = 1.67$ and $n_{OI} = 0.734$.

148
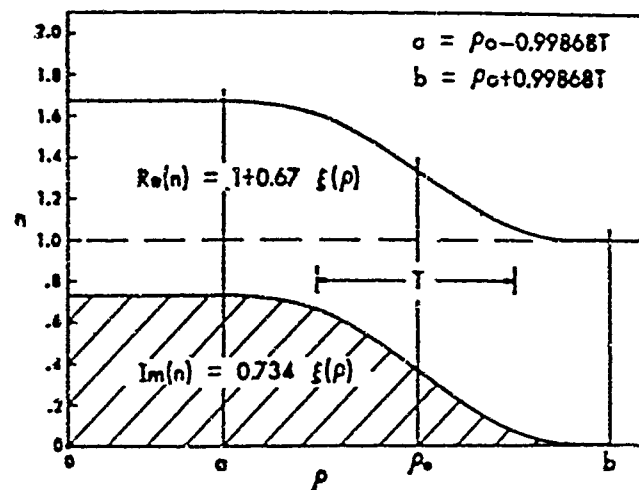
Figure 1. The complex index of refraction for an object
with a diffuse surface. The form factor is of the Green-
Wyatt type and the radial variation is in units of $1/k_{vac}$;
i.e., $\rho = k_{vac}\,\tau$

For the present example the incident frequency has been fixed at 3kMc,
$\nu = 10^{10}\,sec^{-1}$, and $\rho_0 = 5$. Thus the problem concerns an S-band measurement
of a plasma whose mean radius is about 8 cm.

Consider first the effect upon the radar cross section of such a region when
the surface thickness is varied. The curves shown in Figure 2 illustrate this
result for a variety of values of $\omega_\rho (\sim N^{1/2})$ at the uniform interior region of the
plasma scatterer. Rather than express the results in terms of the radar cross
section, the abscissa refers to the backscattered intensity in units of $(kr)^{-2}$
normalized to unit incident flux.

Figure 2. The differential scattered intensity of unpolarized radiation in units of
$(kr)^{-2}$ at 180° shown for various surface thicknesses as a function of plasma fre-
quency ($\rho_0 = 5$, $\omega = 6\pi \times 10^9\,sec^{-1}$, $\nu = 10^{10}\,sec^{-1}$)

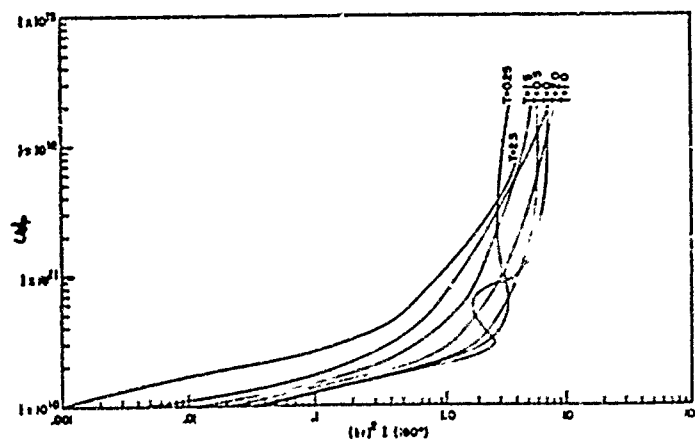Several important results are clearly illustrated by Figure 2. At the smaller electron densities, that is, when the interior plasma frequency is less than the incident angular frequency, small variations in surface thickness cause appreciable variations in the backscattered intensity. This would be expected in general since an increased surface diffuseness usually results in a diminished reflection. This trend is continued throughout the region where the plasma frequency is comparable to the incident angular frequency, except for the particularly sharp surfaces. For these latter exceptions, the reflection coefficients are critically affected for even slight variations in the surface region and thus produce the resonance type phenomena illustrated. It is interesting to note that from a given measurement of backscattered intensity, it is in general impossible to deduce anything concerning the structure of the scatterer. This result is vividly illustrated in Figure 2 since a given backscatter may be produced from an infinite variety of ω_p and T combinations.

Not only is the radar cross section appreciably affected by variations in surface diffuseness, but the scattering at all other angles as well. Assuming for the moment that the source of radiation is unpolarized,[*] then Figures 3 and 4 illustrate the differential scattered intensities for various interior plasma frequencies at two distinct surface thicknesses (0.0 and 1.0, respectively). Thus for the case of larger surface thickness, the scattering characteristics at a particular angle behave in an essentially monotonic manner. For the sharp surface (Figure 3) on the other hand, this simple behavior is no observed. Indeed, the sharp-surfaced structure may be said to have a high Q (at a variety of dielectric constants) which is easily "spoiled", thus resulting in the resonance behavior illustrated. The diffuse structure may be said to always have a poor Q.

If the interior plasma frequency is fixed, then the diffusivity effects upon the differential scattered intensity may be examined directly. Figure 5 illustrates this situation for $\omega_p = 10^{11} \sec^{-1}$. Note the general shifting of the diffraction pattern toward smaller angles with increasing surface diffuseness. For ω_p less than this value a significant drop in the backscattered intensity is also observed.

The above example illustrates that marked variations in the scattering characteristics of plasma volumes may in general be expected subsequent to small variations in surface diffusivity. In addition, large changes in ionization density may be easily "disguised," insofar as conventional radar measurements are concerned, by relatively small changes in surface diffuseness. Applied to larger systems at other frequencies, the above indicated results could have interesting practical applications.

---

[*]Although this is completely unrealistic insofar as microwave sources are concerned, this assumption permits an average differential scattering pattern to be presented. As was so vividly brought out at the Symposium, it is not enough to be just concerned with the effects upon the scattering of certain modifications or loading techniques for a given polarization of the incident radiation. The effects upon two mutually perpendicular polarizations must always be considered simultaneously. Thus, the assumption of an unpolarized source (which, incidentally, renders the computations somewhat more difficult) results in a clear picture of the net effects.
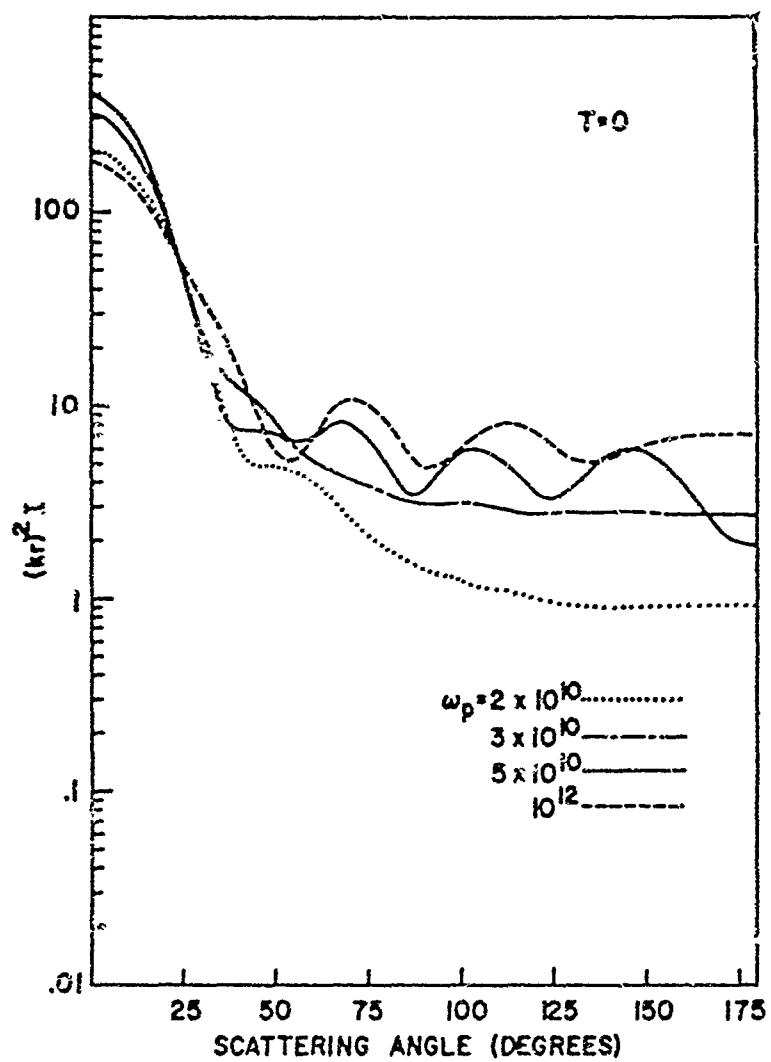
Figure 3. The Variation of the Differential Scattered Intensity in Units of $(kr)^{-2}$ of Unpolarized Radiation as a Function of Plasma Frequency for $T = O(\rho_o = 5$, $\omega = 6\pi \times 10^9 \text{ sec}^{-1}$, $\nu = 10^{10} \text{ sec}^{-1})$
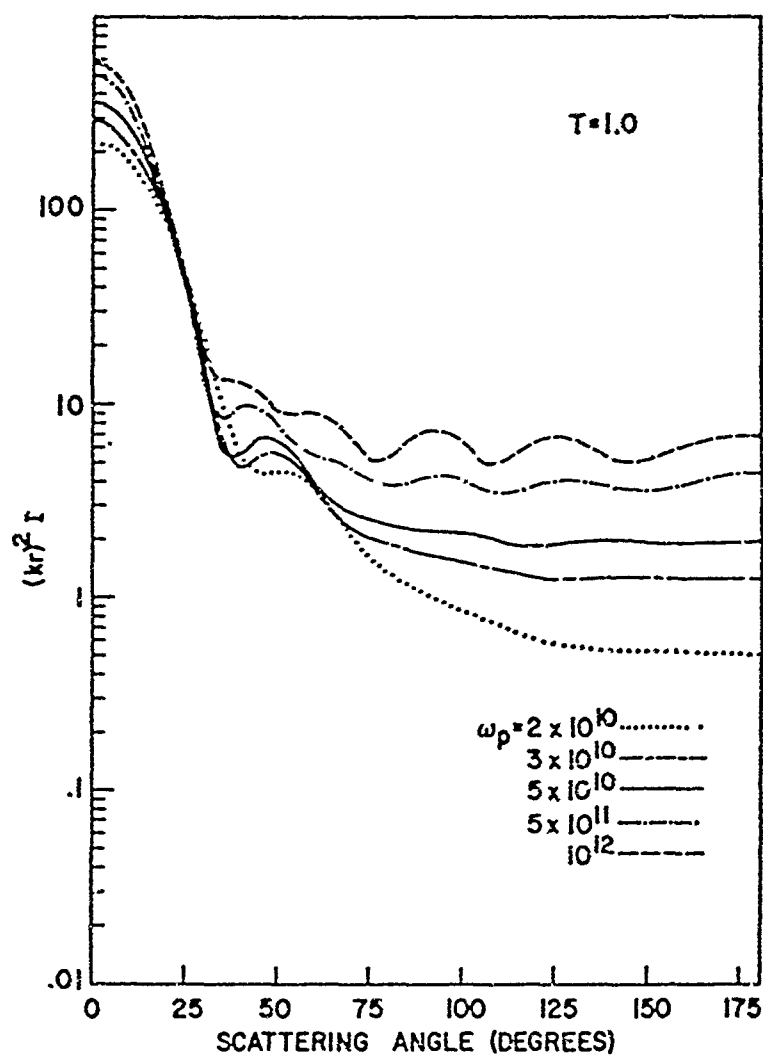
Figure 4. The Variation of the Differential Scattered Intensity in Units of $(kr)^{-2}$ of Unpolarized Radiation as a Function of Plasma Frequency for $T = 1.0 (\rho_o = 5$, $\omega = 6\pi \times 10^9 \text{ sec}^{-1}$, $\nu = 10^{10} \text{ sec}^{-1}$)

152
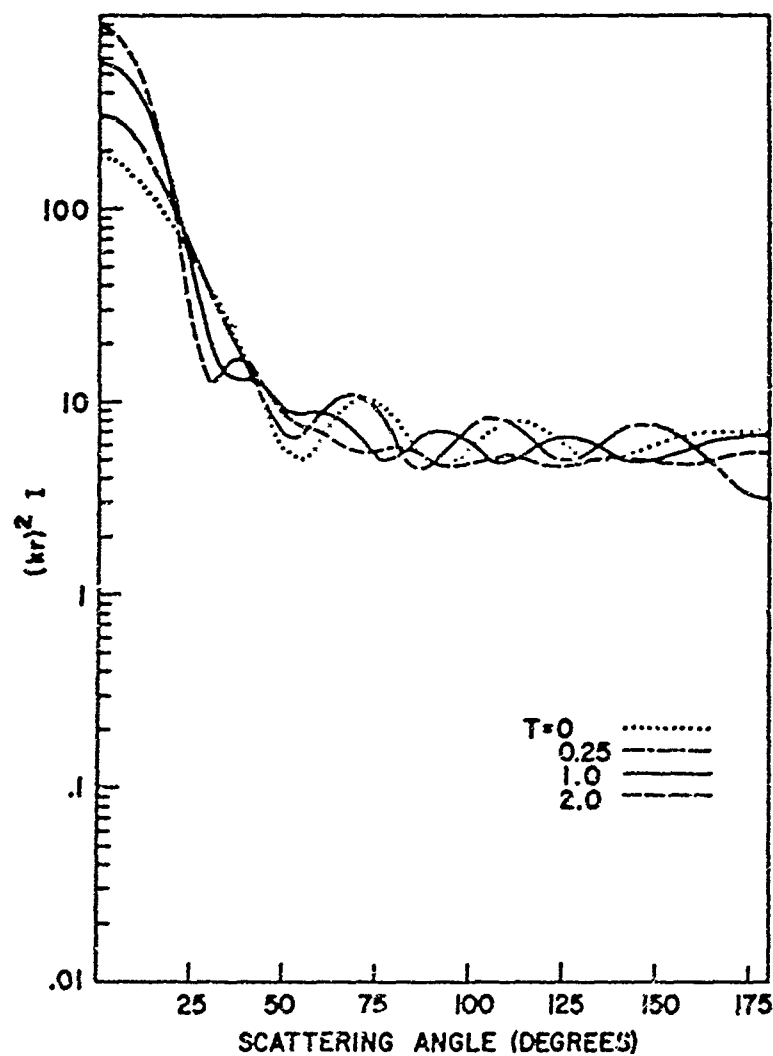
Figure 5. The Variation of the Differential Scattered Intensity of Unpolarized Radiation in Units of $(kr)^{-2}$ with Changing Surface Thickness ($\rho_0 = 5$, $\omega = 6\pi \times 10^9$ sec^{-1}, $\nu = 10^{10}$ sec^{-1} and $\omega_p = 10^{11}$ sec^{-1})

Acknowledgment

It is a pleasure to acknowledge Dr. N. Petersen, earlier discussions with whom initiated some of the impetus for this study.

References

1. Personal communication with Dr. N. Petersen.

2. P. J. Wyatt, Phys. Rev. 127: 1837, 1962.

3. D. Arnush, Electromagnetic Scattering from a Dielectric with Spherical Symmetry, Space Technology Laboratories, Internal Research Note, June 1961.

4. R. J. Garbacz, Electromagnetic Scattering by Radially Inhomogeneous Spheres, Ohio State University Antenna Laboratory Report, Project No. 1670-5546, Ohio State University, Columbus, Ohio, 1962.

5. L. J. Spitzer, Jr., Physics of Fully Ionized Gases, Interscience Publishers, Inc., New York, 1956.

This Document Contains
Missing Page/s That Are
Unavailable In The
Original Document

OR are
Blank pgs.
that have
Been Removed

**BEST
AVAILABLE COPY**

XII. Absorption Resonance Effects in Plasma Spheres

N. Pedersen
Research Directorate
Research and Advanced Development Division
Avco Corporation
Wilmington, Massachusetts

L. Malmstrom
Department of Physics
Harvard University
Cambridge, Massachusetts

1. INTRODUCTION

It is the purpose of this paper to report on theoretical work dealing with the absorption of electromagnetic power by plasma spheres. The electromagnetic energy is propagated to the plasma sphere in the form of plane-wave radiation. The sphere is assumed to be homogeneous and to be surrounded by a medium whose refractive index is near unity. Under these conditions, Mie scattering theory may be used to compute the absorption cross section of the sphere as a function of its complex dielectric constant, its radius, and the frequency of the incident electromagnetic wave. In particular, the conditions for maximum power absorption efficiency will be discussed. It will be shown that strong absorption resonances are to be expected only for cases where the ratio of sphere radius to free space electromagnetic wavelength is less than unity. Consequently, models which assume infinite or semi-infinite media are not applicable and would not yield the absorption resonances that are predicted by the application of electromagn

scattering theory. On the other hand, treatments based on electrostatic or magnetostatic solutions of the wave equation will yield a discrete set of characteristic "resonance" conditions in the dielectric constant or in the permeability but will not lead to a determination of absorption cross section or to the conditions for absorption cross section maxima.

2. APPROACH

Since it is the objective of this work to optimize the efficiency for power absorption in dielectric spheres, the results of formal Mie theory are used to write down the exact expression for absorption cross section. It is first determinted that strong absorption resonances are to be expected only in the low frequency limit. A low frequency approximation is then applied which reduces the problem to that of optimizing the absorption cross section of lossy spheres having small radius to wavelength ratio. This is done by first determining the optimum values of the real and imaginary parts of the appropriate partial wave coefficient and then computing the maximum possible value for the power absorption efficiency as a function of ka, where $k = 2\pi/\lambda$ and a = sphere radius. Next, the optimum values of the real and imaginary parts of the dielectric constant are found as functions of ka by means of performing a power series expansion of the partial wave coefficient in terms of ka. In this step, the condition that $ka \ll 1$ is again used. Since the magnitude of the optimized absorption efficiency is proportional to $(ka)^{-2}$, and since the approximations used become increasingly accurate as ka decreases, this method should be quite valid in regions of very high absorption resonance.

Finally, the effect of an applied magnetic field is investigated and it is found that the existence of the magnetic field serves to decouple the parametric equations for absorption resonance.

3. RESULTS OF FORMAL MIE THEORY

The absorption efficiency factor Q_{abs} for a scatterer is defined as the ratio of its absorption cross section to its projected area. For a sphere this is $Q_{abs} = \sigma_{abs}/\pi a^2$, where σ_{abs} = absorption cross section and a = sphere radius. Likewise, the extinction and scattering efficiency factors are defined as $Q_{ext} = \sigma_{ext}/\pi a^2$ and $Q_{sca} = \sigma_{sca}/\pi a^2$. From conservation of energy, it follows that

$$Q_{abs} = Q_{ext} - Q_{sca}. \tag{1}$$

The extinction and scattering efficiency factors are usually given by the following series representations:

$$Q_{ext} = \frac{2}{x^2} \sum_{n=1}^{\infty} (2n+1) \, Re(a_n + b_n), \tag{2}$$

$$Q_{sca} = \frac{2}{x^2} \sum_{n=1}^{\infty} (2n+1) \left\{ |a_n|^2 + |b_n|^2 \right\}, \tag{3}$$

where $x = ka = 2\pi a/\lambda$, and a_n and b_n are, respectively, the coefficients for the n'th electric and magnetic partial waves. These can be shown to be the contributions due to the induced electric and magnetic dipole, quadrupole, and higher-order moments of the sphere. They may be written as follows:

$$a_n = \cfrac{1}{1 - i \left(\cfrac{n_n(x) \, [y \, j_n(y)]' - \epsilon \, j_n(y) \, [x \, n_n(x)]'}{j_n(x) \, [y \, j_n(y)]' - \epsilon \, j_n(y) \, [x \, j_n(x)]'} \right)}, \tag{4}$$

$$b_n = \cfrac{1}{1 - i \left(\cfrac{\epsilon \, n_n(x) \, [y \, j_n(y)]' - j_n(y) \, [x \, n_n(x)]'}{\epsilon \, j_n(x) \, [y \, j_n(y)]' - j_n(y) \, [x \, j_n(x)]'} \right)}, \tag{5}$$

where the $j_n(y)$ and $n_n(x)$ are spherical Bessel functions of the first and second kinds respectively, $x = ka$, $y = x\sqrt{\epsilon}$, and $\epsilon =$ complex dielectric constant. The prime in Eqs. (4) and (5) indicate derivatives with respect to the argument. Since the Bessel functions will in general be complex, the a_n and b_n will also in general be complex. Substituting Eqs. (2) and (3) into Eq. (1), we have

$$Q_{abs} = \frac{\sigma_{abs}}{\pi a^2} = \frac{2}{x^2} \sum_{n=1}^{\infty} (2n+1) \left\{ Re(a_n) - |a_n|^2 + Re(b_n) - |b_n|^2 \right\}. \tag{6}$$

Equation (6) indicates that it is reasonable to expect resonances in Q_{abs} when resonance exists for one or more of the partial wave coefficients. Such resonances can only occur for plasma-like media with $\epsilon' < 1$, as shown by approximations of the first few partial wave coefficients.

158

A computer code for the computation of the Q's has been developed by J. C. Pedersen of the Avco Corporation. Some results of this program have been checked against published* results of a similar program at RAND Corporation and good agreement was obtained for ka values as low as 0.2 (the lower limit on the published RAND results). Both programs were operable for dielectric constants having a negative real part as well as an imaginary part. Such cases represent plasma spheres. In the case of a plasma, the complex dielectric constant is given by

$$\epsilon = \epsilon' - i\epsilon'' = 1 - \frac{i\frac{n_e e^2}{\epsilon_o M_e}\frac{1}{\omega^2}}{\frac{\omega_g}{\omega} + i} , \tag{7}$$

where n_e = electron density, e = electronic charge, ω_g = electron collision frequency, and ϵ_o = permitivity of free space. It is convenient to define $\eta = (\omega_p/\omega)^2 = \frac{n_e e^2}{\epsilon_o M_e \omega^2}$ and $\gamma = (\omega_g/\omega)$, where ω_p is the plasma frequency. The real and imaginary parts of the dielectric constant are then given by

$$\epsilon' = \frac{1 + \gamma^2 - \eta}{1 + \gamma^2} \tag{8a}$$

$$\epsilon'' = \frac{\eta \gamma}{1 + \gamma^2} . \tag{8b}$$

Some general statements can be made about the limiting values of η and γ as related to absorption. First, it is obvious that no absorption can occur for $\epsilon'' = 0$. Thus, the cases of $\eta = 0$ (no electrons) or $\gamma = 0$ (no collisions) will yield $Q_{abs} = 0$. The case of $\eta = \infty$ with γ finite represents a perfect conductor (imaginary refractive index). No absorption can occur in this case. Finally, for $\gamma = \infty$ and η finite, we have $\epsilon'' = 0$ and again no absorption can occur. It has therefore been shown that any resonances in the absorption cross section will occur for finite values of both η and γ.

A number of sets of computer runs were made for plasma-like spheres, and the results are shown in Figures 1 through 5. Each set of curves is a plot of Q_{abs} vs γ for a particular fixed value of ka, with η the running parameter. The maximum value of Q_{abs} for a given ka is seen to be characterized by a discrete value

*D. Deirmendjian and R. J. Clasen, Light Scattering on Partially Absorbing Homogeneous Spheres of Finite Size, RAND Report R-393-PR, Feb. 1962.
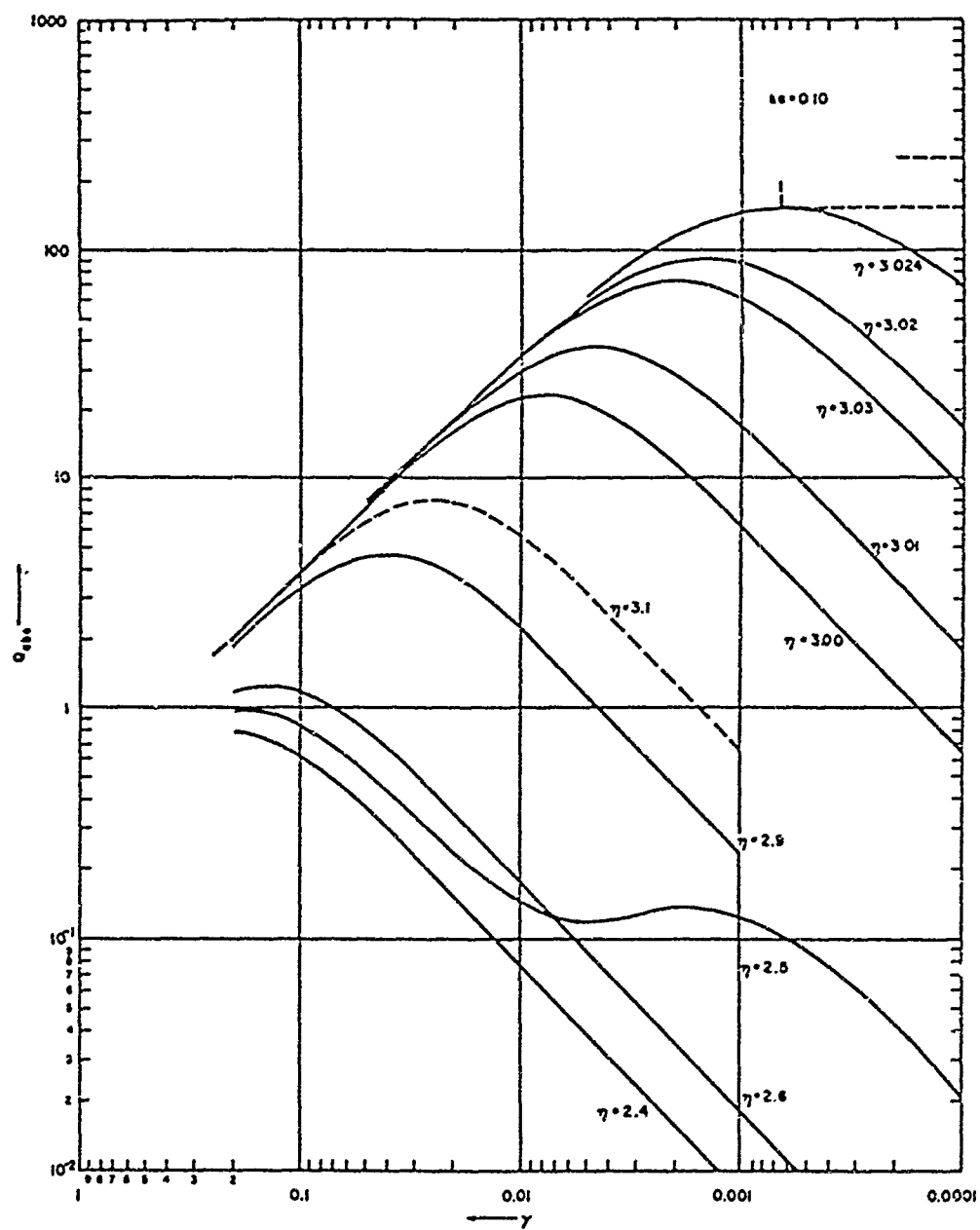
Figure 1. Q_{abs} as a Function of η and γ for $ka = 0.10$
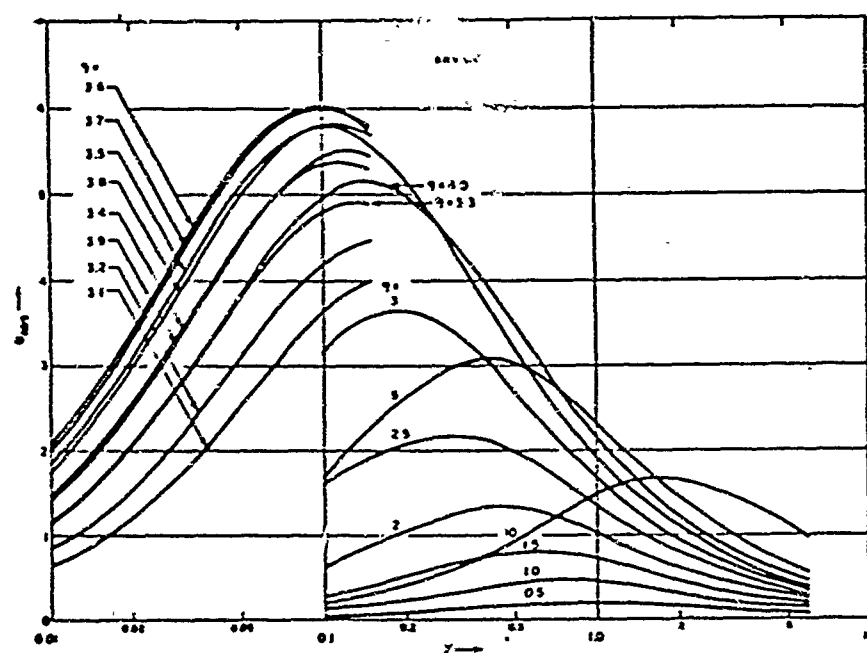
Figure 2. Q_{abs} as a Function of η and γ for ka = 0.5
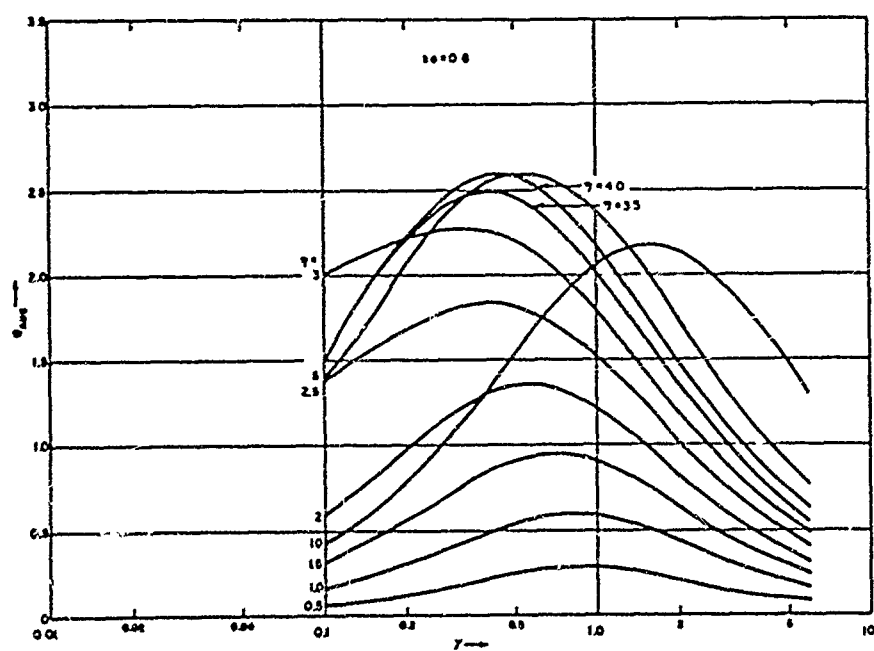
Figure 3. Q_{abs} as a Function of η and γ for ka = 0.8
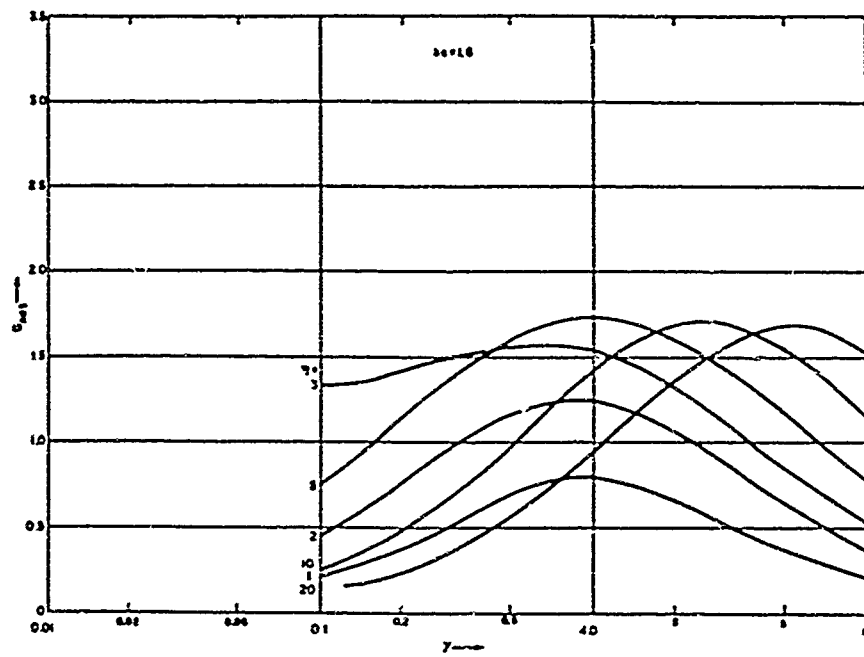
Figure 4. Q_{abs} as a Function of η and γ for ka = 1.6
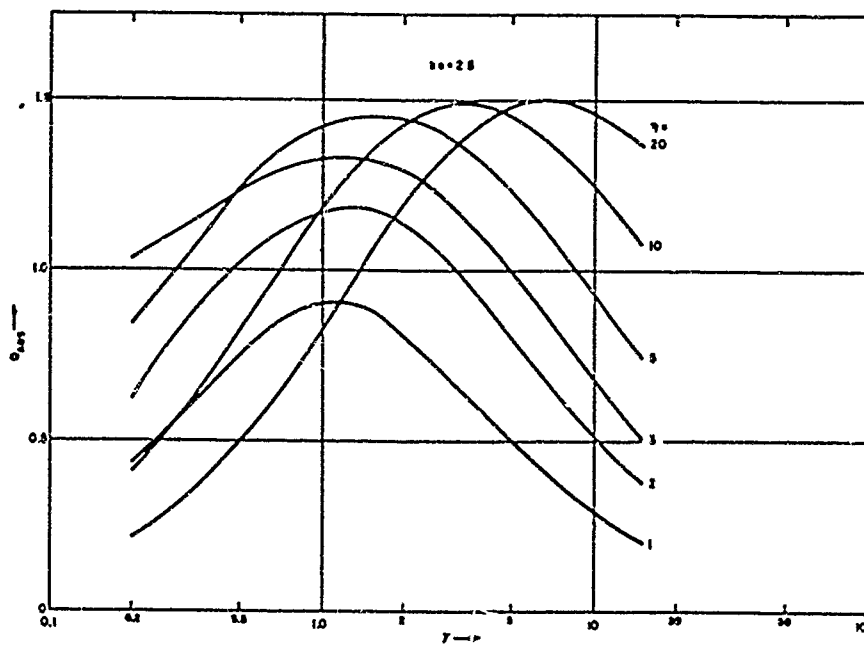
Figure 5. Q_{abs} as a Function of η and γ for ka = 2.5

of η and a discrete value of γ. Thus, for a given ka, this set of values of η and γ represents the resonance condition for Q_{abs}. Of particular interest in these results is the fact that the maximum value of Q_{abs}, which we define as $Q_{abs}(max)$, increases strongly with decreasing ka. The various $Q_{abs}(max)$ in Figures 1 to 5 have been identified with resonances in a_1, the electric dipole partial wave coefficient. For ka values below 0.4, only the a_1 coefficient need be considered. Although resonances due to the higher order a_n coefficients have been observed in some computer runs, these are very much sharper than those due to the electric dipole term and arise from values of γ which are too small to be of practical interest. Since the magnetic permeability was set equal to μ_0, no magnetic resonances were expected in these runs, nor were they found. Resonances due to the b_n can occur only in the case of negative permeability and were therefore not investigated.

4. APPROXIMATIONS TO MIE THEORY

Since small ka implies large $Q_{abs}(max)$, and since it has been demonstrated that the use of a_1 alone will suffice under these conditions, it is next meaningful to make two approximations.

(a) Assume that Q_{abs} results from only the electric dipole term a_1. Find $Q_{abs}(max)$ as a function of ka. In doing this, it will be necessary to find the optimum values of the real and imaginary parts of a_1 for the occurrence of $Q_{abs}(max)$.

(b) Write a_1 as a power series expansion in ka and make the appropriate approximation for ka $\ll 1$. Separate the approximate expression of a_1 into its real and imaginary parts. The optimum value of these, found from (a) above, will then be used to arrive at two equations which define the necessary values of ϵ' and ϵ'' as a function of ka for the occurrence of $Q_{abs}(max)$. Finally, Eq. (8) will be used to obtain a set of equations in η and γ giving the resonance values of these as functions of ka.

For the determination of $Q_{abs}(max)$, assuming a particular a_n to be the only contributor, Eq. (6) reduces to

$$Q_{abs} = \frac{2}{x^2}(2n+1)\left[R_e(a_n) - |a_n|^2 + R_e(b_n) - |b_n|^2\right]. \tag{9}$$

If we now let $a_n = (c+id)^{-1}$, we obtain

$$Q_{abs} = \frac{2}{x^2} (2n+1) \left[\frac{c-1}{c^2+d^2} \right] \tag{10}$$

To find $Q_{abs} = Q_{abs}(max)$, we must have

$$\frac{\partial}{\partial c} \left[\frac{c-1}{c^2+d^2} \right] = \frac{\partial}{\partial d} \left[\frac{c-1}{c^2+d^2} \right] = 0. \tag{11}$$

$$Q_{abs}(max) = \frac{(2n+1)}{2x^2}, \tag{12}$$

or

$$Q_{abs}(max) = \frac{3}{2x^2} \quad \text{(electric dipole resonance)}. \tag{13}$$

Exact machine calculations verify Eq. (13) for values of x below 0.5.

The next step is to calculate the optimum properties of the medium as functions of x. It will be most convenient to first find the absorption resonance conditions: $\epsilon' = f_1(x)$ and $\epsilon'' = g_1(x)$. Equation (8) will then be used to find $\eta = f_2(x)$ and $\gamma = g_2(x)$. For this purpose, it is convenient to write a_1 as a power series expansion in x and to then make a low frequency approximation, making sure that sufficient terms are kept in the denominators to prevent the occurrence of infinities which would otherwise result. Due to the algebraic complexity of this operation, the series expansion for the general a_n term is given in the Appendix. The result is given by Eq. (A-12). Since Eq. (11) led to the result $a = (2+i0)^{-1}$ for $Q_{abs} = Q_{abs}(max)$, we obtain the absorption resonance conditions by equating the real and imaginary parts of the denominator of Eq. (A-12) to 2 and 0 respectively, which yields Eqs. (A-13) and (A-14). We now let $x \ll 1$. The zero'th order approximation of the absorption resonance conditions in Eqs. (13) and (14) is $\alpha = -\frac{n+1}{n}$, $\beta = 0$. This is obviously not of sufficiently high order in x since the x dependence on ϵ' and ϵ'' does not appear. In addition, this result gives zero collision frequency. The next higher-order approximation gives

$$\beta = \frac{(n+1)(2n+1)}{\left[(2n+1)!!\right]^2 (n+1)n^2} x^{2n+1}, \tag{14}$$

$$\alpha = -\frac{n+1}{n} \left[1 + x^2 \frac{2(2n+1)}{n(2n-1)(2n+3)} \right]. \tag{15}$$

In the case of electric dipole resonance (n = 1), we have the resonance conditions:

$$\beta = 2x^3 \tag{16}$$

$$\alpha = -\left[2 + \frac{12}{5}x^2\right]. \tag{17}$$

Substituting Eqs. (16) and (17) into Eqs. (8a) and (8b), we finally get

$$\gamma = \frac{\omega_g}{\omega} = \frac{2}{3}x^3, \tag{18}$$

$$\eta = \frac{\omega_p^2}{\omega^2} = 3 + \frac{12}{5}x^2. \tag{19}$$

Equations (16) and (17) constitute the necessary conditions for electric dipole resonance in the absorption efficiency factor for homogeneous plasma spheres having small radius-to-wavelength ratios. Since Eq. (13) shows that x must be small in order for large absorption efficiencies to occur, Eqs. (18) and (19) are useful in the region of interest.

5. DISCUSSION

It was demonstrated in the last section that large absorption resonances can occur in plasma spheres (Eq. 13). The conditions for electric dipole absorption resonance (Eqs. 18 and 19) show that in the region of strong resonance (small x), the value of η goes to a constant value of 3, while γ is proportional to x^3. Thus, the ratio of plasma frequency ω_p to collision frequency ω_g is proportional to x^{-3}. Thus, for Q_{abs} = 150 (Eq. 13), we would require $\omega_p/\omega_g = \sqrt{\eta}/\gamma \cong 2600$. As x is further decreased, this ratio will greatly increase. It is probably this fact more than any other which will limit the highest physically realizable values of Q_{abs}. Another consideration is the mean free path of electrons within the plasma sphere. This distance is really the mean distance a "hot" electron must travel in order for it to equilibrate with the surrounding ion-neutral atom medium. Obviously, the sphere radius should not be smaller than the mean free path. On the other hand, the radial homogeniety of the plasma sphere is not believed to be too important in this case. The reason is that, since a/λ is small, the wave will "see" a sphere with some effective dielectric constant and some effective radius. These assumptions have been at least partially confirmed by Dr. P. Wyatt* , Defense Research Corporation.

---

*Private communication.

The only real way to predict the degree of physical realizability of this absorption resonance phenomenon is to combine the electro-magnetic resonance conditions (Eqs. 18 and 19) with appropriate physical expressions for the equation of state and the collision frequency, and to derive a set of equivalent thermodynamic resonance conditions. A preliminary calculation of this nature was performed by one of the writers (N. P.) who used the weakly ionized approximation of the Saha equation. Difficulties were encountered in that, in the region of interest (small x), the assumption of weak ionization was not valid. Mr. J. Davis of the Avco Corporation is presently extending this work to include strong ionization. These results, when they are available, will be investigated for violations of the assumption of equilibrium, etc. If the assumptions implicit in the calculation prove to be valid in the resonance region, we will conclude that this is the proper thermodynamic model. If not, we will proceed to the more complicated non-equilibrium case. Present indications are that this may be necessary.

One of the writers (N. P.) has done some preliminary work on the effects of a strong magnetic field on the absorption resonance conditions. The anticipated results are:

$$\frac{\omega_p^2}{\omega_\beta^2} \cong 3 + \frac{12}{5} x^2, \tag{20}$$

$$\frac{\omega_g}{\omega} = \frac{2}{3} x^3, \tag{21}$$

where

$$\omega_\beta = -\frac{e\beta}{m_e} \doteq \text{electron cyclotron frequency.}$$

Although Eqs. (21) and (18) are identical, Eqs. (20) and (19) differ in that ω_β replaces ω in Eq. (19). Thus, the application of a strong $(\omega_\beta >> \omega)$ magnetic field serves to decouple the resonance conditions, and leads to an extra degree of freedom in physically realizing strong absorption resonances. If severe limitations should be shown as a result of the zero magnetic field calculations, the strong field case will be investigated in detail regarding its relaxation of thermodynamic requirements.

When the correct thermodynamic description of the plasma has been found, the power input and the power output will both be written in analytic form. Thus, an analytic equation for steady state can be written. This equation will be set up and the required incident electric field strength will be computed. A more interesting study will be an examination of the steady state equation for stability. Is the

166

plasma sphere, under the (initial) steady state conditions stable against fluctuations of the thermodynamic parameters? This question will hopefully be answered when the thermodynamic resonance conditions are expressed in analytic form.

Acknowledgments

Upon expressing the N_n and j_n in Equation (A-4) as power series in x and/or y, a_n can be expressed as a power series expansion:

$$a_n = \frac{\left[(n+1)(1-\epsilon)\dfrac{y^n}{(2n+1)!!}\left(1-\dfrac{y^2}{2(2n+3)}+\cdots\right) - \dfrac{y^{n+2}}{(2n+3)!!}\left(1-\dfrac{y^2}{2(2n+5)}+\cdots\right)\right]\left[\dfrac{-(2n-1)!!}{x^{n+1}}\right]\left[1+\dfrac{x^2}{2(2n-1)}+\cdots\right]}{\left[+\epsilon\dfrac{y^n}{(2n+1)!!}\left(1-\dfrac{y^2}{2(2n+3)}+\cdots\right)\right]\left[\dfrac{-(2n+1)!!}{x^{n+2}}\right]\left[1+\dfrac{x^2}{2(2n+1)}+\cdots\right]}$$

$$- i \frac{\left[(n+1)(1-\epsilon)\dfrac{y^n}{(2n+1)!!}\left(1-\dfrac{y^2}{2(2n+5)}+\cdots\right) - \dfrac{y^{n+2}}{(2n+3)!!}\left(1-\dfrac{y^2}{2(2n+5)}+\cdots\right)\right]\left[\dfrac{x^{n-1}}{(2n+3)!!}\right]\left[1-\dfrac{x^2}{2(2n+5)}+\cdots\right]}{\left[+\epsilon\dfrac{y^n}{(2n+1)!!}\left(1-\dfrac{y^2}{2(2n+3)}+\cdots\right)\right]\left[\dfrac{x^n}{(2n+1)!!}\right]\left[1-\dfrac{x^2}{2(2n+3)}+\cdots\right]} \tag{A-1}$$

$$a_n = \frac{\left[(n+1)(1-\epsilon)\left(1-\dfrac{y^2}{2(2n+3)}+\cdots\right) - \dfrac{y^2}{2n+3}\left(1-\dfrac{y^2}{2(2n+5)}+\cdots\right)\right]\left[1+\dfrac{x^2}{2(2n-1)}+\cdots\right]}{\left[+\epsilon(2n+1)\left(1-\dfrac{y^2}{2(2n+3)}+\cdots\right)\right]\left[1+\dfrac{x^2}{2(2n+1)}+\cdots\right]}$$

$$- i \frac{\left[(n+1)(1-\epsilon)\left(1-\dfrac{y^2}{2(2n+5)}+\cdots\right) - \dfrac{y^2}{2n+3}\left(1-\dfrac{y^2}{2(2n+3)}+\cdots\right)\right]\left[1-\dfrac{x^2}{2(2n+5)}+\cdots\right]}{\left[+\dfrac{\epsilon x^2}{(2n+3)}\left(1-\dfrac{y^2}{2(2n+3)}+\cdots\right)\right]\dfrac{(2n-1)!!(2n+1)!!}{x^{2n+1}}} \tag{A-2}$$

$$a_n = \frac{1}{1 - i\frac{(2n-1)!!(2n+1)!!}{z^{2n+1}}} \left\{ \left[(n+1)(1-c) - z^2 c \left(\frac{(n+1)(1-c)}{2(2n+3)} + \frac{1}{(2n+3)} \right) \cdots \right] \left[1 + \frac{z^2}{2(2n-1)} \cdots \right] \right.$$
$$\left. + c(2n+1) \left[1 - \frac{cz^2}{2(2n+3)} \cdots \right] \left[1 + \frac{z^2}{2(2n+1)} \cdots \right] \right.$$
$$\left. + (n+1)(1-c) - z^2 c \left(\frac{(m+1)(1-c)}{2(2n+3)} + \frac{1}{(2n+3)} \right) \cdots \right] \left[1 - \frac{z^2}{2(2n+3)} \cdots \right]$$
$$\left. + \frac{cz^2}{(2n+3)} \left[1 - \frac{z^2}{2(2n+3)} \cdots \right] \right\}$$

(A-3)

$$a_n = \frac{1}{1 - i\frac{(2n-1)!!(2n+1)!!}{z^{2n+1}}} \left\{ \left[(n+1)(1-c) + c(2n+1) + z^2 \left[\frac{(n+1)(1-c)}{2(2n-1)} - c \left(\frac{(n+1)(1-c)}{2(2n+3)} + \frac{1}{(2n+3)} \right) + \frac{(2n+1)c}{2(2n+1)} - \frac{(2n+1)cz^2}{2(2n+3)} \right] + \cdots \right. \right.$$
$$\left. \left. + (n+1)(1-c) - z^2 \left[\frac{(n+1)(1-c)}{2(2n+3)} + \frac{1}{(2n+3)} - \frac{1}{(2n+3)} \right] + \cdots \right] \right\}$$

(A-4)

$$a_n = \cfrac{1}{1 - i\,\cfrac{(2n-1)!!\,(2n+1)!!}{(n+1)(1-\epsilon)\,z^{2n+1}}\left[n\epsilon + (n+1)\right] + z^2\left[\cfrac{(n+1)(1-\epsilon)(2n+3)-\epsilon(2n-1)-\epsilon(2n-1)(2n+3)2+(2n-1)(2n+3)\epsilon-(2n+1)(2n+3)\epsilon^2}{2(2n-1)(2n+3)} - z^2\left[\cfrac{(1+\epsilon)}{2(2n-3)}\right] + \cdots\right]} \tag{A-5}$$

$$a_n = \cfrac{1}{1 - i\,\cfrac{(2n-1)!!\,(2n+1)!!}{(n+1)(1-\epsilon)\,z^{2n+1}}\left[n\epsilon + (n+1)\right] + z^2\left[\cfrac{(n+1)(2n+3)-3\epsilon(2n+1)-\epsilon^2 n(2n-1)}{2(2n-1)(2n+3)} - z^2\left[\cfrac{(1+\epsilon)}{2(2n+3)}\right] + \cdots\right]} \tag{A-6}$$

$$a_n = \cfrac{1}{1 - i\,\cfrac{(2n-1)!!\,(2n+1)!!}{(n+1)(1-\epsilon)\,z^{2n+1}}\left[n\epsilon + (n+1)\right] + z^2\left[\cfrac{(n+1)(2n+3)-3\epsilon(2n+1)-\epsilon^2 n(2n-1)}{2(2n-1)(2n+3)} \cdots \left\{1 + z^2\left[\cfrac{1+\epsilon}{2(2n+3)}\right] \cdots\right\}\right]} \tag{A-7}$$

$$a_n = 1 - i\,\frac{(2a-1)!!\,(2a+1)!!}{(a+1)(1-\epsilon)\epsilon^{2a+1}}\left\{[\,a\epsilon+(a+1)]+\epsilon^2\left[\frac{(a+1)(2a+3)-3\epsilon(2a+1)-\epsilon^2 a(2a-1)}{2(2a-1)(2a+3)}+\frac{(1+\epsilon)(a\epsilon+a+1)}{2(2a+3)}\right]+\cdots\right\} \qquad (A-8)$$

$$a_n = 1 - i\,\frac{(2a-1)!!\,(2a+1)!!}{(a+1)(1-\epsilon)\epsilon^{2a+1}}\left\{[\,a\epsilon+(a+1)]+\epsilon^2\left[\frac{(a+1)(2a+3)+2a-1)+\epsilon(2a+1)(2a-1-3)+\epsilon^2(2a-1)(-a+a)}{2(2a-1)(2a+3)}\right]+\cdots\right\} \qquad (A-9)$$

$$a_n = 1 - i\,\frac{(2a-1)!!\,(2a+1)!!}{(a+1)(1-\epsilon)\epsilon^{2a+1}}\left\{[\,a\epsilon+(a+1)]+\epsilon^2\left[\frac{(2a+1)\,(a\epsilon+1)+(a-2)\epsilon}{(2a-1)(2a+3)}\right]+\cdots\right\} \qquad -(A-10)$$

Noting that $\varepsilon = \varepsilon' + i\varepsilon'' = \alpha + i\beta$

$$a_n = \cfrac{-\cfrac{(2n-1)!!\,(2n+1)!!}{(n+1)\,x^{2n+1}}}{1-i\,\eta\left[aa+n+1+x^2\,\dfrac{(2n+1)\left((n+1)+(n-2)\alpha\right)}{(2n-1)(2n+3)}\cdots\right]+i\eta\left[n+x^2\,\dfrac{(2n+1)(n-2)}{(2n-1)(2n+3)}\cdots\right]}\left\{\left\{\dfrac{(1-\alpha)+i\beta}{(1-\alpha)^2+\beta^2}\right\}\right\}$$

(A-11)

$$a_n = \cfrac{-\,i\,\dfrac{(2n-1)!!\,(2n+1)!!}{(n+1)\,x^{2n+1}\left[(1-\alpha)^2+\beta^2\right]}}{(1-\alpha)\left\{aa+n+1+x^2\,\dfrac{(2n+1)(n+1+(n-2)\alpha)}{(2n-1)(2n+3)}\cdots\right\}-\beta^2\left[aa+x^2\,\dfrac{(2n+1)(n-2)}{(2n-1)(2n+3)}\cdots\right]}$$
$$+\,i\beta(1-\omega)\left[n+x^2\,\dfrac{(2n+1)(n-2)}{(2n-1)(2n+3)}\cdots\right]+\left[aa+n+1+x^2\,\dfrac{(2n+1)(n+1+(n-2)\alpha)}{(2n-1)(2n+3)}\cdots\right]\left\}\right\}$$

(A-12)

The maximum value of $(Q_{abs})_n = \dfrac{2n+1}{2x^2}$ will occur for $\varepsilon_0 = \dfrac{1}{2+i0}$.

whence $0 = (1-\alpha)\left[aa+n+1+x^2\,\dfrac{(2n+1)(n+1+(n-2)\alpha)}{(2n-1)(2n+3)}\cdots\right]-\beta^2\left[n+x^2\,\dfrac{(2n+1)(n-2)}{(2n-1)(2n+3)}\cdots\right]$

(A-13)

and $1 = \cfrac{(2n-1)!!\,(2n+1)!!\,\beta}{(n+1)\,x^{2n+1}\left[(1-\alpha)^2+\beta^2\right]}\left\{(1-\alpha)\left[aa+x^2\,\dfrac{(2n+1)(n-2)}{(2n-1)(2n+3)}\cdots\right]+\left[aa+n+1+x^2\,\dfrac{(2n+1)(n+1+(n-2)\alpha)}{(2n-1)(2n+3)}\cdots\right]\right\}$

(A-14)

These equations determine α and β for maximum $(Q_{ab})_a$. The lowest-order approximations are:

$$0 = (1-\alpha)[\alpha+1-\alpha\beta^2] \tag{A-15}$$

$$1 = \frac{(2\alpha-1)!!\,(2\alpha+1)!!\,(\alpha+2)}{(\alpha+1)\,x^{2\alpha-1}[(1-\alpha)^2+\beta^2]}\,\beta \tag{A-16}$$

Since we have effectively let $x \to 0$, we must have $\beta \to 0$ $(x^{2\alpha+1}\to 0)$, whence from the first equation $\alpha \to -\dfrac{\alpha+1}{\alpha}$. Then the second equation becomes:

$$1 = \frac{(2\alpha-1)!!\,(2\alpha+1)!!\,(\alpha+2)_a^2}{(\alpha+1)(2\alpha+1)^2}\frac{\beta}{x^{2\alpha+1}} \quad\text{or}\quad \beta = \frac{(\alpha+1)(2\alpha+1)}{[(2\alpha-1)!!]^2(\alpha+2)_a^2}\,x^{2\alpha+1} \tag{A-17}$$

The next-order approximation to the first equation gives:

$$(1-\alpha)\left[\alpha+\alpha+1+x^2\,\frac{(2\alpha+1)(\alpha+1)+(\alpha-2)\alpha}{(2\alpha-1)(2\alpha+3)}\right] = \emptyset \tag{A-18}$$

$$\alpha = \left\{\alpha+\frac{(2\alpha+1)(\alpha-2)}{(2\alpha-1)(2\alpha+3)}x^2\right\} = -\left[\alpha+1+x^2\,\frac{(\alpha+1)(2\alpha+1)}{(2\alpha-1)(2\alpha+3)}\right] \propto \alpha = -\frac{\alpha+1}{\alpha}\,\frac{\alpha+1+x^2\,\frac{(2\alpha+1)(\alpha+1)}{(2\alpha-1)(2\alpha+3)}}{\alpha+x^2\,\frac{(2\alpha+1)(\alpha-2)}{(2\alpha-1)(2\alpha+3)}} \tag{A-19}$$

$$\alpha = -\left[\frac{\alpha+1}{\alpha}+x^2\,\frac{(2\alpha+1)(\alpha+1)}{\alpha(2\alpha-1)(2\alpha+3)}\right]\left[1-x^2\,\frac{(2\alpha+1)(\alpha-2)}{\alpha(2\alpha-1)(2\alpha+3)}\right] = -\frac{\alpha+1}{\alpha}\left[1+x^2\,\frac{(2\alpha+1)(\alpha+1)}{(2\alpha-1)(2\alpha+3)}-x^2\,\frac{2(2\alpha+1)}{\alpha(2\alpha-1)(2\alpha+3)}\right] \tag{A-20}$$

Thus the maximum value of Q_{abs} $\left(\text{i.e. } \left[\frac{2n+1}{2x^2}\right]\right)$ is attained for:

$$a = -\left[-2 - \frac{12}{5} x^2\right] \quad , \quad \beta = 2x^3 \quad \text{(Electric dipole) (n = 1)} \tag{A-21}$$

$$a = -\left[-\frac{3}{2} + \frac{5}{14} x^2\right] \quad , \quad \beta = \frac{1}{3} x^5 \quad \text{(Electric quadrupole) (n = 2)} \tag{A-22}$$

173

SPECIAL REPORTS

No. 1. Today's Meteorological Rocket Network and Atmospheric Problems of Aerospace Vehicles, *Norman Sissenwine, May 1964, (REPRINT).*

No. 2. Ferrimagnetic Resonance Relations for Magnetocrystalline Anisotropy in Cubic Crystals, *Hans Roland Zapp, April 1964.*

No. 3. Worldwide Collection and Evaluation of Earthquake Data, Final Report on Evaluation of 1960 Seismicity, *R.L. Fisher, R.G. Baker and R.R. Guidroz, June 1964.*

No. 4. Visual Observations Beneath a Developing Tornado, *Ralph J. Donaldson, Jr. and William E. Lamkin, August 1964 (REPRINT).*

No. 5. Bibliography of Rock Deformation, *R.E. Riecker, 1/Lt, USAF, September 1964.*

No. 6. The Modification of Electromagnetic Scattering Cross Sections in the Resonant Region, A Symposium Record, Volume I, *J.K. Schindler, 1/Lt, USAF, R.B. Mack, Editors, September 1964.*